

MESOSCALE STRUCTURAL AND MECHANICAL SIMULATIONS OF CROSS-LINKED
CARBON NANOTUBE MATERIALS

by

ABU HORAIRA BANNA

ALEXEY N. VOLKOV, COMMITTEE CHAIR

KEIVAN DAVAMI

MATTHEW KASEMER

KASRA MOMENI

NING ZHANG

A DISSERTATION

Submitted in partial fulfilment of the requirements
for the degree of Doctor of Philosophy in the
Department of Mechanical Engineering
in the Graduate School of
The University of Alabama

TUSCALOOSA, ALABAMA

2021

Copyright Abu Horaira Banna 2021

ALL RIGHTS RESERVED

ABSTRACT

Relatively poor mechanical properties of carbon nanotube (CNT) bulk materials can be improved by formation of bonds or covalent cross-links (CLs) between nanotubes. In this work, an “effective bond model” of covalent CLs between carbon nanotubes is developed for mesoscopic simulations of cross-linked CNT materials. A general approach for fitting the CL model parameters based on results of atomistic simulations is developed. The best-fit parameters of the CL model are found. The developed effective bond model of CLs is included into a dynamic mesoscopic model of CNT materials, where each nanotube is represented in the form of a chain of stretchable cylindrical segments. The mesoscopic force field in this model accounts for stretching and bending of CNTs, van der Waals interaction between nanotubes, and inter-tube CLs. The model is applied to generate and equilibrate *in silico* pristine and cross-linked CNT fiber and film samples with structural characteristics close to observed in experiments. The structural parameters of CNT fibers and films, including the average bundle size, Herman orientation factor, and tortuosity, are calculated. The quasi-static simulations of large-scale cross-linked CNT films are performed to reveal the load transfer mechanism, as well as effects of CNT length, CL density, material density, and network morphology on mechanical properties under conditions of quasi-static deformation. It is found that stretching of CNT segments is the dominant mode of load transfer in cross-linked CNT film during their stretching, while bending and buckling is the dominant mode of load-transfer during compression. Both tensile modulus and strength of CNT films increase strongly with increasing CNT length. The effect of the nanotube length on mechanical properties, however, is altered by the density of CLs. The mutual effect of the nanotube length and CL density on modulus and strength is described by power scaling laws, where the modulus and strength are functions of the average number of CLs per

nanotube, i.e., the product of the CNT length and CL linear density. The exponents in the scaling laws for the modulus and strength are strongly different from each other. The material density of the film samples weakly affects the specific mechanical properties. The dispersion of nanotubes in the films without formation of thick bundles results in the few-fold increase of the modulus and strength. In qualitative agreement with experimental observations, the in-plane compression of a large thin CNT film results in collective bending of nanotubes and folding of the whole film with minor irreversible structural changes. Depending on the CNT length, the reliefs of the compressed films vary from quasi-one-dimensional wavy surface to complex two-dimensional landscape.

ACKNOWLEDGEMENTS

I would like to thank my adviser, Dr. Alexey N. Volkov, for his continued guidance and support throughout my graduate studies. I am thankful for this opportunity to work with Dr. Volkov who inspired me for the continued research work and continuously motivated me towards excellence. I am forever grateful for the countless hours he spent mentoring, teaching, advising, supporting, and helping me whenever needed regardless how small or what the problem is. All the experiences I gained working with him have laid a strong foundation for my future growth.

I would like to thank the committee members, Dr. Keivan Davami, Dr. Matthew Kasemer, Dr. Kasra Momeni, and Dr. Ning Zhang for their time and support in the completion of the degree. I highly appreciate all the feedbacks and suggestions from the committee members for the improvement of overall quality of my dissertation.

Finally, to my family and friends who lent their time and support during my studies. It would not have been the same without all of you.

This work is supported by NASA Early Stage Innovation grant (NNX16AD99G) and National Science Foundation (award CMMI- 1554589).

CONTENTS

| | |
|--|------|
| ABSTRACT..... | ii |
| ACKNOWLEDGEMENTS..... | iv |
| LIST OF TABLES..... | vii |
| LIST OF FIGURES..... | viii |
| 1 INTRODUCTION..... | 1 |
| 1.1 Carbon Nanotubes and Carbon Nanotube Materials..... | 1 |
| 1.2 Mechanical Properties of CNT Materials..... | 4 |
| 1.3 Mesoscale Modeling of CNT Materials..... | 9 |
| 1.4 Objectives and Outline..... | 11 |
| 2 MESOSCOPIC MODEL OF CROSS-LINKED CNT MATERIALS..... | 14 |
| 2.1 Mesoscopic Model for Dynamic Simulations of CNT Materials..... | 14 |
| 2.1.1 Stretching term of MFF..... | 18 |
| 2.1.2 Bending term of MFF..... | 19 |
| 2.1.3 Inter-tube interaction potential..... | 21 |
| 2.2 Mesoscopic Model of CLs and Its Parameterization..... | 26 |
| 2.2.1 Atomistic simulations of the pullout of a nanotube from a seven-tube bundle..... | 27 |
| 2.2.2 Model of a cross-linked CNT bundle..... | 30 |
| 2.2.3 Effective CL bond models..... | 37 |
| 2.2.4 Effective bond model for large-scale mesoscopic simulations of cross-linked CNT materials..... | 50 |
| 2.2.5 Pullout simulations of a central tube from a seven-tube bundle for regular and random distribution of CLs..... | 54 |
| 2.3 In-house Computational Code..... | 59 |
| 3 IN SILICO GENERATION AND STRUCTURAL CHARACTERIZATION OF CNT MATERIAL SAMPLES..... | 60 |
| 3.1 CNT Fibers..... | 60 |

| | | |
|-------|--|-----|
| 3.1.1 | <i>In silico</i> generation of (10,10) CNT fibers | 62 |
| 3.1.2 | Structural characterization of <i>in silico</i> generated (10,10) CNT fibers..... | 65 |
| 3.2 | CNT Films | 71 |
| 3.2.1 | <i>In silico</i> generation and characterization of (10,10) CNT films | 73 |
| 3.2.2 | <i>In silico</i> generation and characterization of cross-linked (26,0) CNT films | 77 |
| 4 | QUASI-STATIC MECHANICAL SIMULATIONS OF CROSS-LINKED CNT FILMS .. | 84 |
| 4.1 | Computational Setup for In-plane Tension and Compression of CNT Films | 84 |
| 4.2 | Load Transfer in CNT Films at Stretching | 86 |
| 4.3 | Effects of the Nanotube Length and CL Density on the Mechanical Properties of CNT Films Under Tension | 96 |
| 4.4 | Mechanisms of Irreversible Structural Changes and Appearance of Percolating Load Transfer Networks in Cross-linked Films at Tension | 105 |
| 4.5 | Effects of Random Distribution of the Nanotube Length..... | 113 |
| 4.6 | Effects of the Network Structure | 115 |
| 4.7 | Effects of Material Density..... | 120 |
| 4.8 | In-Plane Compression of Cross-Linked CNT Films..... | 122 |
| 4.9 | Effects of Nanotube Length and Network Morphology on the Compression Modes 128 | |
| 5 | CONCLUSIONS | 135 |
| 5.1 | Summary of Results Obtained in the Present Study | 135 |
| 5.2 | Directions for Future Research | 139 |
| 6 | REFERENCES | 141 |

LIST OF TABLES

| | |
|---|-----|
| Table 2.1. Stiffness E_p , maximum stress S_p, max , and displacement Δz_{max} at $S_p = S_p, max$ obtained in Ref. [77] in atomistic simulations of the pullout of a central nanotube from bundles composed of seven (26,0) CNTs at two sets of CL densities n_0 and n_1 | 30 |
| Table 2.2. Best-fit parameters ϵ_0 , r_0 , and a of the CL potential function, Eq. (2.34), and direction parameter γ in Eqs. (2.36) - (2.39) obtained by fitting the stiffness E_p , maximum stress S_p, max , and displacement Δz_{max} at $S_p = S_p, max$, predicted by the bundle model to values given in Table 2.1. The parameters of the cutoff function $S(\tau(r))$ in Eq. (2.34) are equal to $r^* = 3.2 \text{ \AA}$ and $rc = 4.4 \text{ \AA}$ | 49 |
| Table 3.1 Parameters of CNT film samples (lateral size L , thickness H , material density ρ , linear CL density n_{CL} , volumetric CL density $n_{CL, V}$, number of CNTs N_{CNT} , number of CLs N_{CL} , considered in simulations. All samples consist of (10,10) CNTs of 200 nm length each. | 77 |
| Table 3.2. Total number of CNTs, average number of CNTs in the bundle cross section N_B , average bundle diameter D , most probable bundle diameter D_0 , and maximum bundle diameter D_{max} for the <i>in silico</i> generated CNT film samples with continuous and dispersed network structures and various nanotube length LT at a material density $\rho = 0.1 \text{ gcm}^{-3}$. All samples have size $2.5 \mu\text{m} \times 2.5 \mu\text{m} \times 40 \text{ nm}$. In the sample CNW, the random lengths of individual nanotubes in the range $100 \text{ nm} \leq LT \leq 2000 \text{ nm}$ are generated based on Eq. (3.1) at $b = 2.08$ and $a = 430 \text{ nm}$. The samples CN200 – CNW are used for simulation at CL densities from 0.05 nm^{-1} to 2.5 nm^{-1} . The approach for generation of samples DN200 and DN1000 with dispersed nanotubes is described in section 4.6. These two samples are generated at a CL density of 0.05 nm^{-1} | 83 |
| Table 4.1. Root-mean-square (RMS) deviations of values of the tensile modulus E (GPa) and strength S_{max} (MPa) obtained in simulations with samples CN200 – CN1000 in Table 3.2 from the approximations given by Eqs. (4.1), (4.2), (4.3), and (4.4). | 105 |
| Table 4.2. Initial slope of a stress-strain curve E , strength S_{max} , and strain ϵ_{max} at $S = S_{max}$ obtained at stretching of the CNT films samples CN200, DN200, CN1000, and DN1000. | 119 |

LIST OF FIGURES

Figure 1.1. Sketch illustrating formation of a SWCNT from a 2D graphene sheet: (a), side view of an armchair (10,10) CNT with green spheres representing individual carbon atoms; (b), schematic diagram of a 2D graphene sheet rolling into CNT, where \mathbf{Ch} is the chiral vector and \mathbf{Tr} is the translational vector, $\mathbf{Ch} \perp \mathbf{Tr}$ 2

Figure 1.2. Schematic representation of CNT forests, films and fibers (a) [25], SEM image of *in situ* CNT forest (b) [26], film c) [27] and fiber (d) [25]. 3

Figure 1.3. Stress-strain curve of SWCNT films obtained at tensile loading of purified HiPCO SWCNT film (dash-dot green line), as-prepared annealed Elicarb SWCNTs (dashed red line), octadecylamine (ODA) functionalized CNT film (dash-dot-dot orange line), and heavily functionalized -COOH CNT film (solid blue line). The curves are reproduced from Ref. [54]. ... 5

Figure 1.4. Irradiated SWCNT bundles with incident energy and doses 100 eV, 19.65 MGy (a) and 200 eV, 39.3 MGy (b) (deposited atoms are colored red, and CNT atoms are colored blue). Panel (c) shows the pullout stress versus pullout distance for pristine and irradiated bundles [76, 77]. . 8

Figure 1.5. TEM images of cross-linked tubes extracted from the irradiated SWCNT fabrics (a)-(b). Electron beam irradiation improvement of mechanical properties in SWCNT membranes/fabrics under tension (c), tensile modulus E (blue curve) and strength (red curve) versus irradiation dose. Results are reproduced from Ref. [68]. 9

Figure 2.1. Schematic representation of a nanotube section consisting of two mesoscopic segments and three nodes along with a matrix molecule. The position of i th node \mathbf{rit} in the nanotube, radius Rit of the nanotube at node i , torsion angle θ_{it} at node i , position \mathbf{rkm} of matrix molecule k , and radius Rkm of the matrix molecule k are the independent variables that describe the collective dynamics of nanotubes in matrix. The size of the nanotube and matrix molecule are not shown to scale..... 17

Figure 2.2. Schematic representation of bending buckling in the mesoscopic model (a) and the dependence of the bending energy U_{bnd} on the bending angle θ in uniformly bent CNT with a single buckling point appearing in the middle (point B in the inset) when the critical radius of curvature, R_{cr} , is reached (b). The bending energy in (b) is calculated with Eq. (2.10) for $\theta < \theta_{cr}$ and is obtained by minimization of the strain energy associated with bending and buckling, and with Eq. (2.11) $\theta > \theta_{cr}$ [92]. 21

Figure 2.3. Schematic sketch illustrating the introduction of local coordinates $Oxyz$ and geometrical parameters used for characterization of the relative positions of two nonparallel (a) and parallel (b) straight cylindrical CNT segments. The side and top views are shown in panel a; only the side view is shown in panel b. In panel a, the axis x is directed along the segment OO' defining the shortest distance between the axes of the segments. In panel b, the origin of the Cartesian coordinates is chosen so that the axis Ox goes through the left end of the second segment

($\eta_1 = 0$). Cross sections of the segments are shown in panel b, with angles ϕ_1 and ϕ_2 specifying positions of points in the cross sections used for integration over the surfaces of the two segments [91]...... 24

Figure 2.4. Idealized bundle of seven (26,0) SWCNTs of radius $RT = 10.185 \text{ \AA}$ and length $LT = 59.6 \text{ \AA}$ (a) and stress-displacement curve obtained in atomistic simulations of the pullout of the central CNT from the bundle at a linear CL density $n_0 = 0.49 \text{ \AA}^{-1}$ [56] (b). 29

Figure 2.5. Sketch illustrating the initial positions of the central ($k = 1$) and surrounding ($k = 2$) nanotubes and their position in the course of pullout simulations, when CLs are described by the center-to-center geometrical bond model, Eqs. (2.36)-(2.37), (a) and surface-to-surface geometrical bond model, Eqs. (2.38)-(2.39), (b). CLs with initial tilting $\pm b$ are assumed to be continuously distributed along the bundle axis Oz with linear density n_0 , however, only a single CL with positive tilting ($+b$) is shown in the sketch. The angle θ , defining the direction of the effective CL bond, is equal to the angle θ_{12} , characterizing the direction of the CL force and given by Eqs. (2.37) or (2.39), only if the direction parameter γ is equal to 1..... 34

Figure 2.6. Linear potential energy density $uvdW$ of van der Waals interaction between two parallel, straight, and infinitely long (26,0) CNTs versus inter-tube gap δh calculated based on the mesoscopic tubular potential [91] (solid curve), best fit provided by Eq. (2.25) (dashed curve), and harmonic approximation of the tubular potential (dash-dotted curve). 35

Figure 2.7. Stress Sp versus displacement Δz obtained in pullout simulations for a seven-tube bundle with a length of 59.6 \AA composed of (26,0) CNT at CL densities $n_0 = 0.49 \text{ \AA}^{-1}$ and $n_1 = 0.8 \text{ \AA}^{-1}$. The thick solid curve (red) is obtained in atomistic simulations in Ref. [77]. Other curves are obtained based on solution of Eqs. (2.23) with various r_0 , ϵ_0 , a , b and γ , which allow one to fit values of Ep , Sp , max , and Δz_{max} in Table 2.1. In panel (a), dashed (C-C GBM, $r_0 = 3.334 \text{ \AA}$, $\epsilon_0 = 16.54 \text{ eV}$, $a = 6 \text{ 1/\AA}$, $b = 1.07 \text{ \AA}$; green) and dash-dotted (S-S GBM, $r_0 = 2.4 \text{ \AA}$, $\epsilon_0 = 17.9 \text{ eV}$, $a = 1.9 \text{ 1/\AA}$, $b = 1.3 \text{ \AA}$; blue) curves are obtained at $\gamma = 1$. In the panel (b), dashed ($r_0 = 1.225 \text{ \AA}$, $\epsilon_0 = 27.94 \text{ eV}$, $a = 1.2 \text{ 1/\AA}$, $\gamma = 0.65$; green), dash-dotted ($r_0 = 1.958 \text{ \AA}$, $\epsilon_0 = 16.1 \text{ eV}$, $a = 1.4 \text{ 1/\AA}$, $\gamma = 0.63$; blue), and dash-double-dotted ($r_0 = 2.203 \text{ \AA}$, $\epsilon_0 = 14.14 \text{ eV}$, $a = 1.6 \text{ 1/\AA}$, $\gamma = 0.6$; cyan) curves are obtained with the S-S GBM at $b = 0$. The thick curves are calculated assuming variable gap δh between CNTs, which is determined by the Eq. (2.24), while the thin curves in panel (a) are obtained with $\delta h = \delta h_0 = const$ 43

Figure 2.8. Values of parameters r_0 (squares, red), ϵ_0 (triangles, green), and γ (circles, blue) for C-C (a,c) and S-S (b,d) GBMs versus parameters a , which allow one to fit values of Ep , Sp , max , and Δz_{max} obtained in atomistic simulations (Table 2.1) at $n_0 = 0.12 \text{ \AA}^{-1}$ and $n_1 = 0.55 \text{ \AA}^{-1}$ (a,b), as well as at $n_0 = 0.49 \text{ \AA}^{-1}$ and $n_1 = 0.8 \text{ \AA}^{-1}$ (c,d). The symbols correspond to calculated points, while the curves represent the spline functions that interpolate the calculated data and are drawn only to guide the eye. 46

Figure 2.9. Stress Sp versus displacement Δz obtained in the pullout simulations for a seven-tube bundle with length of 59.6 \AA composed of (26,0) CNT at $n_0 = 0.12 \text{ \AA}^{-1}$ and $n_1 = 0.55$

\AA^{-1} (a), as well as at $n_0 = 0.49 \text{\AA}^{-1}$, $n_1 = 0.8 \text{\AA}^{-1}$ (b). The solid curves (red) are obtained in atomistic simulations [77]. Other curves are obtained based on the bundle model with the best-fit parameters in Table 2.2 for the C-C GBM (green dashed curves) and S-S GBM (blue dash-dotted curves)..... 48

Figure 2.10. Stress S_p versus displacement Δz obtained in the pullout simulations of the central nanotube from a seven-tube with a length of 59.6\AA composed of (26,0) CNT. The solid curves are obtained in atomistic simulations [77]. The dashed curves are obtained based on the bundle model and S-S GBM with the parameter set $PH2$ in Table 2.2. The CL density n_0 is equal to 0.29\AA^{-1} (curves 1, red), 0.49\AA^{-1} (curves 2, green), 0.62\AA^{-1} (curves 3, blue), and 0.84\AA^{-1} (curves 4, cyan)..... 50

Figure 2.11. Sketch illustrating definitions of the effective CL bond (dashed line segments; red) between two cylindrical CNT segments, which are utilized in C-C (a) and S-S (b) GBMs. In panel (b), the sketch is simplified, since each vector \mathbf{s}_i is assumed to be orthogonal to vector $\mathbf{r}_{i2} - \mathbf{r}_{i1}$ and co-planar with vectors $\mathbf{r}_{i2} - \mathbf{r}_{i1}$ and $\mathbf{r}_2 - \mathbf{r}_1$ 51

Figure 2.12. Stress S_p versus displacement Δz obtained in the pullout simulations for a seven-tube bundle of length $LT = 12 \text{ nm}$ composed of (26,0) CNT. The dash-double-dotted thin curve is obtained based on Eq. (2.23) at the CL densities $n_0 = n_1 = 0.3 \text{\AA}^{-1}$. Other curves are obtained with the general mesoscopic model at $\Delta lS = 2 \text{ nm}$ (solid thick curves, red) and $\Delta lS = 0.5 \text{ nm}$ (dash-dotted curves, green, and solid thin curve, blue). The mesoscopic simulations are performed with regular (a) and random (b) CL distributions at a temperature of 1 K with exception of the solid thin curve in panel (a), which is obtained at $T = 300 \text{ K}$. Three solid thick curves in panel (b) (red) correspond to three random CL distributions..... 56

Figure 2.13. Stress S_p versus displacement Δz obtained in the pullout simulations for a seven-tube bundle of length $LT = 60 \text{ nm}$ composed of (26,0) CNTs. The dash-double-dotted thin curve is obtained based on Eq. (2.23) at the CL densities $n_0 = n_1 = 0.3 \text{\AA}^{-1}$. Other curves are obtained based on the general mesoscopic model with the regular (a) and random (b) CL distributions at a temperature of 1 K and $\Delta lS = 2 \text{ nm}$ (solid curves, red), $\Delta lS = 1 \text{ nm}$ (dashed curve, blue), and $\Delta lS = 0.5 \text{ nm}$ (dash-dotted curves, green). 58

Figure 3.1. Schematic representation of the procedure used for the generation of CNT fiber samples. The straight CNTs are first randomly added with random inclination with respect to the fiber axis Θ ranging uniformly from zero to a maximum angle Θ_{max} (a). The high temperature annealing followed by a relaxation at 300 K is used to induce self-organization of CNTs into a continuous and metastable network of interconnected bundles (b). Nanotube segments in panel (b) are colored according to their local bundle size..... 62

Figure 3.2. Side and top views of relaxed samples of CNT fibers composed of 400-nm-long (10,10) SWCNTs obtained at various maximum angles of initial inclination of CNTs Θ_{max} equal to 30° (a), 15° (b), 30° (c), and 45° (d). All generated samples have dimensions of $1 \times 1 \times 1 \mu\text{m}^3$ and a material density of 0.01 gcm^{-3} . The figure demonstrates only the central parts of every sample

with the cross section of $500 \text{ nm} \times 500 \text{ nm}$. Individual nanotubes are colored according to the local thickness of bundles defined as the number of segments in a bundle cross-section (a). In every panel, the fiber axis is directed vertically in the top snapshot and normal to the plane of the figure in the bottom snapshot. 64

Figure 3.3. The bundle thickness distributions calculated for computational samples of CNT fibers shown in Figure 3.2 and obtained at various maximum angles of initial inclination of CNTs Θ_{max} equal to 30° (a), 15° (b), 30° (c), and 45° (d). The bundle thickness is expressed in the local number of CNTs present in a bundle cross section, and each bin covers a thickness increment by 1 CNT segment. 67

Figure 3.4. Probability density function of the local angle between the CNT centerline and axis of the fiber calculated for computational samples of CNT fibers shown in Figure 3.2 and obtained at various maximum initial inclination angles of CNT Θ_{max} equal to 30° (circles, red), 15° (nablas, green), 30° (squares, blue), and 45° (triangles, magenta). 68

Figure 3.5. Herman orientation function (HOF, diamonds), average bundle size (NB , circles), and average tortuosity of nanotubes (τ , squares) versus maximum angle of initial inclination of CNT, Θ_{max} , used in the generation of relaxed CNT fibers composed of (10,10) CNTs of 400 nm length each at material density 0.01 gcm^{-3} . The vertical error bars show the mean square deviation of the average tortuosity and bundle size. 70

Figure 3.6. Sketch illustrating the *in silico* preparation of cross-linked CNT films with continuous networks of bundles of nanotubes and subsequent mechanical loading: The initial sample consisting of straight and dispersed nanotubes (a) is subjected to a dynamic simulations at constant mesoscopic temperature and sample volume leading to spontaneous self-assembly of CNTs into a network of bundles. The relaxed sample with a network of bundles (b) is modified by randomly distributed CLs and relaxed again to remove local stresses induced by the disparity between the equilibrium CL length and gaps between nanotubes. The relaxed cross-linked sample (c) is subjected to in-plane stretching or compression, which can result, e.g., in inhomogeneous compression of the film (d). In panel (c), the individual CLs are shown as red spheres. The individual snapshots in panel (a)-(d) are obtained in actual simulations and shown at different degrees of magnification. The distribution of CLs in (c) corresponds to the CL density $n_{CL} = 0.05 \text{ nm}^{-1}$ 72

Figure 3.7. Top views of CNT film samples: (a), sample C_0 , $\rho = 0.05 \text{ gcm}^{-3}$; (b), sample B_0 , $\rho = 0.1 \text{ gcm}^{-3}$; (c), sample A_0 , $\rho = 0.2 \text{ gcm}^{-3}$; and (d), sample D_0 , $\rho = 0.4 \text{ gcm}^{-3}$. The major parameters of the samples can be found in Table 3.1. The sample structures are obtained during 1.1 ns of relaxation before distribution of the CLs. The CNT segments are colored according to their local bundle-thickness, NB . In panels (a) and (b), the whole samples are shown. In panels (c) and (d), only top 40 nm of the samples is visualized. 74

Figure 3.8. Probability density function of the local bundle thickness NB for the four samples B_0 ($\rho = 0.05 \text{ gcm}^{-3}$, cyan curve), C_0 ($\rho = 0.1 \text{ gcm}^{-3}$, blue curve), A_0 ($\rho = 0.2 \text{ gcm}^{-3}$, green curve), and D_0 ($\rho = 0.4 \text{ gcm}^{-3}$, red curve) shown in Figure 3.7. 75

Figure 3.9. Magnified top view of a part of the cross-linked CNT film (sample A_0 , $\rho = 0.2 \text{ gcm}^{-3}$, $nCL = 0.015 \text{ nm}^{-1}$) after relaxation. The CL ends are shown by red dots. 76

Figure 3.10. Top views of CNT films with continuous networks of bundles composed of CNTs of various lengths: $LT = 200 \text{ nm}$ (sample CN200, a), $LT = 400 \text{ nm}$ (sample CN400, b), and $LT = 1000 \text{ nm}$ (sample CN1000, c). Each panel shows the full sample in the horizontal direction and only a quarter of the whole sample in the vertical direction. The individual nanotubes are colored according to the local bundle size NB and the color table for NB shown in panel (a). 79

Figure 3.11. Probability density functions of local bundle size NB (number of nanotubes in the bundle cross section) in $(26, 0)$ CNT films with the nanotube length $LT = 200 \text{ nm}$ (sample CN200, red square) and $LT = 1000 \text{ nm}$ (sample CN1000, green circles) shown in Figure 3.10 (a) and (c). The symbols correspond to calculated values, while the curves are drawn only to guide the eye. 80

Figure 4.1. Computation setup for deformation process in mesoscopic simulations: (a) original approach where the mesoscopic nodes in the clip layers (part of the sample where tubes are colored grey) are moved in opposite directions along Ox axis with constant velocity $VD/2 = 5 \text{ ms}^{-1}$, (b) modified approach, where the positions of all mesoscopic nodes in the deformable part of the film, as well as position of the clip layers, are scaled with the scaling coefficient $VD\Delta t + LD_0/LD_0$ 85

Figure 4.2. Top views of the stretched CNT film at an engineering strain of 0.2. Individual CNTs are colored according to their local strain ϵ . Both (a) and (b) show the same sample, but in (b) all CNT segments where $|\epsilon| \leq 0.004$ are blanked. In panel (a), the letter “L” marks the position of the loop formed during stretching. The black rectangles mark boundaries of the non-deformed sample. 87

Figure 4.3. Top views of a fragment of the CNT film obtained in the course of stretching at engineering strains of 0.11 (a), 0.16 (b), and 0.2 (c). The snapshots illustrate formation of a loop by a bundle marked as L in Figure 4.2(a). Sketch in panel (d) schematically illustrates the loop formation process. 88

Figure 4.4. Side views of the CNT film in the course of stretching in the in-plane (horizontal) direction at various strains: (a), $\epsilon = 0.022$; (b), $\epsilon = 0.056$; (c), $\epsilon = 0.11$; and (d), $\epsilon = 0.2$. Individual CNTs are colored according to the local strain with the color tables given in Figure 4.3(c). 90

Figure 4.5. Total energies of stretching U_{str} , bending U_{bnd} , van der Waals interaction U_{vdW} , and CL U_{CL} versus engineering strain ϵ obtained during stretching simulation of the CNT film. 91

Figure 4.6. Top views of the cross-linked CNT film sample in the course of stretching at engineering strains of 0.011 (a), 0.022 (b), 0.033 (c), and 0.078 (d). The snapshots show only mesoscopic elements of CNTs, where the local strain ϵ exceeds 0.004, while all other elements are blanked. The nanotubes are colored according to the local strain ϵ 93

Figure 4.7. Dependences of the engineering stress S (a) and fraction of broken CLs (b) on the engineering strain ϵ obtained during stretching simulations of the CNT film with C-C (red) and S-S (green) GBMs. The simulations are performed with the best-fit parameter sets $PL1$ and $PL2$ in Table 2.2. The vertical dashed and dash-dotted lines indicate the magnitudes of strain corresponding to the nominal elastic limit $\epsilon E = 0.0045$ and strain at maximum stress $\epsilon_{max} = 0.026$. The simulations with C-C GBM are performed until $\epsilon = 0.08$. In panel (a), letters “A,” “B,” and “C” mark local maximums of stress. 95

Figure 4.8. Stress S versus engineering strain ϵ obtained at stretching of CNT films at a CL density $n_{CL} = 0.05 \text{ nm}^{-1}$ (a), $n_{CL} = 0.2 \text{ nm}^{-1}$ (b), $n_{CL} = 0.5 \text{ nm}^{-1}$ (c), and $n_{CL} = 2.5 \text{ nm}^{-1}$ (d) for various CNT lengths: $LT = 200 \text{ nm}$ (sample CN200, red curves), $LT = 400 \text{ nm}$ (sample CN400, green curves), and $LT = 1000 \text{ nm}$ (sample CN1000, blue curves). 98

Figure 4.9. Tensile modulus E (a), strength S_{max} (b), and strain ϵ_{max} at $S = S_{max}$ (c) versus nanotube lengths LT obtained at stretching of CNT films at a CL density $nL = 0.05 \text{ nm}^{-1}$ (red squares), $nL = 0.2 \text{ nm}^{-1}$ (green triangles), $nL = 0.5 \text{ nm}^{-1}$ (blue diamonds), and $nL = 2.5 \text{ nm}^{-1}$ (cyan circles). In panels (a) and (b), the bold symbols are obtained in mesoscopic simulations, while the corresponding empty symbols represent values of E and S_{max} calculated based on Eqs. (4.3) and (4.4) with the best-fit parameters. The bold symbols correspond to calculated values, while the curves are drawn only to guide the eye. 99

Figure 4.10. Tensile modulus E (a) and strength S_{max} (b) versus average number of CLs per nanotube $N = LTn_{CL}$ obtained at stretching of CNT films with a CL density $n_{CL} = 0.05 \text{ nm}^{-1}$ (red squares), $n_{CL} = 0.2 \text{ nm}^{-1}$ (green triangles), $n_{CL} = 0.5 \text{ nm}^{-1}$ (blue diamonds), and $n_{CL} = 2.5 \text{ nm}^{-1}$ (cyan circles) and with a CNT length $LT = 200 \text{ nm}$, 400 nm , and 1000 nm . The dashed curves in panels (a) and (b) are calculated based on Eqs. (4.1) and (4.2), respectively. 101

Figure 4.11. Reduced modulus E/N (a) strength S_{max}/N (b) versus nanotube lengths LT obtained at stretching of CNT films at a linear CL density $n_{CL} = 0.05 \text{ nm}^{-1}$ (red squares), $n_{CL} = 0.2 \text{ nm}^{-1}$ (green triangles), $n_{CL} = 0.5 \text{ nm}^{-1}$ (blue diamonds), and $n_{CL} = 2.5 \text{ nm}^{-1}$ (cyan circles). The symbols correspond to calculated values, while the curves are drawn only to guide the eye. 102

Figure 4.12. Reduced modulus E/N (a) strength S_{max}/N (b) versus linear CL density n_{CL} obtained during stretching of CNT films with a CNT length $LT = 200 \text{ nm}$ (red squares), $LT =$

400 nm (green triangles), and $LT = 1000$ nm (blue diamonds). The symbols correspond to calculated values, while the curves are drawn only to guide the eye. 103

Figure 4.13. Tensile modulus E versus parameter $N/nCL\gamma$ at $\gamma = 0.25$ (a) and strength S_{max} versus parameter $N/nCL\delta$ at $\delta = 0.07$ (b), obtained at stretching of CNT films with a CL density $nCL = 0.05$ nm⁻¹ (red squares), $nCL = 0.2$ nm⁻¹ (green triangles), $nCL = 0.5$ nm⁻¹ (blue diamonds), and $nCL = 2.5$ nm⁻¹ (cyan circles) and with a CNT length $LT = 200$ nm, 400 nm, and 1000 nm. The symbols correspond to calculated values presented in Figure 4.9. The dashed curves in panels (a) and (b) are calculated based on Eqs. (4.3) and (4.4), respectively..... 104

Figure 4.14. Fraction of broken CLs fb (a) and average bundle size NB b versus engineering strain ϵ obtained at stretching of CNT films with continuous networks of bundles at a CL density $nCL = 0.5$ nm⁻¹ and CNT length $LT = 200$ nm (sample CNT200, red curves), $LT = 400$ nm (sample CN400, green curves), and $LT = 1000$ nm (sample CN1000, blue curves).). In panel (b), the symbols correspond to calculated values, while the curves are drawn only to guide the eye. ... 106

Figure 4.15. Top view of the CNT film sample CN1000 (sample CN1000, $LT = 1000$ nm, $nCL = 0.5$ nm⁻¹) stretched to an engineering strain $\epsilon = 0.0425$. The individual nanotubes are colored according to their local strain ϵ . The black rectangles correspond to the non-deformable clip layers at the left and right boundaries of the sample. 108

Figure 4.16. Probability density functions of local nanotube strain ϵ calculated for non-deformed films with the continuous networks of bundles of nanotubes at $LT = 200$ nm and $nCL = 0.05$ nm⁻¹ (red solid curve), $LT = 200$ nm and $nCL = 0.5$ nm⁻¹ (green solid curve), $LT = 1000$ nm and $nCL = 0.5$ nm⁻¹ (blue dashed curve), as well as $LT = 1000$ nm and $nCL = 2.5$ nm⁻¹ (cyan dashed curve) 109

Figure 4.17. Top view of the CNT film shown in Figure 4.15 (sample CN1000) stretched to an engineering strain $\epsilon = 0.0425$, where only nanotubes included into the percolating load transfer network for the threshold strain $\epsilon_{th} = 0.001$ are shown. The nanotube segments shown in red and blue are stretched and compressed, respectively. The black rectangles correspond to the non-deformable clip layers at the left and right boundaries of the sample. 110

Figure 4.18. Top views of the percolating load transfer networks in CNT films composed of nanotubes with lengths $LT = 200$ nm (sample CN200, a), $LT = 400$ nm (sample CN400, b), and $LT = 1000$ nm (sample CNT1000, c) at a CL density $nCL = 0.5$ nm⁻¹ stretched to an engineering strains $\epsilon = 0.008$. Each simulation snapshot shows only segments of nanotubes belonging to a percolating network composed of CNT parts stretched or compresses above the threshold strain value $\epsilon_{th} = 0.001$, connected with each other through CLs, and included into a network percolating the sample in the direction of applied deformation. Other CNT segments are blanked. The CNT segments shown in red and blue are stretched and compressed, respectively. The vertical sides of the bounding boxes correspond to the boundaries of the deformable parts of the films. Each panel shows the full sample in the horizontal direction and only a quarter of the whole sample in the vertical direction. 112

Figure 4.19. Fraction of percolating network fP versus nanotube length LT in films with a CL density $nL = 0.5 \text{ nm}^{-1}$ (magenta rectangles) and $nL = 2.5 \text{ nm}^{-1}$ (cyan circles) stretched to an engineering strain $\varepsilon = 0.008$ (a) and versus engineering strain ε at a CL density $nL = 0.5 \text{ nm}^{-1}$ for $LT = 200 \text{ nm}$ (green triangles) and $LT = 200 \text{ nm}$ (red gradients). The calculation of fP is performed at $\varepsilon_{th} = 0.001$. The symbols correspond to calculated values, while the curves are drawn only to guide the eye. 113

Figure 4.20. (a), Probability density functions of local bundle sizes NB in CNT films with the constant nanotube length $LT = 620 \text{ nm}$ (sample CN620, green triangles) and with random nanotube lengths distributed according to Eq. (3.1) with $b = 2.08$ and $a = 430 \text{ nm}$ (sample CNW, orange gradients). (b), Stress S versus engineering strain ε at stretching of films with the CNT length $LT = 620 \text{ nm}$ (sample CN620, green curve) and random distribution of the nanotube length (sample CNW, orange curve) at a CL density of $nL = 0.5 \text{ nm}^{-1}$ 114

Figure 4.21. Top views of non-deformed CNT films composed of dispersed CNTs with lengths $LT = 200 \text{ nm}$ (sample DN200 in Table 3.2, a) and $LT = 1000 \text{ nm}$ (sample DN1000 in Table 3.2, b) generated at CL density $nL = 0.05 \text{ nm}^{-1}$. Each panel shows the full sample in the horizontal direction and only a quarter of the whole sample in the vertical direction. The individual nanotubes are colored according to the local bundle size NB with the color table for NB shown in panel (a). 116

Figure 4.22. Top views of CNT films composed of dispersed CNTs with lengths $LT = 200 \text{ nm}$ (sample DN200 in Table 3.2, a) and $LT = 1000 \text{ nm}$ (sample DN1000 in Table 3.2, b) and at a CL density $nL = 0.05 \text{ nm}^{-1}$ stretched to a strain $\varepsilon = 0.032$. Each panel shows the full sample in the horizontal direction and only a quarter of the whole sample in the vertical direction. The individual nanotubes are colored according to the local bundle size NB with the color table for NB shown in panel (a). 117

Figure 4.23. Fraction of broken CLs fb (a) and average bundle size NB b versus engineering strain ε obtained at stretching of CNT films at a CL density $nCL = 0.05 \text{ nm}^{-1}$ and a CNT length $LT = 200 \text{ nm}$ (red solid and magenta dashed curves) and $LT = 1000 \text{ nm}$ (cyan solid and magenta dashed curves). The solid curves are obtained for samples CN200 and CN1000 shown in Figure 3.10(a) and (c), respectively, with continuous networks (CN) of bundles of nanotubes. The dashed curves are obtained for samples DN200 and DN1000 shown in Figure 4.21(a) and (b), respectively, where the non-deformed films consist of dispersed nanotubes (DN). In panel (b), the results are presented only for DN samples, and the symbols correspond to calculated values, while the curves are drawn only to guide the eye (see Table 3.2 for the sample parameters). 118

Figure 4.24. Stress S versus engineering strain ε obtained at stretching of CNT films with a CNT length $LT = 200 \text{ nm}$ (a) and $LT = 1000 \text{ nm}$ (b). The red and cyan curves are obtained for the samples CN200 and CN1000, with continuous networks of bundles of nanotubes. The green and magenta curves are obtained for the film samples DN200 and DN1000 shown in Figure 4.21(a) and (b), respectively. 119

Figure 4.25. Stress (a) and specific stress S/ρ (b) versus engineering strain ϵ obtained in stretching simulations of samples composed of (10,10) CNTs at a material densities $\rho = 0.05 \text{ gcm}^{-3}$ (curves 1, cyan), 0.1 gcm^{-3} (curves 2, green), 0.2 gcm^{-3} (curves 3, blue), 0.4 gcm^{-3} (curves 4, red), and linear CL density $nCL = 0.15 \text{ nm}^{-1}$. Panel (c) shows the specific modulus E/ρ and specific strength S_{max}/ρ versus material density..... 121

Figure 4.26. Top views of CNT film samples under stretching at a strain $\epsilon = 0.02$ with density $\rho = 0.05 \text{ gcm}^{-3}$ (a), 0.2 gcm^{-3} (b), 0.4 gcm^{-3} (c) and CL density $nCL = 0.15 \text{ nm}^{-1}$. Mesoscopic elements that are not part of the percolating load transfer networks or included into the clip layers are not shown. The mass fractions of percolating load transfer network fp in panel (a), (b), and (c) is equal to 0.07, 0.13, and 0.09, respectively..... 122

Figure 4.27. Top views of the CNT film after compression at an engineering strain of -0.14. Individual CNT are colored according to their local strain ϵ . Both (a) and (b) show the same sample, but in (b) all CNT segments where $|\epsilon| \leq 0.004$ are blanked. Black rectangles mark boundaries of the non-deformed sample..... 123

Figure 4.28. Side views of the CNT film in the course of compression in the in-plane (horizontal) direction at various strains: (a), $\epsilon = -0.033$; (b), $\epsilon = -0.056$; (c), $\epsilon = -0.078$; (d), $\epsilon = -0.1$; and (e), $\epsilon = -0.14$. Individual CNTs are colored according to the local CNT strain with the color table given in Figure 4.27(a)..... 125

Figure 4.29. Total energies of stretching U_{str} , bending U_{bnd} , van der Waals interaction U_{vdW} , and CL U_{CL} versus engineering strain ϵ obtained during compression simulation of the CNT film. 126

Figure 4.30. Engineering stress S (a) and fraction of broken CLs (b) versus engineering strain ϵ obtained during stretching simulations of the CNT film. 126

Figure 4.31. (a)-(b) Three-dimensional views of (26,0) CNT films with nanotube length $LT = 1000 \text{ nm}$, film thickness $H = 40 \text{ nm}$, material density $\rho = 0.1 \text{ gcm}^{-3}$, lateral sample size $L = 2.5 \mu\text{m}$ (a) and $5 \mu\text{m}$ (b) at a CL density $nCL = 0.05 \text{ nm}^{-1}$ compressed in the in-plane direction to a strain of $\epsilon = -0.04$. In all panels, individual nanotubes are colored according to their height (coordinate z in panel (a) and (b)). (c) AFM images (top view) of wrinkling of CNT membrane at sample strain $\epsilon = -0.05$. The scale in panel (c) is $5 \mu\text{m}$. Picture in panel (c) is taken from Ref. [137]. 127

Figure 4.32. Three-dimensional views of CNT films with a nanotube length $LT = 200 \text{ nm}$ (sample CN200, a) and $LT = 1000 \text{ nm}$ (sample CN1000 b) at a CL density $nCL = 0.05 \text{ nm}^{-1}$ compressed along x direction to a strain of $\epsilon = -0.055$. The individual nanotubes are colored according to the height (coordinate z) that is counted from the bottom of the non-deformed films..... 129

Figure 4.33. Side views of CNT films after in-plane compression at a strain of $\epsilon = -0.055$ for various nanotube length: $LT = 200$ nm (sample CN200, a), $LT = 400$ nm (sample CN400, b), $LT = 1000$ nm (sample CN1000, c), and random Weibull distribution of LT , Eq. (3.1), with $b = 2.08$ and $a = 430$ nm (sample CNW, d). The CL density is equal to $n_{CL} = 0.05 \text{ nm}^{-1}$. The individual nanotubes are colored according to their local strain ϵ and color table shown in panel (a). Panels (a) and (c) corresponds to the films shown in Figure 4.32(a) and (b), respectively. 131

Figure 4.34. Fraction of broken CLs f_b (a) and average bundle size N_B (b) versus engineering strain $|\epsilon|$ obtained at compression of CNT films with continuous networks of bundles at a CL density $n_{CL} = 0.05 \text{ nm}^{-1}$ and CNT length $LT = 200$ nm (sample CNT200, red curves and squares), $LT = 400$ nm (sample CN400, green curves and triangles), and $LT = 1000$ nm (sample CN1000, blue curves and gradients). In panel (b), the symbols correspond to calculated values, while the curves are drawn only to guide the eye. 132

Figure 4.35. Three-dimensional view of the CNT film with a nanotube length $LT = 200$ nm (sample CN200) at a CL density $n_{CL} = 0.05 \text{ nm}^{-1}$ compressed along x direction to a strain $\epsilon = -0.125$. Individual nanotubes are colored according to the height (coordinate z) that is counted from the bottom of the non-deformed film. 133

CHAPTER 1

INTRODUCTION

1.1 Carbon Nanotubes and Carbon Nanotube Materials

A carbon nanotube (CNT) is a molecule of carbon atoms with hollow tubular shape (Figure 1.1(a)). Depending on the number of shells that forms the wall of a CNT, CNTs can be further classified into two categories. The nanotubes which can be obtained by rolling a single graphene sheet are known as single walled carbon nanotubes (SWCNTs). The nanotubes which consist of multiple cylindrical shells are known as multiwalled carbon nanotubes (MWCNTs). The atomic structure of a SWCNT can be produced by rolling a graphene sheet [1,2], along the chiral vector \mathbf{C}_h

$$\mathbf{C}_h = n_1 \mathbf{a}_1 + n_2 \mathbf{a}_2 \quad (1.1)$$

where \mathbf{a}_1 and \mathbf{a}_2 are the unit cell basis vectors of the 2D lattice of the graphene sheet (Figure 1.1(b)). If the graphene sheet in Figure 1.1(b) is rolled in such a way that the origin of the chiral vector \mathbf{C}_h touches its end, then one can get a nanotube with unique periodic arrangements of atoms and with the nanotube axis directed along the translational vector \mathbf{T}_r , which is perpendicular to \mathbf{C}_h . The chirality of a nanotube (n_1, n_2) is defined by a pair of its chiral indices n_1 and n_2 . The diameters of the nanotube can be calculated $D_T = \sqrt{3} l_c (n_1^2 + n_2^2 + n_1 n_2) / \pi$, where $l_c = 0.1421 \text{ \AA}$ is the lattice constant in graphene [109]. If $n_1 = n_2$, then the resulting

configuration is known as “armchair” CNT. Figure 1.1(a) shows such an armchair (10,10) CNT. The chiral angle $\theta_{ch} = \arctan [\sqrt{3}n_2 / (2n_1 + n_2)]$ in this case is equal to 30° . If $n_2 = 0$, then the obtained nanotube is known as the “zigzag” CNT with the chiral angle equal to 0° . All other nanotubes when $0^\circ < \theta_{ch} < 30^\circ$ are known as “chiral” CNTs.

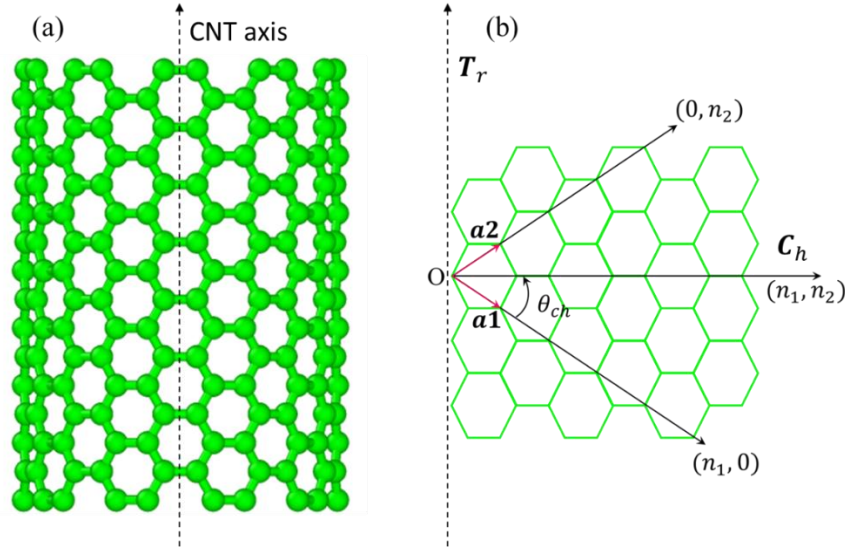


Figure 1.1. Sketch illustrating formation of a SWCNT from a 2D graphene sheet: (a), side view of an armchair (10,10) CNT with green spheres representing individual carbon atoms; (b), schematic diagram of a 2D graphene sheet rolling into CNT, where C_h is the chiral vector and T_r is the translational vector, $C_h \perp T_r$.

Since the report of Sumio Iijima on the synthesis of CNTs [3], the CNTs have drawn attraction to many scientists and engineers due to its superior mechanical, thermal, and electrical properties. An individual CNT is one of the strongest and stiffest materials in nature with Young’s modulus about 1 TPa, strength of 30–130 GPa, and elongation at break of 15–30 % [4,5,6,7,8,9,10]. Depending on the material density and production method, the CNT materials exist in many forms, from low-density aerogels and sponges with densities of $\sim 0.01 \text{ gcm}^{-3}$

[11,12], to medium-density CNT films [13,14,15,16], “forests” [17,18], mats, and “buckypaper” [19,20] with densities of $\sim 0.1 \text{ gcm}^{-3}$, and to high-density super-aligned CNT fibers [21,22,23], forests [18] and films [24] with CNT arrangements approaching the ideal hexagonal packing limit (Figure 1.2).

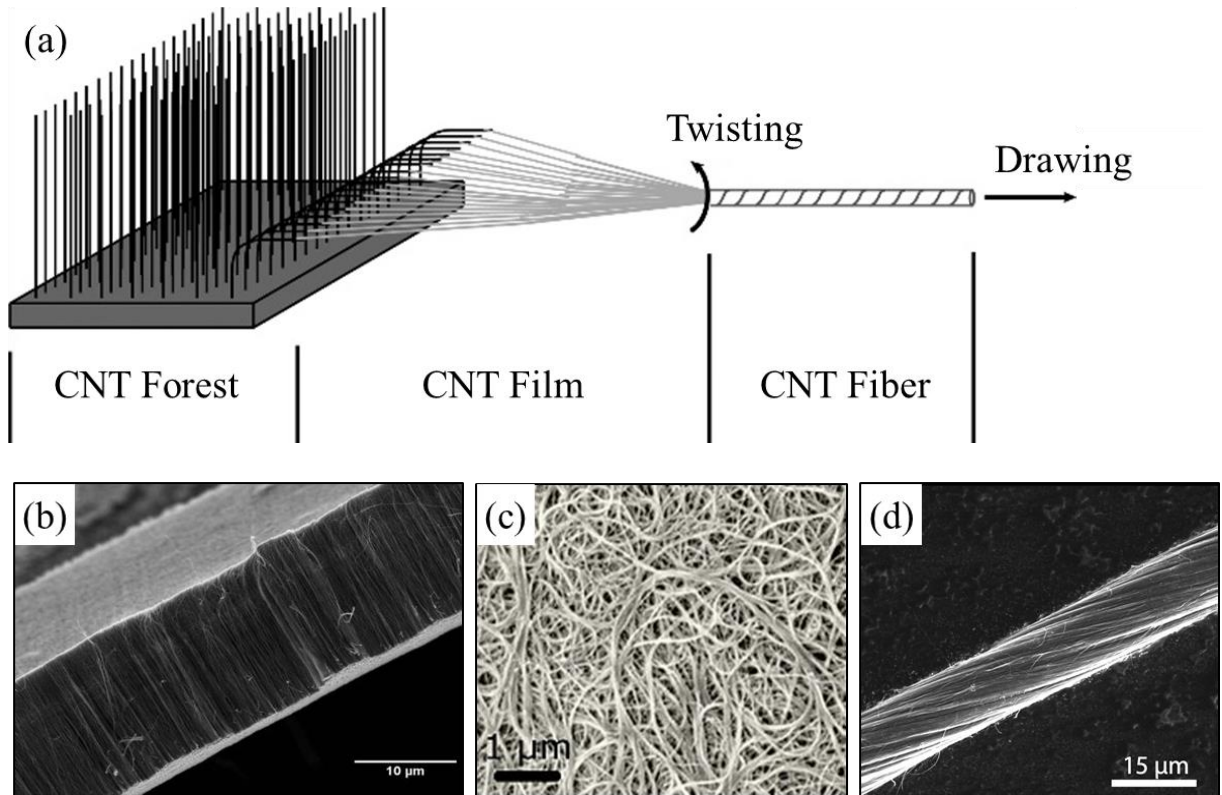


Figure 1.2. Schematic representation of CNT forests, films and fibers (a) [25], SEM image of *in situ* CNT forest (b) [26], film (c) [27] and fiber (d) [25].

In aerogels, films, forests, and fibers, CNTs form hierarchical structures through self-assembly due to van der Waals interaction between nanotubes. The substantial research efforts are targeted at exploiting the extreme properties of individual CNTs from macro level applications like automobile structure or space elevator to nano level applications in electronics and optics. Due to high strength, light weight, and excellent energy absorption capacity, the CNT

materials are promising candidates also for applications such as ballistic protection materials, including body armor [28], and artificial muscles [29]. The unique physical nanotube properties stimulated intensive studies targeted at revealing the potential of CNT materials for advanced electronic and optoelectronic applications [30], from on-chip thermal interface materials [31,32,33], to energy harvesting [34], flexible electronics and sensing [35], photoluminescence and imaging [36], and to generation of terahertz radiation [37]. The thin CNT films with random network of interconnected bundles of single-walled nanotubes, in particular, are considered as one of the primary candidates for low-cost flexible electronics [38]. Due to its outstanding electrical conductivity, as well as mechanical strength and high surface area, CNTs have been suggested as a material for use in supercapacitor electrodes [39]. The semiconducting SWCNTs is superior candidate for the channel materials in the field-effect-transistors (FETs) since they have shown much better performance than silicon-based transistors [40].

1.2 Mechanical Properties of CNT Materials

The efficient use of CNT materials in applications requires tuning the mechanical properties. For instance, good resilience and small modulus are needed for thermal interface materials, while ability to sustain cyclic large-strain reversible bending and stretching deformations is important for flexible electronics [38]. However, the pristine CNT materials are networks of entangled bundles and nanotubes, and applied load in such materials results in inter-tube sliding inside thick bundles [41]. The resisting friction forces are low [42,43,44,45,46]. The weak van der Waals interaction between CNTs also introduces low barriers for inter-tube sliding, and, thus, the superior properties of individual CNTs are not fully realized in their assemblies [47,48]. The experimentally measured Young's modulus and strength of CNT films vary in the range from ~100 MPa to ~3 GPa and from ~2 MPa to ~30 MPa, correspondingly

[49,50,51,52,53,54,55,56,57]. In particular, the experimental stress-strain curves of pristine and functionalized SWCNT films shown in Figure 1.3 demonstrate the modulus in the range of 1-3 GPa and strength in the range of 2-30 MPa that are two-three orders of magnitude smaller than the modulus and strength of individual SWCNTs [54]. The material density in these samples varies between 0.42 gcm^{-3} and 0.87 gcm^{-3} , and average bundle diameters ranges from 9.3 nm to 21 nm.

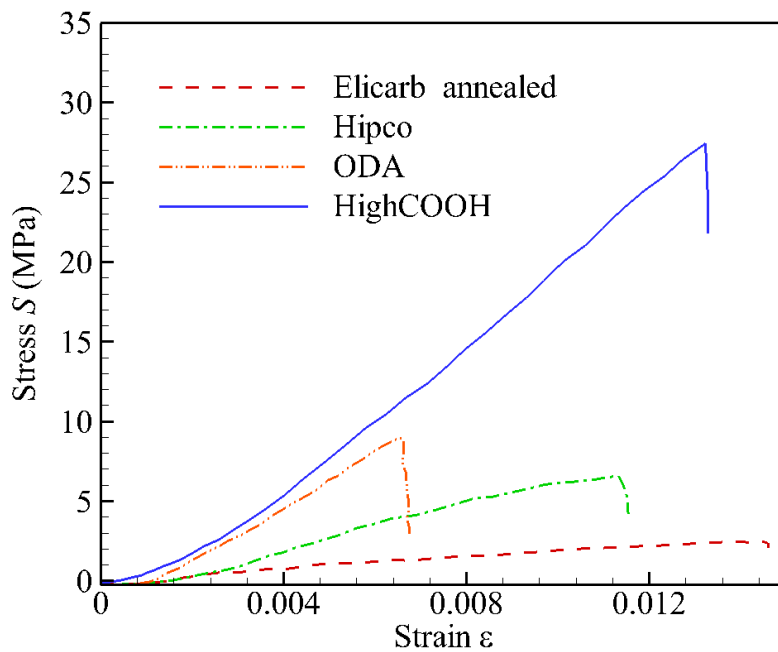


Figure 1.3. Stress-strain curve of SWCNT films obtained at tensile loading of purified HiPCO SWCNT film (dash-dot green line), as-prepared annealed Elicarb SWCNTs (dashed red line), octadecylamine (ODA) functionalized CNT film (dash-dot-dot orange line), and heavily functionalized -COOH CNT film (solid blue line). The curves are reproduced from Ref. [54].

The mechanical properties of light-weight CNT materials can be improved by increasing the degree of connectivity of the nanotube network. If the material density is fixed, then the CNT

length, the degree of nanotube entanglement, as well as the characteristic bundle thickness and length, can be considered as the factors that affect the network connectivity and load transfer. The multiple experimental and theoretical studies of CNT-reinforced composites with polymer and metal matrix materials, e.g., [58,59,60,61] reports an increasing reinforcing ability of nanotubes with increasing CNT length. The studies of the length-dependent mechanical properties of “pure” CNT materials, e.g., buckypaper, are scarce, and the understanding of how the CNT length affects the network morphology and load transfer is still elusive. For instance, the coarse-grained mesoscopic simulations in Ref. [62] surprisingly predicted that Young’s modulus of SWCNT buckypaper strongly decreases with increasing CNT length. The porosity and pore size are found to increase with increasing CNT length. On the contrary, the authors of Ref. [63] found in coarse-grained molecular dynamics simulations that the CNT length only marginally affects the elastic properties of buckypaper in the frequency-independent regime. In the experimental study [64], the authors fabricated buckypaper with varying lengths and found that the material composed of the millimeter-long CNT has twice larger tensile strength compared to the material composed of micrometer-long CNT, while the modulus does not change. The experimental study [65] revealed, contrary to Ref. [62], that the MWCNT buckypaper with shorter nanotubes had larger pore sizes than that with longer nanotubes.

Another approach for improving load transfer between individual CNTs is based on introducing defects in the atomic lattices of interacting CNTs and formation of covalent bonds or cross-links (CLs) between carbon atoms belonging to different nanotubes [48,58,59,60,61,62,63,64,65,66,67]. CLs can be induced by irradiation of CNT materials with electron [48,58,59,60,61,62,63,64,65,66,67,68,69,70,71] or ion [72,73,74,75,76,77] beams, as well as by chemical functionalization of nanotubes with subsequent formation of bonds between

molecular groups attached to different CNTs [71,78]. It is experimentally found that the elastic modulus and strength of CNT bundles exhibit up to order-of-magnitude increase after cross-linking by electron beams [13,70]. The tensile modulus and strength of SWCNT sheets demonstrate up to three-fold and five-fold increase, respectively, after cross-linking by electron beams [68], while both chemical functionalization and electron beam irradiation result in ~50% improvement of the CNT sheet strength [71]. The atomistic simulations show that the presence of CLs formed by single interstitial atoms in idealized bundles can increase the bundle strength up to 60 GPa [79].

The formation of CLs between carbon atoms belonging to different nanotubes or different shells in MWCNTs is associated with the formation of various atomic defects in the lattices of CNT walls, including interstitial carbon atoms, divacancies, Frenkel defects [66,67,68,] and bridges formed by multiple interstitial atoms [72,76]. The load transfer through CLs in small CNT systems, including individual double and multi-walled CNT, two nanotubes as well as small bundles of nanotubes, are studied in atomistic models such as MD simulations [72,73,74,75,76,77,83,79,80,81], density functional theory [48], and in combined MD-tight binding quantum mechanical simulations [68] for a number of small CNT systems including individual double and multi-walled CNT [68,72,74,75,82], two parallel or crossed CNT [72], and small CNT bundles [72,76,77,83,82]. Figure 1.4 illustrates the degree of improvement in the shear load transfer in cross-linked SWCNT bundles [76,77] obtained in atomistic simulations of pulling-out the central tube from the seven-tube bundles, where the CLs are generated through the preliminary irradiation of the bundle with energetic carbon ions. The results shown in Figure 1.4(c) indicate a strong increase in tensile modulus and strength with increasing irradiation dosage compared to a pristine bundle. The strength of an individual CL depends on the defect

type with interstitials and Frenkel defects being the weakest and strongest ones, correspondingly [68,82]. After CL breaking, defects in the form of interstitial atoms promote reformation of new CLs, the process that strongly increases the effective dynamic friction of CNT [75,77].

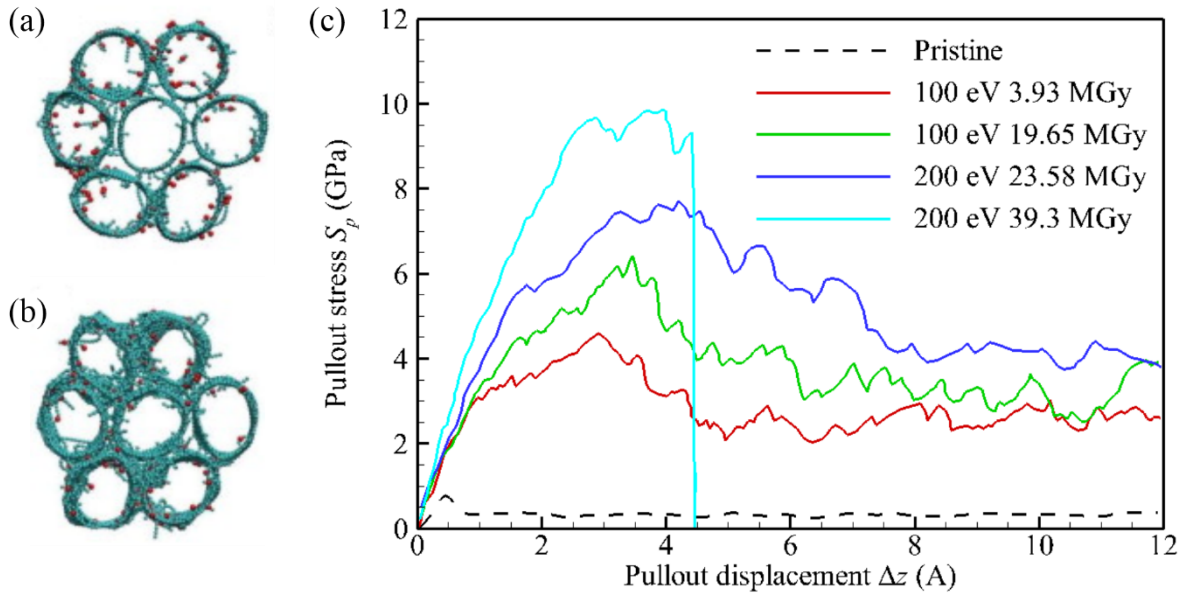


Figure 1.4. Irradiated SWCNT bundles with incident energy and doses 100 eV, 19.65 MGy (a) and 200 eV, 39.3 MGy (b) (deposited atoms are colored red, and CNT atoms are colored blue). Panel (c) shows the pullout stress versus pullout distance for pristine and irradiated bundles [76, 77].

The irradiation improvement in mechanical properties in experimental macroscopic SWCNT membranes from Ref. [68] is illustrated in Figure 1.5. After electron beam irradiation, due to knocking-out of some atoms from the sidewalls of nanotubes and bundles, the bundles and nanotubes walls become etched (Figure 1.5(a)-(b)). The existence of CLs is validated by Raman spectroscopy and TEM characterization. CLs along with dangling carbons significantly change the CNT morphology and blur the previously clear and straight CNT walls. More than six-fold

increase in tensile strength and modulus of the SWCNT membranes is demonstrated in this work.

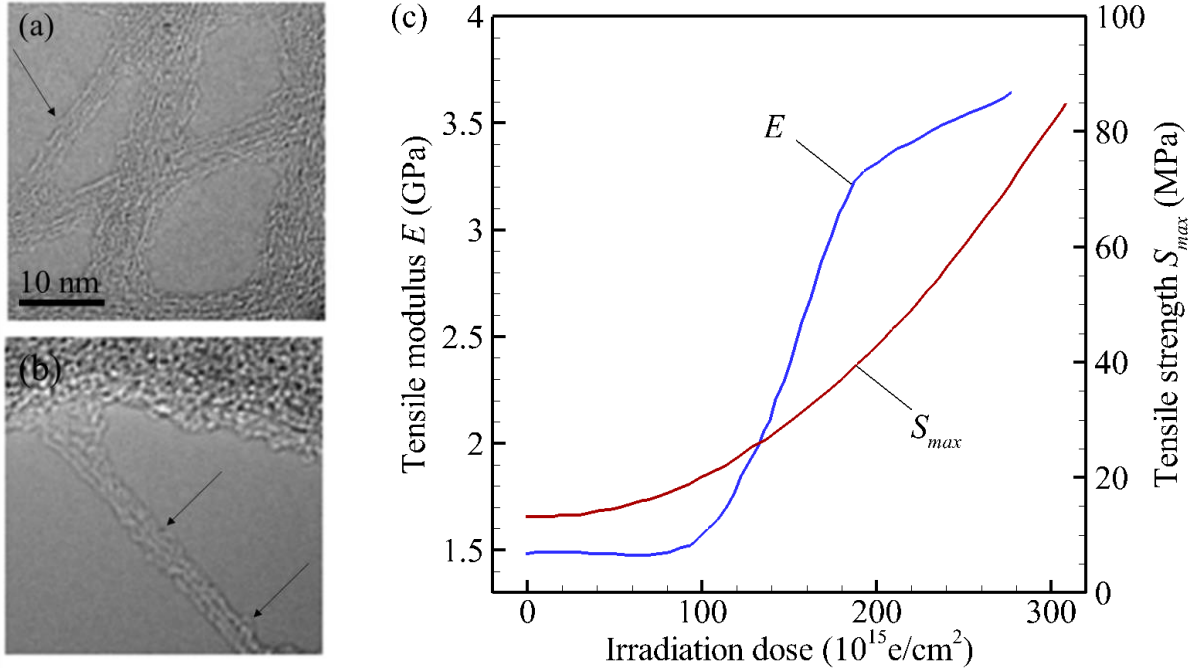


Figure 1.5. TEM images of cross-linked tubes extracted from the irradiated SWCNT fabrics (a)-(b). Electron beam irradiation improvement of mechanical properties in SWCNT membranes/fabrics under tension (c), tensile modulus E (blue curve) and strength (red curve) versus irradiation dose. Results are reproduced from Ref. [68].

1.3 Mesoscale Modeling of CNT Materials

The MD simulations are widely used to study elastic properties, interfacial properties based on pull out tests, chemical functionalization and load transfer mechanisms [84,85,86]. However, due to limitations of contemporary computing resources, the MD simulations are restricted both in length and time scales. Although the results of atomistic simulations provide invaluable information on the theoretical limits of the load transfer improvement due to cross-

linking associated with various types of defects, it is difficult to translate the obtained results into properties of random CNT materials such as films, buckypaper, forests, and aerogels, where CNTs form continuous networks of bundles. In real CNT materials, the material properties can strongly depend on the morphology of network. The theoretical study of structure-property relations in random CNT network materials requires samples with sizes that are a few times larger than the length of individual nanotubes. Such samples include at least thousands of nanotubes.

Continuum models [87,88] are also applied to theoretically study mechanical properties of individual CNTs and CNT materials. The continuum mechanics approaches that treat individual CNTs as beams, thin shells or solids in cylindrical shapes has been successfully used to study the response of CNT materials in the elastic deformation regime. However, the continuum models lack the physics that can explain interfacial properties of CNT materials and cannot predict the response at large deformations in the inelastic regime. Therefore, the structure-property relations of CNT network materials should be studied at intermediate length scales, i.e., at a mesoscale. The structure-property relationships for CNT network materials can be established with the coarse-grained mesoscopic models that neglect atomic structure of individual nanotubes but retain geometrical information about the shape of nanotubes and their assembly into a network.

Although various versions of mesoscopic models for CNT materials were proposed, e.g., Refs. [62,63,82,89,90,91,92,93,94,95], the effect of the material reinforcement via covalent CLs was studied only in Refs. [96,97,98]. In these works, the CNT material is either represented by a system of straight and dispersed nanotubes [96], a bundle with initial hexagonal packing of nanotubes [97,98] or a film with continuous network of CNTs [97,98]. The model of cross-

linked CNT materials suggested in Ref. [96] is based on the geometrical Cox model [99] and does not allow one to perform dynamic simulations of CNT materials, so it was used for predicting only the elastic properties of CNT films. The mesoscopic model of CLs suggested in Ref. [97] is based on a non-physical assumption that CL do not induce a force in the normal to the CNT surfaces direction. This assumption contradicts the microscopic picture of load transfer via individual CLs, so that model cannot be used to simulate mechanical processes in CNT materials, accompanying with variations of the inter-tube gaps, as well as dynamic alignment or misalignment of nanotubes. This model also provides only pure linear response to applied shear displacement, while stress-displacement curves obtained in atomistic pullout simulations are strongly non-linear [77]. As a result, it can fail to simultaneously predict the exact values of shear stiffness, strength, and fracture displacement. In addition, knowledge, the parameters of the mesoscopic CL models used in known mesoscopic simulations were never validated and verified against results of atomic-level simulations. These weaknesses of the existing mesoscopic CL models are addressed in our work. None of the known mesoscopic simulations also addressed the effect of CNT length on mechanical properties of cross-linked CNT materials which is investigated in this work using the mesoscale model of cross-linked CNT materials.

1.4 Objectives and Outline

This study has three major objectives. The first objective is to develop and parameterize the discrete CL model for mesoscopic simulations. The CL model describes the bonded interactions between nanotubes formed by a single interstitial carbon atom, when each CL represents a covalent bond formed between nanotubes in the real material. The parameterization of the CL model is performed based on the results of atomistic simulations of pulling the central tube from a cross-linked seven-tube bundle. It is shown that the best-fit parameters of the CL

model strongly depend on the underlying geometrical bond model and are not equal to the corresponding parameters of carbon-carbon bonds adopted in the empirical potentials designed for atomistic simulations. For the developed CL model, the parameters set are found which are recommended for mesoscopic simulations of materials composed of (26,0) CNTs under conditions, when CLs are predominantly formed by individual interstitial carbon atoms.

The second objective is to perform *in silico* generation and structural characterization of pristine and cross-linked CNT fibers and films. The quasi-equilibrium pristine (10,10) CNT fibers, and (10,10) and (26,0) films with varying material densities, CL densities, lateral sample sizes, film thicknesses, and nanotube lengths are generated and equilibrated through dynamic simulations of self-assembly of dispersed and straight CNTs into continuous networks of CNT bundles. A good agreement between *in silico* and experimental structural parameters of fibers and films are obtained. The numerical parameters to tune CNT fibers and films network morphology is identified.

The third objective is to study quasi-static mechanical properties of cross-linked CNT films. The simulations are targeted at revealing the effects of various physical parameters, including CL density, nanotube length, and sample morphology, on mechanical properties, load transfer, and compression modes. The conditions of quasi-static loading, when the mechanical response of CNT films is independent of the loading rate, are identified. The combined effect of CL density and nanotube length on elastic modulus, strength and strain at strength is explained based on stretching simulations of large films with sample size at least 2.5 times larger than the CNT lengths. The effect of random distribution of CNT lengths is also investigated. The strong effect of sample morphology on mechanical properties and structural evolution is observed during stretching deformation process. The load transfer mechanism in cross-linked CNT films is

explained in terms of potential energy distributions, stress-strain diagrams, evolution of CL breaking inside the sample, local deformation of mesoscopic CNT segments. The effects of various physical factors on compressive properties of CNT films are explained through the analysis of evolving percolating load transfer networks that consists of CNT segments participating in the load transfer. Different deformation modes of free-standing CNT films that are observed at in-plane compression of CNT films are also discussed in this part of the work.

The coarse-grained model of CNT materials is considered in Chapter 2 along with the details of development and parametrization of the mesoscopic CL models. Chapter 3 is dedicated to *in silico* generation and structural characterizations of CNT fibers and films. In Chapter 4, the results of mesoscopic mechanical simulations of cross-linked films are discussed. In Chapter 5, the summary and major conclusions are provided along with brief discussion of future research directions.

CHAPTER 2

MESOSCOPIC MODEL OF CROSS-LINKED CNT MATERIALS

2.1 Mesoscopic Model for Dynamic Simulations of CNT Materials

The coarse-grained mesoscopic model of CNT materials utilized in this work was initially proposed in Ref. [82], further developed in Refs. [92,91,98], and then used to study mechanical properties of forests of vertically aligned pristine CNTs [100,101] and cross-linked CNT films [98,102]. In this model, a CNT can be represented by a chain of “breathing flexible cylinder,” where every cylindrical segment consists of multiple carbon atoms (Figure 2.1). Each segment is defined by two adjacent nodes along the tube axis. The equations of motion for each node are used to predict variation of the position vector, local radius, and the torsional angle associated with this node in time.

The following Lagrangian L describes the system of interacting CNTs and matrix molecules/polymer units in the following generic form [82]

$$\begin{aligned}
L = & \frac{1}{2} \sum_i m_i^t \left(\frac{d\mathbf{r}_i^t}{dt} \right)^2 + \frac{1}{2} \sum_k m_k^m \left(\frac{d\mathbf{r}_k^m}{dt} \right)^2 + \frac{1}{2} \sum_i M_i^t \left(\frac{dR_i^t}{dt} \right)^2 + \frac{1}{2} \sum_k M_k^m \left(\frac{dR_k^m}{dt} \right)^2 \quad (2.1) \\
& + \frac{1}{2} \sum_i M_i^\theta \left(\frac{d\theta_i^t}{dt} \right)^2 - \sum_i U_i^{str} - \sum_i U_i^{bnd} - \sum_i U_i^{R^t} - \sum_i U_i^\theta \\
& - \sum_i U_i^{str-R^t} - \sum_i U_i^{str-bnd} - \sum_i U_i^{str-\theta} - \sum_{i,k} U_{ik}^{t-m} \\
& - \sum_{i,k} U_{ik}^{t-m(bond)} - \sum_{i,j} U_{ij}^{t-t} - \sum_{i,j} U_{ij}^{t-t(bond)} - \sum_{kl} U_{kl}^{m-m} \\
& - \sum_{kl} U_{kl}^{m-m(bond)} - \sum_k U_k^{R^m},
\end{aligned}$$

where \mathbf{r}_i^t is the position vector of i th node in a nanotube, \mathbf{r}_k^m is the position vector of k th unit of the matrix, R_i^t is the radius of the nanotube at node i , R_k^m is the radius of matrix unit k , θ_i^t is the torsion angle at the i th node in a nanotube, m_i^t is the mass of a part of the nanotube, represented by the node i , m_k^m is the mass of the k th unit of the matrix, M_i^t and M_k^m are the inertia parameters [103] of the internal breathing motion of the nanotube at node i and matrix unit k , respectively, M_i^θ is the inertia parameter for the twisting motion of the nanotube.

The potential energy of the system is composed of internal energy of nanotubes, bonded and nonbonded interaction between nanotubes, bonded and nonbonded interactions among the matrix units, bonded and nonbonded interactions among nanotubes and matrix units and internal breathing of matrix units. A part of the mesoscopic force field (MFF) that describes the internal interactions within the CNT accounts for stretching, bending, torsion, radial breathing along with the coupled stretching-bending, stretching-torsion and stretching-breathing interactions.

Correspondingly, the internal potential energy of a nanotube consists of stretching energy U^{str} defined as a function of axial deformations of nanotube segments, bending energy U^{bnd} defined

as a function of the local curvatures of the nanotube segments, breathing energy U^{R^t} defined as a function of the local radii R_i^t at each node i along the nanotube, torsion energy U^θ defined as a function of the torsional deformations of nanotubes, while terms U^{str-R} and $U^{str-bnd}$ describe coupling between stretching of two adjacent segments defined as function of radial contraction at the node and local curvature at the node respectively. U^{t-t} is the nonbonded van der Waals energy between nanotubes, $U^{t-t(bond)}$ is the bonded interaction energy between nanotubes. In this work, it is assumed that bonded interaction between nanotubes is induced by individual CLs. Development and parameterization of the model of CL is a part of this dissertation and will be discussed further in section 2.2. U^{t-m} is the potential energy for nonbonded van der Waals interaction between matrix molecules and nanotubes, $U^{t-m(bond)}$ describes the bonded interaction between matrix molecules and nanotubes due to the formation of chemical bonds, U^{m-m} and $U^{m-m(bond)}$ describe the nonbonded and bonded interactions among the matrix units, and U^{R^m} is the internal breathing potential [103] for the matrix units.

The equations of motion for the five sets of independent variables in the system $\{q\} = \{\mathbf{r}_i^t, \mathbf{r}_k^m, R_i^t, R_k^m, \theta_i^t\}$ can be directly obtained from the Lagrangian given by Eqs. (2.1), as

$$\frac{d}{dt} \frac{\partial L}{\partial \dot{q}_i} - \frac{\partial L}{\partial q_i} = 0. \quad (2.2)$$

Here, index i represents the elements from the set of independent variables $\{q\}$. By integrating Eq. (2.2), the trajectories of individual mesoscopic nodes can be obtained at the mesoscopic length and time scale following techniques similar to molecular dynamics. A significant advantage of the MFF described above is that, the distances between the “virtual surfaces” of the dynamic elements of the model are calculated “on the fly,” during a particular external interaction. This representation of the shapes of the dynamic elements in the model drastically

reduces the number of the independent degrees of freedom and increases computational efficiency of the model. The functional forms and proper parameterization of the potentials included into the MFF can be chosen based on the results of experimental study and/or atomistic simulations. Analytical functions can be used at small deformations, while tabulated values of energies and forces can be used to describe complex behavior at large deformations.

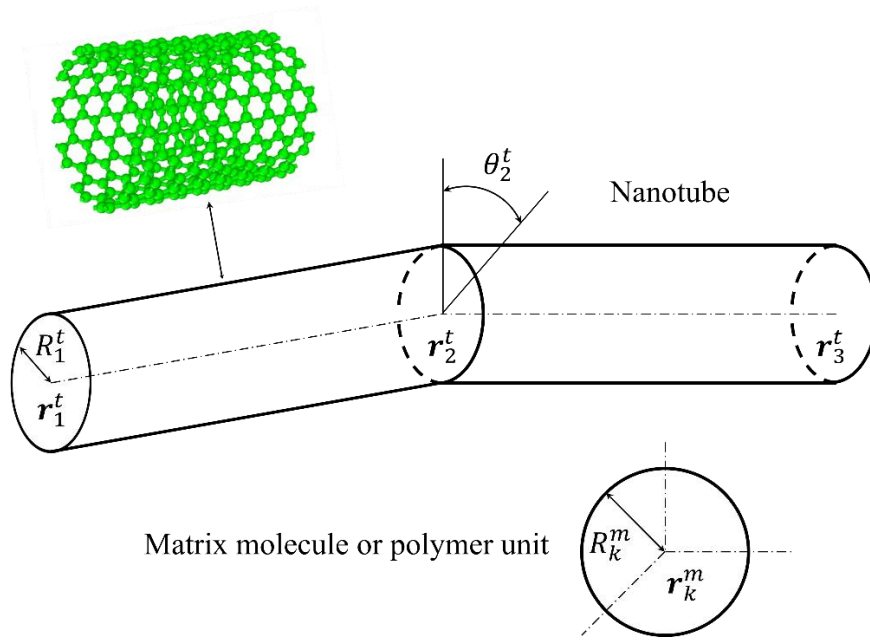


Figure 2.1. Schematic representation of a nanotube section consisting of two mesoscopic segments and three nodes along with a matrix molecule. The position of i th node r_i^t in the nanotube, radius R_i^t of the nanotube at node i , torsion angle θ_i^t at node i , position r_k^m of matrix molecule k , and radius R_k^m of the matrix molecule k are the independent variables that describe the collective dynamics of nanotubes in matrix. The size of the nanotube and matrix molecule are not shown to scale.

In the present work, the MFF is used only to describe assembly of SWCNTs and CLs between them without breathing modes and torsional deformations. The position of every nanotube k in a material sample composed of N_T nanotubes can be defined by nodes with position vectors $\mathbf{r}_{(k)i}$ ($i = 1, \dots, N_k$; N_k is the number of nodes in CNT k). The total number of nodes N in the material sample is given by $N = N_T N_k$. Two neighbor nodes $\mathbf{r}_{(k)i}$ and $\mathbf{r}_{(k)i+1}$ completely define the position of segment i . The current state of the material is defined by positions of all mesoscopic nodes $\mathbf{X} = (\mathbf{X}_1, \dots, \mathbf{X}_{N_T})$, where $\mathbf{X}_k = (\mathbf{r}_{(k)1}, \dots, \mathbf{r}_{(k)N_k})$. The Lagrangian L of such CNT assembly thus reduces to the following expression

$$L = \frac{1}{2} \sum_i m_i \left(\frac{d\mathbf{r}_i}{dt} \right)^2 - U, \quad (2.3)$$

where, m_i and \mathbf{r}_i are the mass and position vector of CNT segment i , respectively, and total potential energy U of the CNT material during mechanical loading is

$$U = U_{str} + U_{bnd} + U_{vdW} + U_{CL}, \quad (2.4)$$

where U_{str} is the harmonic potential energy of stretching of CNT, U_{bnd} is the term combining the harmonic potential of bending with the buckling, U_{vdW} is the potential energy of van der Waals interactions between nanotubes, and U_{CL} is the potential energy of CL.

2.1.1 Stretching term of MFF

As the mesoscopic model is aimed mainly at large-scale phenomena, local changes in shapes of the nanotubes associated with nonlinear behavior at large deformations are not expected to play a major role [82]. Therefore, the representation of CNT as cylinders may remain valid in the nonlinear elastic/plastic regime, and a harmonic approximation is sufficient to describe the axial deformation of mesoscopic segments. In this case, the potential energy of stretching can be represented in the form

$$U_{str} = \sum_{i=1}^{N-1} L_{i,i+1}^0 \frac{1}{2} K_{str} \varepsilon_{i,i+1}^2 = \sum_{i=1}^{N-1} L_{i,i+1}^0 \frac{1}{2} K_{str} \left(\frac{L_{i,i+1} - L_{i,i+1}^0}{L_{i,i+1}^0} \right)^2, \quad (2.5)$$

where $L_{i,i+1}^0$ is the non-deformed length of mesoscopic nanotube segment between node i and $i + 1$, $L_{i,i+1}$ is the length of deformed nanotube segment, and K_{str} is the stretching force constant. The parameterization of the stretching force constant K_{str} is performed based on series of atomistic simulations for various CNT chirality [82], and the linear trend between K_{str} and equilibrium radius of CNT R_{eq}^r (in Å) can be fitted by the following expression [82]

$$K_{str} = 86.64 + 100.56 R_{eq}^r. \quad (2.6)$$

2.1.2 Bending term of MFF

At small curvature, the bending potential U_{bnd} can be approximated by a harmonic function [82]

$$\begin{aligned} U_{bnd} &= \frac{1}{2} K_{bnd} \sum_{i=1}^{N-1} L_{i,i+1}^0 \left(\frac{1}{R_{i,i+1}^{curv}} \right)^2 \\ &\approx \frac{1}{2} K_{bnd} \sum_{i=2}^{N-1} \left\{ \frac{1}{2} L_{i,i-1}^0 \left(\frac{1}{R_i^{curv}} \right)^2 + \frac{1}{2} L_{i,i+1}^0 \left(\frac{1}{R_i^{curv}} \right)^2 \right\}, \end{aligned} \quad (2.7)$$

where $L_{i,i+1}^0$ is the non-deformed length of mesoscopic nanotube segment between node i and $i + 1$, $R_{i,i+1}^{curv}$ is the radius of curvature of the mesoscopic CNT segment between nodes i and $i + 1$, R_i^{curv} is the radius of curvature of at node i , and K_{bnd} is the bending force constant. The bending force constant K_{bnd} is determined with respect to equilibrium radius of nanotube R_{eq}^r (in Å) by the following power law fit which is obtained based on the results of atomistic simulations [82]

$$K_{bnd} = 63.8 R_{eq}^r{}^{2.93}. \quad (2.8)$$

At large bending angles corresponding to buckled nanotubes, the bending stiffness can reduce significantly. Buckling reduces the bending energy at the interconnections between nanotubes and creates barriers for CNT sliding. Such sliding barriers due to buckling is found to essential for stability of the CNT network materials [92]. In the pre-buckling state, the bending energy term for a single nanotube can be written as [92]

$$U_{bnd} = \int_A^C \frac{1}{2} \frac{K_{bnd}}{R^2} dl, \quad (2.9)$$

where R is the local radius of curvature of the elastic line of the nanotube, and the integration is performed along the length l of the elastic line (Figure 2.2(a)). For a uniformly bent nanotube of length L_T , the bending angle θ is related to R as L_T/R , and Eq. (2.9) reduces to

$$U_{bnd} = \frac{K_{bnd}\theta^2}{2L_T}. \quad (2.10)$$

For the bending energy of a buckled nanotube, the predictions of atomistic simulations can be well reproduced by the following formulation of the bending energy term

$$U_{bnd} = K_{bcl}\psi^n + \int_A^B \frac{1}{2} \frac{K_{bnd}}{R^2} dl + \int_B^C \frac{1}{2} \frac{K_{bnd}}{R^2} dl, \quad (2.11)$$

where $K_{bcl}\psi^n$ is the energy of the buckling kink in the mesoscopic model, ψ is the angle between two tangents to the elastic line at the point of kink (point B in Figure 2.2(a)). The transition from Eq. (2.10) to (2.11) in the description of the bending energy takes place when R drops down to the critical curvature for the onset of buckling, R_{cr} , e.g., when $R_B = R_{cr}$ in Figure 2.2(a). To ensure that U_{bnd} is approximately proportional to θ in the postbuckling state, the value of n is set to unity. The remaining parameters of the bending energy term depend on the radius and chirality of CNT and can be chosen based on the results of atomistic simulations performed for uniformly bent CNT with a single buckling kink, as shown in Figure 2.2.

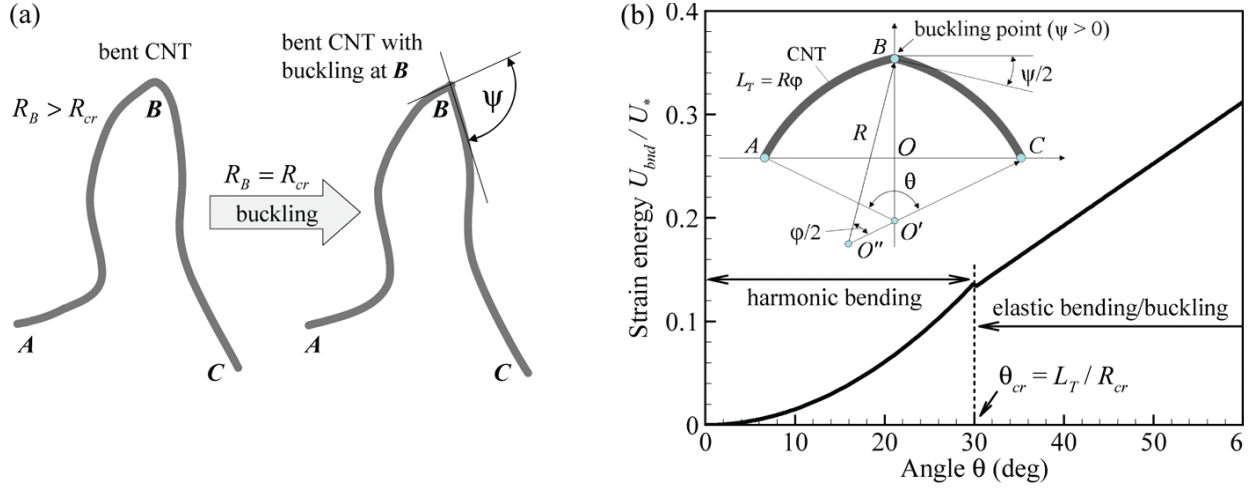


Figure 2.2. Schematic representation of bending buckling in the mesoscopic model (a) and the dependence of the bending energy U_{bnd} on the bending angle θ in uniformly bent CNT with a single buckling point appearing in the middle (point B in the inset) when the critical radius of curvature, R_{cr} , is reached (b). The bending energy in (b) is calculated with Eq. (2.10) for $\theta < \theta_{cr}$ and is obtained by minimization of the strain energy associated with bending and buckling, and with Eq. (2.11) $\theta > \theta_{cr}$ [92].

2.1.3 Inter-tube interaction potential

A distinct feature of the present model is the use of the computationally compact and efficient tubular potential method [104] based on the mesoscopic tubular potentials [91], which describe van der Waals interactions between mesoscopic CNT elements of arbitrary length and orientation and enables self-assembly of nanotubes into continuous networks of bundles. In the mesoscopic tubular potential method, the van der Waals inter-tube interaction potentials are obtained by integrating the interatomic potential over the continuous surfaces of the interacting nanotubes. As a result, the tubular potential method ensures the absence of corrugation of the inter-tube potential for curved nanotubes and eliminates strong artificial inter-tube friction,

which prohibits self-assembly of nanotubes into continuous network of bundles and characteristic, e.g., for the bead-and-spring model of CNT materials [105]. The parametrization of the tubular potential is based on the carbon-carbon interatomic potential describing nonbonding interactions in graphitic structures. To calculate the non-bonding interaction energy between the two mesoscopic segments, the Lennard-Jones interatomic potential with smooth cutoff [115]

$$\varphi_{vdW}(r_a) = 4\varepsilon_{vdW} \left[\left(\frac{\sigma}{r_a} \right)^{12} - \left(\frac{\sigma}{r_a} \right)^6 \right] C(r_a), \quad (2.12)$$

where, r_a is the distance between interacting atoms, i.e. distance between interacting tube surfaces, ε_{vdW} and σ are the parameters of the potential that define the energy and length scales of the carbon-carbon interaction respectively, and $C(r_a)$ is the cutoff function, is integrated over the surfaces of the interacting segments, while the atomic configuration is represented by an averaged continuous distribution of atoms with a surface density n_σ . The functional form of the cutoff function and the parameters of the potential are adopted from AIREBO potential [114] commonly used in atomistic modeling of carbon nanostructures and molecular hydrocarbon systems. The cutoff function is defined as $C(r_a) = S(\tau(r_a))$, where

$$S(\tau) = H(-\tau) + H(\tau)H(1 - \tau)[1 - \tau^2(3 - 2\tau)], \quad (2.13)$$

$\tau(r_a) = (r_a - r_{c0})/(r_c - r_{c0})$, $r_{c0} = 2.16\sigma$, $r_c = 3\sigma$ [106], and $H(\tau)$ is the Heaviside step function.

In the mesoscopic model, the relative position of two CNT segments can be described by six independent geometric parameters as illustrated in Figure 2.3. where h denotes the shortest distance between the two CNT axes, α is the angle between them, η_1 and η_2 represent the ends of one CNT segment, and ξ_1 and ξ_2 are the ends for the second CNT segment. The CNT are

aligned along the O and O' axes. The interaction potential between two CNT segments with equal radii R_T can be expressed as [91]

$$\begin{aligned}
 & U_{SS}(h, \alpha, \xi_1, \xi_2, \eta_1, \eta_2) \\
 &= n_\sigma^2 R_T^2 \int_{\xi_1}^{\xi_2} \int_0^{2\pi} \int_{\eta_1}^{\eta_2} \int_0^{2\pi} \varphi_{vdW}(r_a(h, \alpha, \xi, \phi_1, \eta, \phi_2)) d\phi_2 d\eta d\phi_1 d\xi, \tag{2.14}
 \end{aligned}$$

where the integration is performed along the segments axes ξ and η , and over the angles ϕ_1 and ϕ_2 that specify positions of points in the cross sections of segments (see Figure 2.3(b)). The distance between two points on the surfaces of the segments is expressed through the six geometric parameters as

$$\begin{aligned}
 & r_a(h, \alpha, \xi, \phi_1, \eta, \phi_2) \\
 &= \left[(h + R_T(\cos \phi_2 - \cos \phi_1))^2 \right. \\
 &+ (R_T(\sin \phi_2 \cos \alpha - \sin \phi_1) - \eta \sin \alpha)^2 \\
 &+ (R_T \sin \phi_2 \sin \alpha + \eta \cos \alpha - \xi)^2 \left. \right]^{1/2}. \tag{2.15}
 \end{aligned}$$

Although Eq. (2.15) is sufficient to describe the interaction of two segments of arbitrarily orientation and length, the accuracy is acceptable only with a large number of quadrature points, making the calculation too costly during the simulation. Furthermore, the six independent parameters in this equation make the tabulation of the potential impractical. The number of independent geometric variables can be reduced if one or two of the limits of integration in Eq. (2.14) are set to infinity, defining the potentials for interaction between a finite segment and a semi-infinite nanotube (U_{Se}) and between a segment and an infinitely long nanotube ($U_{S\infty}$) as below.

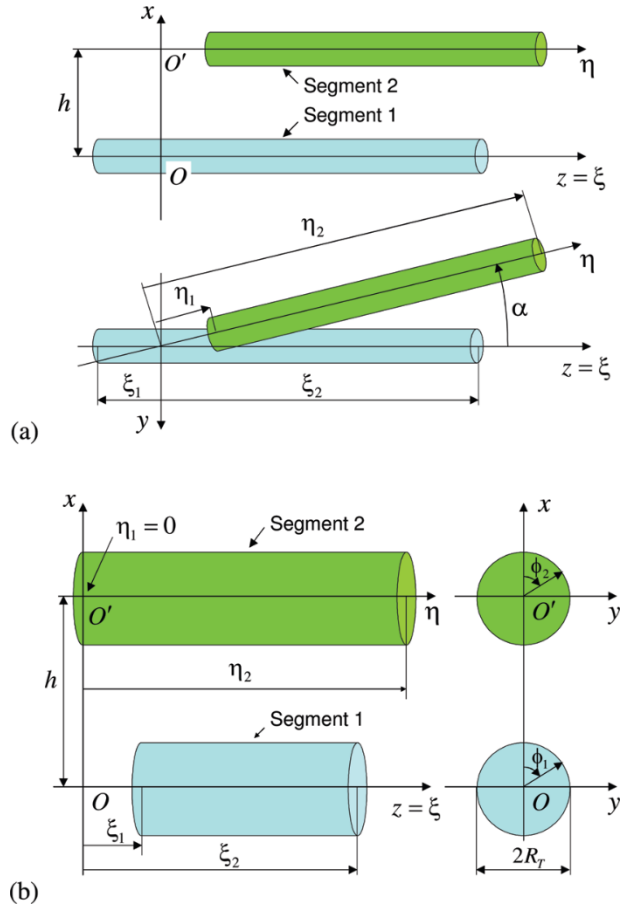


Figure 2.3. Schematic sketch illustrating the introduction of local coordinates $Oxyz$ and geometrical parameters used for characterization of the relative positions of two nonparallel (a) and parallel (b) straight cylindrical CNT segments. The side and top views are shown in panel a; only the side view is shown in panel b. In panel a, the axis x is directed along the segment OO' defining the shortest distance between the axes of the segments. In panel b, the origin of the Cartesian coordinates is chosen so that the axis Ox goes through the left end of the second segment ($\eta_1 = 0$). Cross sections of the segments are shown in panel b, with angles ϕ_1 and ϕ_2 specifying positions of points in the cross sections used for integration over the surfaces of the two segments [91].

$$U_{Se}(h, \alpha, \xi_1, \xi_2, \eta_1) = \lim_{\eta_2 \rightarrow -\infty} U_{SS}(h, \alpha, \xi_1, \xi_2, \eta_1, \eta_2), \quad (2.16)$$

$$U_{S\infty}(h, \alpha, \xi_1, \xi_2) = \lim_{\substack{\eta_1 \rightarrow -\infty \\ \eta_2 \rightarrow \infty}} U_{SS}(h, \alpha, \xi_1, \xi_2, \eta_1, \eta_2). \quad (2.17)$$

All possible inter-tube interaction in a system of CNTs can be defined by Eqs. (2.16) and (2.17). The majority of inter-tube interactions can be described by Eq. (2.17), because of the high aspect ratio of CNTs. Relatively small fraction of interactions that are affected by the effects of CNT ends can be described by Eq. (2.16). However, both Eqs. (2.16) and (2.17) depend on five independent variables and are impractical to calculate in terms of computer memory. Therefore, a series of approximations are made to reduce the number of independent variables for both potentials $U_{S\infty}$ and U_{Se} . Further approximations allow one to reduce the number of independent variables. Below, only a brief description of the approach for reducing the number of independent variables for potential between a nanotube segment and infinitely long nanotube is provided. The description of the approximate potential energy between a nanotube segment and a semi-infinite nanotube can be found in Ref. [91].

For a segment interacting with an infinitely long nanotube, the potential can be defined by the integral of the density of the interaction potential $u_{\infty}(h, \alpha, \xi)$ along the axis of the segment

$$U_{S\infty}(h, \alpha, \xi_1, \xi_2) = \int_{\xi_1}^{\xi_2} u_{\infty}(h, \alpha, \xi) d\xi. \quad (2.18)$$

When the segment is parallel to the nanotube ($\sin \alpha = 0$), the potential density does not depend on ξ , and Eq. (2.18) becomes

$$U_{S\infty||}(h, \xi_1, \xi_2) = (\xi_2 - \xi_1)u_{\infty||}(h), \quad (2.19)$$

where $u_{\infty||}(h)$ is the potential density for parallel and infinitely long nanotubes defined as

$$u_{\infty||}(h) = n_{\sigma}^2 R_T^2 \int_0^{2\pi} \int_{-\infty}^{\infty} \int_0^{2\pi} \varphi_{vdW}(r_a(h, \phi_1, \eta, \phi_2)) d\phi_2 d\eta d\phi_1 \quad (2.20)$$

$$\text{and } r_a(h, \alpha, \xi, \phi_1, \eta, \phi_2) = \left[(h + R_T(\cos \phi_2 - \cos \phi_1))^2 + R_T^2(\sin \phi_2 - \sin \phi_1)^2 + \eta^2 \right]^{1/2}.$$

In the form of Eq. (2.20), the potential energy density for parallel tubes is a function of h only and can be easily calculated for a given interatomic potential φ_{vdW} . The calculations can be organized in a one-dimensional table with high accuracy, which can be used for mesoscopic simulations. The potential for parallel tubes in Eq. (2.20) can be extended for arbitrary tube orientations with simple geometric manipulations and including a set of scaling functions to adjust discrepancy. The detail description of this method along with the treatment of the semi-infinite case is provided in Ref. [91].

2.2 Mesoscopic Model of CLs and Its Parameterization

The development and parameterization of the mesoscopic CL model for arbitrary CNT network materials is a major part of this study. In MFF, the CL energy can be described by the following expression

$$U_{CL} = \sum_{m=1}^{N_{CL}} \varphi(r_m(\mathbf{X})), \quad (2.21)$$

where $\varphi(r)$ is the potential energy of a single mesoscopic CL with the bond length $r_m(\mathbf{X})$, i.e., the distance between the end points of CL m and N_{CL} is the total CL number in a material sample. It is assumed that the CL number in an *in silico* generated sample is equal to the number of CLs in the corresponding real material and every term in the right-hand side of Eq. (2.21) describes the transfer of mechanical load between CNTs via an individual discrete CL. The functional form and parameterization of the mesoscopic CL model is obtained based on the results of atomistic simulations of pulling out the central tube from a cross-linked seven-tube bundle obtained in Refs. [76,77]. Selected results from Ref. [77] are described in section 2.2.1.

The development and parameterization of a model of cross-linked seven-tube bundle, which accounts for the local variation of the inter-tube gap due to the balance between van der Waals interactions and load transfer through CLs is described in section 2.2.2 and 2.2.3. The CL model developed in this work naturally produces both the normal and tangential forces to the nanotube surfaces and, thus, accounts for the CL contribution to the balance of normal forces. The model is also capable of accurate matching of the strongly non-linear stress-displacement curves obtained in atomistic pullout simulations. In section 2.2.4, a general approach to implement the “effective bond model” for large-scale mesoscopic simulations is described. The stress-displacement curves obtained in mesoscopic simulations are compared with the corresponding curves established in atomistic simulations of the pullout test for seven-tube bundles under identical conditions in section 2.2.5 .

2.2.1 Atomistic simulations of the pullout of a nanotube from a seven-tube bundle

In this section, a brief review of the results of atomistic simulations obtained in Refs.[76,77] is given, which is used to parameterize the mesoscopic model of covalent CLs. In these works, the authors simulated the pullout of a central nanotube from cross-linked bundles, consisting of seven hexagonally arranged (26,0) CNTs with radius $R_T = 10.185 \text{ \AA}$ and length $L_T = 59.6 \text{ \AA}$ (Figure 2.4(a)). The CLs between CNTs are formed by irradiation of the bundles with energetic carbon atoms. The irradiation produces random structures of CLs, so that the individual bundle samples, obtained under fixed irradiation conditions, differ from each other by the total CL number and types of individual CLs, although CLs formed by individual interstitial atoms with one sp^3 - sp^2 and two sp^2 - sp^2 bonds represent the most abundant type of defects [76]. In the relaxed cross-linked bundles, the central CNT was drawn along the bundle axis at a rate of

10 ms⁻¹ maintaining periodic boundary conditions. The simulations were performed with the modified REBO empirical interatomic potential [107].

A typical dependence of the pullout stress S_p on the pullout displacement Δz , i.e., displacement of the right end of the central tube, is shown in Figure 2.4(b). Here

$$S_p = -\frac{F_p}{A_p}, \quad (2.22)$$

F_p is the total pullout force exerted on atoms in the central nanotube along the bundle axis, $A_p = 2\pi R_T L_T \theta / 30^\circ$ is the characteristic CNT surface area, and angle $\theta = 20.3^\circ$ corresponds to a half of area on the surface of the central CNT, where CLs can be formed. This stress-displacement curve is obtained at a linear CL density at the central CNT equal of $n_0 = 0.49 \text{ \AA}^{-1}$ and total linear CL density between all surrounding CNTs equal to $n_1 = 0.8 \text{ \AA}^{-1}$. The linear CL density between any pair of neighboring CNTs in the bundle is equal to either $n_0/6$ or $n_1/6$.

The pullout process includes the elastic regime, when the bond breaking does not occur, inelastic regime, when the shear load induces CL breaking and reorganization, and sliding regime, when the initial CLs are broken and the force that resists CNT sliding is a result of transient breaking and formation of new CLs. In the present work, the effects related to the CL reformation in the sliding regime is not considered. The major elastic property of a bundle in the pullout process is stiffness $E_p = \delta h_0 \cdot dS_p/d(\Delta z)|_{\Delta z=0}$ (δh_0 is the equilibrium distance between two CNTs without CLs). The load transfer in the inelastic regime can be characterized by the maximum stress $S_{p,max}$ and displacement Δz_{max} at $S_p = S_{p,max}$.

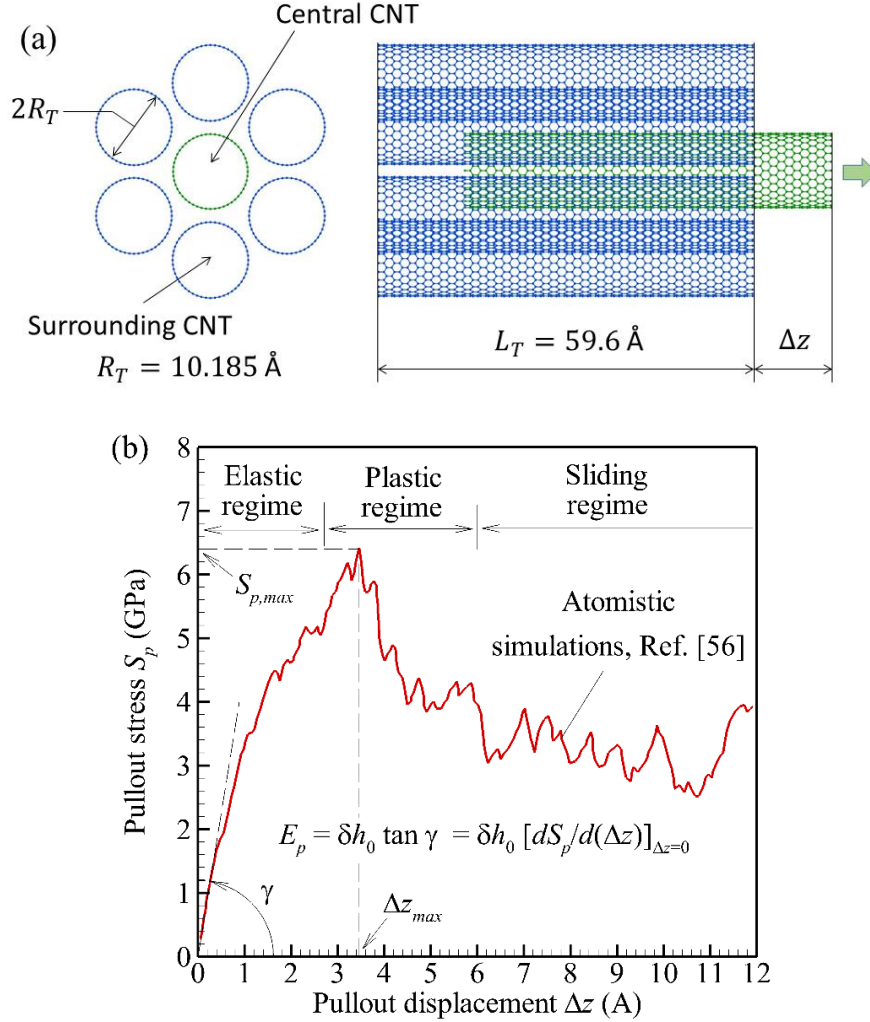


Figure 2.4. Idealized bundle of seven (26,0) SWCNTs of radius $R_T = 10.185 \text{ \AA}$ and length $L_T = 59.6 \text{ \AA}$ (a) and stress-displacement curve obtained in atomistic simulations of the pullout of the central CNT from the bundle at a linear CL density $n_0 = 0.49 \text{ \AA}^{-1}$ [56] (b).

At relatively low CL densities, when $n_0 < \sim 0.2 \text{ \AA}^{-1}$, $\Delta z_{max} \sim 1 \text{ \AA}$ and only marginally varies with n_0 . At relatively high CL densities, when $n_0 > \sim 0.2 \text{ \AA}^{-1}$, $\Delta z_{max} > \sim 3 \text{ \AA}$ and increases with increasing n_0 . To account for the effects of CL density, two parameter sets of the mesoscopic CL model, which allow one to fit the results of atomistic simulations in the low-density case at $n_0 = 0.12 \text{ \AA}^{-1}$ and in the high-density case at $n_0 = 0.49 \text{ \AA}^{-1}$ are searched for.

The values of n_0 , n_1 , E_p , $S_{p,max}$, and Δz_{max} for these cases extracted from results of Ref. [77] are presented in Table 2.1.

Table 2.1. Stiffness E_p , maximum stress $S_{p,max}$, and displacement Δz_{max} at $S_p = S_{p,max}$ obtained in Ref. [77] in atomistic simulations of the pullout of a central nanotube from bundles composed of seven (26,0) CNTs at two sets of CL densities n_0 and n_1 .

| n_0 (1/Å) | n_1 (1/Å) | E_p (GPa) | $S_{p,max}$ (GPa) | Δz_{max} (Å) |
|-------------|-------------|-------------|-------------------|----------------------|
| 0.12 | 0.55 | 7.19 | 2.98 | 0.92 |
| 0.49 | 0.8 | 11 | 6.4 | 3.45 |

2.2.2 Model of a cross-linked CNT bundle

The goal of this section is to introduce a model that can predict the pullout force in a bundle of CNTs, taking into account the effects of curvature of nanotubes, their stretching, and load transfer between CNTs via CL and van der Waals interaction. Although such a model can be generalized for a broad class of CNT systems, here, it is considered only for a system of interest, i.e., a bundle consisting of a central CNT and six surrounding CNTs. All surrounding nanotubes are assumed to be identical, so one can consider only one pair of the central and surrounding CNTs. Hereinafter, parameters of nanotubes are denoted by the subscript k with $k = 1$ standing for the central CNT and $k = 2$ standing for the surrounding CNT.

In the initial state at time $t = 0$, each CNT of radius R_T and length L_T is assumed to be straight and parallel to the axis Oz . The coordinate Z_k ($0 \leq Z_k \leq L_T$) defines positions of points in nanotube k at $t = 0$, so that Z_k serves as the Lagrangian coordinate of continuum mechanics (Figure 2.5). The deformation of nanotube k along the bundle axis is described by a function

$z_k(Z_k, t)$ such that $z_k(Z_k, t) - Z_k$ is equal to the displacement of a point in nanotube k with the initial coordinate Z_k at time t along the axis Oz . The pullout displacement is equal to $\Delta z = Z_1(L_T, t) - L_T$. The central nanotube remains straight during the pullout test due to radially symmetrical loading from surrounding CNTs, while the radial distance from the axis of the central CNT to a point at the axis of the surrounding CNT is assumed to be equal to $2R_T + \delta h(Z_2, t)$, where $\delta h(Z_2, t)$ is the gap between surfaces of CNTs 1 and 2.

The equations that define functions $z_k(Z_k, t)$ can be obtained as equations of motion for the nanotube material along the axis Oz . For straight nanotubes, such equations can be derived in the form of one-dimensional macroscopic linear elasticity equations [108]. These equations retain their form also for curved CNTs and can be written as

$$\rho \frac{\partial^2 z_k}{\partial t^2} = K_{str} \frac{\partial^2 z_k}{\partial Z_k^2} + F_{kz}, \quad k = 1, 2, \quad (2.23)$$

where $\rho = 2\pi R_T n_\sigma m$ is the linear mass density (mass of nanotube material per unit length), m is the mass of a single carbon atom, $n_\sigma = 4/(3\sqrt{3}l_c^2)$ is the surface density of atoms for a SWCNT, $l_c = 1.421 \text{ \AA}$ is the graphene lattice constant [109], K_{str} is the CNT stretching force constant, and F_{kz} is the z-component of linear density of force exerted on CNT k by CLs between CNTs 1 and 2. For SWCNTs, the stretching force constant can be calculated based on Eq. (2.7). A steady-state analog of Eqs. (2.23), where F_{kz} is defined by the shear modulus in the form adopted in continuum mechanics, was used for analysis of interaction of straight and parallel fibers and CNTs in Ref. [108]. Contrary to that work, here, the variation of the gap between nanotubes $\delta h(Z_2, t)$ is accounted and calculation of F_{kz} is based on a model of individual CLs between nanotubes without introducing the shear modulus.

The function $\delta h(Z_2, t)$ is calculated based on an equation of balance of radial components of the van der Waals and CL forces exerted on a material volume of CNT 2 from the central CNT and two neighboring surrounding CNTs. Assuming that the curvature of the surrounding CNT is small, and any bundle cross section retains a shape of a regular hexagon with the edge length of $2R_T + \delta h(Z_2, t)$, one can write the force balance equation

$$F_{2x}(Z_2, t) + F_{2z}(Z_2, t) + 2F_{vdW}(\delta h(Z_2, t)) = 0. \quad (2.24)$$

The van der Waals force density is assumed to be defined as $F_{vdW} = -\partial u_{vdW}/\partial(\delta h)$, where $u_{vdW}(\delta h)$ is the linear density of the van der Waals interaction potential between two infinitely long, straight, and parallel nanotubes with the gap δh between their surfaces. The density $u_{vdW}(\delta h)$ can be calculated, *e.g.*, by integrating the continuous distribution of van der Waals forces between circular nanotubes [91,110,111,112]. The van der Waals energy density $u_{\infty||}(h)$ in Eq. (2.20) is first calculated based on the mesoscopic approach [91] (solid curve in Figure 2.6). Then it is approximated by the Lennard-Jones potential [110]

$$u_{vdW}(\delta h) = \frac{\varepsilon_{vdW}}{n - m} \left[m \left(\frac{\delta h_0}{\delta h} \right)^n - n \left(\frac{\delta h_0}{\delta h} \right)^m \right], \quad (2.25)$$

where the energy well depth ε_{vdW} and equilibrium gap between nanotubes δh_0 are equal to values predicted by the mesoscopic potential density, while m and n are chosen to ensure that Eq. (2.25) provides the exact values of the gap δh_* at $u_{vdW}(\delta h_*) = 0$ and force stiffness $K_{vdW} = \partial F_{vdW}/\partial(\delta h)|_{\delta h=\delta h_0}$. For (26,0) CNTs, $\varepsilon_{vdW} = 0.123 \text{ eV}\text{\AA}^{-1}$, $\delta h_0 = 3.15 \text{ \AA}$, $\delta h_* = 2.686 \text{ \AA}$, $K_{vdW} = 0.4585 \text{ eV}\text{\AA}^{-3}$, $m = 3.94$, and $n = 9.4$. The potential $u_{vdW}(\delta h)$ given by Eq. (2.25) is shown in Figure 2.6 by the dashed curve.

The relatively poor approximation provided by Eq. (2.25) at $\delta h > 5 \text{ \AA}$ does not affect further results, since this gap size is larger than the adopted cutoff distance 4.4 \AA of the effective

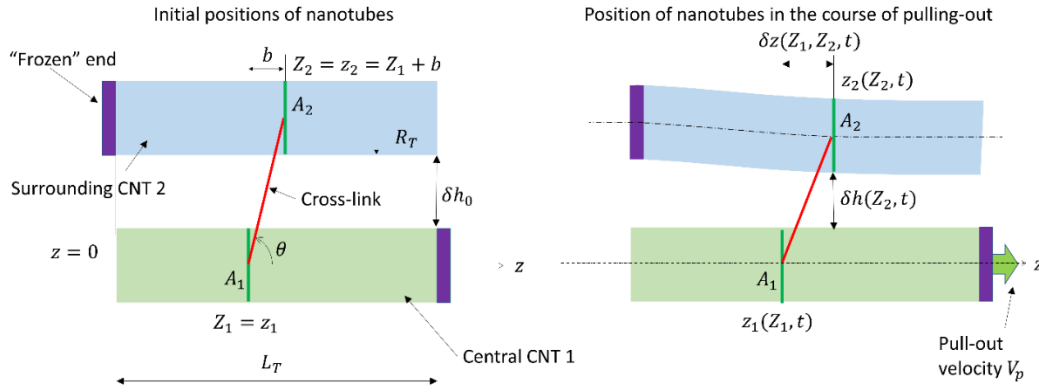
CL potential function. A harmonic approximation of the potential density in the form $u_{vdW}(\delta h) = K_{vdW}(\delta h - \delta h_0)^2/2$ (dash-dotted blue curve in Figure 2.6) introduces too large error and cannot be used for the purposes of the present study. In Eq. (2.24), F_{2x} is the x -component of the linear density of force exerted on the surrounding CNT by CLs between the central and surrounding CNTs, F_{2z} is the linear density of force exerted on CNT 2 from CL between this CNT and another neighboring surrounding CNT, and F_{vdW} is linear density of radial force exerted on a CNT due to van der Waals interaction with a neighboring CNT. For a pair of neighboring CNTs, both F_{2z} and F_{vdW} are normal to the axis Oz and directed along a line connecting the CNT centers on the bundle cross section. In order to define F_{kz} and F_{2x} in Eqs. (2.23) and (2.24), the distribution of CLs along CNTs can be characterized by the density function $N_{12}(Z_1, Z_2, t)$, such that $N_{12}(Z_1, Z_2, t)dZ_1dZ_2$ is equal to the number of CL between the segment $(Z_1, Z_1 + dZ_1)$ of the central CNT and the segment $(Z_2, Z_2 + dZ_2)$ of a surrounding CNT. Then the forces in Eqs. (2.23) and (2.24) can be calculated as follows:

$$F_{1z}(Z_1, t) = 6 \int_0^{L_T} N_{12}(Z_1, Z_2, t) F(r_{12}(Z_1, Z_2, t)) \frac{\partial r_{12}}{\partial \delta h}(Z_1, Z_2, t) dZ_2, \quad (2.26)$$

$$F_{2z}(Z_2, t) = - \int_0^{L_T} N_{12}(Z_1, Z_2, t) F(r_{12}(Z_1, Z_2, t)) \frac{\partial r_{12}}{\partial \delta Z_{12}}(Z_1, Z_2, t) dZ_1, \quad (2.27)$$

$$F_{2x}(Z_2, t) = - \int_0^{L_T} N_{12}(Z_1, Z_2, t) F(r_{12}(Z_1, Z_2, t)) \frac{\partial r_{12}}{\partial \delta Z_{12}}(Z_1, Z_2, t) dZ_1, \quad (2.28)$$

(a) Center-to-center geometrical bond model (C-C GBM)



(b) Surface-to-surface geometrical bond model (S-S GBM)

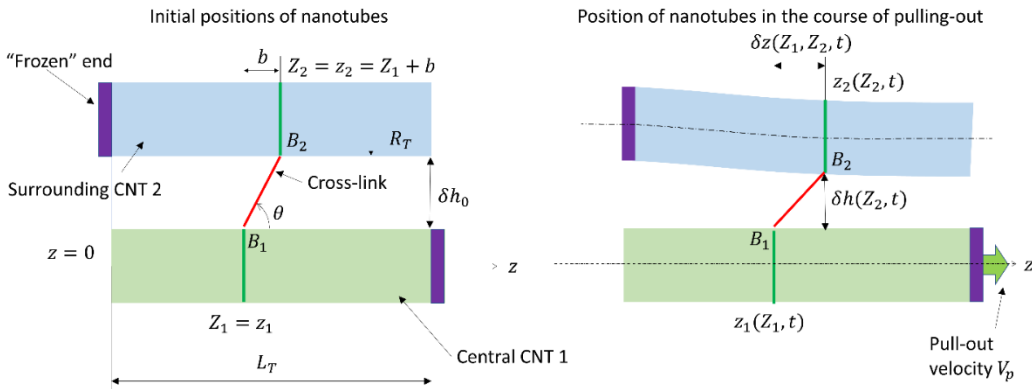


Figure 2.5. Sketch illustrating the initial positions of the central ($k = 1$) and surrounding ($k = 2$) nanotubes and their position in the course of pullout simulations, when CLs are described by the center-to-center geometrical bond model, Eqs. (2.36)-(2.37), (a) and surface-to-surface geometrical bond model, Eqs. (2.38)-(2.39), (b). CLs with initial tilting $\pm b$ are assumed to be continuously distributed along the bundle axis Oz with linear density n_0 , however, only a single CL with positive tilting ($+b$) is shown in the sketch. The angle θ , defining the direction of the effective CL bond, is equal to the angle θ_{12} , characterizing the direction of the CL force and given by Eqs. (2.37) or (2.39), only if the direction parameter γ is equal to 1.

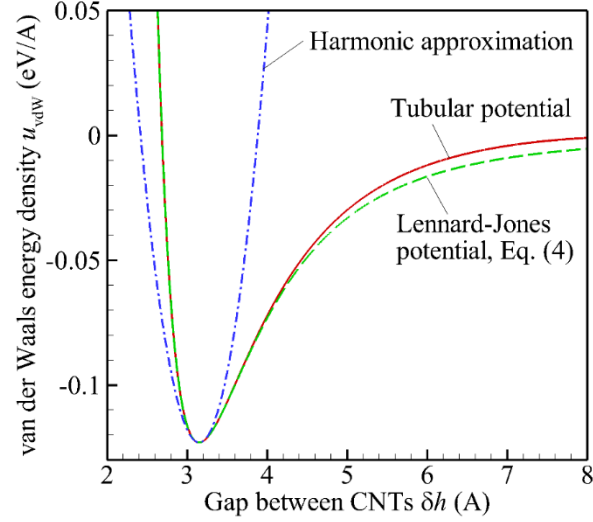


Figure 2.6. Linear potential energy density u_{vdW} of van der Waals interaction between two parallel, straight, and infinitely long (26,0) CNTs versus inter-tube gap δh calculated based on the mesoscopic tubular potential [91] (solid curve), best fit provided by Eq. (2.25) (dashed curve), and harmonic approximation of the tubular potential (dash-dotted curve).

where $r_{12}(Z_1, Z_2, t)$ is the length of a mesoscopic CL bond connecting points with coordinates Z_1 and Z_2 at time t , and $F(r) = -\partial\varphi/\partial r$ is the force exerted on CNT 1 from a single CL of length r with the potential energy $\varphi(r)$. The force F_{22} can be defined as

$$F_{22}(Z_2, t) = - \int_0^{L_T} N_{22}(Z_2', Z_2, t) F(r_{22}(Z_2', Z_2, t)) \sin \theta_{22}(Z_2', Z_2, t) dZ_2', \quad (2.29)$$

where $N_{22}(Z_2', Z_2, t)$, is the CL density function for a pair of neighboring surrounding CNTs such that $N_{22}(Z_2', Z_2, t) dZ_2' dZ_2$ is equal to the number of CLs between the segments $(Z_2', Z_2' + dZ_2')$ and $(Z_2, Z_2 + dZ_2)$ of these surrounding CNTs, $r_{22}(Z_2', Z_2, t)$ is the length of an effective CL bond connecting the points with coordinates Z_2' and Z_2 on these CNTs, and $\theta_{22}(Z_2', Z_2, t)$ is

the angle between the direction of the force induced by a single CL and the axis Oz . The total pullout force F_p in Eq. (2.22) then can be calculated as

$$F_p(t) = - \int_0^{L_T} F_{1z}(Z_1, t) dZ_1. \quad (2.30)$$

In Eqs. (2.26)-(2.29), the geometrical functions $r_{12}(Z_1, Z_2, t)$, $\theta_{12}(Z_1, Z_2, t)$, $r_{22}(Z_2', Z_2, t)$, and $\theta_{22}(Z_2', Z_2, t)$, are defined by an adopted effective bond model.

In order to study the pullout process without changing the lengths of nanotubes, Eq. (2.23) are solved with the initial and boundary conditions

$$\text{At } t = 0: 0 \leq Z_k \leq L_T: z_k(Z_k, 0) = Z_k, \quad \frac{\partial z_k}{\partial t}(Z_k, 0) = 0, \quad k = 1, 2, \quad (2.31)$$

$$\text{At } Z_1 = Z_2 = 0: \quad \frac{\partial z_1}{\partial t}(0, t) = V_p, \quad z_2(0, t) = 0, \quad (2.32)$$

$$\text{At } Z_1 = Z_2 = L_T: \quad \frac{\partial z_1}{\partial t}(L_T, t) = V_p, \quad z_2(L_T, t) = L_T, \quad (2.33)$$

where V_p is the pullout velocity, so that the pullout distance is equal to $\Delta z = V_p t$. These conditions mimic the initial and boundary conditions for infinitely long bundles considered in atomistic simulations in Ref. [77]. A preliminary study showed that the results obtained based on Eq. (2.23) are only marginally sensitive to the value of the pullout velocity if $V_p \leq 10 \text{ ms}^{-1}$, so that the single value of $V_p = 1 \text{ ms}^{-1}$ or 0.01 \AA ps^{-1} is chosen for all simulations. It ensures that the simulation results correspond to quasi-static deformation of nanotubes. The initial conditions for the inter-tube gap δh are not necessary, since it is defined by a non-evolutionary Eq. (2.24). At the initial time $t = 0$, the values of $\delta h(Z_2, 0)$ depend on the initial CL density.

In the general case of arbitrary continuous CL distributions given by the density functions $N_{12}(Z_1, Z_2, t)$ and $N_{22}(Z_2', Z_2, t)$, Eqs. (2.23) fall into the class of non-linear integro-differential equations. Such general equations must be used if the individual CLs in the initial state have random properties, e.g., different lengths, or CL densities dynamically change due to breaking

and formation of new CLs in the sliding regime. Hereinafter, the model based on Eqs. (2.23) and (2.24) is referred to as the “bundle model” in order to distinguish it from the general mesoscopic model of CNT network materials considered in Section 2.2.4.

2.2.3 Effective CL bond models

The potential function for a single mesoscopic CL is adopted in the form of a model Morse potential with a smooth cutoff function $S(\tau)$:

$$\varphi(r) = \varepsilon_0 e^{-a(r-r_0)} [e^{-a(r-r_0)} - 2] S(\tau(r)), \quad (2.34)$$

where ε_0 is the potential well depth, r_0 is the equilibrium CL length, and a is a parameter, affecting the bond stiffness $2a^2\varepsilon_0$. The function $S(\tau)$ is chosen in the form of a fifth-degree polynomial $S(\tau) = 1 - t^3(10 - 15t + 6t^2)$ at $0 \leq \tau \leq 1$ with $S(\tau) = 1$ at $\tau < 0$ and $S(\tau) = 0$ at $\tau > 1$, where $\tau(r) = (r - r_*)/(r_c - r_*)$, r_c is the cutoff distance and r_* is the maximum distance, where the Morse potential is not affected by the cutoff. This form of the cutoff function ensures monotonous variation of the CL force $-\partial\varphi/\partial r$ with r at relatively small a . The values $r_* = 3.2 \text{ \AA}$ and $r_c = 4.4 \text{ \AA}$ are chosen for further simulations based on results of a preliminary study as minimum values of r_* and r_c , which make the results of simulations insensitive to further increase of r_* and r_c . These values of r_* and r_c are only slightly different from doubled values of corresponding cutoff parameters equal to 1.7 \AA and 2 \AA adopted in REBO [113] and AIREBO [114] empirical interatomic potentials for a single C-C bond in the state of sp^2 hybridization. It can be expected, since the parameters of Eq. (2.34) are fitted to the results of the pullout test for bundles, where the majority of CLs is formed by individual interstitial atoms [76].

For CLs formed by individual interstitial atoms, ε_0 and r_0 in Eq. (2.34) can be also estimated as the double energy and double equilibrium length of sp^2 - sp^2 bond in graphite, with

values of 9.86 eV and 2.82 Å predicted by the REBO potential. The value of a can be assumed to be equal to the stiffness parameter of the exponential approximations of the major attractive term in the carbon-carbon bond energy, e.g., $\sim 4.7 \text{ 1Å}^{-1}$ in the REBO potential. A similar approach to estimating ε_0 was suggested in Ref. [97] for CLs formed by interstitial atoms with two sp^3 - sp bonds, where value $\varepsilon_0 = 7.2 \text{ eV}$ was deduced based on the Tersoff empirical interatomic potential [115], while r_0 was assumed to be equal to the equilibrium inter-tube gap of 3.35 Å. In Section 2.2.3, it is shown that such simple approximations do not allow one to accurately match the results of atomistic simulations and, moreover, the best-fit values of ε_0 , r_0 , and a depend on the adopted geometrical model of the effective CL bond.

In the center-to-center geometrical bond model (hereinafter, C-C GBM), an individual CL is assumed to “connect” points A_1 and A_2 placed at the axes (or centerlines) of corresponding CNTs, but the CL length r_{12} is calculated by subtracting $2R_T$ from the distance between points A_1 and A_2 (Figure 2.5). In this case,

$$r_{12}(Z_1, Z_2, t) = \sqrt{[2R_T + \delta h(Z_2, t)]^2 + \delta z_{12}^2(Z_1, Z_2, t)} - 2R_T, \quad (2.35)$$

where $\delta z_{12}(Z_1, Z_2, t) = z_2(Z_2, t) - z_1(Z_1, t)$. The preliminary simulations showed that, if Eq. (2.35) is used to calculate the CL length, then the results obtained based on the bundle model of section 2.2.2 either can be fitted to results of atomistic simulations with excessively large values of a equal to 10 – 15 1Å^{-1} or cannot be fitted at all with any choice of parameters in Eq. (2.34). This problem is solved by empirical modification of Eq. (2.35) with additional parameter γ in the form:

$$r_{12}(Z_1, Z_2, t) = \sqrt{[2R_T + \delta h(Z_2, t)]^2 + \gamma \delta z_{12}^2(Z_1, Z_2, t)} - 2R_T. \quad (2.36)$$

Then

$$\frac{\partial r_{12}}{\partial \delta h}(Z_1, Z_2, t) = \gamma \frac{\delta z_{12}(Z_1, Z_2, t)}{r_{12}(Z_1, Z_2, t) + 2R_T}, \quad (2.37)$$

$$\frac{\partial r_{12}}{\partial \delta z_{12}}(Z_1, Z_2, t) = \frac{\delta h(Z_2, t) + 2R_T}{r_{12}(Z_1, Z_2, t) + 2R_T}.$$

The components of the force produced by a single CL along the bundle axis and in the normal to the bundle axis direction, $F_z = F \cos \theta_{12}$ and $F_x = F \sin \theta_{12}$ (here, $\theta_{12}(Z_1, Z_2, t)$ is the angle between the direction of the CL force and the axis Oz in Figure 2.5), are related to each other as $F_z/F_x = \tan \theta_{12} = \gamma \tan \theta$, where θ is the angle between the effective CL bond (red line segments in Figure 2.5) and the axis Oz . The variation of γ , thus, allows one to change the ratio F_z/F_x and, correspondingly, the direction of the CL force compared to direction predicted by the nominal position of the effective CL bond. Hereinafter, the parameter γ is referred to as the “direction parameter” and considered as an additional fitting parameter of the effective CL model that must be found together with parameters ε_0 , r_0 , and a in Eq. (2.34). The values of $r_{22}(Z_2', Z_2, t)$ and $\sin \theta_{22}(Z_2', Z_2, t)$ for a CL between a pair of surrounding CNTs in a bundle are given by similar equations, where $\delta z_{12}(Z_1, Z_2, t)$ must be replaced with $\delta z_{22}(Z_2', Z_2, t)$.

In the surface-to-surface geometrical bond model (hereinafter, S-S GBM), it is assumed that the effective CL bond “connects” points B_1 and B_2 placed at the surfaces of CNTs (Figure 2.5). When this model is applied together with Eqs. (2.23), additional assumption that the normal vector to any CNT cross section is directed along the axis Oz at any time is adopted. This assumption is justified by relatively small curvature of surrounding CNTs developed in the course of the pullout test. Then the CL length can be calculated as

$$r_{12}(Z_1, Z_2, t) = \sqrt{\delta h^2(Z_2, t) + \gamma \delta z_{12}^2(Z_1, Z_2, t)}, \quad (2.38)$$

where, likewise C-C GBM, the direction parameter γ is introduced. Then

$$\frac{\partial r_{12}}{\partial \delta h} = \gamma \frac{\delta z_{12}(Z_1, Z_2, t)}{r_{12}(Z_1, Z_2, t)}, \quad (2.39)$$

$$\frac{\partial r_{12}}{\partial \delta z_{12}} = \frac{\delta h(Z_2, t)}{r_{12}(Z_1, Z_2, t)}.$$

The values of $r_{22}(Z_2', Z_2, t)$ and $\sin \theta_{22}(Z_2', Z_2, t)$ for a CL between a pair of surrounding CNTs are given by similar equations, where $\delta z_{12}(Z_1, Z_2, t)$ must be replaced with $\delta z_{22}(Z_2', Z_2, t)$.

The C-C and S-S GBMs are different from each other by the effective “rigidity” of the CL bond. The rate of change of the CL length r_{12} with displacement δz_{12} is characterized by the derivative $\partial r_{12} / \partial (\delta z_{12})$. It is smaller for the C-C GBM compared to S-S GBM, i.e., the same δz_{12} results in smaller variation of r_{12} , when it is calculated based on the C-C GBM. As a result, the effective CL bond is substantially “softer” for the C-C GBM than for the S-S GBM. In addition, the S-S GBM is potentially capable of introducing torsional deformation of nanotubes via CL forces. The torsional deformation, however, is expected to be of marginal importance for the pullout tests. At the same time, the C-C GBM can be potentially useful as a part of mesoscopic models where nanotubes are represented by as chains of line segments. The major goal of simulations based on the bundle model given by Eqs. (2.23)-(2.33) is to parameterize the effective CL bond model and to choose the best-fit values of ε_0 , r_0 , a , and γ , which provide quantitative agreement with the stress-displacement curves obtained in atomistic simulations. For this purpose, the simulations based on Eqs. (2.23)-(2.33) are performed under conditions that closely resemble the conditions of atomistic simulations described in Section 2.2.1 and, in particular, for the same CNT radius R_T , bundle length L_T , and CL densities n_0 and n_1 .

The solution of the boundary value problem given by Eqs. (2.23)-(2.33) depends on parameters in Eqs. (2.34), (2.36)-(2.39) and the initial values and variation in time of the CL

density functions $N_{12}(Z_1, Z_2, t)$ and $N_{22}(Z_2', Z_2, t)$. The simulations based on the bundle model is performed in order to find parameters of the effective bond model that dominate the mechanical behavior of the cross-linked CNT systems, when the effects of CL reformation are marginal. Under these conditions, it is assumed that that $N_{12}(Z_1, Z_2, t) = N_{12}(Z_1, Z_2, 0)$, $N_{22}(Z_2', Z_2, t) = N_{22}(Z_2', Z_2, 0)$, and in the initial state when $\delta h = \delta h_0$ all CLs have the same length l_0 ($l_0 \geq \delta h_0$) and are distributed homogeneously along the bundle with densities n_0 and n_1 . If $l_0 > \delta h_0$, then the effective CL bonds are tilted with respect to the bundle axis. Since two tilting directions are statistically equiprobable, one can assume that a half of CLs has “positive” tilting direction, when coordinates of CL ends are related as $Z_2 = Z_1 + b$, and another half of CLs has “negative” tilting direction when $Z_2 = Z_1 - b$ (Figure 2.5). The tilting parameter b is related to l_0 as $(l_0 + 2R_T)^2 = [2R_T + \delta h_0]^2 + \gamma b^2$ in model 1 and as $l_0^2 = \delta h_0^2 + \gamma b^2$ in model 2.

$$N_{12}(Z_1, Z_2, 0) = \frac{n_0}{12} [\delta(Z_2 - (Z_1 + b)) + \delta(Z_2 - (Z_1 - b))], \quad (2.40)$$

$$N_{22}(Z_2', Z_2, 0) = \frac{n_1}{12} [\delta(Z_2 - (Z_2' + b)) + \delta(Z_2 - (Z_2' - b))], \quad (2.41)$$

where, $\delta(z)$ is the Dirac delta function. A series of preliminary simulations is performed to reveal the effect of various parameters included into the bundle model. In Figure 2.7, the thin dashed and dash-dotted curves are obtained with the same model parameters as corresponding thick curves, but with the assumption that the inter-tube gap δh is constant and equal to δh_0 throughout the simulation. These results indicate that the variation of the inter-tube gap is strong and cannot be neglected. All further results, therefore, obtained for variable inter-tube gap predicted by Eq. (2.24).

The preliminary simulations illustrated in Figure 2.7 also show that the results of atomistic simulations can be matched by the bundle model assuming $b = 0$. In a case of large CL density, which is characterized by relatively large Δz_{max} , the variation of b is to some extent interchangeable with variation of γ and can have a positive feedback on the agreement with atomistic simulations, as it is illustrated in Figure 2.7. In particular, the results obtained with the C-C GBM at $\gamma = 1$ can closely fit the results of atomistic simulations at a certain b (thick dashed curve in Figure 2.7). For S-S GBM, the variation of b at $\gamma = 1$ allows one to formally match values of E_p , $S_{p,max}$, and Δz_{max} , but the stress-displacement curves in this case contain a second maximum (thick dash-dotted curve in Figure 2.7). Two maxima appear because the CL with positive and negative tilting break at different Δz . In fact, it is found that variation of b at $\gamma \neq 1$ is redundant and does not allow one to improve the agreement with atomistic simulations. Based on this conclusion, the search for the best-fit parameters is performed only at $b = 0$ and $l_0 = \delta h_0$. At $b = 0$ and $\gamma \neq 1$, a weak secondary maximum in the stress-displacement curve can also appear at large CL densities (Figure 2.7), but the corresponding minimum is always shallow independently of γ and allows one to reproduce the change in the curve slope in the inelastic regime. At $b = 0$, Eqs. (2.40)-(2.41) reduce to

$$N_{12}(Z_1, Z_2, 0) = \frac{n_0}{6} \delta(Z_2 - Z_1), \quad (2.42)$$

$$N_{22}(Z_2', Z_2, 0) = \frac{n_1}{6} \delta(Z_2 - Z_2'). \quad (2.43)$$

After inserting these distributions into Eqs. (2.26)-(2.29), one can obtain, e. g., F_{1z} in the form

$$F_{1z} = n_0 F(r_{12}(Z_1, Z_1, t)) \cos \theta_{12}(Z_1, Z_1, t). \quad (2.44)$$

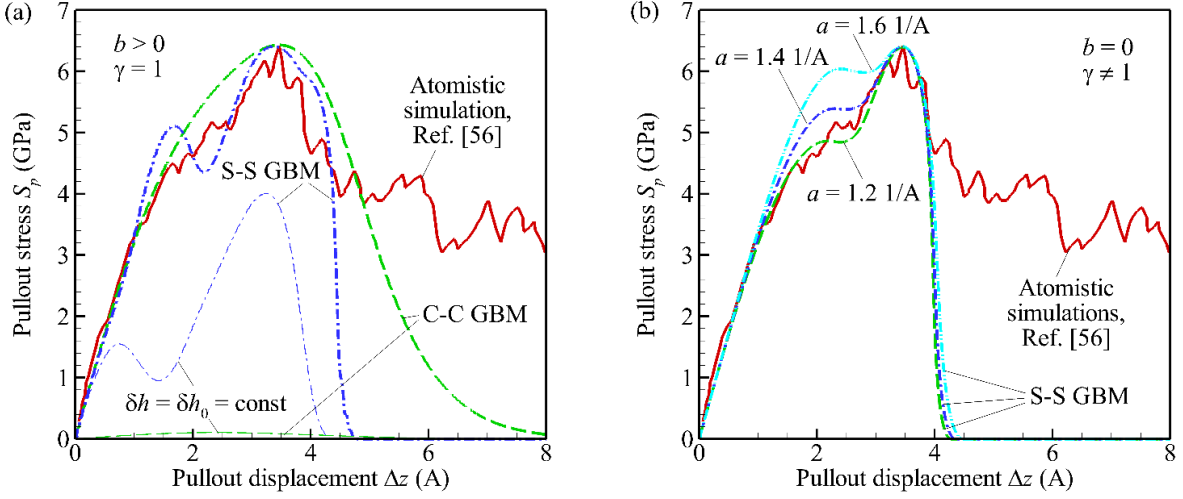


Figure 2.7. Stress S_p versus displacement Δz obtained in pullout simulations for a seven-tube bundle with a length of 59.6 \AA composed of $(26,0)$ CNT at CL densities $n_0 = 0.49 \text{ \AA}^{-1}$ and $n_1 = 0.8 \text{ \AA}^{-1}$. The thick solid curve (red) is obtained in atomistic simulations in Ref. [77]. Other curves are obtained based on solution of Eqs. (2.23) with various r_0 , ε_0 , a , b and γ , which allow one to fit values of E_p , $S_{p,max}$, and Δz_{max} in Table 2.1. In panel (a), dashed (C-C GBM, $r_0 = 3.334 \text{ \AA}$, $\varepsilon_0 = 16.54 \text{ eV}$, $a = 6 \text{ 1/\AA}$, $b = 1.07 \text{ \AA}$; green) and dash-dotted (S-S GBM, $r_0 = 2.4 \text{ \AA}$, $\varepsilon_0 = 17.9 \text{ eV}$, $a = 1.9 \text{ 1/\AA}$, $b = 1.3 \text{ \AA}$; blue) curves are obtained at $\gamma = 1$. In the panel (b), dashed ($r_0 = 1.225 \text{ \AA}$, $\varepsilon_0 = 27.94 \text{ eV}$, $a = 1.2 \text{ 1/\AA}$, $\gamma = 0.65$; green), dash-dotted ($r_0 = 1.958 \text{ \AA}$, $\varepsilon_0 = 16.1 \text{ eV}$, $a = 1.4 \text{ 1/\AA}$, $\gamma = 0.63$; blue), and dash-double-dotted ($r_0 = 2.203 \text{ \AA}$, $\varepsilon_0 = 14.14 \text{ eV}$, $a = 1.6 \text{ 1/\AA}$, $\gamma = 0.6$; cyan) curves are obtained with the S-S GBM at $b = 0$. The thick curves are calculated assuming variable gap δh between CNTs, which is determined by the Eq. (2.24), while the thin curves in panel (a) are obtained with $\delta h = \delta h_0 = const.$

The equations for F_{2z} , F_{2x} , and F_{22} can be obtained in the form similar to Eq. (2.44).

With such source terms, Eq. (2.23) becomes hyperbolic differential equation. These equations include the CL equilibrium energies per unit length $n_0 \varepsilon_0$ and $n_1 \varepsilon_0$ instead of individual values of n_0 , n_1 , and ε_0 . The simulation results, correspondingly, do not change if quantities n_0 , n_1 , and ε_0 vary at constant $n_0 \varepsilon_0$ and $n_1 \varepsilon_0$.

Once CLs are distributed according to Eqs. (2.40)-(2.41), the gap between nanotubes homogeneously changes in order to enforce the balance of radial forces. Thus, in a case when $r_0 \neq \delta h_0$, the CLs are pre-strained in the initial state. In the model with zero tilting, $b = 0$, the degree of the initial pre-straining depends on the parameters of the potential function $\varphi(r)$ and CL densities n_0 and n_1 , but is independent of the direction parameter γ .

To reveal the effect of CL densities on the best-fit parameters of the effective bond model, the bundle model is applied for the pullout test under conditions of low- and high-density cases listed in Table 2.1. In both cases, such parameters ε_0 , r_0 , a , and γ are found that allow one to exactly match the values of E_p , $S_{p,max}$, and Δz_{max} , deduced from atomist simulations. For each case considered in Table 2.1, two sets of the best-fit parameters are determined, one for the C-C GBM and another one for the S-S GBM.

The approach to finding the best-fit parameters is based on the analysis of the contour lines corresponding to $E_p = const$, $S_{p,max} = const$, and $\Delta z_{max} = const$ on the plane of parameters (ε_0, r_0) obtained at fixed a and γ . Multiple simulations are performed with iteratively varying a and γ in order to make these contour lines crossing in a single point on the plane (ε_0, r_0) .

Since the number of fitting parameters (ε_0 , r_0 , a , and γ) is larger than the number of fitted quantities (E_p , $S_{p,max}$, and Δz_{max}), the choice of fitting parameters is non-unique. One can

select one fitting parameter, for instance, a , and then find numerically other best-fit parameters as functions of a in the form $\varepsilon_0 = \varepsilon_0(a)$, $r_0 = r_0(a)$, and $\gamma = \gamma(a)$. These functions for all considered cases are shown in Figure 2.8. At low CL density, the best-fit value of ε_0 is a conservative quantity and varies within $\sim 5\%$ for both C-C and S-S GBMs. At high CL density, ε_0 varies in a broader range. The best-fit value of ε_0 can be both substantially larger and smaller than a value of 9.86 eV expected for a double sp^2 - sp^2 bond in graphite. At low CL density, the best-fit value of r_0 varies in the range from $\sim 2.5 \text{ \AA}$ to 3 \AA and is close to the size of the equilibrium gap between nanotubes equal to 3.15 \AA . In this case, the degree of pre-straining of CLs in the initial state is moderate. At high CL density, the best-fit value of r_0 varies from $\sim 0.8 \text{ \AA}$ to 2.3 \AA . It implies much larger degree of pre-straining.

The best-fit values of γ for the C-C GBM are in a few times larger than for S-S GBM. The larger “softness” of the geometrical bond in the C-C GBM must be “compensated” by increasing stiffness of the potential function given by Eq. (2.25). The results shown in Figure 2.8 illustrate strikingly large difference between the best-fit values of a and ε_0 in the cases of low and high CL densities. In the low-density case, a varies in the large range from $\sim 3 \text{ \AA}^{-1}$ to $\sim 11 \text{ \AA}^{-1}$, which includes the maximum values $\sim 4.7 \text{ \AA}^{-1}$ of the stiffness parameter in the exponential approximation of the major attractive term in the REBO potential. The value of ε_0 varies from $\sim 5.4 \text{ eV}$ to $\sim 5.8 \text{ eV}$ which is reasonably close to the double energy of 9.86 eV for a carbon-carbon bond in graphite used in the REBO potential. In the high-density case, the best-fit values of a are much smaller and vary between $\sim 1.2 \text{ 1/\AA}$ and $\sim 1.6 \text{ 1/\AA}$, while values of ε_0 vary in a broad range from $\sim 15 \text{ eV}$ to $\sim 55 \text{ eV}$. Thus, in the high-density case, the effective stiffness of CLs is much smaller compared to the low-density case. This difference is attributed to the crowding effect of CLs.

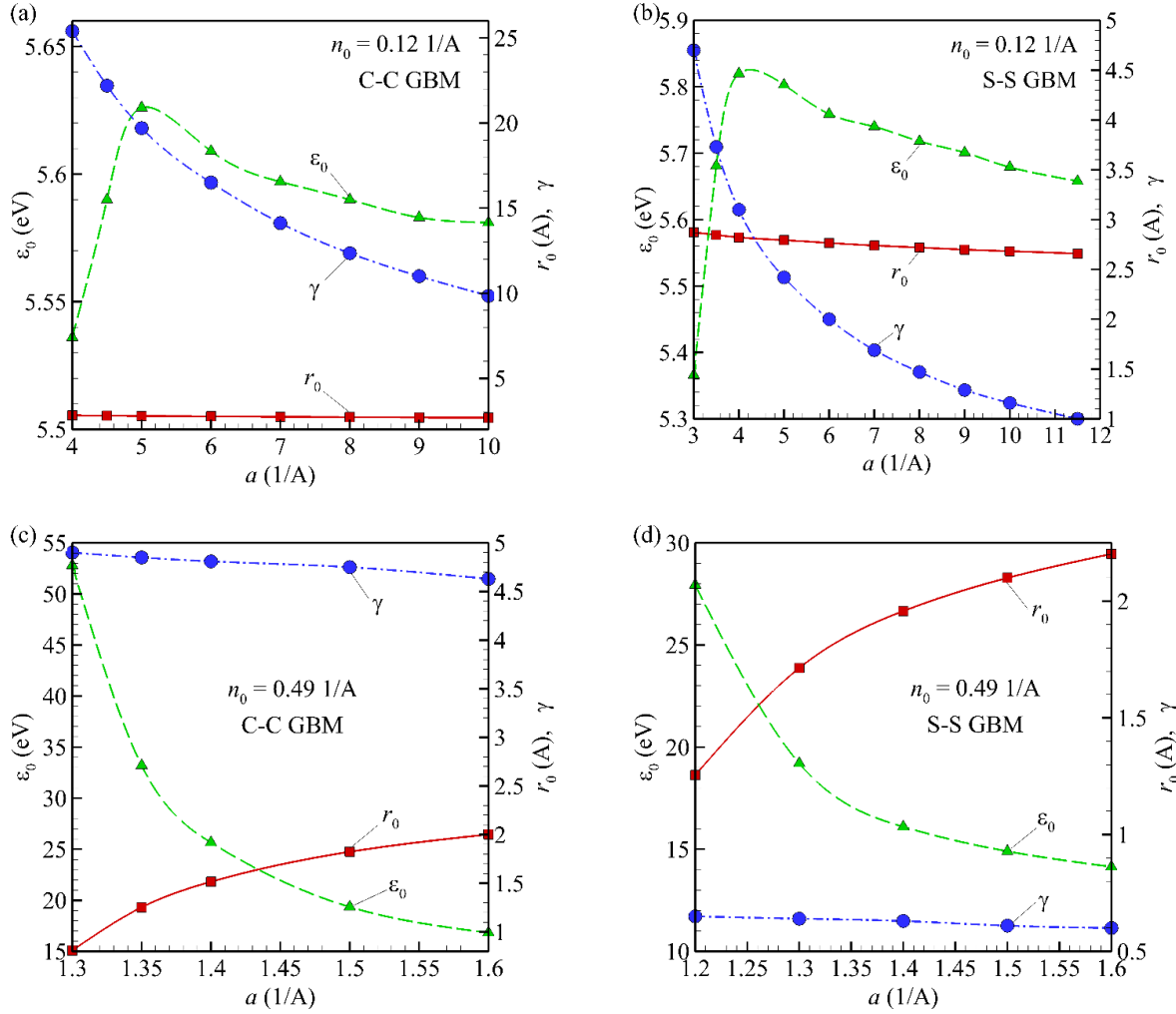


Figure 2.8. Values of parameters r_0 (squares, red), ϵ_0 (triangles, green), and γ (circles, blue) for C-C (a,c) and S-S (b,d) GBMs versus parameters a , which allow one to fit values of E_p , $S_{p,max}$, and Δz_{max} obtained in atomistic simulations (Table 2.1) at $n_0 = 0.12 \text{ \AA}^{-1}$ and $n_1 = 0.55 \text{ \AA}^{-1}$ (a,b), as well as at $n_0 = 0.49 \text{ \AA}^{-1}$ and $n_1 = 0.8 \text{ \AA}^{-1}$ (c,d). The symbols correspond to calculated points, while the curves represent the spline functions that interpolate the calculated data and are drawn only to guide the eye.

In the case of low density, CLs are independent of each other, so the effective parameters of a CL correspond to a solitary interstitial atom bonded with atoms in the crystalline lattices of nanotubes. In the high-density case, relatively short distances between neighboring CLs affect

load transfer through them, increasing the effective number of participating atoms and, thus, effective ε_0 , but simultaneously making CLs less stiff. Our calculations suggest that the crossover between the regimes of independent and crowded CLs occurs at $n_0 \sim 0.2 \text{ \AA}^{-1}$. This hypothesis, however, must be verified in atomic-level simulations.

The obtained results suggest that it is practically impossible to achieve quantitative agreement between the mesoscopic and atomistic simulations if the direction parameter γ is equal to 1. The results of atomistic simulations can be fitted by the bundle model at $\gamma = 1$ only for S-S GBM in the low-density case when $a = 11.5 \text{ 1/\AA}$. This value of a is difficult to justify from the physical standpoint, since it is much larger than, e.g., the maximum value of the stiffness parameter in the attractive term for C-C bonds adopted in the REBO potential.

Since the best-fit parameters are not-unique, additional arguments are applied to choose the sets of parameters, recommended for future use in mesoscopic simulations of CNT network materials (Section 2.2.4). For small CL density, any choice of parameters from Figure 2.8 results in the stress-displacement curves which are only marginally different from each other. The best-fit parameters that obtained at $a = 5 \text{ \AA}^{-1}$ are chosen, since this value of a is close to the maximum value of stiffness parameters adopted for C-C bonds in the REBO potential.

For large CL density, it is beneficial to use the best-fit parameters with small values of a , since in this case the stress-displacement curves obtained based on the bundle model become qualitatively similar to the atomistic one, as it is illustrated in Figure 2.9. At the same time, smaller values of a imply excessively small values of r_0 and, correspondingly, excessively large degree of initial CL pre-straining.

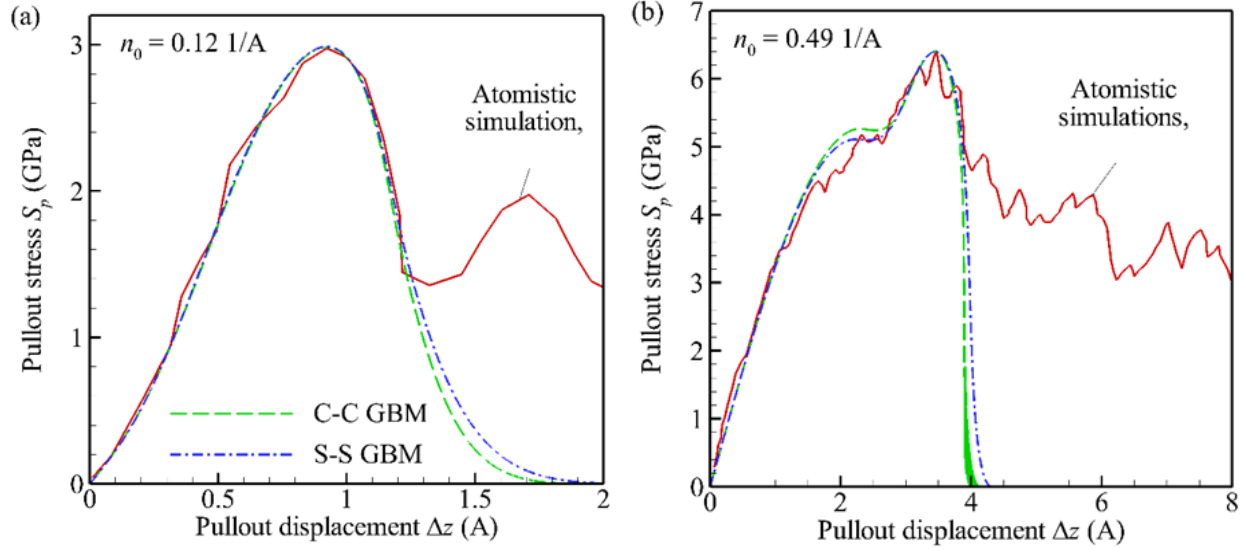


Figure 2.9. Stress S_p versus displacement Δz obtained in the pullout simulations for a seven-tube bundle with length of 59.6 \AA composed of $(26,0)$ CNT at $n_0 = 0.12 \text{ \AA}^{-1}$ and $n_1 = 0.55 \text{ \AA}^{-1}$ (a), as well as at $n_0 = 0.49 \text{ \AA}^{-1}$, $n_1 = 0.8 \text{ \AA}^{-1}$ (b). The solid curves (red) are obtained in atomistic simulations [77]. Other curves are obtained based on the bundle model with the best-fit parameters in Table 2.2 for the C-C GBM (green dashed curves) and S-S GBM (blue dash-dotted curves).

It makes the mesoscopic computational model (Section 2.2.4) non-robust when it is applied for cross-linked CNT materials, since the individual CLs with small r_0 can be broken not only due to material deformation, but also under the effect of thermal fluctuations. Based on these considerations, for simulations at large CL densities, the best-fit parameters corresponding to $a = 1.3 \text{ \AA}^{-1}$ are recommended.

Table 2.2. Best-fit parameters ε_0 , r_0 , and a of the CL potential function, Eq. (2.34), and direction parameter γ in Eqs. (2.36) - (2.39) obtained by fitting the stiffness E_p , maximum stress $S_{p,max}$, and displacement Δz_{max} at $S_p = S_{p,max}$, predicted by the bundle model to values given in Table 2.1. The parameters of the cutoff function $S(\tau(r))$ in Eq. (2.34) are equal to $r_* = 3.2 \text{ \AA}$ and $r_c = 4.4 \text{ \AA}$.

| C-C GBM | | | | | | S-S GBM | | | | |
|---------|--------|-----------------|-------|----------|------|---------|-----------------|-------|----------|------|
| n_0 | r_0 | ε_0 | a | γ | | r_0 | ε_0 | a | γ | |
| (1/Å) | (Å) | (eV) | (1/Å) | | | (Å) | (eV) | (1/Å) | | |
| 0.12 | PL_1 | 2.79 | 5.63 | 5 | 19.7 | PL_2 | 2.79 | 5.8 | 5 | 2.42 |
| 0.49 | PH_1 | 0.81 | 52.8 | 1.3 | 4.9 | PH_2 | 1.71 | 19.2 | 1.3 | 0.64 |

The best-fit parameters recommended for simulations with (26,0) CNT at both large and small CL densities based on C-C and S-S GBMs are listed in Table 2.2. The stress-displacement curves predicted by both GBMs with these parameters are only marginally different (Figure 2.9). The chosen values of parameters also provide reasonable agreement with the results of atomistic simulations [77] in a range of CL density (Figure 2.9).

The parameters for CLs between (10,10) CNTs are also determined by fitting the results of atomistic simulations of pullout process obtained based on AIREBO interatomic potential [116]. For S-S GBM, the CL model parameters are $r_0 = 2.904 \text{ \AA}$, $\varepsilon_0 = 10.73 \text{ eV}$, $a = 5$, $\gamma = 1.72 \text{ \AA}$.

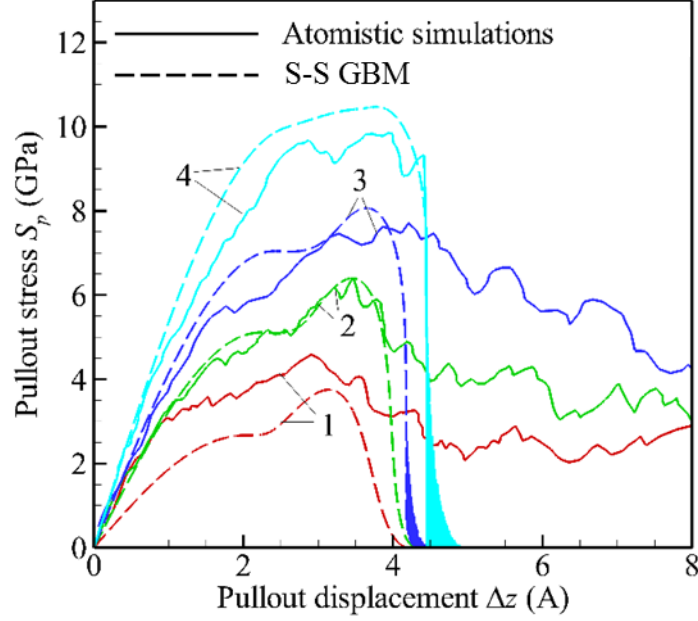


Figure 2.10. Stress S_p versus displacement Δz obtained in the pullout simulations of the central nanotube from a seven-tube with a length of 59.6 \AA composed of $(26,0)$ CNT. The solid curves are obtained in atomistic simulations [77]. The dashed curves are obtained based on the bundle model and S-S GBM with the parameter set PH_2 in Table 2.2. The CL density n_0 is equal to 0.29 \AA^{-1} (curves 1, red), 0.49 \AA^{-1} (curves 2, green), 0.62 \AA^{-1} (curves 3, blue), and 0.84 \AA^{-1} (curves 4, cyan).

2.2.4 Effective bond model for large-scale mesoscopic simulations of cross-linked CNT materials

In order to use the developed effective bond model in mesoscopic simulations with the MFF given by Eq. (2.4), it is necessary to define the CL length r_m in Eq. (2.21) as a function of coordinates of the mesoscopic nodes. Here, the definition of r_m for a CL “connecting” a pair of arbitrary cylindrical CNT segments of radii R_1 and R_2 is introduced, assuming that the positions of two mesoscopic nodes at the centers of bases of segment i are defined by vectors \mathbf{r}_{i1} and \mathbf{r}_{i2} (Figure 2.11). Then the length of segment i is equal to $L_i = |\mathbf{r}_{i2} - \mathbf{r}_{i1}|$, and the orientation of the

segment axis is given by a unit vector $\mathbf{l}_i = (\mathbf{r}_{i2} - \mathbf{r}_{i1})/L_i$. The positions of two ends of the effective CL bond can be defined using parameters t_i ($0 \leq t_i \leq 1$), such that the position vector \mathbf{r}_i of the projection of the CL end belonging to segment i onto its axis is equal to

$$\mathbf{r}_i = \mathbf{r}_{i1} + t_i(\mathbf{r}_{i2} - \mathbf{r}_{i1}), \quad i = 1, 2, \quad (2.45)$$

where t_i are considered as constant parameters, which are determined at a time when the CL is formed. Then the forces \mathbf{F}_{ij} exerted on all node of the considered segments can be calculated as

$$\mathbf{F}_{ij} = -\frac{\partial \varphi}{\partial \mathbf{r}_{ij}} = -\frac{d\varphi}{dr} \frac{\partial r}{\partial \mathbf{r}_{ij}}. \quad (2.46)$$

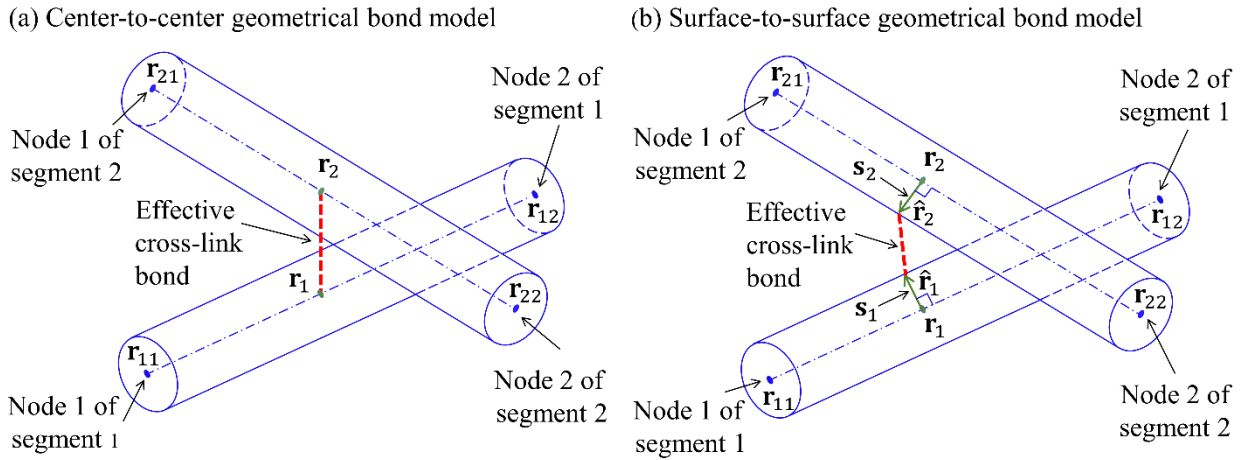


Figure 2.11. Sketch illustrating definitions of the effective CL bond (dashed line segments; red) between two cylindrical CNT segments, which are utilized in C-C (a) and S-S (b) GBMs. In panel (b), the sketch is simplified, since each vector \mathbf{s}_i is assumed to be orthogonal to vector $\mathbf{r}_{i2} - \mathbf{r}_{i1}$ and co-planar with vectors $\mathbf{r}_{i2} - \mathbf{r}_{i1}$ and $\mathbf{r}_2 - \mathbf{r}_1$.

For the C-C GBM, Eq. (2.36) can be generalized in the form $(r + R_1 + R_2)^2 = \mathbf{p}_1^2$, where r is the length of the effective bond and $\mathbf{p}_1 = -\mathbf{p}_2 = \mathbf{r}_2 - \mathbf{r}_1$. For S-S GBM, a simplified case is considered, when CLs do not produce torsional load. Then vectors $\mathbf{s}_i = R_i \mathbf{n}_i$ are

introduced such that each \mathbf{s}_i is orthogonal to the axis of segment i and co-planar with vectors $\mathbf{r}_{i2} - \mathbf{r}_{i1}$ and $\mathbf{r}_2 - \mathbf{r}_1$, (here $\mathbf{n}_i = (\mathbf{p}_i - (\mathbf{p}_i \cdot \mathbf{l}_i)\mathbf{l}_i)/B_i$ and $B_i = |\mathbf{p}_i - (\mathbf{p}_i \cdot \mathbf{l}_i)\mathbf{l}_i|$), and assume that the positions of the CL ends are given by vectors

$$\hat{\mathbf{r}}_i = \mathbf{r}_i + \mathbf{s}_i. \quad (2.47)$$

Hereinafter, the symbol “ $\hat{}$ ” is used to denote parameters specific for S-S GBM. Then $\hat{r}^2 = \hat{\mathbf{p}}_1^2$, where $\hat{\mathbf{p}}_1 = -\hat{\mathbf{p}}_2 = \hat{\mathbf{r}}_2 - \hat{\mathbf{r}}_1$.

In order to introduce the direction parameter γ one can note that the CL length, e.g., in the C-C GBM, can be represented in the form $(r + R_1 + R_2)^2 = \mathbf{d}_i^2 + (\mathbf{p}_i - \mathbf{d}_i)^2$, where $\mathbf{d}_i = (\mathbf{p}_i \cdot \mathbf{n}_i)\mathbf{n}_i$ is a component of \mathbf{p}_i orthogonal to the axis of segment i . Then the lengths of vectors \mathbf{d}_i and $\mathbf{p}_i - \mathbf{d}_i$ can be considered as analogs of $\delta z_{12} + 2R_T$ and δh in Eq. (2.35) and the CL bond length r can be defined as

$$(r + R_1 + R_2)^2 = \frac{1}{2} \sum_{i=1}^2 [\mathbf{d}_i^2 + \gamma(\mathbf{p}_i - \mathbf{d}_i)^2] = \gamma \mathbf{p}_1^2 + \frac{\gamma - 1}{2} (\mathbf{d}_1^2 + \mathbf{d}_2^2). \quad (2.48)$$

For S-S GBM, similar arguments result in the following equation with respect to the CL length \hat{r} :

$$\hat{r}^2 = \frac{1}{2} \sum_{i=1}^2 [\hat{\mathbf{d}}_i^2 + \gamma(\hat{\mathbf{p}}_i - \hat{\mathbf{d}}_i)^2] = \gamma \hat{\mathbf{p}}_1^2 + \frac{\gamma - 1}{2} (\hat{\mathbf{d}}_1^2 + \hat{\mathbf{d}}_2^2), \quad (2.49)$$

where $\hat{\mathbf{d}}_i = (\hat{\mathbf{p}}_i \cdot \mathbf{n}_i)\mathbf{n}_i$. In a case of parallel segments, Eqs. (2.48) and (2.49) are identical to Eqs. (2.36) and (2.38). The gradients $\partial r / \partial \mathbf{r}_{ij}$ (for the C-C GBM) and $\partial \hat{r} / \partial \mathbf{r}_{ij}$ (for the S-S GBM) of the effective bond length, which are necessary to find forces \mathbf{F}_{ij} exerted by a CL to the ends of corresponding CNT segments in the mesoscopic model of nanotube materials are calculated according to Eq.(2.46). These gradients can be obtained by direct differentiation of Eqs. (2.48)

and (2.49). For calculations of derivatives, it is convenient, however, to represent the CL length in the form of composite functions of the segment end coordinates.

For instance, for the C-C GBM, the CL length r as a function of \mathbf{r}_{11} can be written as:

$$r = r(\mathbf{p}_1(\mathbf{r}_{11}), \mathbf{s}_1(\mathbf{p}_1(\mathbf{r}_{11}), \mathbf{l}_1(\mathbf{r}_{11})), \mathbf{s}_2(\mathbf{p}_2(\mathbf{r}_{11}))). \quad (2.50)$$

Then the direct differentiation of Eq. (2.50) results in

$$\frac{\partial r}{\partial \mathbf{r}_{11}} = -\gamma(1-t_1) \frac{\mathbf{p}_1}{r} + \frac{\gamma-1}{2} \left[(1-t_1) \frac{\mathbf{d}_1-\mathbf{d}_2}{r} - \frac{(\mathbf{p}_1 \cdot \mathbf{l}_1) \mathbf{d}_1}{L_1 r} \right]. \quad (2.51)$$

The equation for other gradients can be either obtained using similar approach or re-written from Eq. (2.51) using the symmetry arguments as

$$\frac{\partial r}{\partial \mathbf{r}_{12}} = -\gamma t_1 \frac{\mathbf{p}_1}{r} + \frac{\gamma-1}{2} \left[t_1 \frac{\mathbf{d}_1-\mathbf{d}_2}{r} + \frac{(\mathbf{p}_1 \cdot \mathbf{l}_1) \mathbf{d}_1}{L_1 r} \right], \quad (2.52)$$

$$\frac{\partial r}{\partial \mathbf{r}_{21}} = -\gamma(1-t_2) \frac{\mathbf{p}_2}{r} + \frac{\gamma-1}{2} \left[(1-t_2) \frac{\mathbf{d}_2-\mathbf{d}_1}{r} - \frac{(\mathbf{p}_2 \cdot \mathbf{l}_2) \mathbf{d}_2}{L_2 r} \right], \quad (2.53)$$

$$\frac{\partial r}{\partial \mathbf{r}_{22}} = -\gamma t_2 \frac{\mathbf{p}_2}{r} + \frac{\gamma-1}{2} \left[t_2 \frac{\mathbf{d}_2-\mathbf{d}_1}{r} + \frac{(\mathbf{p}_2 \cdot \mathbf{l}_2) \mathbf{d}_2}{L_2 r} \right]. \quad (2.54)$$

For the S-S GBM, when the CL length \hat{r} is given by Eq.(2.49), a similar approach results in the following equations for gradients:

$$\frac{\partial \hat{r}}{\partial \mathbf{r}_{11}} = (1-t_1) \mathbf{A}_1 - \mathbf{B}_1, \quad (2.55)$$

$$\frac{\partial \hat{r}}{\partial \mathbf{r}_{12}} = t_1 \mathbf{A}_1 + \mathbf{B}_1, \quad (2.56)$$

$$\frac{\partial \hat{r}}{\partial \mathbf{r}_{21}} = (1-t_2) \mathbf{A}_2 - \mathbf{B}_2, \quad (2.57)$$

$$\frac{\partial \hat{r}}{\partial \mathbf{r}_{22}} = t_2 \mathbf{A}_2 + \mathbf{B}_2, \quad (2.58)$$

where

$$\mathbf{A}_1 = -\gamma \frac{\hat{\mathbf{p}}_1}{\hat{r}} + \mathbf{G}_1 - \mathbf{G}_2 + \frac{\gamma - 1}{2} \left[\frac{\hat{\mathbf{d}}_1 - \hat{\mathbf{d}}_2}{\hat{r}} \right], \quad (2.59)$$

$$\mathbf{B}_1 = \frac{(\mathbf{p}_1 \cdot \mathbf{l}_1)}{L_1} \mathbf{G}_1 + \frac{(\hat{\mathbf{p}}_1 \cdot \mathbf{l}_1)}{\hat{r}} h \frac{\mathbf{s}_1}{L_1} + \frac{\gamma - 1}{2} \left[\frac{(\hat{\mathbf{p}}_1 \cdot \mathbf{n}_2)}{R_2} \frac{(\mathbf{p}_1 \cdot \mathbf{l}_1)}{\hat{r}} \frac{\mathbf{s}_1}{L_1} \right], \quad (2.60)$$

$$\mathbf{A}_2 = -\gamma \frac{\hat{\mathbf{p}}_2}{\hat{r}} + \mathbf{G}_2 - \mathbf{G}_1 + \frac{\gamma - 1}{2} \left[\frac{\hat{\mathbf{d}}_2 - \hat{\mathbf{d}}_1}{\hat{r}} \right] = -\mathbf{A}_1, \quad (2.61)$$

$$\mathbf{B}_2 = \frac{(\mathbf{p}_2 \cdot \mathbf{l}_2)}{L_2} \mathbf{G}_2 + \frac{(\hat{\mathbf{p}}_2 \cdot \mathbf{l}_2)}{\hat{r}} h \frac{\mathbf{s}_2}{L_2} + \frac{\gamma - 1}{2} \left[\frac{(\hat{\mathbf{p}}_2 \cdot \mathbf{n}_1)}{R_1} \frac{(\mathbf{p}_2 \cdot \mathbf{l}_2)}{\hat{r}} \frac{\mathbf{s}_2}{L_2} \right], \quad (2.62)$$

$$\mathbf{G}_i = h \frac{R_i \hat{\mathbf{p}}_i - (\hat{\mathbf{p}}_i \cdot \mathbf{l}_i) \mathbf{l}_i - (\hat{\mathbf{p}}_i \cdot \mathbf{n}_i) \mathbf{n}_i}{B_i \hat{r}}, \quad (2.63)$$

$$h = \gamma + \frac{\gamma - 1}{2} \left[\frac{\hat{\mathbf{p}}_1 \cdot \mathbf{n}_1}{R_1} + \frac{\hat{\mathbf{p}}_2 \cdot \mathbf{n}_2}{R_2} \right]. \quad (2.64)$$

Eqs. (2.51)-(2.54) and (2.55)-(2.58) can be simplified in a case $\gamma = 1$, when all term in square brackets do not contribute to forces. It is also worth noting that the developed mesoscopic CL force field provides zero total torque, *i.e.*, for any pair of CNT segments and any CL “connecting” these segments,

$$\sum_{i=1}^2 \sum_{j=1}^2 \mathbf{r}_{ij} \times \mathbf{F}_{ij} = 0, \quad (2.65)$$

and, thus, it ensures conservation of the angular momentum

2.2.5 Pullout simulations of a central tube from a seven-tube bundle for regular and random distribution of CLs

In this section, the results of pullout simulations for a seven-tube bundle obtained with the bundle model and is compared to the general mesoscopic model. For this purpose, both models is applied to bundles of lengths $L_T = 12$ nm (Figure 2.12) and $L_T = 60$ nm (Figure 2.13) at the CL densities $n_0 = n_1 = 0.3 \text{ \AA}^{-1}$. All simulations are performed based on the S-S

GBM with the parameter set designated as PH_2 in Table 2.2. The simulations based on the general mesoscopic model are performed with the periodic boundary conditions in the direction of the bundle axis using the minimum image conversion technique [117] in Berendsen's thermostat [118] maintaining constant "mesoscopic" temperature of 1 K. The length Δl_S of mesoscopic segments varies from 5 Å to 20 Å, while the cell size ΔZ of the computational mesh for solving Eqs. (2.23) is equal to 1 Å.

The comparison of the bundle and general mesoscopic models is necessary, since these models differ from each other by a number of details. In the bundle model, CLs are distributed continuously, while in the general mesoscopic model CLs are discrete and can be randomly distributed along the bundle. The effects related to the discrete nature of CLs in the mesoscopic model potentially can be pronounced and make significant contribution to the overall difference between computational results obtained with the two models. Other differences between models are related to the geometrical models of curved CNTs, absence of bending deformation in Eqs. (2.23), forms of the van der Waals interaction potentials and boundary conditions, replacement of a dynamic equation for radial motion of nanotubes by the balance Eq. (2.24) in the bundle model, and peculiarities of calculations of the CL length. The total effect of these factors does not vanish in the limit of infinitely small ΔZ and Δl_S . Correspondingly, the simulation results obtained with two models do not exactly converge to each other with decreasing ΔZ and Δl_S .

In a case of a regular CL distribution, it is assumed that every pair of neighboring segments from different CNTs is bonded by a single CL that connects the segment surfaces, so that the CL densities are equal to $n_S = 6/\Delta l_S$. The simulations are then performed with the energy parameter in Eq. (8) equal to $\varepsilon_S = \varepsilon_0(n_0/n_S)$ instead of ε_0 .

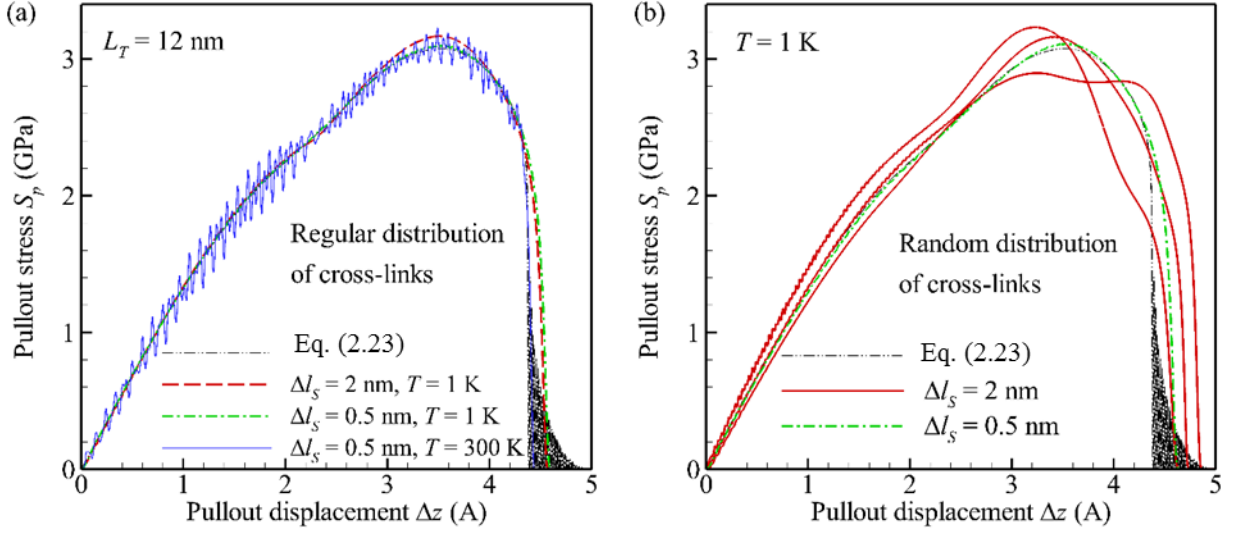


Figure 2.12. Stress S_p versus displacement Δz obtained in the pullout simulations for a seven-tube bundle of length $L_T = 12$ nm composed of (26,0) CNT. The dash-double-dotted thin curve is obtained based on Eq. (2.23) at the CL densities $n_0 = n_1 = 0.3 \text{ \AA}^{-1}$. Other curves are obtained with the general mesoscopic model at $\Delta l_s = 2$ nm (solid thick curves, red) and $\Delta l_s = 0.5$ nm (dash-dotted curves, green, and solid thin curve, blue). The mesoscopic simulations are performed with regular (a) and random (b) CL distributions at a temperature of 1 K with exception of the solid thin curve in panel (a), which is obtained at $T = 300$ K. Three solid thick curves in panel (b) (red) correspond to three random CL distributions.

The results of such simulations are compared with the results obtained based on the bundle model with ε_0 and $n_0 = n_1$, since the solution of the bundle model does not change if n_0 and ε_0 vary at $n_0 \varepsilon_0 = \text{const}$. In a case of random CL distribution, the same z coordinate of both ends of a CL is drawn at random from homogeneous distribution between 0 and L_T . The total CL number, average CL density n_s , and value of ε_s are determined by the segment length Δl_s similarly to the case of the regular CL distribution.

For the regular CL distribution, the stress-displacement curves obtained in the mesoscopic simulations closely approach the curve obtained based on the bundle model with decreasing Δl_s for both $L_T = 12$ nm (Figure 2.12) and $L_T = 60$ nm (Figure 2.13). The value of stiffness E_p obtained in the mesoscopic simulations at $\Delta l_s = 0.5$ nm, in particular, is less than 1% different from the value predicted by the bundle model. An additional simulation performed for $L_T = 12$ nm and $\Delta l_s = 0.5$ nm at a temperature of 300 K (thin solid curve in Figure 2.12) shows that an increasing mesoscopic temperature can introduce relatively strong thermal noise in the pullout stress, but it does not change the general behavior of the stress-displacement curve.

In the case of smallest Δl_s considered, the maximum stress obtained in the mesoscopic simulations with the short bundle is only about 0.5% different compared to the maximum stress obtained with the bundle model. This difference rises up to ~3% for the longer bundle (Figure 2.13), when a plateau at a level of maximum stress appears and the stress obtained with the mesoscopic model periodically oscillates. Further decrease in the segment length does not eliminate this difference. It is attributed to relatively large local bending of nanotubes, which is realized under conditions of massive CL breaking in the inelastic regime. For strongly curved CNTs, the difference between two models is expected, since the bundle model utilizes simplified methods to account for curvature and does not account for the contribution of bending deformation to the elastic energy of nanotubes. The stress oscillation at a plateau corresponding to the maximum stress in Figure 2.13 appears due to the periodic breaking of discrete CLs. The oscillation magnitude and period rapidly decrease with decreasing segment length.

In the case of random CL distribution, various random distributions results in distinct stress-displacement curves, e.g., see solid curves in Figure 2.12 and Figure 2.13. Then, for short

bundles (Figure 2.12), the value of E_p varies within $\pm 9\%$ with respect to the stiffnesses predicted by the bundle model.

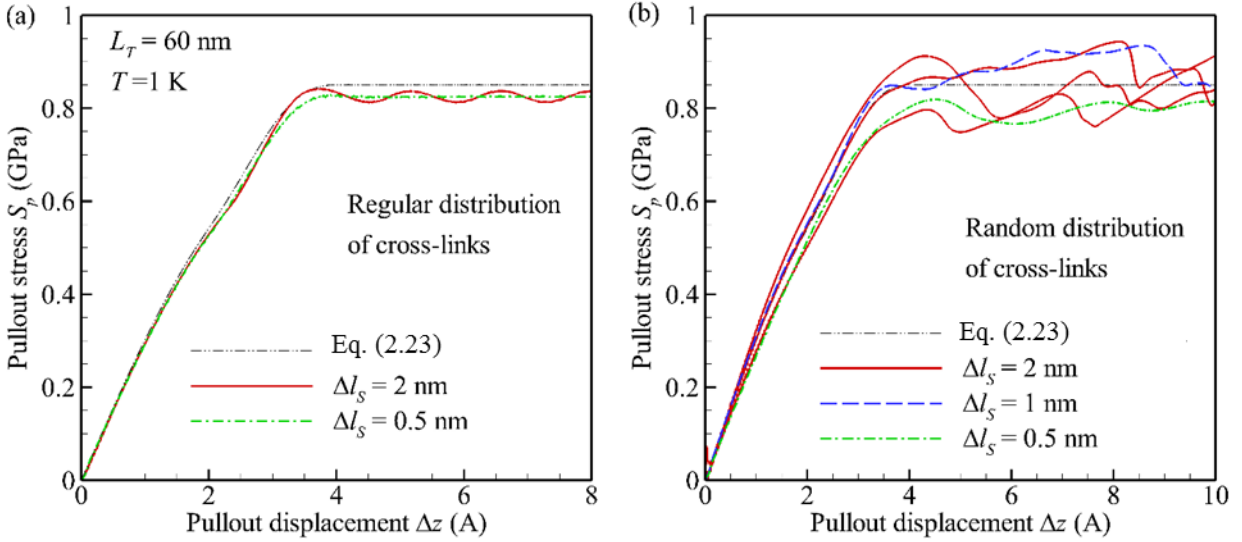


Figure 2.13. Stress S_p versus displacement Δz obtained in the pullout simulations for a seven-tube bundle of length $L_T = 60$ nm composed of $(26,0)$ CNTs. The dash-double-dotted thin curve is obtained based on Eq. (2.23) at the CL densities $n_0 = n_1 = 0.3 \text{ \AA}^{-1}$. Other curves are obtained based on the general mesoscopic model with the regular (a) and random (b) CL distributions at a temperature of 1 K and $\Delta l_S = 2$ nm (solid curves, red), $\Delta l_S = 1$ nm (dashed curve, blue), and $\Delta l_S = 0.5$ nm (dash-dotted curves, green).

For longer bundles (Figure 2.13), the values of E_p for different random CL distributions are close to each other and the randomness in the CL distribution induces stress variations only at a plateau, when the pullout process is dominated by CL breaking. In all considered cases, the maximum stress for random CL distributions is less than 10% different compared to S_p predicted by the bundle model.

The comparison of results obtained with two models allows one to conclude that the results of the pullout test obtained with the general mesoscopic model are in good agreement with the results predicted by the bundle model based on Eq. (2.23). The bundle model, however, is advantageous for fitting the effective bond model to atomistic simulations compared to the general mesoscopic model, since the former allows one to fast explore the multi-dimensional parameter space.

2.3 In-house Computational Code

The in-house computational code TMD used in this work was initially developed by Dr. Alexey N. Volkov [119] as a general purpose program for MD-type simulations with high-aspect-ratio “tubular” particles, and adapted further to simulate mesoscopic cross-linked CNT materials, where CLs, i.e., bonded potential, is implemented in the form of model Morse potential. The current version of the code is written in Fortran 90 with both serial and parallel processing implementation. In the parallel mode, TMD uses spatial decomposition techniques to partition the simulation domain into smaller sub-domains. The code integrates Newton’s equations of motion for a collection of interacting particles, e.g. atoms, molecules, coarse-grained CNTs. The TMD keeps track of such nearby short-range interacting particles using the neighbor lists. The Berendsen thermostat and barostat algorithms are used to maintain desired mesoscopic temperature and pressure. The TMD solver output coordinates and other particle quantities, e.g. velocities, energies, and microscopic stress.

CHAPTER 3

IN SILICO GENERATION AND STRUCTURAL CHARACTERIZATION OF CNT MATERIAL SAMPLES

Computational CNT material samples can be “grown” by lengthening the nanotubes over the course of a simulation [120] or the straight, fully sized nanotubes can be made to self-organize into continuous network of bundles through dynamic simulations [121]. The latter option, i.e., dynamic self-assembly, is more straightforward, and has already been proven to be effective in generation of CNT materials with random orientation of nanotubes [93,82,91]. The ability to simulate the dynamic process of spontaneous self-assembly of nanotubes into thick interconnected bundles is a distinct feature of MFF used in the present study, which completely eliminates artificial barriers for inter-tube sliding. The bead-and-spring coarse-grained model initially suggested for simulations of CNT material in Ref. [65] and then used in Refs. [62, 63] introduces barriers for inter-tube sliding at finite size of spherical beads representing mesoscopic elements of CNT. It can preclude dynamic formation of thick bundles. In this work, all *in silico* generated material samples of CNT forests and films are produced through dynamic self-assembly simulations.

3.1 CNT Fibers

CNT fibers are composed of nanotubes that have preferential orientation along a selected direction. In this work, the length of individual CNTs are assumed to be smaller than the size of

the computational system, and the nanotubes are arranged into a continuous network of bundles. The assumptions are similar to the computational samples of “buckypaper” investigated in a number of earlier studies, *e.g.*, Refs. [90,93,91,122,123,124,125,126,127,128,129,130,131]. In contrast to the vertically aligned CNT (VACNT) arrays, where one end of each nanotube is fixed at the substrate, in the CNT fibers, both ends of the CNT are free to move during the self-organization into the network structure. The absence of fixed CNT ends in the CNT fibers increases mobility of individual nanotubes and sets a lower limit on the range of the material density where stable continuous networks can be obtained. The minimum density that ensures formation of stable structures, however, strongly depends on the CNT length. The results of mesoscopic simulations suggest that, in the absence of CNT defects and inter-tube CLs, the three-dimensional isotropic CNT networks composed of 400-nm-long CNTs are unstable for densities below $\sim 0.0025 \text{ gcm}^{-3}$. In the discussion below, the procedure of generation of computational samples is illustrated for fibers composed of 400-nm-long (10,10) SWCNTs and having a material density of 0.01 gcm^{-3} . Although the increasing degree of alignment of CNTs along the fiber axis reduces stability of the CNT network at given material density, it is found that CNTs form metastable network structures in all considered fiber sample. This ability of CNTs to form low-density continuous metastable networks is in agreement with experimental observations, which, in accordance with review [132], reports density of CNT fibers in the range from $5.5 \cdot 10^{-4}$ to 2.16 gcm^{-3} . The results of the structural characterization of CNT fibers generated *in silico* are related to experimental data reported for low-density CNT fibers produced, *e.g.*, by the direct spinning method [133]. Since the detailed results of experimental characterization of low-density CNT fibers are scarce, a connection is made between structural

properties of computational samples with experimental data on CNT fibers of medium density, e.g., [134].

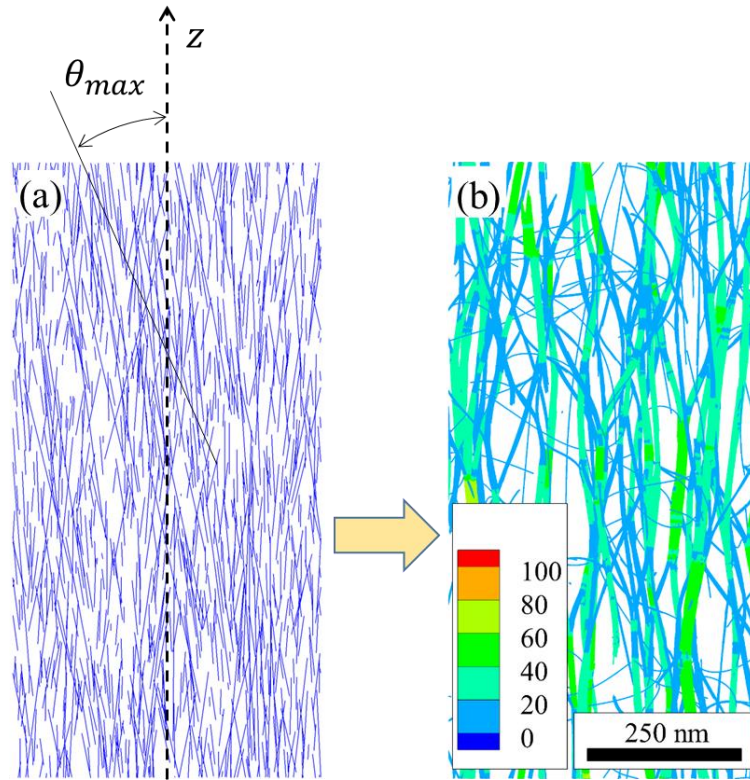


Figure 3.1. Schematic representation of the procedure used for the generation of CNT fiber samples. The straight CNTs are first randomly added with random inclination with respect to the fiber axis θ ranging uniformly from zero to a maximum angle θ_{max} (a). The high temperature annealing followed by a relaxation at 300 K is used to induce self-organization of CNTs into a continuous and metastable network of interconnected bundles (b). Nanotube segments in panel (b) are colored according to their local bundle size.

3.1.1 *In silico* generation of (10,10) CNT fibers

The initial samples of CNT fibers composed of straight and dispersed CNTs are prepared by the acceptance and rejection method using the periodic boundary conditions in all three

directions. The positions of centers of CNTs, which are sequentially added to the system, are chosen at random within the simulation box, and the directions of CNT axes are randomly picked from a uniform distribution within a cone with the apex angle Θ_{max} with respect to the predefined axis of the fiber. A new CNT is added to the sample only if the minimum gap between the surfaces of the new and any of the CNT already present in the sample is larger than a predefined minimum distance. The minimum distance between CNTs in the generation of CNT fibers was set to be smaller than the equilibrium distance between nanotubes, i.e., 3.44 Å for (10,10) CNT and equal to 3 Å. As a result, the initial samples contain some fraction of pairs of CNTs experiencing inter-tube repulsive force. This initial repulsive interaction is sufficient for triggering self-assembly of CNTs into a network even in a constant-volume and constant-energy simulation, without the temperature control through a computational thermostat. Several representative configurations of CNT fiber generated with an approach described above for different maximum angle of initial inclination, Θ_{max} , varying from 3° to 45°, are shown in Figure 3.2. The *in silico* sample preparation procedure consists of a 3-ns-long high-temperature stage when the “mesoscopic” temperature of the system is kept at a level of 10,000 K, followed by a relaxation stage at a temperature of 300 K, both performed using the Berendsen thermostat algorithm [118]. The high-temperature stage leads to the fast formation of a continuous network structure, while the relaxation stage lasts until the formation of a steady-state structure, which occurs within 5-9 ns after the end of the high-temperature stage. The variation of the maximum initial inclination angle allows one to obtain CNT fibers with controllable structural characteristics.

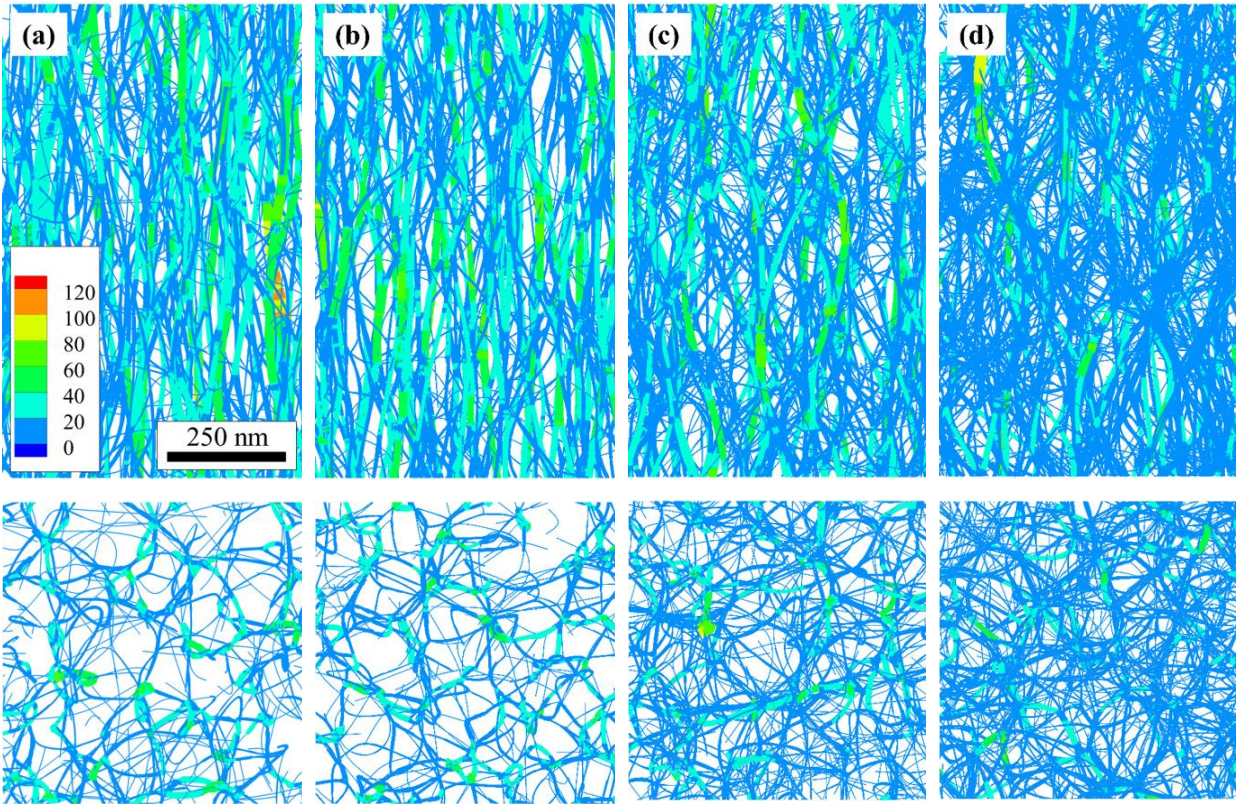


Figure 3.2. Side and top views of relaxed samples of CNT fibers composed of 400-nm-long (10,10) SWCNTs obtained at various maximum angles of initial inclination of CNTs θ_{max} equal to 3° (a), 15° (b), 30° (c), and 45° (d). All generated samples have dimensions of $1 \times 1 \times 1 \mu\text{m}^3$ and a material density of 0.01 gcm^{-3} . The figure demonstrates only the central parts of every sample with the cross section of $500 \text{ nm} \times 500 \text{ nm}$. Individual nanotubes are colored according to the local thickness of bundles defined as the number of segments in a bundle cross-section (a). In every panel, the fiber axis is directed vertically in the top snapshot and normal to the plane of the figure in the bottom snapshot.

3.1.2 Structural characterization of *in silico* generated (10,10) CNT fibers

At small $\Theta_{max} = 3^\circ-15^\circ$, the structure is dominated by relatively thick and almost straight bundles containing 15-50 CNTs with large columnar pores between them (Figure 3.2(a) and Figure 3.2(b)). The bundle thickness distributions are characterized by a broad maximum at 10-25 segments in a bundle cross section (Figure 3.3(a) and Figure 3.3(b)) and the average number of CNT segments in a bundle cross-section, $\langle N_B \rangle$, equal to ~ 25 . Qualitatively, the bundle size distributions generated at small inclination angles resemble those obtained for VACNT arrays in Ref. [135]. The most probable tilts of CNT segments with respect to the fiber axis of 8° (Figure 3.4) and the values of the Herman orientation factor (HOF; Figure 3.5) are similar to the corresponding values listed for CNT forests [135]. HOF is defined as $HOF = [3\langle \cos^2 \theta \rangle - 1]/2$, where θ is the local angle between a nanotube and the vertical axis, and the angle brackets $\langle \rangle$ denote averaging over all CNT segments in a sample. The HOF quantifies the extent of the orientation of nanotubes with respect to an axis of interest, and ranges from -0.5 to 1, where values of -0.5, 0, and 1 correspond to perpendicular alignment, isotropic orientation, and parallel alignment with respect to the axis, respectively. Thus, in the range of $\Theta_{max} \leq 15^\circ$, the procedure for the generation of CNT networks developed in this work results in highly aligned CNT samples with a rather weak dependence of the structural parameters on the precise value of Θ_{max} .

With further increase in Θ_{max} above 15° , the structures of relaxed samples exhibit stronger dependence on Θ_{max} . An increasing Θ_{max} results in the progressively increasing degree of entanglement of CNTs in the network structures, which is obvious from visual inspection of structures shown in Figure 3.2(c) and Figure 3.2(d). Quantitatively, the increasing degree of entanglement is reflected in increasing average tortuosity $\langle \tau \rangle$ of nanotubes (Figure 3.5), where

the tortuosity of a CNT is measured as $\tau = C/L_T$, with C and L_T being the distance between two ends of the CNT and its length.

The formation of elongated, columnar pores in aligned fibers is in agreement with experimental observations, where the pore length (along the axis of the fiber) to the porod chord length (average lateral size of pores) obtained in synchrotron small-angle X-ray scattering (SAXS) measurements vary in the ranges 159 – 221 nm and 20.3 – 13.1 nm, correspondingly, with their ratio spanning the range from 7.8 to 16.9 [133]. The visual examination of fiber samples in Figure 3.2(a) and Figure 3.2(b) reveals that pores in these samples have a length on the order of 300-400 nm and lateral size of ~100 nm with aspect ratio equal to 3-4. Less aligned samples obtained at larger Θ_{max} and shown in Figure 3.2(c) and Figure 3.2(d) have smaller pores with the pore length on the order of 200-300 nm with the lateral pore size of ~30-50 nm and aspect ratio 6-10, which fall into the experimental range of Ref. [133]. It is believed that smaller in average pore size in experimental samples compared to the computational samples can be explain by larger material density of experimental samples, which was not specified in Ref. [133].

At sufficiently large Θ_{max} , e.g., $\Theta_{max} = 45^\circ$, there is a substantial number of CNT segments in the relaxed samples, which are oriented perpendicularly to the axis of the fiber (Figure 3.3). In this case, the number of CNT segments in a bundle has a peak at one and exhibits monotonous decrease with increasing number of CNT segments in a bundle (Figure 3.2(d)). Although such samples can include bundles as thick as those in samples generated with $\Theta_{max} \leq 15^\circ$, the distribution demonstrates a strong depletion of bundles with more than 30 CNTs in a cross-section and, correspondingly the average bundle size decreases from 25 at $\Theta_{max} \leq 15^\circ$ to 15 at $\Theta_{max} = 45^\circ$ (Figure 3.5).

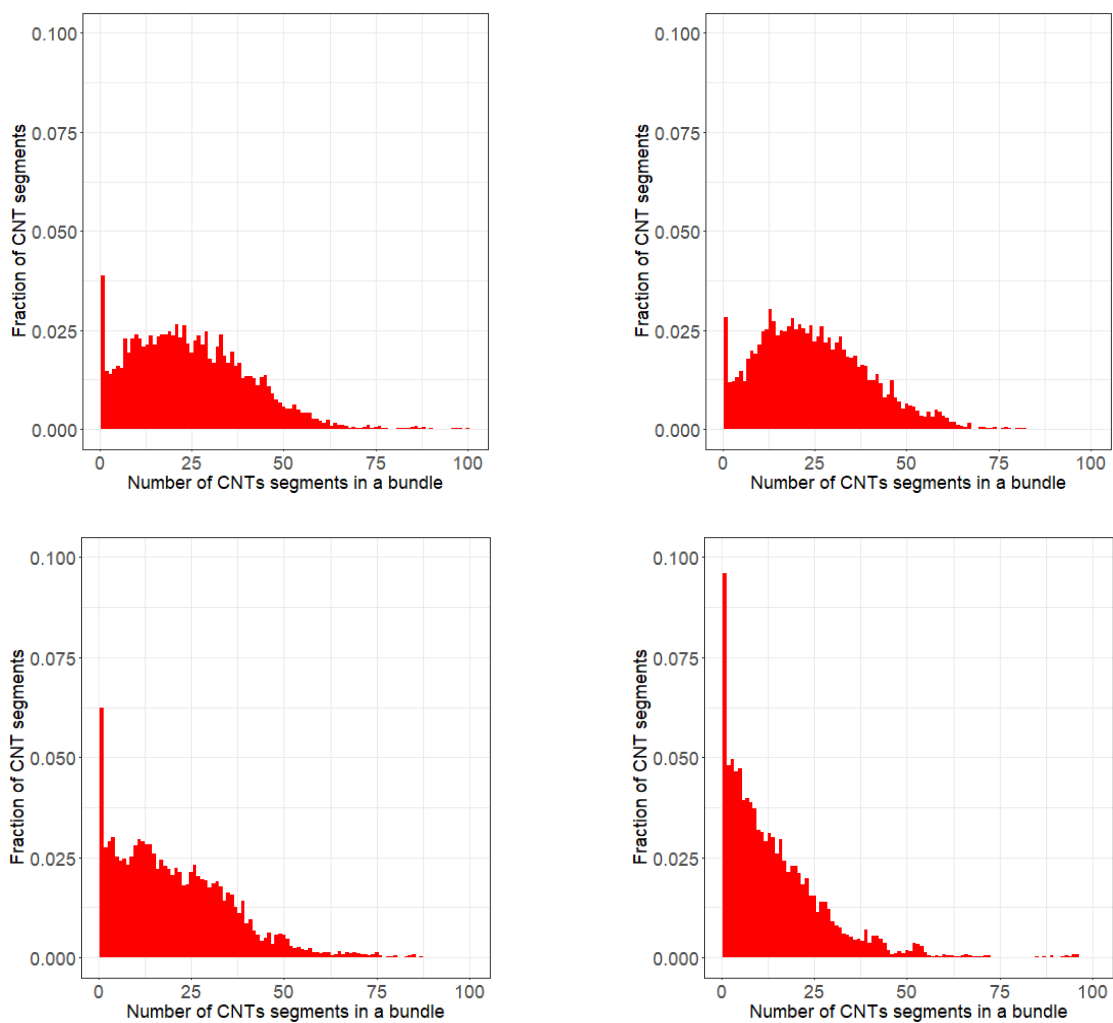


Figure 3.3. The bundle thickness distributions calculated for computational samples of CNT fibers shown in Figure 3.2 and obtained at various maximum angles of initial inclination of CNTs θ_{max} equal to 3° (a), 15° (b), 30° (c), and 45° (d). The bundle thickness is expressed in the local number of CNTs present in a bundle cross section, and each bin covers a thickness increment by 1 CNT segment.

The larger $\langle N_B \rangle$ in the case of the fiber sample can be attributed to the additional freedom of individual CNTs that are not tethered to a substrate and are free to slide with respect to others, as well as to smaller density and increased duration of the high-temperature stage used in the

generation of fiber samples. Preliminary simulations performed for thin CNT films [93,91] demonstrated that all these factors favor an increase in the average bundle size in the continuous CNT networks.

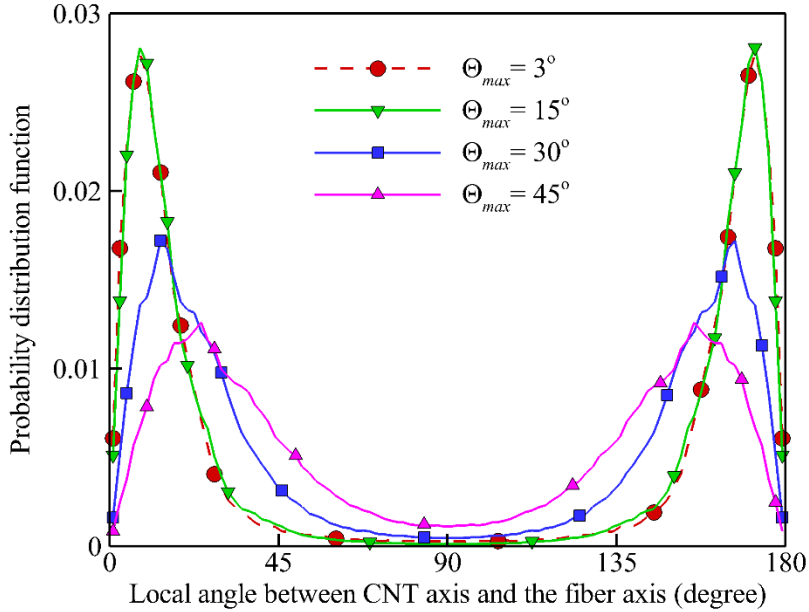


Figure 3.4. Probability density function of the local angle between the CNT centerline and axis of the fiber calculated for computational samples of CNT fibers shown in Figure 3.2 and obtained at various maximum initial inclination angles of CNT Θ_{max} equal to 3° (circles, red), 15° (nablas, green), 30° (squares, blue), and 45° (triangles, magenta).

In Ref. [134], it was found that fibers composed of SWCNTs with diameters 1 -2 nm consists of bundles of 10 – 30 nm in diameter. In order to translate the thickness of a bundle in terms of the number of segments in the bundle cross section N_B given in Figure 3.3 into the diameter D of an “equivalent” cylindrical bundle, one can assume that every CNT in the cross section of a bundle occupies area of hexagon with the radius of the inscribed circle $R_T + \delta_e/2$, where $R_T = 0.6785$ nm is the radius of (10,10) SWCNTs and $\delta_e = 0.314$ nm is the equilibrium

gap between nanotubes. Then $D = (2R_T + \delta_e)\sqrt{6N_B/(\pi\sqrt{3})} = 1.67\sqrt{N_B}$ nm. This equation results in $D \approx 7.5$ nm at $N_B = 20$ which is close to the typical average value $\langle N_B \rangle$ in the samples shown in Figure 3.5 and in $D_B \approx 11.8$ nm at $N_B = 50$, which corresponds to a substantial fraction of bundles in all generated fiber samples. Thus, the range of bundle sizes specific for *in silico* generated samples agrees with the range of bundle size measure in experimental samples, but bundles in the computational fiber samples tend to be systematically thinner than in Ref. [134]. This can be explained by much higher density of experimental fibers in Ref. [134] where the pore size was estimated in the range from ~ 1.5 nm to ~ 30 nm.

The network structures of CNT fibers exhibit almost linear relationships between the major structural parameters, including HOF, average bundle size $\langle N_B \rangle$, and average tortuosity $\langle \tau \rangle$, on the maximum angle of initial inclination Θ_{max} , if Θ_{max} is larger than about 15° (Figure 3.5). At $\Theta_{max} \leq 15^\circ$, the computational samples exhibit weak, if any, dependence of HOF, $\langle N_B \rangle$, and $\langle \tau \rangle$ on Θ_{max} . It is interesting to note that the decrease of HOF in the course of the relaxation of the initial samples composed of straight and dispersed CNTs (open diamonds in Figure 3.5) is almost the same, 10 - 17%, for samples generated with different values of Θ_{max} . This observation allows one to easily chose the required value of Θ_{max} in the initial sample in order to match the HOF of an *in silico* generated fiber sample to the experimental sample with known HOF. The existence of the linear relationships between the structural parameters and Θ_{max} at $\Theta_{max} \geq 15^\circ$ makes it possible to pick an appropriate value of Θ_{max} in the sample generation procedure in order to obtain samples with desired values of HOF or $\langle N_B \rangle$. The relationship between $\langle N_B \rangle$ and HOF, however, is not unique and can be further adjusted by varying other parameters of the *in silico* sample preparation procedure, such as the duration and/or annealing temperature (temperature of the high-temperature stage of sample generation).

By simultaneously varying several parameters of the sample preparation procedure, one can achieve fine control over the degree of anisotropy characterized by the HOF and the degree of connectivity of nanotubes characterized by the averaged bundle size, to match those of a particular experimental sample.

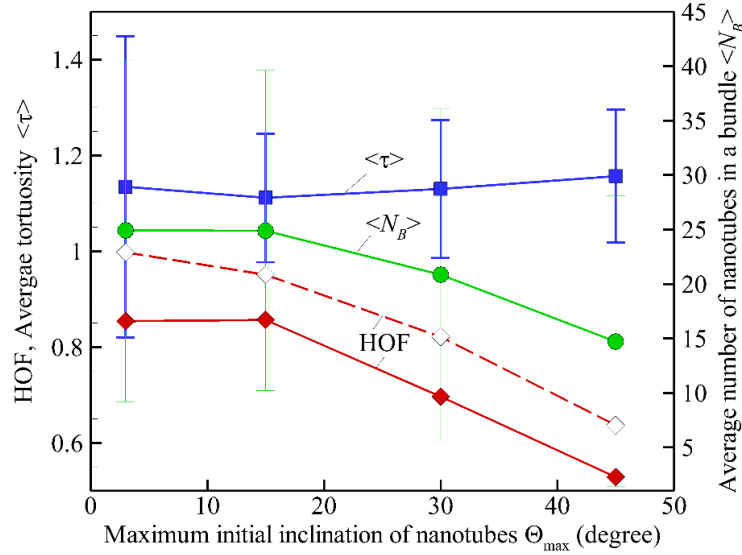


Figure 3.5. Herman orientation function (HOF, diamonds), average bundle size ($\langle N_B \rangle$, circles), and average tortuosity of nanotubes ($\langle \tau \rangle$, squares) versus maximum angle of initial inclination of CNT, Θ_{max} , used in the generation of relaxed CNT fibers composed of (10,10) CNTs of 400 nm length each at material density 0.01 gcm^{-3} . The vertical error bars show the mean square deviation of the average tortuosity and bundle size.

The approach to generation of CNT fiber samples utilized in the present work based on the initially distributed straight and non-aligned nanotubes has severe restrictions on the material density, because of large excluded volume of high-aspect ratio nanotubes. In particular, it is found that it is not possible to generate cubic samples of $1 \mu\text{m}^3$ in volume composed of 400-nm-long CNTs with the material density larger than $\sim 0.1 \text{ gcm}^{-3}$. The larger material densities can be

achieved, however, by gradual reducing the sample volume in the course of self-organization of initially dispersed CNTs into a network. Using this approach, it was possible to obtain relaxed fiber samples with density up to 0.6 gcm^{-3} . Such super aligned fiber structures will be considered in detail elsewhere.

3.2 CNT Films

The multi-step approach to generate pristine *in silico* CNT films are somewhat similar to the approach that is followed to generate CNT fibers. At first, a CNT sample with straight and dispersed nanotubes at a given material density with the periodic boundary conditions in the in-plane directions are generated by acceptance-rejection method (Figure 3.6(a)). Then a dynamic simulation of spontaneous self-assembly of CNTs into a quasi-equilibrium network composed of pristine nanotubes is performed for 1 ns at an elevated mesoscopic temperature of 10000 K to increase mobility of individual nanotubes and promote rapid formation of bundles with a formation of a continuous network of nanotubes. At this self-assembling stage, the volume of the film is constrained in the out-of-plane direction by two pistons that exert short-range repulsive forces on neighboring CNTs. The initial self-assembly is followed by an additional relaxation at a mesoscopic temperature of 300 K for 0.1 ns, when the overall bundle structure only marginally changes, but the arrangement of individual CNTs in thick bundles becomes close to the hexagonal one (Figure 3.6(b)). After this, CLs are added into the quasi-equilibrated sample randomly with homogenous distribution (Figure 3.6(c)), and then the sample is relaxed in thermostat at a temperature of 300 K and barostat at zero pressure before the onset of deformation (Figure 3.6(d)).

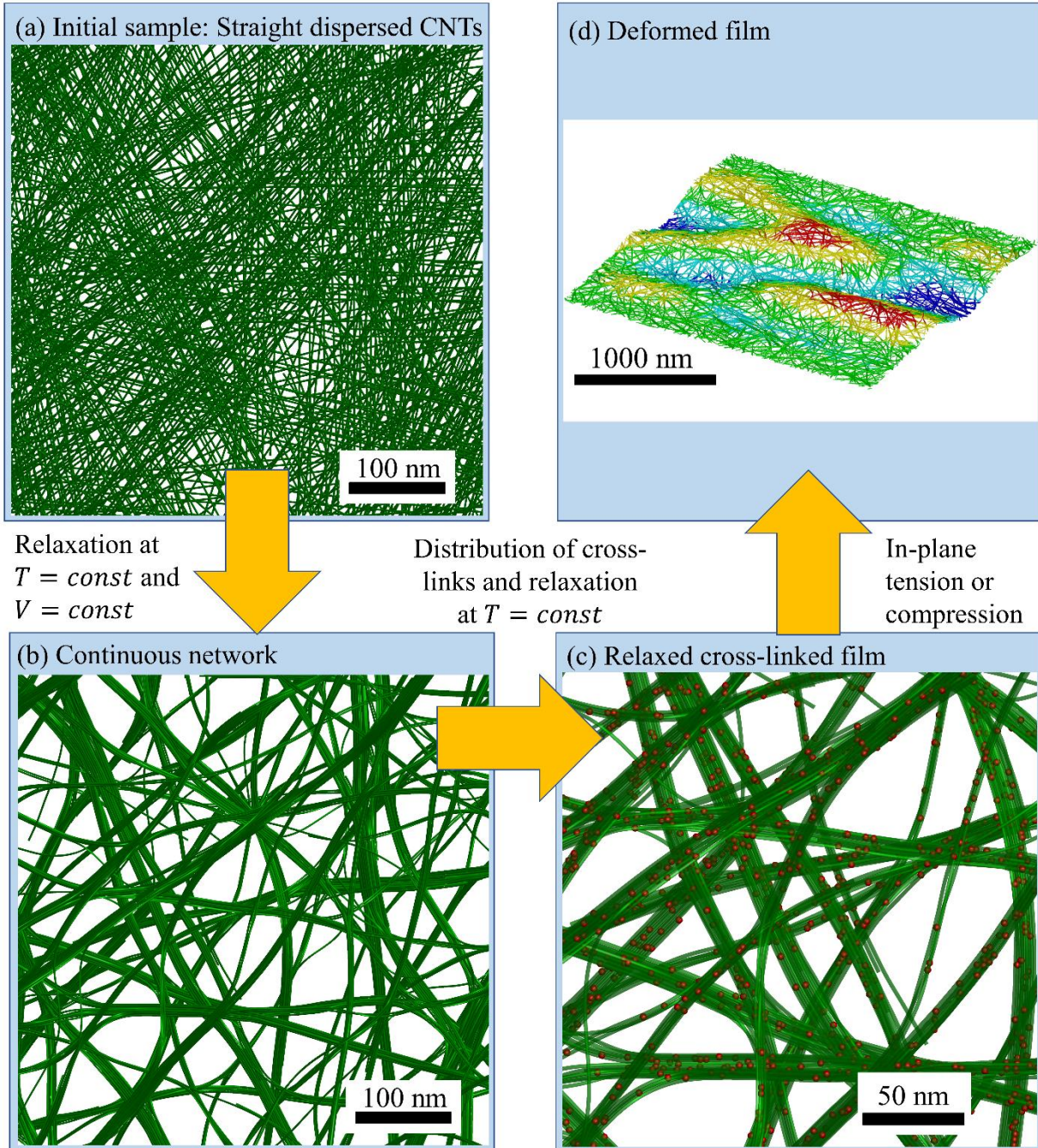


Figure 3.6. Sketch illustrating the *in silico* preparation of cross-linked CNT films with continuous networks of bundles of nanotubes and subsequent mechanical loading: The initial sample consisting of straight and dispersed nanotubes (a) is subjected to dynamic simulations at constant mesoscopic temperature and sample volume leading to spontaneous self-assembly

of CNTs into a network of bundles. The relaxed sample with a network of bundles (b) is modified by randomly distributed CLs and relaxed again to remove local stresses induced by the disparity between the equilibrium CL length and gaps between nanotubes. The relaxed cross-linked sample (c) is subjected to in-plane stretching or compression, which can result, e.g., in inhomogeneous compression of the film (d). In panel (c), the individual CLs are shown as red spheres. The individual snapshots in panel (a)-(d) are obtained in actual simulations and shown at different degrees of magnification. The distribution of CLs in (c) corresponds to the CL density $n_{CL} = 0.05 \text{ nm}^{-1}$.

3.2.1 *In silico* generation and characterization of (10,10) CNT films

Figure 3.7 shows the top views of quasi-equilibrium free standing *in silico* film samples composed of (10,10) SWCNTs with four different material densities $\rho = 0.05, 0.1, 0.2,$ and 0.4 gcm^{-3} , that are produced applying the method described in the beginning section 3.2. It is observed that the distribution of bundle size N_B , which is defined as the number of CNT segments in a bundle cross-section, increases with increasing material density ρ (Figure 3.8).

For a given N_B , an equivalent diameter of a circular bundle can be calculated as

$D = (2R_T + \delta h_0)[6N_B/(\pi\sqrt{3})]^{1/2}$. The average bundle diameter $\langle D \rangle$ of film samples with material densities $\rho = 0.05, 0.1, 0.2, 0.4 \text{ gcm}^{-3}$ are 6.7, 8, 10.5 and 11.4 nm, respectively. These values are in good agreement with the experimentally measured values of 4 nm and 16 nm in a buckypaper composed of SWCNTs [136].

Once a quasi-equilibrium pristine film sample is generated, then CLs are added into the sample randomly with homogenous distribution using acceptance-rejection method until a desired density of CLs is reached inside the sample.

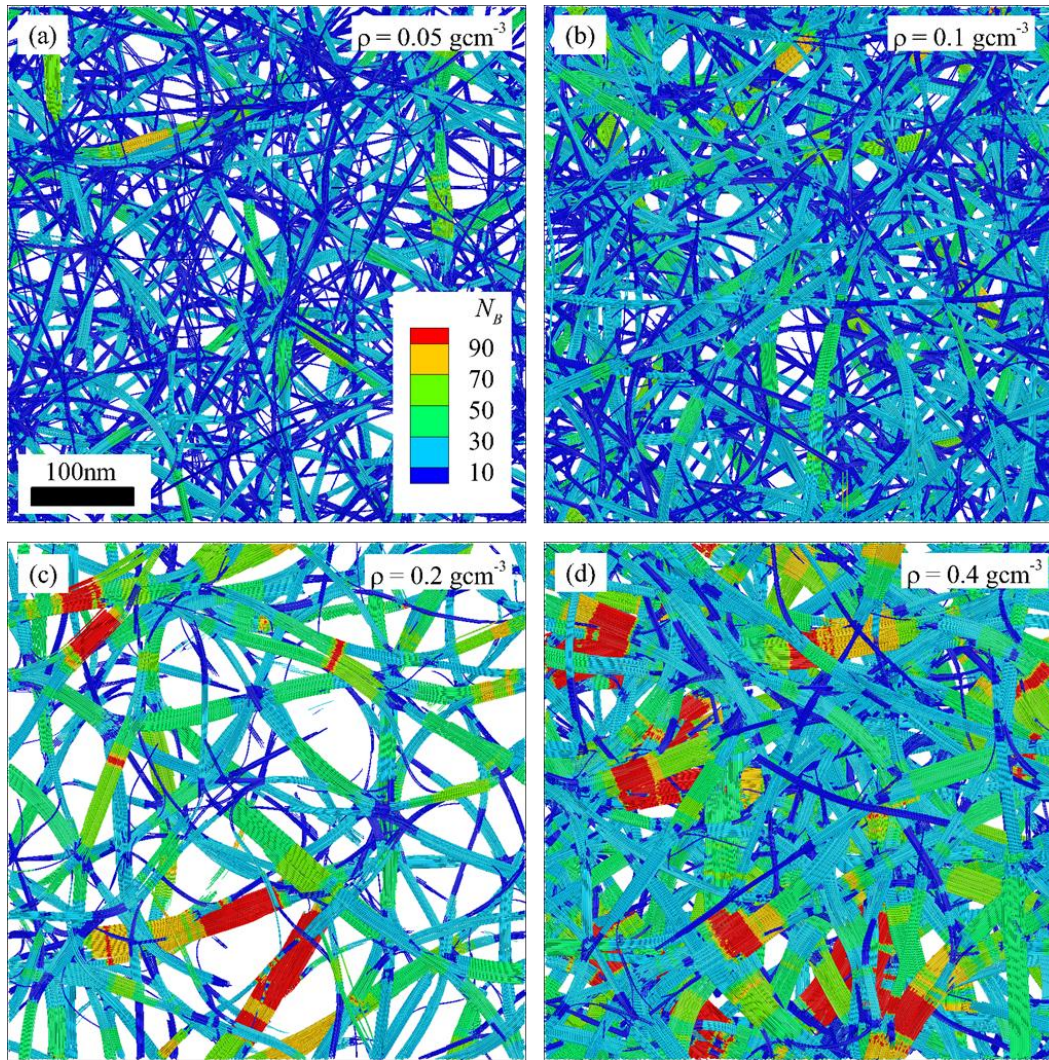


Figure 3.7. Top views of CNT film samples: (a), sample C₀, $\rho = 0.05 \text{ gcm}^{-3}$; (b), sample B₀, $\rho = 0.1 \text{ gcm}^{-3}$; (c), sample A₀, $\rho = 0.2 \text{ gcm}^{-3}$; and (d), sample D₀, $\rho = 0.4 \text{ gcm}^{-3}$. The major parameters of the samples can be found in Table 3.1. The sample structures are obtained during 1.1 ns of relaxation before distribution of the CLs. The CNT segments are colored according to their local bundle-thickness, N_B . In panels (a) and (b), the whole samples are shown. In panels (c) and (d), only top 40 nm of the samples is visualized.

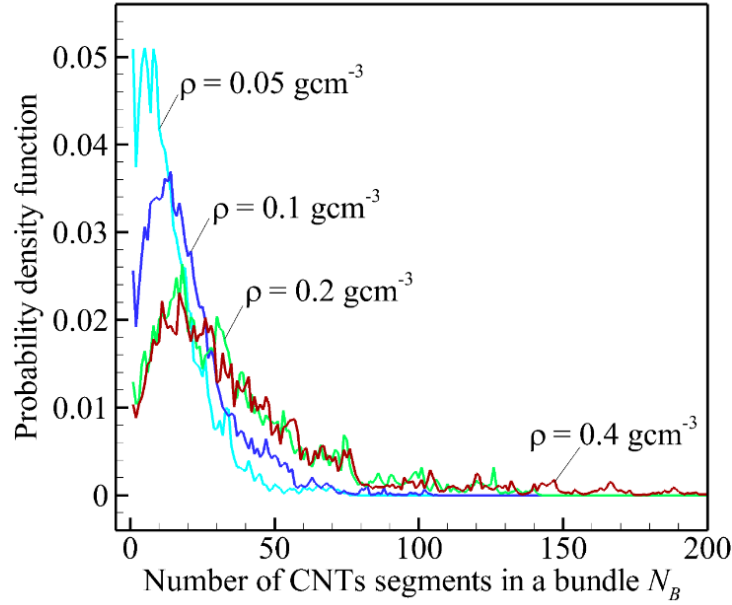


Figure 3.8. Probability density function of the local bundle thickness N_B for the four samples B_0 ($\rho = 0.05 \text{ gcm}^{-3}$, cyan curve), C_0 ($\rho = 0.1 \text{ gcm}^{-3}$, blue curve), A_0 ($\rho = 0.2 \text{ gcm}^{-3}$, green curve), and D_0 ($\rho = 0.4 \text{ gcm}^{-3}$, red curve) shown in Figure 3.7.

At first, a random point on a CNT surface associated with a mesoscopic node is found, and then it is considered as the one end of a potential CL m . Then the neighbors list of the considered node is identified and checked if any neighboring mesoscopic node can accommodate the other end of the CL, while ensuring the initial CL length r_{m0} is close to the equilibrium inter-tube distance δh_0 between pristine nanotubes. If such a CL is found, it is accepted, otherwise it is rejected. Hence, a discrete CL m is associated with two mesoscopic nodes, and the length of the CL r_m is given by the position vectors of the two nodes and relative position of the CL ends on the nanotube segments. This acceptance and rejection process is repeated until a desired number of CLs $N_{CL} = N_T L_T n_{CL} / 2$, where L_T is the nanotube length and n_{CL} is the linear density of CLs, is generated. For (10,10) SWCNTs, the S-S GBM has an equilibrium length $r_0 = 2.904 \text{ \AA}$ and

for (26,0) SWCNT the equilibrium length is $r_0 = 2.79 \text{ \AA}$ [98]. In both cases, the equilibrium length of CLs is smaller than the equilibrium inter-tube distance $\delta h_0 = 3.44 \text{ \AA}$. Because of this, the generated CLs are in pre-strained form inside the sample. Therefore, further relaxation of the pre-strained cross-linked film sample is performed to produce an equilibrated sample for mechanical deformation.

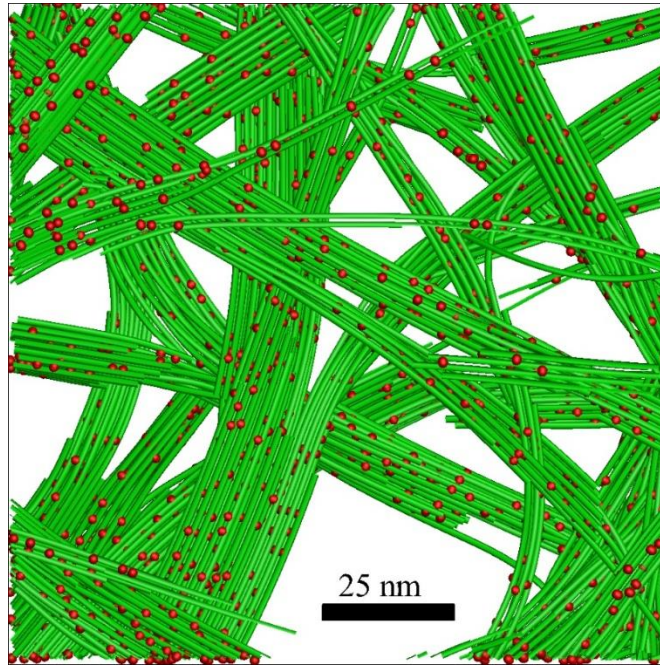


Figure 3.9. Magnified top view of a part of the cross-linked CNT film (sample A_0 , $\rho = 0.2 \text{ gcm}^{-3}$, $n_{CL} = 0.015 \text{ nm}^{-1}$) after relaxation. The CL ends are shown by red dots.

The relaxation of the free-standing films changes the material density in less than 5 %. One of such a relaxed cross-linked film samples A_0 with material density $\rho = 0.2 \text{ gcm}^{-3}$, CNT length $L_{CNT} = 200 \text{ nm}$, lateral size $L = 500 \text{ nm}$, thickness $H = 100 \text{ nm}$ and linear CL density $n_{CL} = 0.15 \text{ nm}^{-1}$ is shown in Figure 3.9. Magnified view of part this sample is shown in Figure 3.9, where the CL ends as are shown red spheres. The CL ends connect nanotubes in a bundle as

well as it connects different bundles and nanotubes. The major parameters of generated film samples composed of (10,10) CNTs are summarized in Table 3.1.

Table 3.1 Parameters of CNT film samples (lateral size L , thickness H , material density ρ , linear CL density n_{CL} , volumetric CL density $n_{CL,V}$, number of CNTs N_{CNT} , number of CLs N_{CL} , considered in simulations. All samples consist of (10,10) CNTs of 200 nm length each.

| Sample | L (nm) | H (nm) | ρ (gcm ⁻³) | n_{CL} (nm ⁻¹) | $n_{CL,V}$ (nm ⁻³) | N_{CNT} | N_{CL} |
|----------------|----------|----------|-----------------------------|------------------------------|--------------------------------|-----------|----------|
| A ₀ | 500 | 100 | 0.2 | 0.15 | 0.0046 | 7829 | 117435 |
| A ₁ | 500 | 100 | 0.2 | 0.01 | 0.0003 | 7829 | 7829 |
| A ₂ | 500 | 100 | 0.2 | 0.03 | 0.0009 | 7829 | 23487 |
| A ₃ | 500 | 100 | 0.2 | 0.1 | 0.0031 | 7829 | 78290 |
| A ₄ | 500 | 100 | 0.2 | 0.3 | 0.0093 | 7829 | 234870 |
| A ₅ | 500 | 100 | 0.2 | 0.5 | 0.0154 | 7829 | 391450 |
| B ₀ | 500 | 400 | 0.05 | 0.15 | 0.0012 | 7708 | 115620 |
| C ₀ | 500 | 400 | 0.1 | 0.15 | 0.0023 | 15415 | 231225 |
| D ₀ | 500 | 40 | 0.4 | 0.15 | 0.0092 | 5795 | 86925 |

3.2.2 *In silico* generation and characterization of cross-linked (26,0) CNT films

The method described in section 3.2.1 is used to generate the CNT film samples composed of (26, 0) zigzag CNTs of constant length L_T varying from 200 nm to 1000 nm at an initial material density ρ of 0.1 gcm⁻³ with a lateral size of 2.5 $\mu\text{m} \times 2.5 \mu\text{m}$ and film thicknesses of 40 nm. The chosen material density is within the typical range of density, from $\sim 0.05 \text{ gcm}^{-3}$ to $\sim 0.6 \text{ gcm}^{-3}$, reported in multiple experimental studies of CNT films and

buckypaper, e.g., Refs. [29, 33, 52]. The thickness of 40 nm is within the range of thickness from 10 nm to 100 nm for the ultrathin CNT films synthesized and studied, e.g., in Ref. [137] and [138]. The structures of continuous networks generated in samples with the constant CNT length of 200 nm, 400 nm, and 1000 nm are shown in Figure 3.10. The networks consist of interconnected bundles that include from a few nanotubes to a few tens of nanotubes. Visually, the obtained network structures resemble the structures of thin CNT films and buckypaper revealed in the experimental SEM and TEM images [139,140,141,142]. At the same time, the film structures in Figure 3.10 are significantly different from the samples of buckypaper *in silico* generated in Refs. [62] and [63].

The relaxed structures of the *in silico* generated CNT films are somewhat different depending on the CNT length. The average bundle size is one of the major structural properties of the CNT network, as the bundle thickness affects the number of interconnects or junctions between bundles and determines the degree of the network connectivity. It was experimentally shown that the variation of the bundle size correlates with the variation of the mechanical properties of films composed of SWCNTs [143].

To characterize the bundles sizes in the *in silico* generated CNT films, the number of nanotubes N_B in the bundle cross sections corresponding to each mesoscopic element is determined and then the probability density functions (PDFs) of N_B are calculated. These PDFs are shown in Figure 3.11. With an increasing CNT length, the thickness of nanotube bundles N_B , in average, slowly increases, from 9.48 at $L_T = 200$ nm to 11.8 at $L_T = 1000$ nm (Table 3.2).

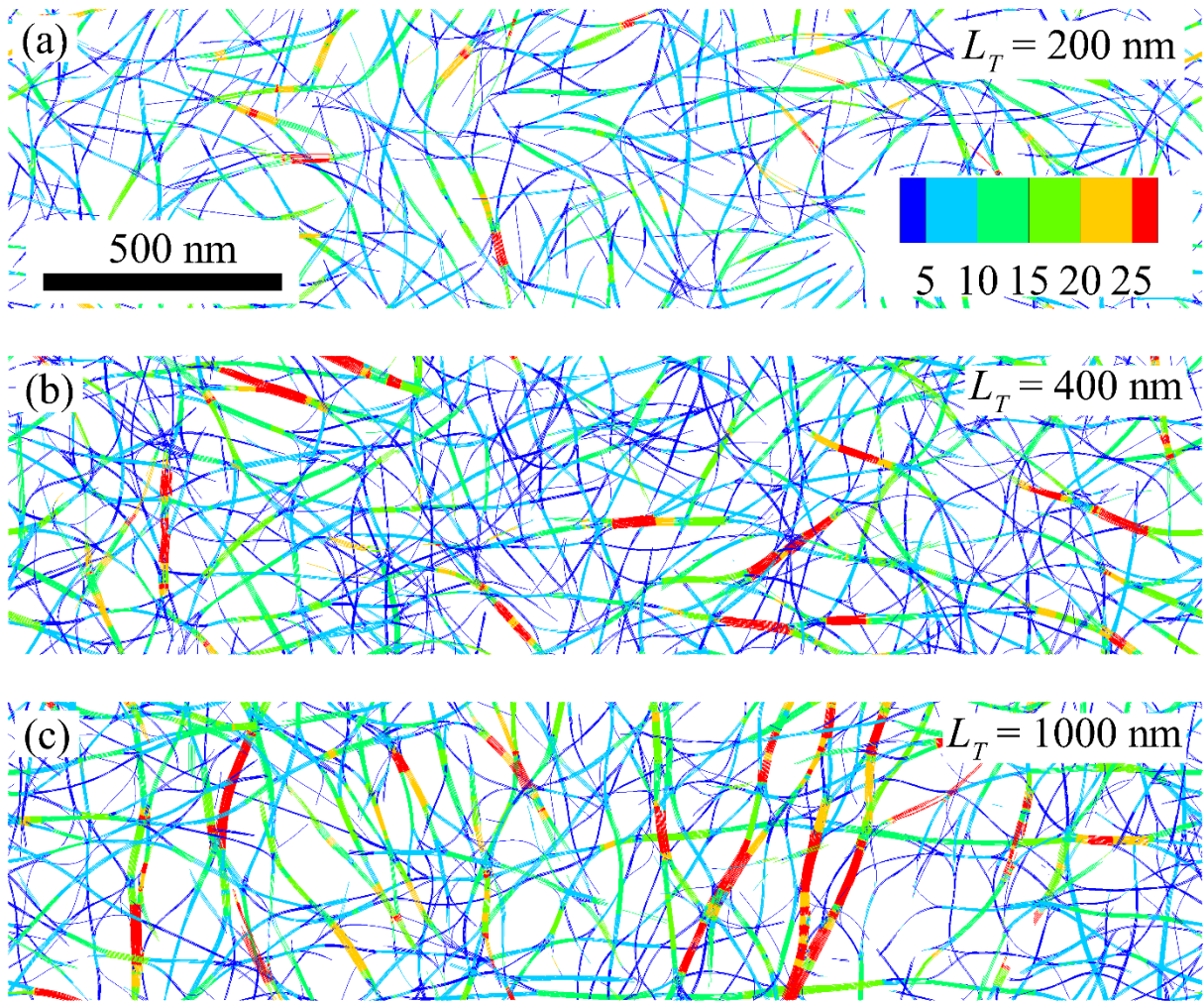


Figure 3.10. Top views of CNT films with continuous networks of bundles composed of CNTs of various lengths: $L_T = 200$ nm (sample CN200, a), $L_T = 400$ nm (sample CN400, b), and $L_T = 1000$ nm (sample CN1000, c). Each panel shows the full sample in the horizontal direction and only a quarter of the whole sample in the vertical direction. The individual nanotubes are colored according to the local bundle size N_B and the color table for N_B shown in panel (a).

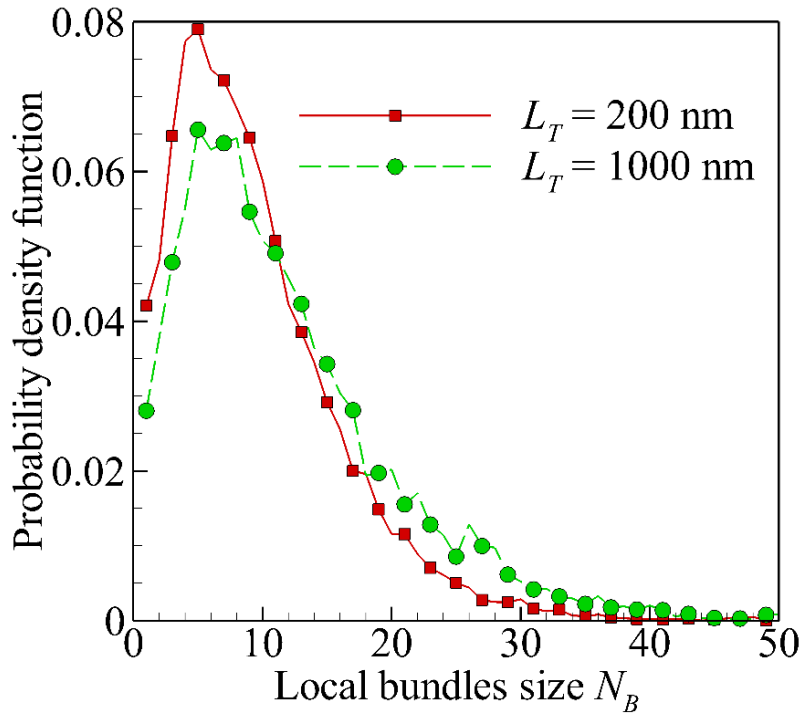


Figure 3.11. Probability density functions of local bundle size N_B (number of nanotubes in the bundle cross section) in (26, 0) CNT films with the nanotube length $L_T = 200$ nm (sample CN200, red square) and $L_T = 1000$ nm (sample CN1000, green circles) shown in Figure 3.10 (a) and (c). The symbols correspond to calculated values, while the curves are drawn only to guide the eye.

The average $\langle D \rangle$, most probable D_0 , and maximum D_{max} diameters of equivalent circular bundles are listed in Table 3.2. All these bundle diameters only marginally increase with increasing length of individual nanotubes in samples CN200 – CN1000. For instance, $\langle D \rangle$ increases less than 10 % when the CNT length increases five times. Thus, the adopted approach for the generation of CNT films with nanotubes of different lengths allows to obtain films with nearly the same bundle size distributions.

For all samples considered, the typical bundle diameters agree with the values of $D_0 = 15$ nm, $\langle D \rangle = 13.5$ nm, and $D_{max} = 34$ nm that can be deduced from the experimentally measured bundles size distribution in a low-density SWCNT network in aqueous solution [144]. The average bundle diameters $\langle D \rangle$ for *in silico* generated CNT films are also within the range from 7.6 nm to 8.48 nm and close to the range from 9.8 nm to 21 nm experimentally determined for various SWCNT films in Refs. [68] and [143], respectively. The boundaries of that range, however, are assumed to be somewhat overestimated in Ref. [19], as the experimental resolution did not allow to account for bundles with diameters below ~ 4 nm. A somewhat increased bundles size reported in Refs. [68] and [143] can be also explained by a few-fold larger density of the CNT films used in experiments compared to the density of films used in the present work, as the average bundle size increases with increasing material density [135].

The linear CL density (number of CL ends per unit length of nanotubes) n_{CL} varies from 0.05 nm⁻¹ to 2.5 nm⁻¹. The volume CL density is equal to $n_V = n_{CL}\rho/(2\rho_T)$ ($\rho_T = 2\pi mR_T n_\sigma$ is the linear density of the nanotube material, m is the mass of a carbon atom, $n_\sigma = 4/(3\sqrt{3}l_c^2)$ is the surface density of atoms for a SWCNT, $l_c = 1.421$ Å is the lattice constant in graphene[109]) and varies from $5.17 \cdot 10^{-4}$ nm⁻³ to $2.59 \cdot 10^{-2}$ nm⁻³. All considered cross-linked samples are characterized by a small degree of cross-linking $f_{CL} = n_{CL}/(2\pi R_T n_\sigma)$ which varies from $2.05 \cdot 10^{-4}$ to $1.03 \cdot 10^{-2}$.

In addition, a CNT film sample with the variable nanotube length is considered, where the individual nanotubes have random lengths according to the Weibull distribution with the probability density function

$$f(L_T) = \left(\frac{b}{a}\right) \left(\frac{L_T}{a}\right)^{b-1} \exp\left[-\left(\frac{L_T}{a}\right)^b\right]. \quad (3.1)$$

The shape parameter $b = 2.08$ and scale parameter $a = 430$ nm are chosen to fit the experimental distribution of the nanotube length obtained in Ref.[58]. Eq. (3.1) is used to generate random lengths of CNT in the initial sample from the range $100 \text{ nm} \leq L_T \leq 2000 \text{ nm}$. For this cutoff distribution, the average nanotube length is equal to 620 nm. The CNTs shorter than 100 nm are excluded from consideration since such nanotubes cannot form a continuous network [92]. The nanotubes longer than 2000 nm are excluded since the chosen sample size in the direction of applied deformation ($2.5 \text{ }\mu\text{m}$) must be larger than the length of an individual nanotube to avoid the effect related to the finite sample size and looping of nanotubes through periodic boundaries.

The major properties of the thin film samples considered in this work are listed in Table 3.2. The samples with the continuous networks of nanotubes and constant CNT length $L_T = 200$ nm, 400 nm, 620 nm, and 1000 nm are denoted as CN200, CN400, CN620, and CN1000 correspondingly. The sample with continuous network of bundles and randomly distributed CNT length are denoted as CNW. Samples denoted as DN200 and DN1000 are samples with dispersed network structure with tube lengths $L_T = 200$ nm and 1000 nm, and the generation of these samples is described in section 4.6. The average number of nanotubes in a bundle $\langle N_B \rangle$, average bundle diameter $\langle D \rangle$, most probable bundle diameter D_0 , and maximum bundle diameter D_{max} for these *in silico* generated CNT film samples are presented in the Table 3.2 together with the total number of nanotubes in each sample. The samples CN200 – CNW are used for simulation at CL densities from 0.05 nm^{-1} to 2.5 nm^{-1} , while DN200 and DN1000 samples are generated at a CL density of 0.05 nm^{-1} .

Table 3.2. Total number of CNTs, average number of CNTs in the bundle cross section $\langle N_B \rangle$, average bundle diameter $\langle D \rangle$, most probable bundle diameter D_0 , and maximum bundle diameter D_{max} for the *in silico* generated CNT film samples with continuous and dispersed network structures and various nanotube length L_T at a material density $\rho = 0.1 \text{ gcm}^{-3}$. All samples have size $2.5 \mu\text{m} \times 2.5 \mu\text{m} \times 40 \text{ nm}$. In the sample CNW, the random lengths of individual nanotubes in the range $100 \text{ nm} \leq L_T \leq 2000 \text{ nm}$ are generated based on Eq. (3.1) at $b = 2.08$ and $a = 430 \text{ nm}$. The samples CN200 – CNW are used for simulation at CL densities from 0.05 nm^{-1} to 2.5 nm^{-1} . The approach for generation of samples DN200 and DN1000 with dispersed nanotubes is described in section 4.6. These two samples are generated at a CL density of 0.05 nm^{-1} .

| Film sample | L_T (nm) | Network structure | Total number Of CNT | $\langle N_B \rangle$ | $\langle D \rangle$ (nm) | D_0 (nm) | D_{max} (nm) |
|-------------|------------|-------------------|---------------------|-----------------------|--------------------------|------------|----------------|
| CN200 | 200 | Continuous | 25729 | 9.48 | 7.6 | 5.52 | 18.6 |
| CN400 | 400 | Continuous | 12864 | 10.5 | 8 | 6.05 | 18.6 |
| CN620 | 620 | Continuous | 8301 | 11.6 | 8.41 | 6.05 | 22.1 |
| CN1000 | 1000 | Continuous | 5147 | 11.8 | 8.48 | 5.52 | 19.6 |
| CNW | Random | Continuous | 9666 | 9.02 | 7.42 | 4.94 | 16.9 |
| DN200 | 200 | Dispersed | 25729 | 1.17 | 2.67 | 2.47 | 6.53 |
| DN1000 | 1000 | Dispersed | 5147 | 1.24 | 2.75 | 2.47 | 6.99 |

CHAPTER 4

QUASI-STATIC MECHANICAL SIMULATIONS OF CROSS-LINKED CNT FILMS

4.1 Computational Setup for In-plane Tension and Compression of CNT Films

The *in silico* generated cross-linked film samples are subjected to the in-plane tensile and compressive deformation under conditions of a constant mesoscopic temperature T_D . For this purpose, the periodic boundary conditions is released by “cutting” CNTs that cross the sample boundaries perpendicular to the Ox direction (horizontal direction in Figure 4.1) and introduce clip layers of 50 nm thickness. In Figure 4.1, such clip layers are the part of the sample where tubes are colored grey. In the course of sample deformation, the mesoscopic nodes in the clip layers are moved in opposite directions along Ox axis (Figure 4.1(a)) with constant velocity $V_D/2 = 5 \text{ ms}^{-1}$, so that V_D is the total deformation velocity and the strain rate is equal to $\dot{\epsilon} = V_D/L_{D0}$, where L_{D0} is the size of the deformable part of the sample between clip layers. It is found, however, that for relatively large computational samples considered in the present work, this approach provides the results independent of the strain rate and sample size only if the deformation velocity is smaller than 1 ms^{-1} . This excessively small value of V_D precludes from performing stretching simulations based on the existing deformation approach under condition of quasi-static loading. To overcome this difficulty, a modified approach is used for sample deformation, when at each time step of duration Δt the positions of all mesoscopic nodes are

scaled in the deformable part of the film, as well as position of the clip layers (Figure 4.1(b)), with the scaling coefficient $(V_D \Delta t + L_{D0})/L_{D0}$, where L_{D0} is the initial size of the deformable part of the sample between the clip layers. In preliminary simulations, it is found that this modified approach allows one to obtain the results of stretching simulations independent of the strain rate $\dot{\epsilon} = V_D/L_{D0}$ and sample size if $\dot{\epsilon} \leq 0.025 \text{ ns}^{-1}$. It is also found that the original and modified approaches result the same initial slope of the stress-strain curves if V_D is smaller than 1 ms^{-1} .

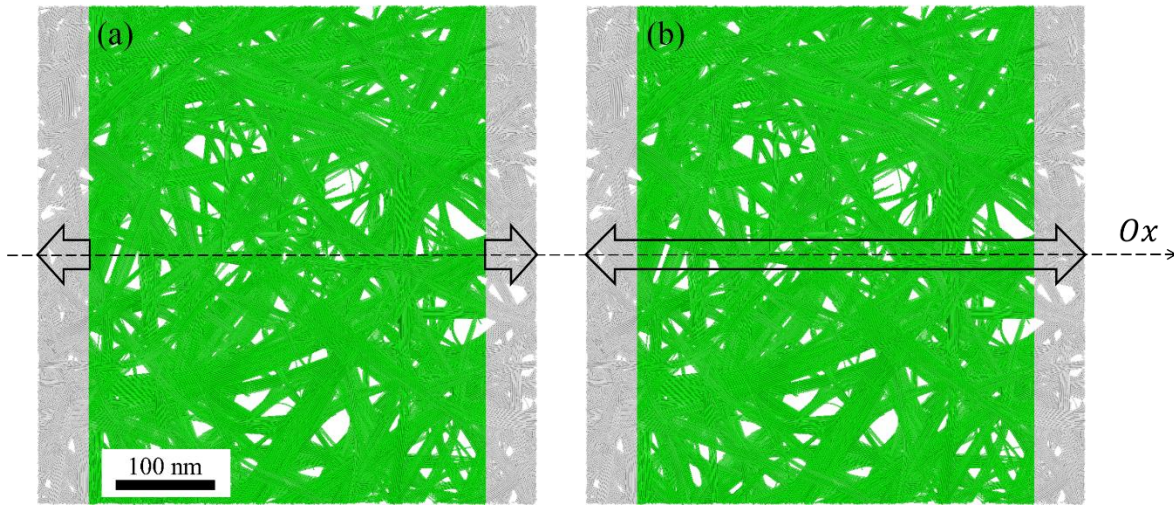


Figure 4.1. Computation setup for deformation process in mesoscopic simulations: (a) original approach where the mesoscopic nodes in the clip layers (part of the sample where tubes are colored grey) are moved in opposite directions along Ox axis with constant velocity $V_D/2 = 5 \text{ ms}^{-1}$, (b) modified approach, where the positions of all mesoscopic nodes in the deformable part of the film, as well as position of the clip layers, are scaled with the scaling coefficient $(V_D \Delta t + L_{D0})/L_{D0}$.

To quantify the response of samples on the applied engineering strain $\epsilon = V_D t/L_D$, the engineering stress $S = (|F_1| + |F_2|)/(2A_x)$ is calculated, where F_1 and F_2 are the total forces

exerted on the left and right clip layers from the deformable part of the sample along the deformation direction and A_x is the area of a sample cross section before the onset of deformation and after the generation of the quasi-equilibrated sample. To distinguish between tensile and compressive deformations, whenever necessary, the sign rule is used, assuming that the tensile deformation corresponds to positive S and ε , while the compressive deformation is characterized by negative S and ε .

4.2 Load Transfer in CNT Films at Stretching

The load transfer mechanism in cross-linked CNT films was preliminary studied for a CNT film sample composed of (26, 0) CNT of length $L_T = 400$ nm at material density of 0.1 gcm^{-3} and CL density $n_{CL} = 0.05 \text{ \AA}^{-1}$ with the lateral sizes $1 \text{ \mu m} \times 1 \text{ \mu m}$ and film thicknesses of 40 nm. This sample consists of 2079 nanotubes and includes 207900 CLs. The simulation results shown in all subsequent section are obtained with the S-S GBM and the best-fit parameter set PL_2 in Table 2.2 with exception of Figure 4.7, where the results obtained based on C-C and S-S GBMs are compared with each other. Every CNT in these samples is discretized into mesoscopic segments with an equilibrium length of 2 nm. The average material density in this sample after relaxation is about 5.5% smaller than the density of the initial sample composed of dispersed CNTs. During the deformation process, the mesoscopic temperature is kept at 30 K.

In the deformed films, the majority of CNTs are also not strained above this level and, thus, they do not participate in the load transfer (Figure 4.2). The stretching of the whole film induced both local stretching and compression of certain nanotubes above the level of 0.004. Such nanotubes are shown by red and blue in Figure 4.2(a) In order to better visualize the nanotubes participating in the load transfer, in Figure 4.2(b), all CNTs are blanked with the absolute local strain below 0.004. As one can see, a few nanotubes that are colored red form a

percolating network that results in the transfer of mechanical load between the left and right boundaries of the film. Due to the existence of this network, the material can resist to stretching even at a strain of 0.2.

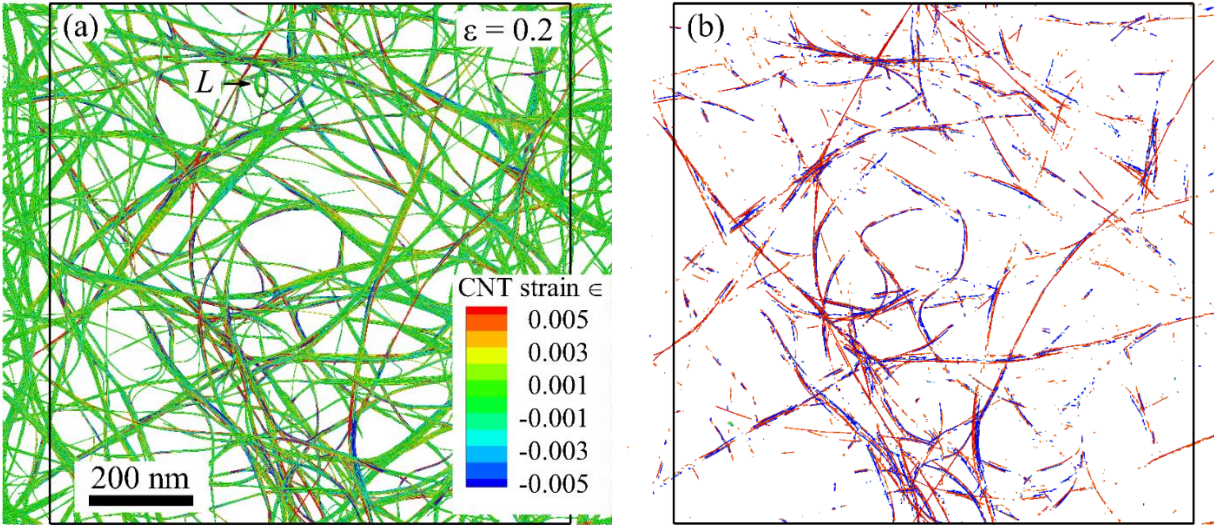


Figure 4.2. Top views of the stretched CNT film at an engineering strain of 0.2. Individual CNTs are colored according to their local strain ϵ . Both (a) and (b) show the same sample, but in (b) all CNT segments where $|\epsilon| \leq 0.004$ are blanked. In panel (a), the letter “L” marks the position of the loop formed during stretching. The black rectangles mark boundaries of the non-deformed sample.

During stretching, local compression of bundles can locally increase the bundle curvature and even results in formation of loops. An example of such a loop is marked by letter “L” in Figure 4.3(a). The mechanism of formation of this loop is illustrated by a series of zoomed snapshots in Figure 4.3(a) - (c). The loop is formed in a freely suspended part of a bundle, whose ends are moved towards each other because they are connected via CLs to other CNTs participating in the transfer of mechanical load. This process is schematically shown in Figure

4.3(d). The mobility of CNTs is also promoted by the release of stretching and bending energy after CL breaking, and can increase velocity of certain CNT segments a few times larger than V_D .

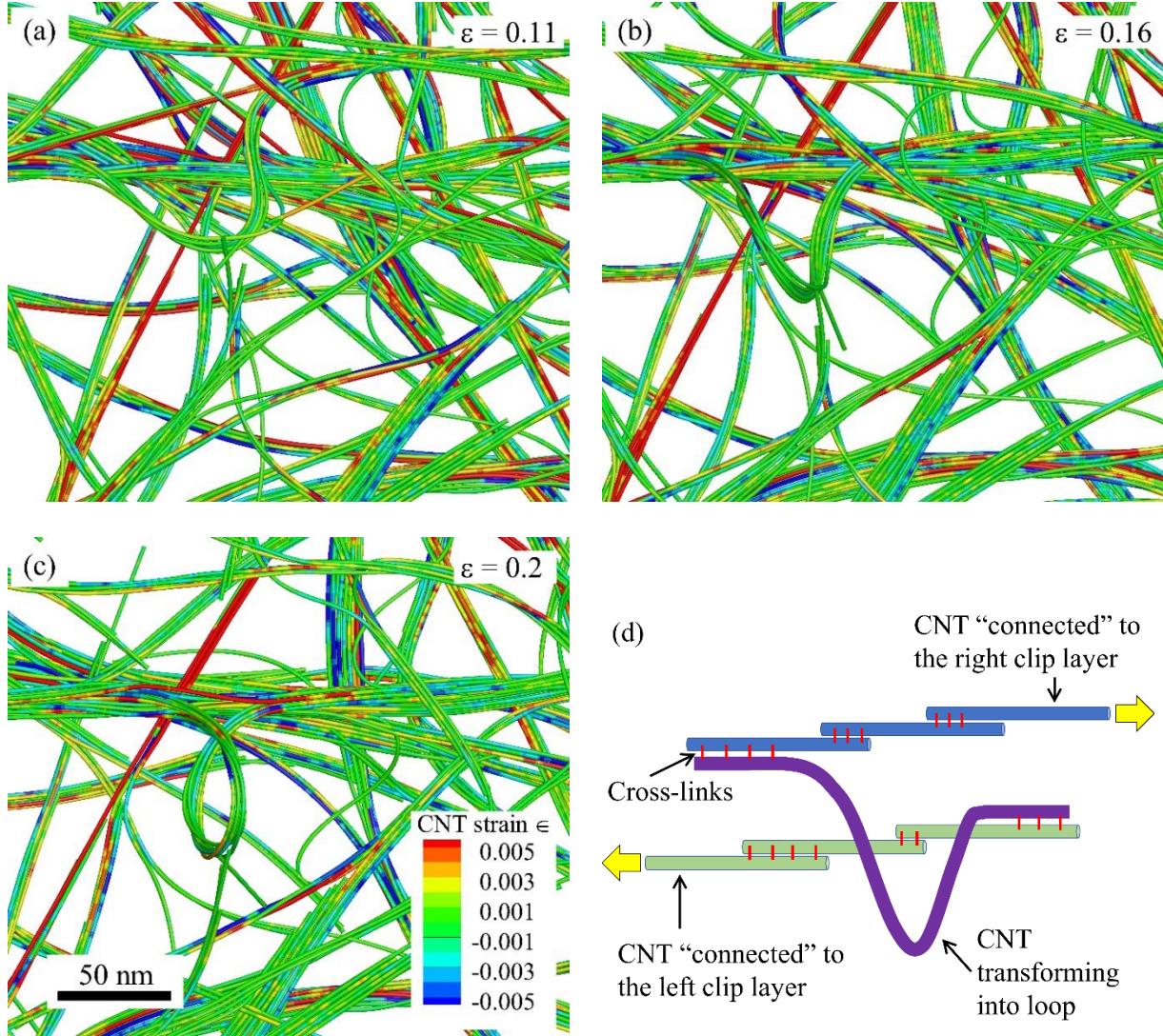


Figure 4.3. Top views of a fragment of the CNT film obtained in the course of stretching at engineering strains of 0.11 (a), 0.16 (b), and 0.2 (c). The snapshots illustrate formation of a loop by a bundle marked as L in Figure 4.2(a). Sketch in panel (d) schematically illustrates the loop formation process.

The local release of stretching and bending energy after CL breaking results in the unbending of some bundles and overall increase of the sample cross sectional area in the central part of the sample (Figure 4.4). This finding correlates with the negative Poisson coefficient observed experimentally for thin CNT films at a moderate tensile deformation [145]. The local increase in the film thickness, however, is strongly non-homogeneous across the film plane. In order to characterize it, the film plane is divided into a two-dimensional mesh of cells. Then the local Poisson coefficient $\nu = -(h - h_0)/(h_0\varepsilon)$ for cells in the central part of the sample (h and h_0 are the cell-averaged film thicknesses in the deformed and non-deformed states, correspondingly) shown in Figure 4.4(a) results in values from about -1 to ~0.5 with the average value about -0.1.

Large local variation of ν is related to high porosity of the film, its small initial thickness, and relatively large size of certain bundles, which equivalent diameters are as large as 25% of the film thickness. More accurate calculations of the average Poisson coefficient require simulations with film samples of larger thickness.

The analysis of components of the total potential energy of the sample given by Eq. (2.4) shows that the film stretching is dominated by interaction of nanotubes via CLs and stretching of individual nanotubes, while variations of the elastic energy of the CNT bending and energy of van der Waals interaction are relatively small (Figure 4.5).

The elastic energy of stretching of individual nanotubes increases in more than order of magnitude when the strain varies from zero to ~0.026 and then slowly decreases with further increase in the sample strain. The absolute value of the CL energy monotonously decreases, mostly due to the continuous process of CL breaking. The bending energy slowly increases,

since formation of structures with high bending energy, e.g., the loop illustrated in Figure 4.3, becomes more significant than unbending of other bundles.

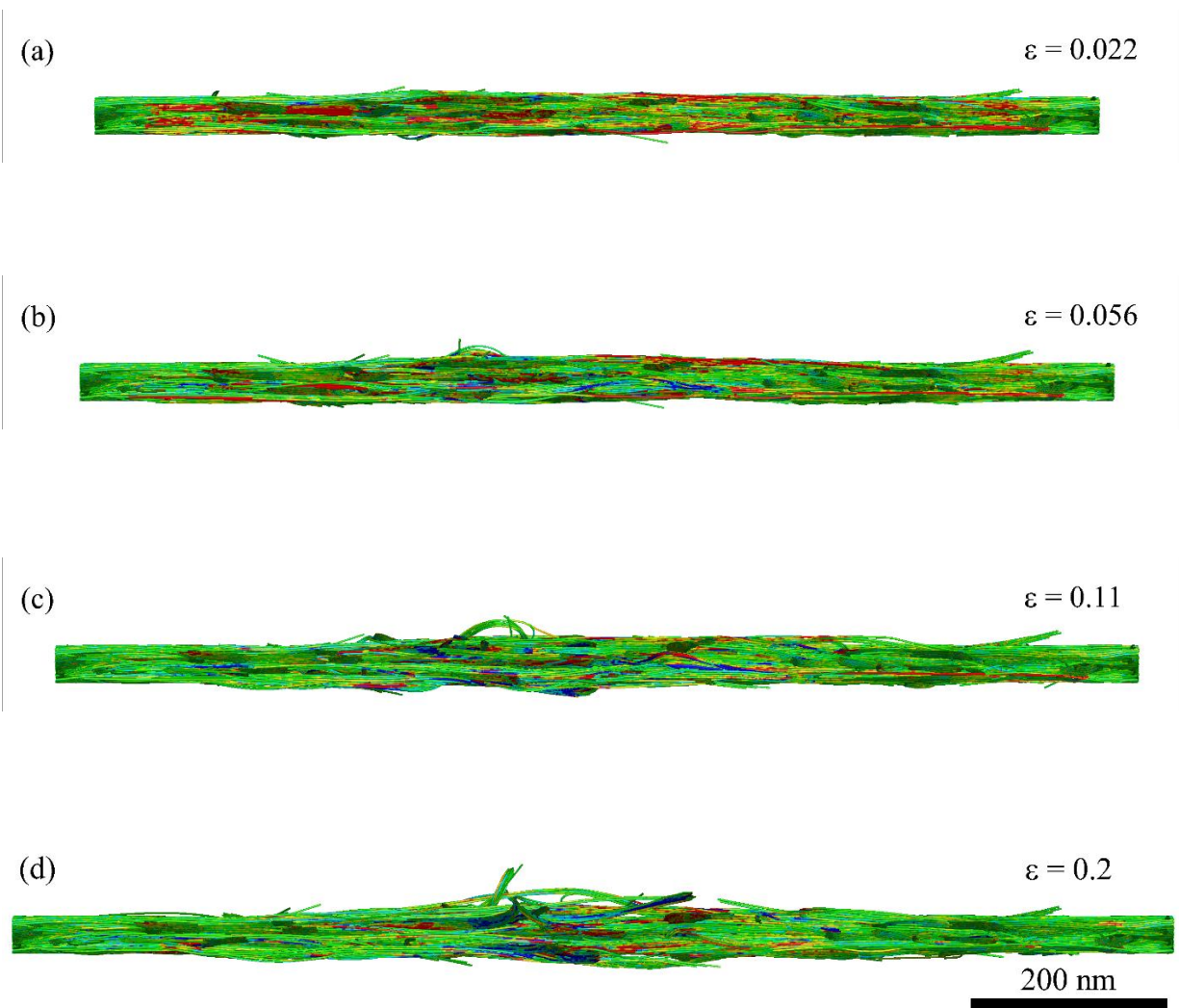


Figure 4.4. Side views of the CNT film in the course of stretching in the in-plane (horizontal) direction at various strains: (a), $\epsilon = 0.022$; (b), $\epsilon = 0.056$; (c), $\epsilon = 0.11$; and (d), $\epsilon = 0.2$. Individual CNTs are colored according to the local strain with the color tables given in Figure 4.3(c).

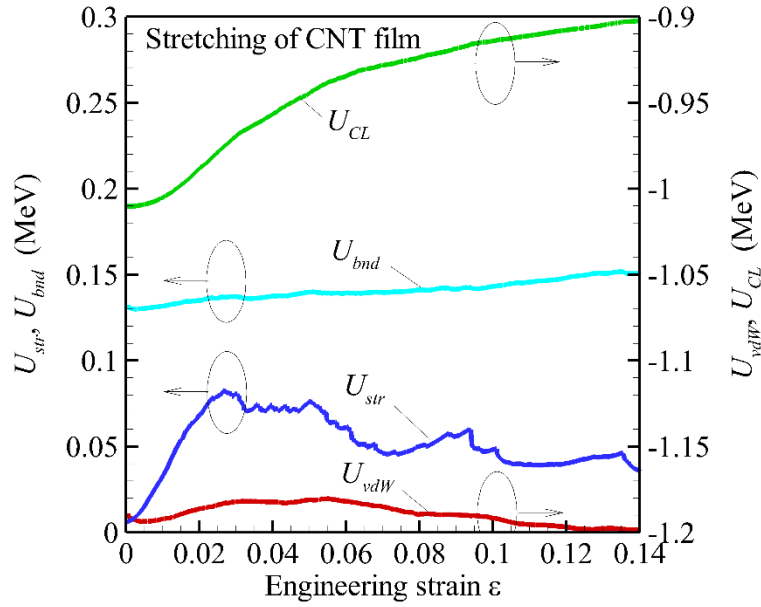


Figure 4.5. Total energies of stretching U_{str} , bending U_{bnd} , van der Waals interaction U_{vdW} , and CL U_{CL} versus engineering strain ε obtained during stretching simulation of the CNT film.

In order to further characterize the dominant effect related to straining individual nanotubes, snapshots of deformed film samples is analyzed, where all CNT segments with local CNT strain smaller than the 0.004 are blanked (Figure 4.6). In the considered strain range, $\varepsilon \leq 0.2$, the stretched CNTs form a percolating network of nanotubes, which participate in the transfer of mechanical load. This “load transfer network” predominantly consists of bundles spanning the sample along the direction of the applied deformation and, at every particular time, includes only a small fraction of CNTs. The number of nanotubes involved into the load transfer network initially increases with increasing strain (Figure 4.6(a)-(b)) up to the sample strain ~ 0.026 , corresponding to the maximum elastic energy of stretching in Figure 4.5. With further increase in the sample strain, the CL breaking results in the release of the strain energy, so that the number of CNT segments involved into the load transfer network starts to decrease (Figure

4.6(c)). During this late stage of the deformation process, the load transfer network is a subject of strong re-organization (Figure 4.6(b)-(d)). The CL breaking induces relatively large displacement of nanotubes and “activates” new CL, which did not participate in the load transfer earlier. As a result, even at strain $\epsilon = 0.2$, the sample contains a few percolating paths providing the transfer of mechanical load between the left and right clip layers.

During the whole deformation process the maximum local strain in individual CNTs ϵ does not exceed 0.02. The magnitude of the local strain ϵ is comparable with the sample strain ϵ only during the initial elastic deformation of the film, when the effect of the CL breaking is marginal. In the inelastic deformation regime, the local strains in individual CNTs remain limited and become disconnected from the sample strain. The maximum local strains in individual nanotubes during the whole process is smaller than the threshold strain corresponding to the tensile breaking of nanotubes in the cross-linked bundles. Atomistic simulations showed that the breaking of individual (26,0) CNTs in the stretched cross-linked bundles occurs at $\epsilon = 0.09$ to $\epsilon = 0.12$ [77]. In the mesoscopic simulations, the individual CNTs are stretched below the threshold for tensile breaking, and thus this process can be neglected in the computational model.

In addition to stretching of the cross-linked sample, the stretching simulations for corresponding samples without CLs is also performed. In all cases, when the deformation velocity is sufficiently small and the dynamic, finite-strain-rate effects are not pronounced, it is found that the strains in individual nanotubes remain on a level specific for the relaxed, non-deformed film. It occurs since van der Waal interaction between CNTs does not introduce strong barriers for inter-tube sliding and the applied mechanical loading results in the relative motion of nanotubes rather than in their stretching or compression. Thus, the formation of a distinct load

transfer network is a peculiarity of the cross-linked CNT networks. The load transfer networks evolving in CNT film samples at stretching are further analyzed in section 4.4.

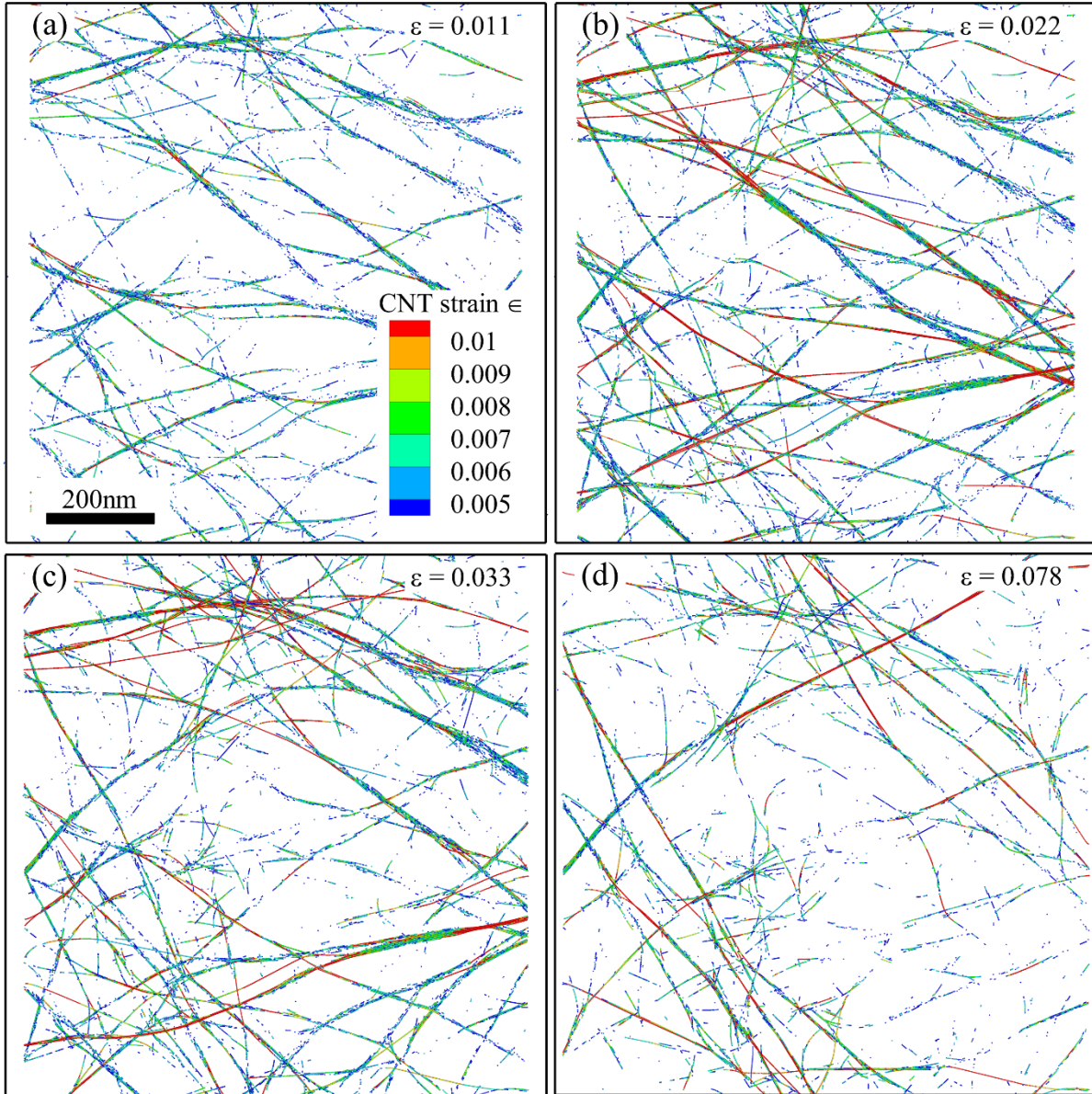


Figure 4.6. Top views of the cross-linked CNT film sample in the course of stretching at engineering strains of 0.011 (a), 0.022 (b), 0.033 (c), and 0.078 (d). The snapshots show only mesoscopic elements of CNTs, where the local strain ϵ exceeds 0.004, while all other elements are blanked. The nanotubes are colored according to the local strain ϵ .

The typical dependences between the engineering stress S and engineering strain ε are shown in Figure 4.7(a). The red and green curves in Figure 4.7 are obtained with C-C and S-S GBMs and the best-fit parameter sets corresponding to $a = 5 \text{ \AA}^{-1}$, which are designated as PL_1 and PL_2 in Table 2.2. As one can see, if the best-fit parameters for both models correspond to the same value of a , the stress-strain curves predicted by both models are only marginally different.

The same degree of agreement between the stress-strain curves calculated with both geometrical models at a fixed a is also obtained in simulations with $a = 4, 6, \text{ and } 7 \text{ \AA}^{-1}$. The first broken CL (Figure 4.7(b)) appears at a strain of ~ 0.0006 , however, the stress follows the linear dependence on strain up to an order-of-magnitude large strain, so that the nominal elastic limit is defined as the maximum strain ε_E when the fraction of the broken CLs does not exceed 0.01%. Then, for both GBMs, ε_E is almost the same and equal to ~ 0.0045 . The maximum stress of $S_{max} = \sim 60 \text{ MPa}$ is achieved at strain $\varepsilon_{max} = \sim 0.026$. The fraction of broken CLs at $\varepsilon = \varepsilon_{max}$ remains as small as 2.4% and only slightly exceeds 10% at $\varepsilon = 0.2$.

The variation of stress versus strain in Figure 4.7(a) is in a good agreement with the previous analysis of the elastic stretching energy variation (Figure 4.5) and evolving load transfer network (Figure 4.6). The maximum stress corresponds to the maximum of the elastic stretching energy and maximum “thickening” of the load transfer network. At $\varepsilon > \varepsilon_{max}$, the CNT material does not demonstrate distinct fracture behavior with abrupt drop of stress to zero. On the contrary, the stress only continuously decreases, e.g., from $\sim 60 \text{ MPa}$ to $\sim 20 \text{ MPa}$ when strain increases from 0.026 to 0.07.

The gradual decrease in stress is explained by the re-organization of the load transfer network in the inelastic regime of deformation (Figure 4.6(c) and (d)), when breaking of some CLs promotes the relative motion of nanotubes, “activates” new CLs, and forms new percolating

paths for load transfer across the sample. Such a behavior under stretching is characteristic for viscoelastic materials. The viscoelastic behavior at large strains are observed experimentally for CNT strands [146] and thin films [147].

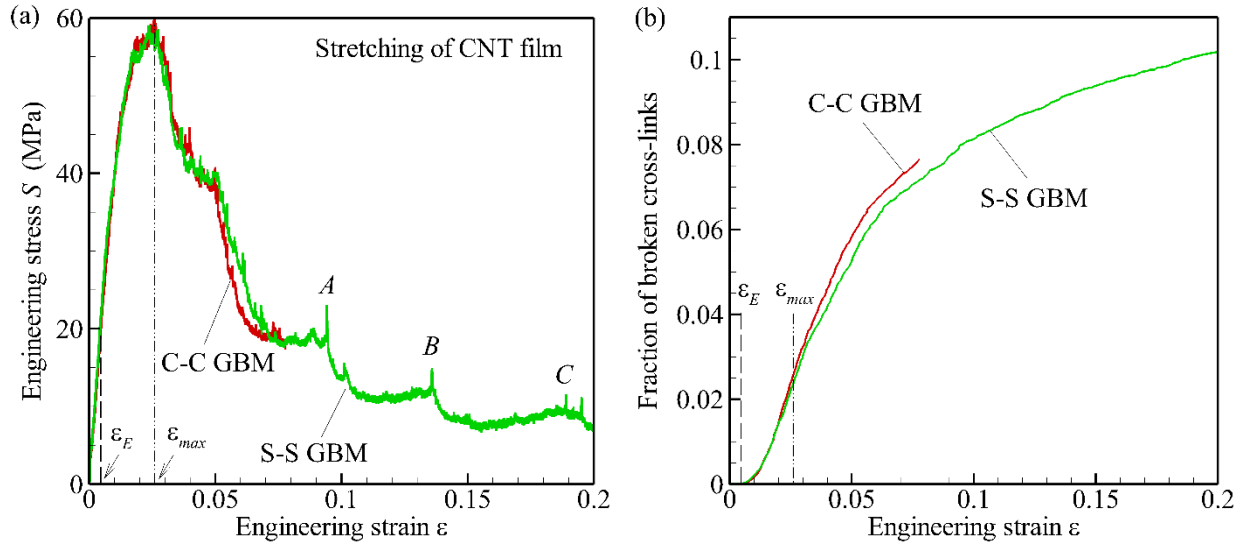


Figure 4.7. Dependences of the engineering stress S (a) and fraction of broken CLs (b) on the engineering strain ϵ obtained during stretching simulations of the CNT film with C-C (red) and S-S (green) GBMs. The simulations are performed with the best-fit parameter sets PL_1 and PL_2 in Table 2.2. The vertical dashed and dash-dotted lines indicate the magnitudes of strain corresponding to the nominal elastic limit $\epsilon_E = 0.0045$ and strain at maximum stress $\epsilon_{max} = 0.026$. The simulations with C-C GBM are performed until $\epsilon = 0.08$. In panel (a), letters “A,” “B,” and “C” mark local maximums of stress.

Local maximums of stress marked by letters "A", "B", and "C" in Figure 4.7(a) appears at times, when CL breaking results in the fast re-organization of the load transfer network and activation of new paths for load transfer. The non-monotonous behavior of the stress at $\epsilon > \epsilon_{max}$ with

multiple sawtooth spikes was observed in experiments on stretching of thin CNT films with the thickness of 40 - 200 nm [145].

The elastic modulus E , maximum stress S_{max} , and strain ϵ_{max} at $S = S_{max}$ of the film are determined based on stress-strain curve obtained with S-S GBM. A value of $E = 4.48$ GPa is calculated as a slope of a linear fit in the range $0.001 \leq \epsilon \leq 0.004$, while $S_{max} = 57.5$ MPa and $\epsilon_{max} = 0.026$ correspond to the maximum of a fourth-order polynomial fit to the stress-strain curve in the range $0.016 \leq \epsilon \leq 0.03$. These values of E , S_{max} , and ϵ_{max} agree with experimental values reported for CNT films where cross-linking is induced by electron beam irradiation, e.g., in Ref. [68]. In that work, depending on the irradiation dosage, the measured tensile modulus, strength, and strain at failure of thin SWCNT films vary from ~ 1.5 GPa to ~ 3.5 GPa, from ~ 15 MPa to ~ 75 MPa, and from ~ 0.015 to ~ 0.037 , correspondingly. Similar, but somewhat smaller values, e.g., Young's modulus 0.89 GPa to 2.06 GPa, strength 6 MPa to 26 MPa, and strain at failure 0.011 to 0.013, are reported for CNT films and sheets, where CLs are produced by chemical functionalization of CNT [148,149].

4.3 Effects of the Nanotube Length and CL Density on the Mechanical Properties of CNT Films Under Tension

To investigate the effects of various physical parameters, e.g., CNT length L_T , CL density n_{CL} , average bundle-size $\langle N_B \rangle$, on the mechanical properties under tension, large-scale simulations are performed for (26,0) CNT film with lateral sample size $L = 2.5 \mu\text{m}$, film thickness $H = 40$ nm and material density $\rho = 0.1 \text{ gcm}^{-3}$. The preparation of these samples is described in section 3.2.2 and major structural parameters can be found in Table 3.2. The results are described in the following sections 4.3, 4.4, 4.5, and 4.6.

The variation of the engineering stress S with engineering strains in samples with various length of nanotubes and various CL density is shown in Figure 4.8. The high-frequency variation of these curves is explained by the finite size of the considered film samples. The magnitude of this noise depends on both sample size and CL density, with the smallest magnitude observed in samples with largest CL density (Figure 4.8(d)). The calculated stress-strain curves with gradual decrease of stress at strains that are larger than the strain ε_{max} at the maximum stress S_{max} is typical for viscoelastic materials.

The values of the tensile modulus E , defining the slope of the stress-strain curves at zero strain, strength S_{max} , which is equal to the maximum engineering stress observed in a simulation, and strain ε_{max} at $S = S_{max}$ are shown in Figure 4.9. At a fixed CL density, E and S_{max} increase roughly proportionally to the nanotube length. The rate of this increase is not constant but strongly changes depending on n_{CL} . For example, at $n_{CL} = 2.5 \text{ nm}^{-1}$, S_{max} demonstrates five-fold increase when L_T increases from 200 nm to 1000 nm, while at smaller n_{CL} the slopes of curves in Figure 4.9(b) are smaller. The strain ε_{max} is more conservative parameter. The simulations reveal only moderate changes of ε_{max} around a value of 0.02 depending on the nanotube length and CL density when $n_{CL} \leq 0.5 \text{ nm}^{-1}$ (Figure 4.9(c)). Further increase of the CL density to 2.5 nm^{-1} , however, induce two-three time increase in ε_{max} .

The predicted values of the modulus and strength of cross-linked CNT films are close to values reported in the experimental studies on cross-linked CNT films and buckypaper in Ref. [68].

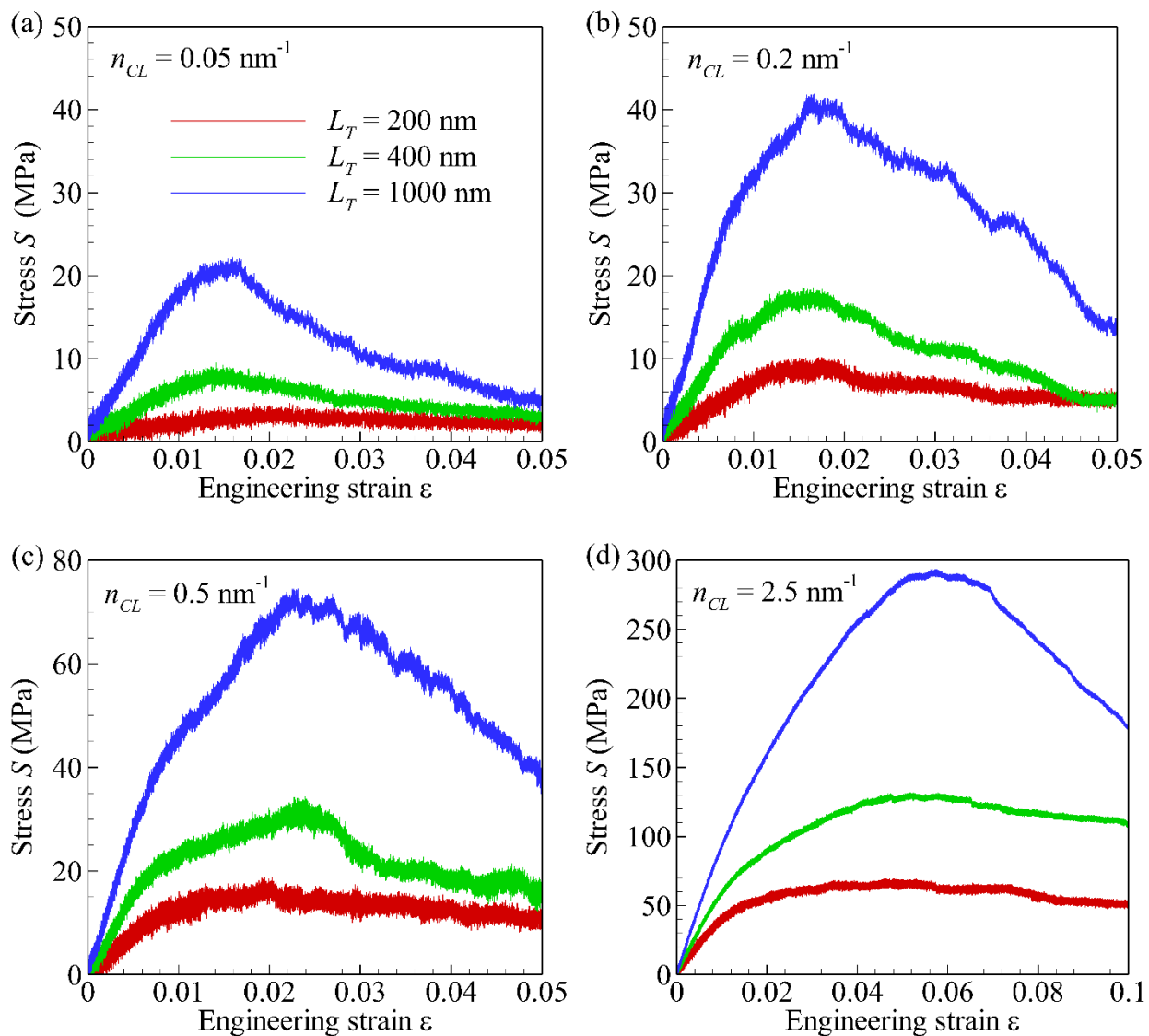


Figure 4.8. Stress S versus engineering strain ϵ obtained at stretching of CNT films at a CL density $n_{CL} = 0.05 \text{ nm}^{-1}$ (a), $n_{CL} = 0.2 \text{ nm}^{-1}$ (b), $n_{CL} = 0.5 \text{ nm}^{-1}$ (c), and $n_{CL} = 2.5 \text{ nm}^{-1}$ (d) for various CNT lengths: $L_T = 200$ nm (sample CN200, red curves), $L_T = 400$ nm (sample CN400, green curves), and $L_T = 1000$ nm (sample CN1000, blue curves).

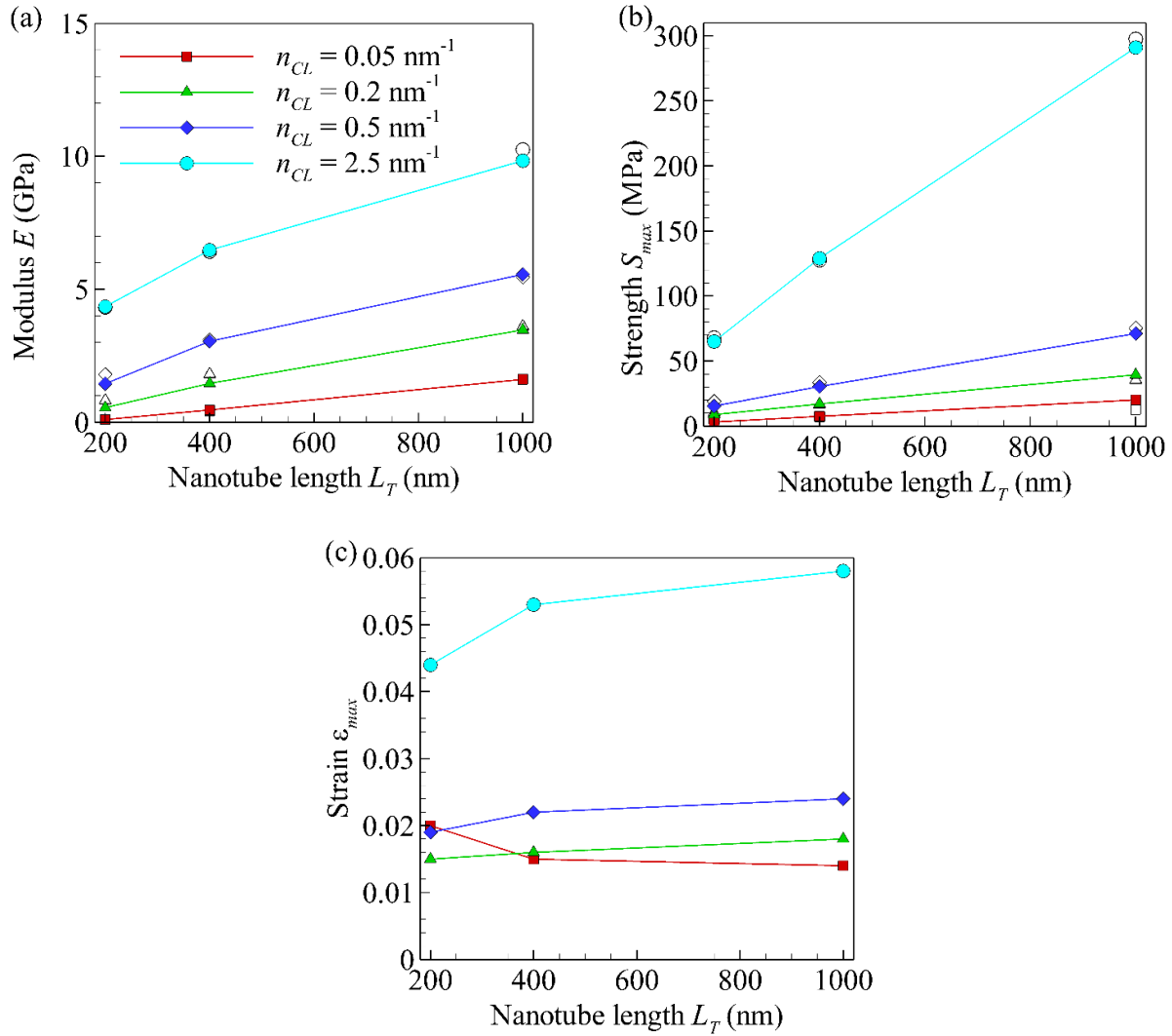


Figure 4.9. Tensile modulus E (a), strength S_{max} (b), and strain ϵ_{max} at $S = S_{max}$ (c) versus nanotube lengths L_T obtained at stretching of CNT films at a CL density $n_L = 0.05 \text{ nm}^{-1}$ (red squares), $n_L = 0.2 \text{ nm}^{-1}$ (green triangles), $n_L = 0.5 \text{ nm}^{-1}$ (blue diamonds), and $n_L = 2.5 \text{ nm}^{-1}$ (cyan circles). In panels (a) and (b), the bold symbols are obtained in mesoscopic simulations, while the corresponding empty symbols represent values of E and S_{max} calculated based on Eqs. (4.3) and (4.4) with the best-fit parameters. The bold symbols correspond to calculated values, while the curves are drawn only to guide the eye.

In Ref. [68] the measured tensile modulus, strength, and strain at failure of SWCNT films at a density of 0.6 gcm^{-3} with the electron irradiation-induced CLs vary from $\sim 1.5 \text{ GPa}$ to $\sim 3.5 \text{ GPa}$, from $\sim 15 \text{ MPa}$ to $\sim 75 \text{ MPa}$, and from 0.015 to ~ 0.037 , respectively, depending on the irradiation dosage. The small values of S_{max} deduced from the simulations for the films at a small CL density of 0.05 nm^{-1} agree with the experimental measurements for SWCNT films. The strength at break of various CNT films was found to decrease exponentially with the increase in material porosity determined as $P = 1 - \rho/\rho_{CNT}$ (here $\rho_{CNT} = 1.5 \text{ gcm}^{-3}$), and is equal to $\sim 2 \text{ MPa}$ at a porosity P of 0.72 [36]. In films of this work, $P = 0.93$ and the value of S_{max} for pristine films, thus, can be even smaller than 2 MPa .

The results presented in Figure 4.8 and Figure 4.9 indicate that effect of the nanotube length on major mechanical properties of cross-linked CNT films is altered by the CL density. The analysis of the computational results shows that the major factor that determines the modulus and strength is the average number of CLs per nanotube $N = L_T n_{CL}$. The values of E and S_{max} found in the mesoscopic simulations at various L_T and n_{CL} tend to fall on an universal curve for each parameter as a function of N (Figure 4.10). These universal dependences can be approximated by the power-type scaling laws

$$E = A(N - N_*)^\alpha, \quad (4.1)$$

$$S_{max} = BN^\beta. \quad (4.2)$$

The least-square fitting of Eqs. (4.1) and (4.2) to the data point shown in Figure 4.10(a) and Figure 4.10(b), respectively, results in $A = 0.23 \text{ GPa}$, $N_* = 8$, $\alpha = 0.49$, $B = 0.34 \text{ MPa}$, and $\beta = 0.86$. Eqs. (4.1) and (4.2) with these best-fit parameters are shown in Figure 4.10 by dashed curves. Thus, the scaling of E and S_{max} is described by the power laws with quite

different exponents, $\alpha \sim 1/2$ for E and $\beta \sim 1$ for S_{max} . The parameter N_* in Eq. (4.1) can be considered as a such critical CL number per nanotube that the CNT films cannot sustain elastic deformation at $N < N_*$. The prefactors A and B in Eqs. (4.1) and (4.2) are not universal constants but can depend on the structural parameters of the CNT networks, e.g., average bundle size. The data in Figure 4.10 are moderately well approximated by Eqs. (4.1) and (4.2) with unique values of A and B , because all data points are obtained for CNT film samples CN200, CN400, and CNT1000 with similar structural parameters as shown in section 3.2.2.

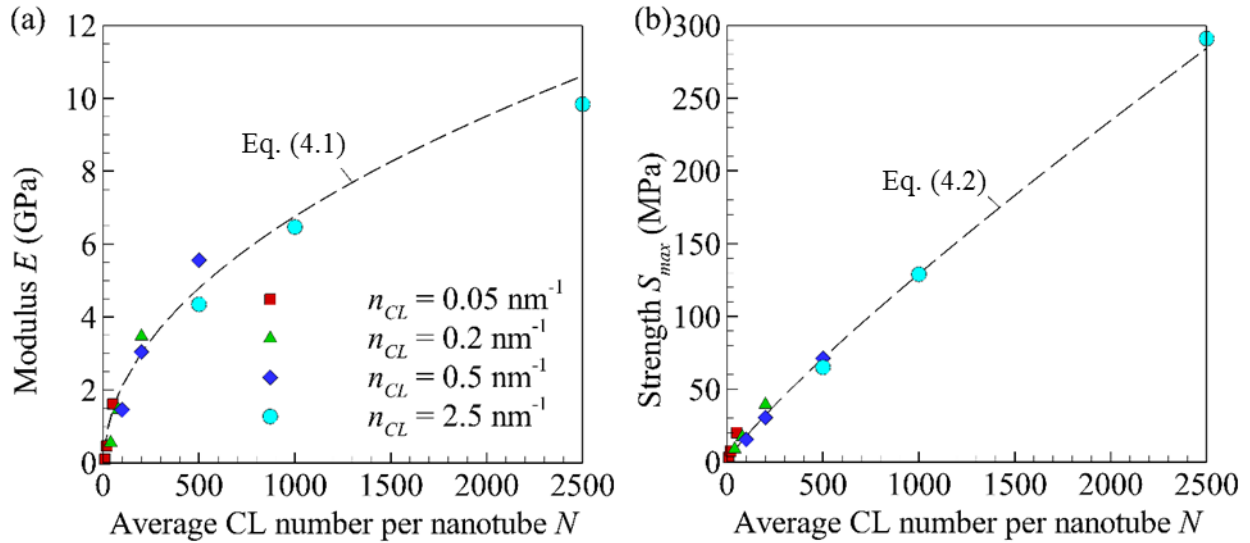


Figure 4.10. Tensile modulus E (a) and strength S_{max} (b) versus average number of CLs per nanotube $N = L_T n_{CL}$ obtained at stretching of CNT films with a CL density $n_{CL} = 0.05 \text{ nm}^{-1}$ (red squares), $n_{CL} = 0.2 \text{ nm}^{-1}$ (green triangles), $n_{CL} = 0.5 \text{ nm}^{-1}$ (blue diamonds), and $n_{CL} = 2.5 \text{ nm}^{-1}$ (cyan circles) and with a CNT length $L_T = 200 \text{ nm}$, 400 nm , and 1000 nm . The dashed curves in panels (a) and (b) are calculated based on Eqs. (4.1) and (4.2), respectively.

There is some non-negligible deviation of the data points from the scaling laws as one can conclude from the results shown in Figure 4.10. The degree of deviation of the data points

for E and S_{max} from the universal curves can be significantly reduced assuming that the arguments for the universal curves are represented in the form $\xi = N/(L_T^\theta n_{CL}^\omega)$, where the exponents $\theta < 1$ and $\omega < 1$ can be different for E and S_{max} . For the power scaling laws, when E or S_{max} are proportional to a power of ξ , the choice of θ and ω is non-unique, since the resulting equations actually depend only on $\omega - \theta$. To choose the unique values of θ and ω we first plot the reduced tensile modulus E/N and strength S_{max}/N as functions of the CNT length (Figure 4.11) and CL density (Figure 4.12).

The values of E/N and strength S_{max}/N vary in much narrower ranges compared to E and S_{max} in Figure 4.9. It confirms that the average number of CLs per nanotube N is the major parameter that determines the modulus and strength. The results shown in Figure 4.11 and Figure 4.12 also suggest that the values of E/N and strength S_{max}/N primarily depend on the CL density.

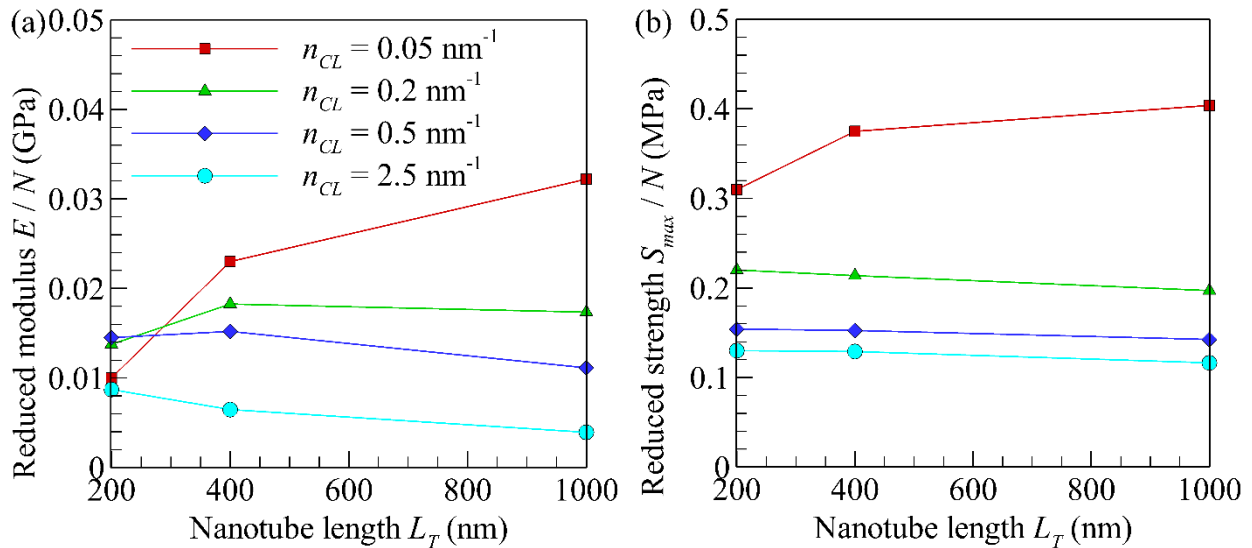


Figure 4.11. Reduced modulus E/N (a) strength S_{max}/N (b) versus nanotube lengths L_T obtained at stretching of CNT films at a linear CL density $n_{CL} = 0.05 \text{ nm}^{-1}$ (red squares),

$n_{CL} = 0.2 \text{ nm}^{-1}$ (green triangles), $n_{CL} = 0.5 \text{ nm}^{-1}$ (blue diamonds), and $n_{CL} = 2.5 \text{ nm}^{-1}$ (cyan circles). The symbols correspond to calculated values, while the curves are drawn only to guide the eye.

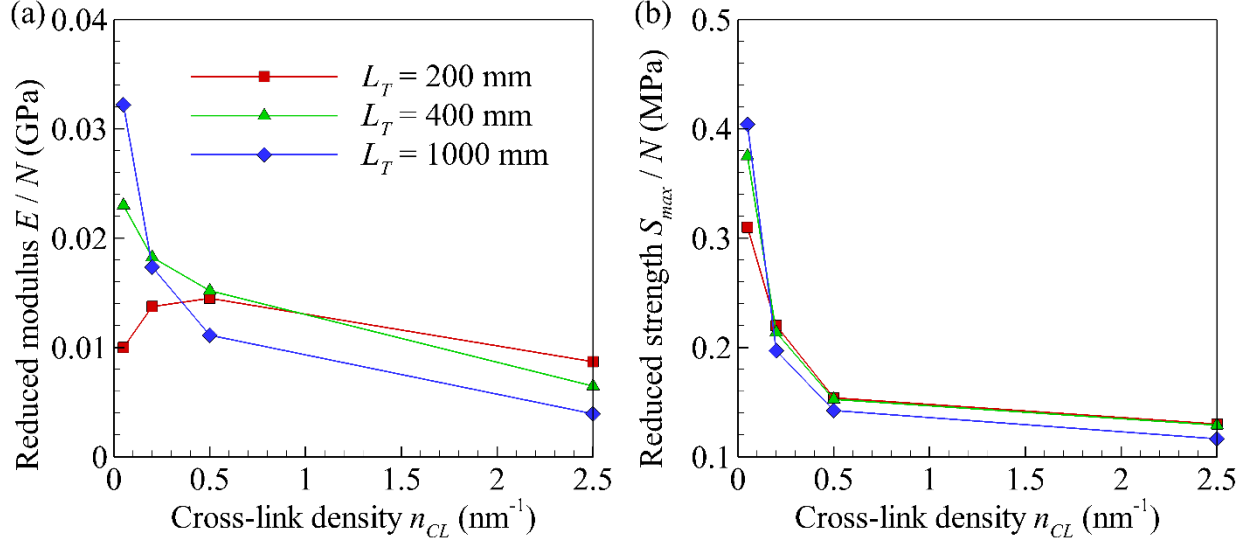


Figure 4.12. Reduced modulus E/N (a) strength S_{max}/N (b) versus linear CL density n_{CL} obtained during stretching of CNT films with a CNT length $L_T = 200$ nm (red squares), $L_T = 400$ nm (green triangles), and $L_T = 1000$ nm (blue diamonds). The symbols correspond to calculated values, while the curves are drawn only to guide the eye.

The effect of n_{CL} is particularly strong at small CL density when $n_{CL} < 0.5 \text{ nm}^{-1}$. Based on this conclusion, scaling variables in the form N/n_{CL}^γ for E and N/n_{CL}^δ for S_{max} is chosen, where n_{CL} is in nm^{-1} . Then the appropriate values of γ and δ are looked for, which provides the minimum root-mean-square (RMS) deviations of the data points from the approximating equations adopted in the form of Eqs. (4.3) and (4.4), i.e.,

$$E = C + A \left(\frac{N}{n_{CL}^\gamma} \right)^\alpha, \quad (4.3)$$

$$S_{max} = D + B \left(\frac{N}{n_{CL}^\delta} \right)^\beta. \quad (4.4)$$

The least-square fitting results in $C = -2.26$ GPa, $A = 0.6$ GPa nm $^{-\gamma}$, $\gamma = 0.25$, $\alpha = 0.4$, $D = 3.17$ MPa, $B = 0.2$ MPa nm $^{-\delta}$, $\delta = 0.07$, and $\beta = 0.94$. With these parameters, the data points E and S_{max} almost ideally fall on universal curves as functions of N/n_{CL}^γ and N/n_{CL}^δ (Figure 4.13).

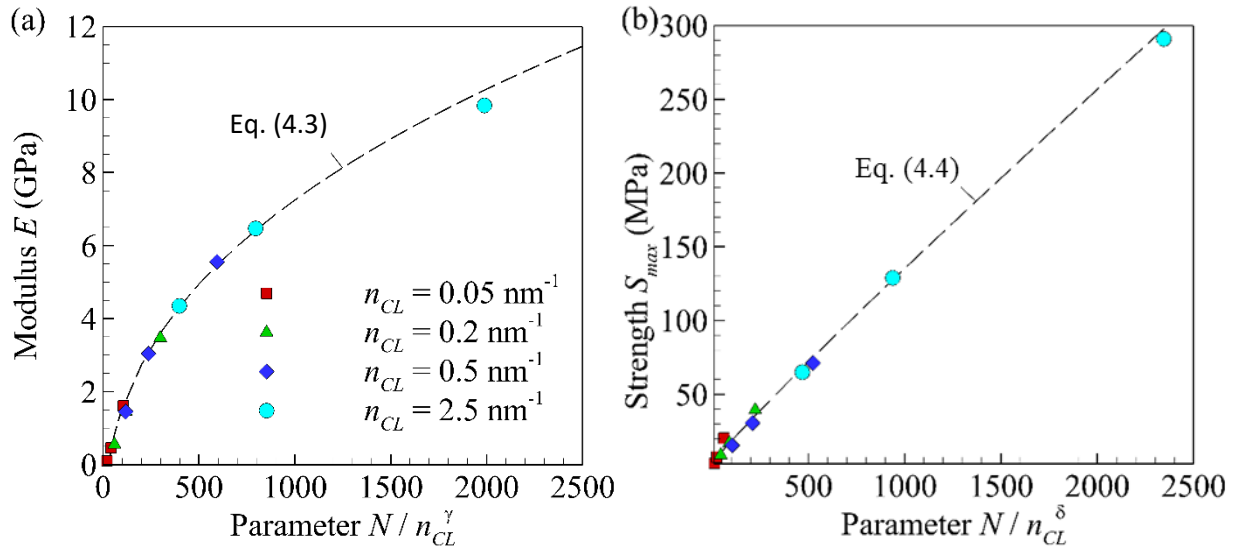


Figure 4.13. Tensile modulus E versus parameter N/n_{CL}^γ at $\gamma = 0.25$ (a) and strength S_{max} versus parameter N/n_{CL}^δ at $\delta = 0.07$ (b), obtained at stretching of CNT films with a CL density $n_{CL} = 0.05$ nm $^{-1}$ (red squares), $n_{CL} = 0.2$ nm $^{-1}$ (green triangles), $n_{CL} = 0.5$ nm $^{-1}$ (blue diamonds), and $n_{CL} = 2.5$ nm $^{-1}$ (cyan circles) and with a CNT length $L_T = 200$ nm, 400 nm, and 1000 nm. The symbols correspond to calculated values presented in Figure 4.9. The dashed curves in panels (a) and (b) are calculated based on Eqs. (4.3) and (4.4), respectively.

Although the best-fit values of the exponents α and β for the sets of fitting equations in the form of Eqs. (4.1)-(4.2) and (4.3)-(4.4) are somewhat different, the ratio β/α is large in both cases and varies between 1.76 and 2.35. It indicates a strong difference in scaling between the

modulus and strength as functions of the CNT length and CL density. The approximations in the form of Eqs. (4.3) and (4.4) provide the RMS deviations that are 1.5 and 2 times smaller compared to the deviations for corresponding scaling laws in the form of Eqs. (4.1) and (4.2) (Table 4.1).

Table 4.1. Root-mean-square (RMS) deviations of values of the tensile modulus E (GPa) and strength S_{max} (MPa) obtained in simulations with samples CN200 – CN1000 in Table 3.2 from the approximations given by Eqs. (4.1), (4.2), (4.3), and (4.4).

| | E | | S_{max} | |
|---------------|-----------|-----------|-----------|-----------|
| | Eq. (4.1) | Eq. (4.3) | Eq. (4.2) | Eq. (4.4) |
| RMS deviation | 0.46 | 0.2 | 5.2 | 3.2 |

4.4 Mechanisms of Irreversible Structural Changes and Appearance of Percolating Load Transfer Networks in Cross-linked Films at Tension

Non-reversible inelastic deformation of CNT networks occurs due to two factors, namely, breaking of CLs and irreversible changes in the network structure as a result of the bundling and de-bundling processes. The fracture of nanotubes at tension is accounted for in the mesoscopic model of this work, but never happen under condition considered in the present work. The fraction of broken CLs f_b for films CN200-CN100 is shown in Figure 4.14(a). Although the number of broken CLs is relatively small for the range of strain considered in this figure, it has a crucial effect on the load transfer through the network, as most of broken CLs connect the nanotubes that serve as interconnects between thick bundles. The rate of CL breaking increases with increasing length of nanotubes. The fraction of broken CLs remains negligible until

$\varepsilon = 0.005$ and after that it starts to grow fast. At tension, a relatively early onset of CL breaking pre-determines the low elastic limit $\varepsilon_e = 0.005$. At $\varepsilon > \varepsilon_e$ the mechanical response of CNT films on stretching is not purely elastic. In additional simulations it is confirmed, where relaxation of films is performed at constant elongations above the elastic limit at $\varepsilon_e = 0.005$ and found that the stress relaxes with time as expected for viscoelastic materials [150]. At $\varepsilon > \varepsilon_{max}$, the rate of CL breaking decreases and the fraction of broken CLs tends to saturate.

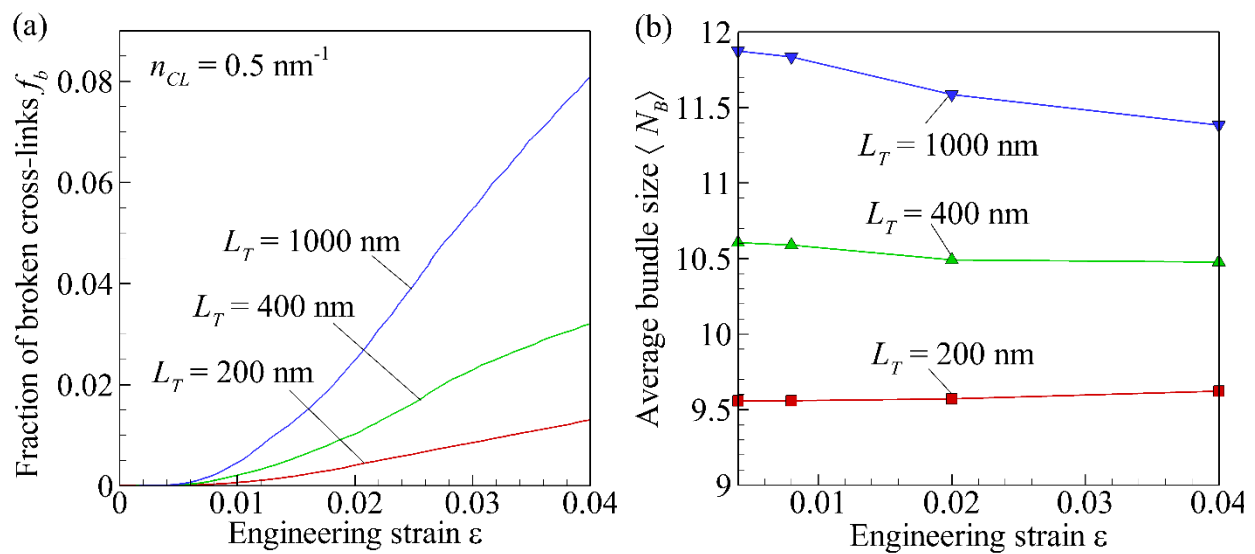


Figure 4.14. Fraction of broken CLs f_b (a) and average bundle size $\langle N_B \rangle$ (b) versus engineering strain ε obtained at stretching of CNT films with continuous networks of bundles at a CL density $n_{CL} = 0.5 \text{ nm}^{-1}$ and CNT length $L_T = 200 \text{ nm}$ (sample CNT200, red curves), $L_T = 400 \text{ nm}$ (sample CN400, green curves), and $L_T = 1000 \text{ nm}$ (sample CN1000, blue curves). In panel (b), the symbols correspond to calculated values, while the curves are drawn only to guide the eye.

To characterize the degree of non-reversible changes in the film network structure at stretching due to bundling and de-bundling, the average bundle size is calculated and plotted as a

function of strain in Figure 4.14(b). The obtained results suggest that the process of de-bundling provides relatively small contribution to the overall non-reversible changes in the network structure. The de-bundling effect is more pronounced for the film composed of long, 1000 nm long CNTs. Only marginal de-bundling occurs during stretching of the film composed of short, 200 nm long CNTs.

To characterize the involvement of individual nanotubes into the transfer of mechanical load, the stretched film is plotted in Figure 4.15, where the individual nanotubes are colored according to their local strain $\epsilon = \Delta l/l_0$, where $l_0 = 2$ nm is the equilibrium length of a mesoscopic CNT segment and Δl is its elongation. In the relaxed non-deformed samples, the absolute majority of nanotubes are only marginally stretched, when ϵ is well below 0.005. It can be concluded, e.g., based on the analysis of the PDFs of ϵ at various degree of deformation shown in Figure 4.16. In the deformed sample illustrated in Figure 4.15, the nanotube elements shown in red and blue have the absolute value of local strain exceeding 0.005. The load transfer between two clip layers in the deformed state occurs mostly through the nanotube parts that are stretched and compressed above the level of strain in the non-deformed sample. For the film sample shown in Figure 4.15, a large fraction of the film material is only marginally stretched and, thus, produces small contribution to the overall load transfer. The nanotube segments that provide significant contribution to the overall load transfer are connected through CLs with the clip layers and, thus, form a percolating network in the direction of the applied deformation.

To describe the variation of the degree of the network connectivity at evolving deformation, an approach is developed, which allows to identify the part of the whole film that forms a load transfer network percolating the sample in the direction of the applied deformation.

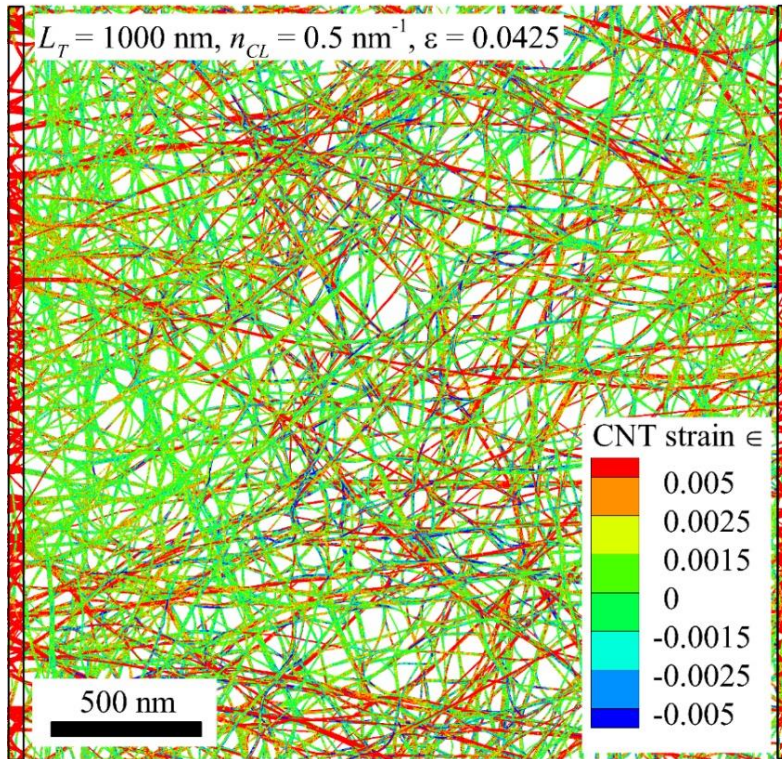


Figure 4.15. Top view of the CNT film sample CN1000 (sample CN1000, $L_T = 1000 \text{ nm}$, $n_{CL} = 0.5 \text{ nm}^{-1}$) stretched to an engineering strain $\epsilon = 0.0425$. The individual nanotubes are colored according to their local strain ϵ . The black rectangles correspond to the non-deformable clip layers at the left and right boundaries of the sample.

To define the percolating load transfer network, a list of all mesoscopic elements are first created that are stretched or compressed above the threshold strain ϵ_{th} , i.e., all mesoscopic elements with $|\epsilon| > \epsilon_{th}$. Then only such elements in that list is retained, which are “connected” through the closest neighbor elements of the same CNT or by CL with other elements from the list to the CNT segments crossing the clip layer boundaries.

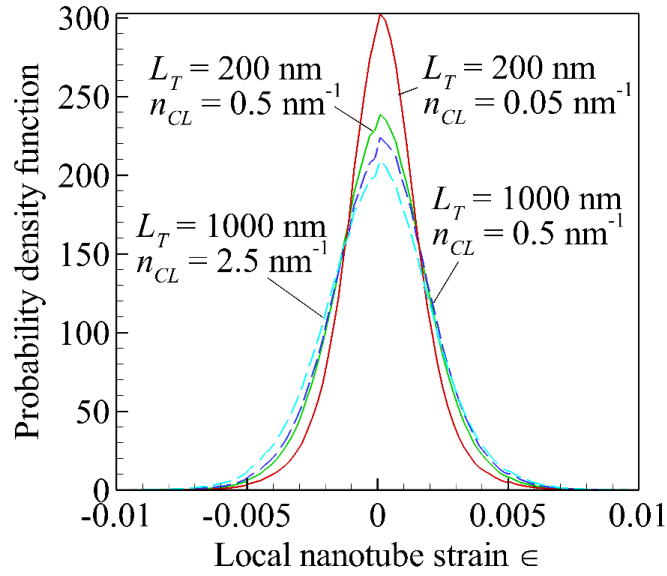


Figure 4.16. Probability density functions of local nanotube strain ϵ calculated for non-deformed films with the continuous networks of bundles of nanotubes at $L_T = 200$ nm and $n_{CL} = 0.05$ nm⁻¹ (red solid curve), $L_T = 200$ nm and $n_{CL} = 0.5$ nm⁻¹ (green solid curve), $L_T = 1000$ nm and $n_{CL} = 0.5$ nm⁻¹ (blue dashed curve), as well as $L_T = 1000$ nm and $n_{CL} = 2.5$ nm⁻¹ (cyan dashed curve) .

The list of segments and the mass fraction f_p of the material included into such percolating network depends on the threshold strain ϵ_{th} . The choice of ϵ_{th} for comparison of connectivity in samples with strongly different network structures, e.g., films with continuous networks and films with dispersed CNTs is a non-trivial problem, as different magnitude of stretching of individual nanotubes is expected in samples with strongly different structures. At the same time, for samples with roughly the same structure of bundles, like samples CN200 - CN1000 in Table 3.2, the particular value ϵ_{th} used for the analysis of the percolating network does not affect the conclusions. The calculations of the percolating networks in sample CN200 - CN1000 at various values of ϵ_{th} show that even relatively small value $\epsilon_{th} \sim 0.001$ can be used for the analysis of the

connectivity variation if these values correspond to no percolating network in the non-deformed samples. Although the non-deformed samples contain a substantial fraction of segments stretched and compressed above this level of strain (Figure 4.16), these segments do not form a percolating network. The percolating load transfer network shown in Figure 4.17 corresponds the film sample shown in Figure 4.15.

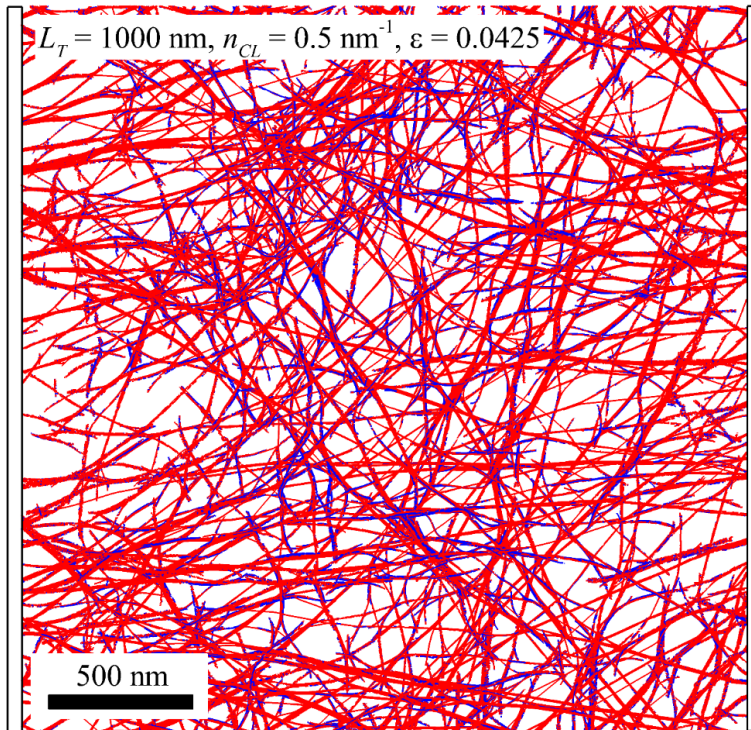


Figure 4.17. Top view of the CNT film shown in Figure 4.15 (sample CN1000) stretched to an engineering strain $\epsilon = 0.0425$, where only nanotubes included into the percolating load transfer network for the threshold strain $\epsilon_{th} = 0.001$ are shown. The nanotube segments shown in red and blue are stretched and compressed, respectively. The black rectangles correspond to the non-deformable clip layers at the left and right boundaries of the sample.

The fraction f_p of material included into the percolating network can be used as a measure of the evolving connectivity in the network of cross-linked nanotubes, which predetermines the resistance of the network to the applied deformation. The effect of the CNT length on the formation of the percolating load transfer network is illustrated in Figure 4.18. An increase in L_T results in much broader percolating network involving larger fraction of the whole network. The stress-strain curves correlate with the variation of f_p such that an increase in f_p always corresponds to the increasing stress in stretched films with increasing CNT length or CL density. For instance, when stretched samples CN200-CN1000 are compared at various deformation states, the films with larger tensile stress always have larger fraction f_p of material included into the percolating network. The data shown in Figure 4.9(a) and Figure 4.19(a) exemplify such a relation, since the elastic modulus E and f_p are increasing functions of nanotube length. The fraction of material involved in the percolating network f_p is shown in Figure 4.19(b) as a function of strain ε for the film samples with the nanotube length equal to 200 nm and 1000 nm. In both cases, the maximum of f_p occurs at $\varepsilon = \varepsilon_{max}$ and, thus, correlates with the maximum of the tensile stress. An initial increase of f_p under conditions of CL breaking is explained by the changes in the load transfer network, which does not remain constant and evolves during the deformation process. The breaking of CLs deactivates existing paths of load transfer through a network and simultaneously activates new ones. The fraction of CLs that connect CNT parts included into the percolating network (not shown in Figure 4.19) and, thus, participating in the load transfer, varies like the fraction of CNT material included into the percolating network. The existence of the percolating load transfer network during the whole deformation process explains the gradual decrease in stress at $\varepsilon > \varepsilon_{max}$ instead of distinct fracture behavior. It is characteristic for all stress-strain curves obtained in our simulations.

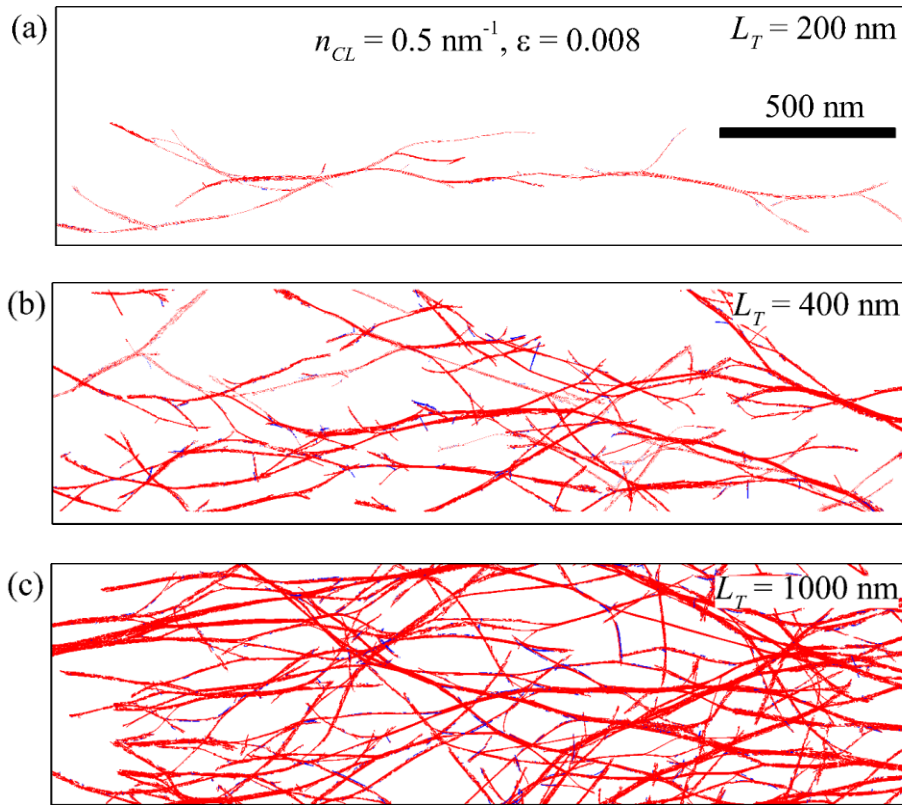


Figure 4.18. Top views of the percolating load transfer networks in CNT films composed of nanotubes with lengths $L_T = 200 \text{ nm}$ (sample CN200, a), $L_T = 400 \text{ nm}$ (sample CN400, b), and $L_T = 1000 \text{ nm}$ (sample CNT1000, c) at a CL density $n_{CL} = 0.5 \text{ nm}^{-1}$ stretched to an engineering strains $\epsilon = 0.008$. Each simulation snapshot shows only segments of nanotubes belonging to a percolating network composed of CNT parts stretched or compresses above the threshold strain value $\epsilon_{th} = 0.001$, connected with each other through CLs, and included into a network percolating the sample in the direction of applied deformation. Other CNT segments are blanked. The CNT segments shown in red and blue are stretched and compressed, respectively. The vertical sides of the bounding boxes correspond to the boundaries of the deformable parts of the films. Each panel shows the full sample in the horizontal direction and only a quarter of the whole sample in the vertical direction.

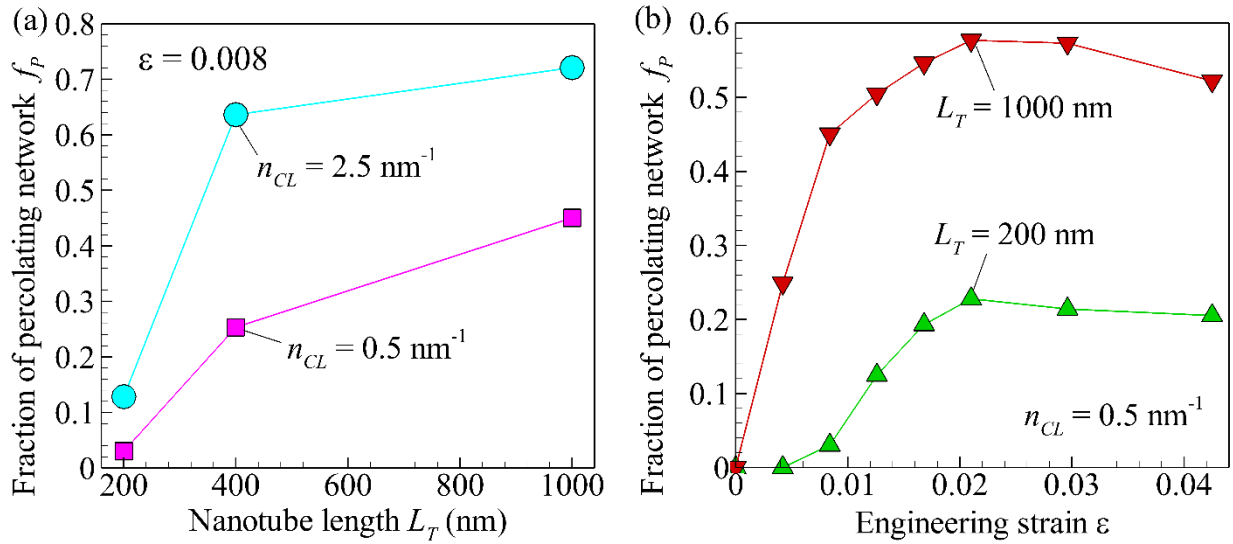


Figure 4.19. Fraction of percolating network f_p versus nanotube length L_T in films with a CL density $n_L = 0.5 \text{ nm}^{-1}$ (magenta rectangles) and $n_L = 2.5 \text{ nm}^{-1}$ (cyan circles) stretched to an engineering strain $\epsilon = 0.008$ (a) and versus engineering strain ϵ at a CL density $n_L = 0.5 \text{ nm}^{-1}$ for $L_T = 200 \text{ nm}$ (green triangles) and $L_T = 200 \text{ nm}$ (red gradients). The calculation of f_p is performed at $\epsilon_{th} = 0.001$. The symbols correspond to calculated values, while the curves are drawn only to guide the eye.

4.5 Effects of Random Distribution of the Nanotube Length

The results of a stretching simulation performed for the sample with random distribution of the nanotube length (sample CNW in Table 3.2) is compared with the results obtained for the sample with the constant CNT length (sample CN620 in Table 3.2), where $L_T = 620 \text{ nm}$ is equal to the average CNT length in the sample CNW. Compared to the sample CN620, the network in the non-deformed sample CNW includes significantly larger number of thin bundles with $N_B \sim 5$ and smaller number of thicker bundles with $N_B \sim 20$ (Figure 4.20(a)). The overall structure of the

sample CNW is close to the structure of the sample CN200 composed of 200 nm long nanotubes with similar values of the average and most probable equivalent bundle diameters (Table 3.2). The simulations of cross-linked films CNW and CN620 at a CL density of 0.5 nm^{-1} predict practically the same tensile modulus E (Figure 4.20(b)). The increased values of S_{max} and ε_{max} in the sample CNW are attributed to the effect of relatively small number of nanotubes, which are much longer than the average CNT length. The obtained results suggest, however, that the overall effects of the dispersion of the nanotube length on both structural network properties and tensile mechanical properties are only moderate.

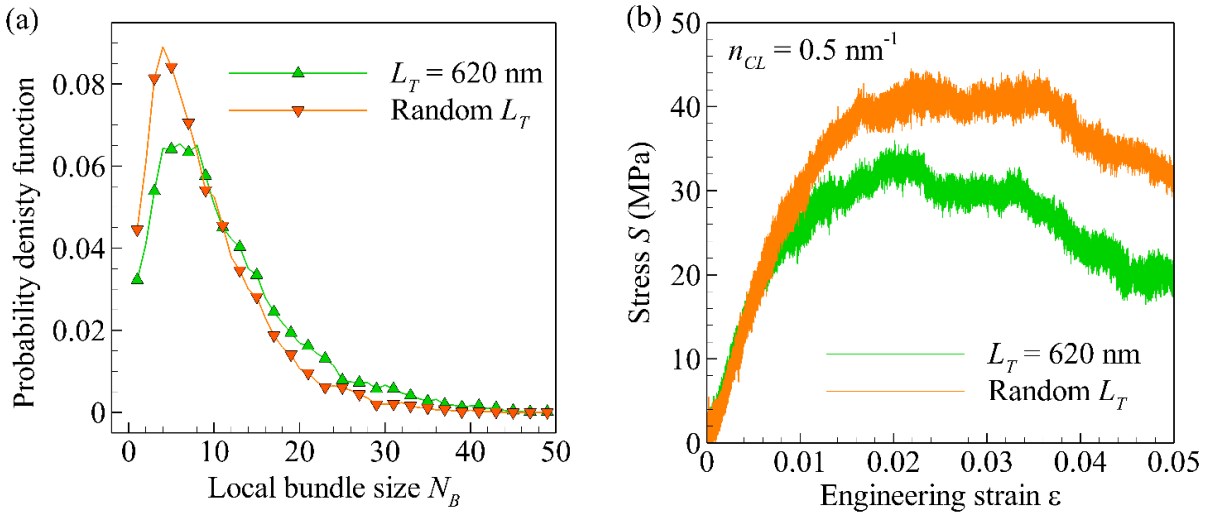


Figure 4.20. (a), Probability density functions of local bundle sizes N_B in CNT films with the constant nanotube length $L_T = 620 \text{ nm}$ (sample CN620, green triangles) and with random nanotube lengths distributed according to Eq. (3.1) with $b = 2.08$ and $a = 430 \text{ nm}$ (sample CNW, orange gradients). (b), Stress S versus engineering strain ε at stretching of films with the CNT length $L_T = 620 \text{ nm}$ (sample CN620, green curve) and random distribution of the nanotube length (sample CNW, orange curve) at a CL density of $n_L = 0.5 \text{ nm}^{-1}$.

4.6 Effects of the Network Structure

To study the effect of the network structure on the mechanical properties of CNT films, simulations with the samples are performed, where the spontaneous self-assembly of nanotubes into bundles is impeded by CLs and the nanotubes remains dispersed before the onset of deformation. For this purpose, CLs to the initial samples of straight and dispersed nanotubes is added. Then the sample is relaxed in a thermostat at a mesoscopic temperature of 300 K during 0.2 ns with pistons constraining the film volume. Finally, the pistons are removed, and the free-standing film is relaxed additionally for 0.02 ns in at the same temperature of 300 K and at zero pressure. At a CL density $n_{CL} = 0.05 \text{ nm}^{-1}$, this approach leads to films with a steady-state structure, where almost all nanotubes are dispersed, and the average bundle size is less than two (Table 3.2). The structure of such samples with the nanotube lengths of 200 nm and 1000 nm before the onset of deformation is illustrated in Figure 4.21. During relaxation of the sample DN200, only 27 CLs out of 128619 total CLs in the sample are broken. No CL breaking is observed during relaxation of the sample DN1000.

Contrary to films with a continuous network of bundles of nanotubes, deformation of films with dispersed nanotubes results in strong reformation of the network structure, as it is illustrated in Figure 4.22 for a strain of 0.032. Massive breaking of CLs during stretching (Figure 4.23(a)), releases constraints for nanotube self-assembly and stretching of the films is accompanied with the bundling process (Figure 4.23(b)). The rate of CL breaking in average, is much higher in films with dispersed nanotubes. The process of bundle formation also creates large pores.

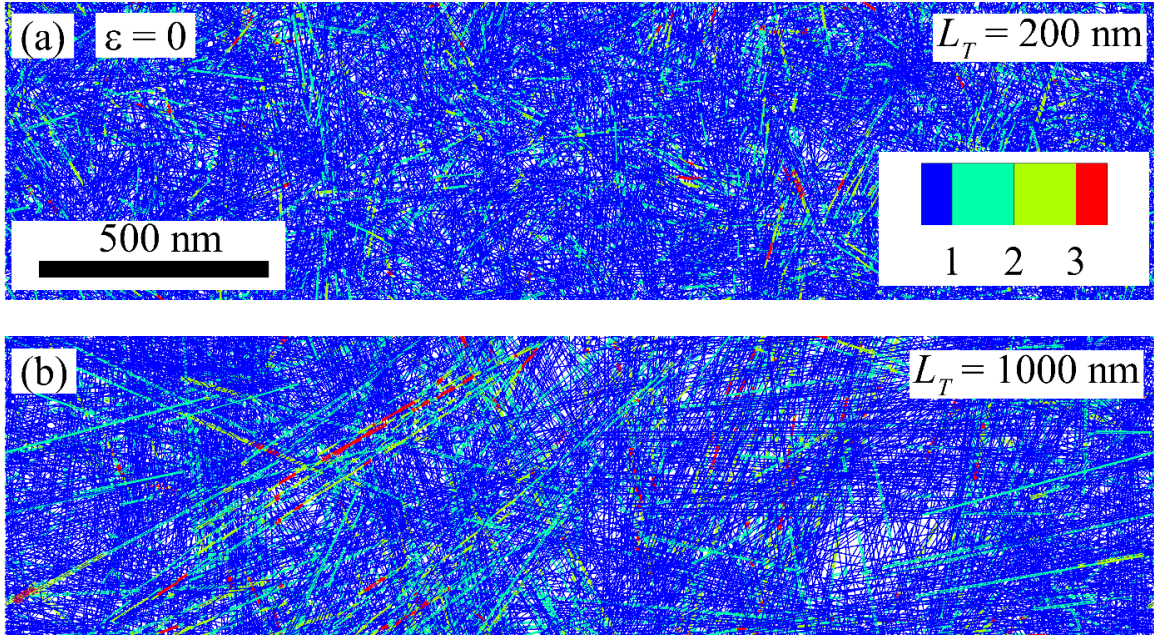


Figure 4.21. Top views of non-deformed CNT films composed of dispersed CNTs with lengths $L_T = 200 \text{ nm}$ (sample DN200 in Table 3.2, a) and $L_T = 1000 \text{ nm}$ (sample DN1000 in Table 3.2, b) generated at CL density $n_L = 0.05 \text{ nm}^{-1}$. Each panel shows the full sample in the horizontal direction and only a quarter of the whole sample in the vertical direction. The individual nanotubes are colored according to the local bundle size N_B with the color table for N_B shown in panel (a).

The films with dispersed nanotubes exhibit an order-of-magnitude increase in the initial slopes of the stress-strain curves, as well as from three- to six-fold increase in the material strength compared to samples with the continuous networks of bundles of nanotubes with the same CNT length and CL density (Figure 4.24 and Table 4.2). This increase in the mechanical properties is associated with better network connectivity provided by CLs in the samples of dispersed nanotubes. The strain ε_{max} only weakly depends on the sample structure. At the same time, even initial phase of deformation of samples with dispersed nanotubes is inelastic, since the

process of CL breaking starts immediately after the onset of deformation (Figure 4.23(a)) and is accompanied with fast increase in the average bundle size (Figure 4.23(b)). The bundle formation accompanying with the nucleation of large pores results in a fast drop of stress with increasing strain at $\epsilon > \epsilon_{max}$, so that at $\epsilon \sim 0.04$ the stress in films of dispersed nanotubes reduced to the stress in corresponding films with continuous networks of bundles of nanotubes.

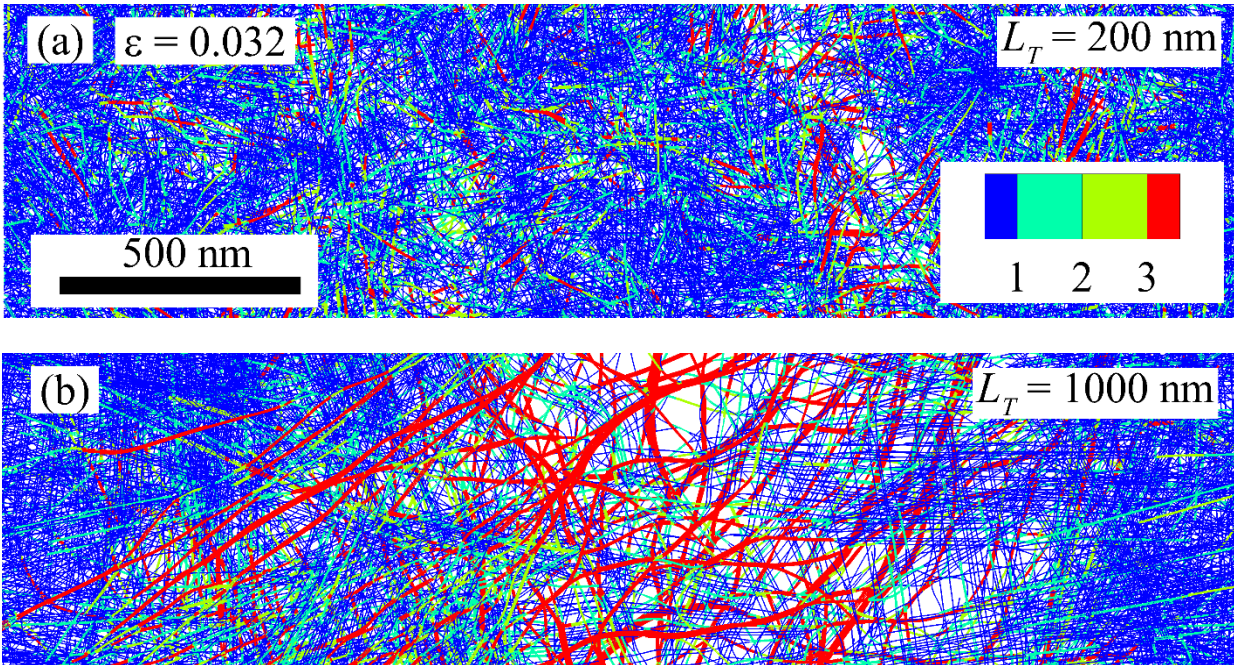


Figure 4.22. Top views of CNT films composed of dispersed CNTs with lengths $L_T = 200 \text{ nm}$ (sample DN200 in Table 3.2, a) and $L_T = 1000 \text{ nm}$ (sample DN1000 in Table 3.2, b) and at a CL density $n_L = 0.05 \text{ nm}^{-1}$ stretched to a strain $\epsilon = 0.032$. Each panel shows the full sample in the horizontal direction and only a quarter of the whole sample in the vertical direction. The individual nanotubes are colored according to the local bundle size N_B with the color table for N_B shown in panel (a).

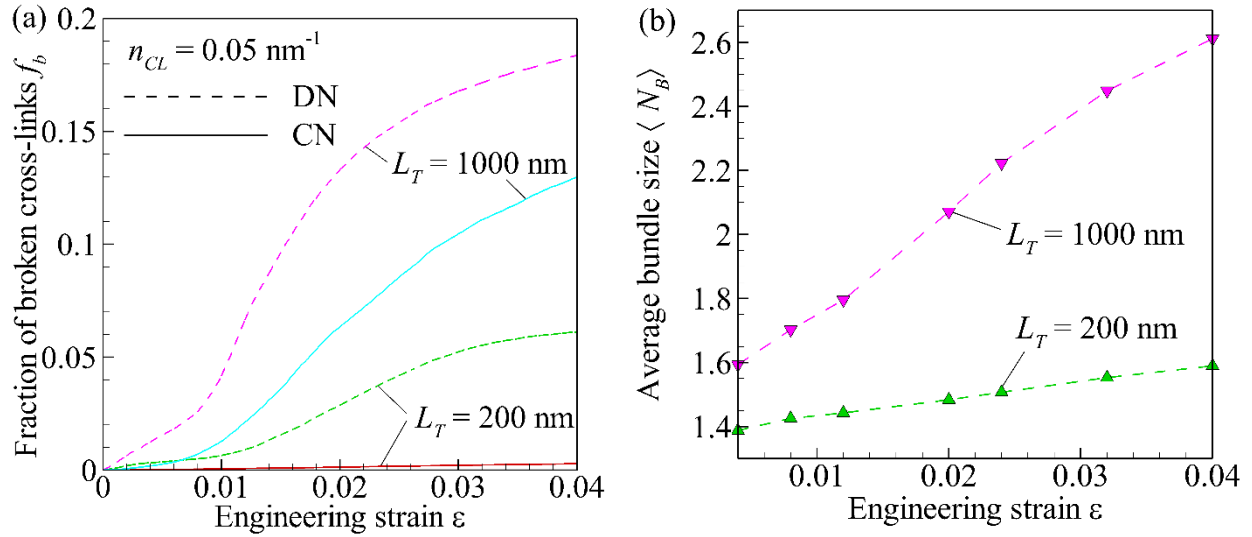


Figure 4.23. Fraction of broken CLs f_b (a) and average bundle size $\langle N_B \rangle$ (b) versus engineering strain ϵ obtained at stretching of CNT films at a CL density $n_{CL} = 0.05 \text{ nm}^{-1}$ and a CNT length $L_T = 200 \text{ nm}$ (red solid and magenta dashed curves) and $L_T = 1000 \text{ nm}$ (cyan solid and magenta dashed curves). The solid curves are obtained for samples CN200 and CN1000 shown in Figure 3.10(a) and (c), respectively, with continuous networks (CN) of bundles of nanotubes. The dashed curves are obtained for samples DN200 and DN1000 shown in Figure 4.21(a) and (b), respectively, where the non-deformed films consist of dispersed nanotubes (DN). In panel (b), the results are presented only for DN samples, and the symbols correspond to calculated values, while the curves are drawn only to guide the eye (see Table 3.2 for the sample parameters).

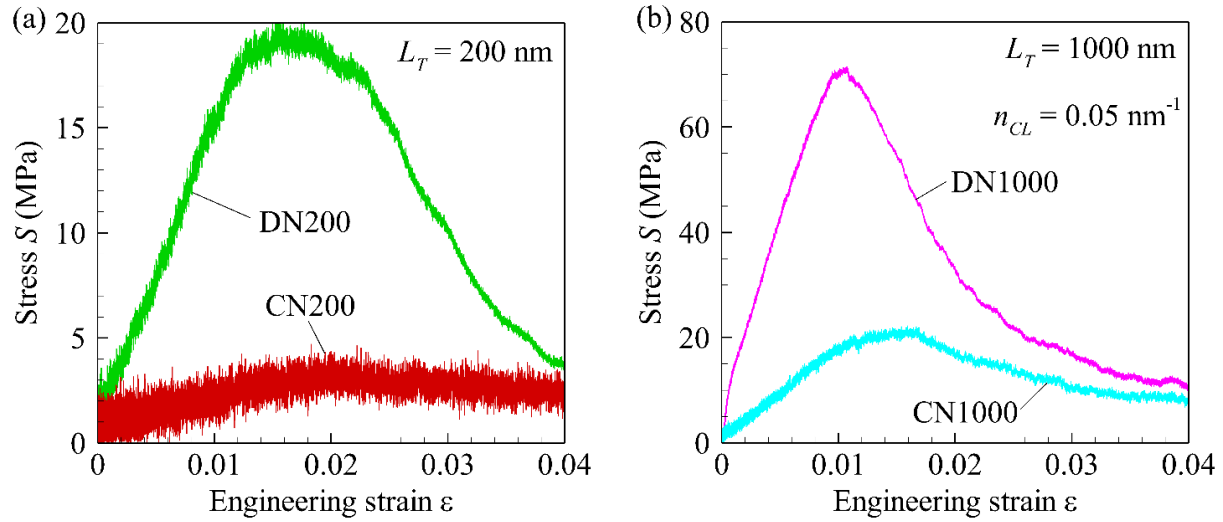


Figure 4.24. Stress S versus engineering strain ε obtained at stretching of CNT films with a CNT length $L_T = 200$ nm (a) and $L_T = 1000$ nm (b). The red and cyan curves are obtained for the samples CN200 and CN1000, with continuous networks of bundles of nanotubes. The green and magenta curves are obtained for the film samples DN200 and DN1000 shown in Figure 4.21(a) and (b), respectively.

Table 4.2. Initial slope of a stress-strain curve E , strength S_{max} , and strain ε_{max} at $S = S_{max}$ obtained at stretching of the CNT films samples CN200, DN200, CN1000, and DN1000.

| Film sample | L_T (nm) | Network structure | E (GPa) | S_{max} (MPa) | ε_{max} |
|-------------|------------|-------------------|-----------|-----------------|---------------------|
| CN200 | 200 | Continuous | 0.1 | 3.1 | 0.02 |
| DN200 | 200 | Dispersed | 1.3 | 19.3 | 0.017 |
| CN1000 | 1000 | Continuous | 1.5 | 20.8 | 0.015 |
| DN1000 | 1000 | Dispersed | 15 | 68.5 | 0.011 |

4.7 Effects of Material Density

The effect of material density on mechanical properties during stretching is studied using (10,10) CNT films with CNT length $L_T = 200$ nm, sample size $L = 0.5$ μm , film thickness $H = 100$ nm, and material density ρ varying from 0.05 gcm^{-3} to 0.4 gcm^{-3} , and are discussed in section 4.7. Preparation of these samples are described in section 3.2.1 and major structural parameters can be found in Table 3.1. All these samples have a linear CL density $n_{CL} = 0.15$ nm^{-1} and nanotube length $L_T = 200$ nm. Figure 4.25 shows the stress-strain curves (a) along with specific stress (S/ρ) versus strain curves (b). The results suggest weak effect of material density on the mechanical properties in terms of specific modulus E/ρ and specific strength S_{max}/ρ . For 8 times variation in material density ρ , only 1.5 times variation in specific modulus E/ρ and 1.4 times variation in specific strength is observed (Figure 4.25 (c)). These results agree with the observations made in section 4.3, where it is demonstrated that mechanical properties of cross-linked CNT films is majorly determined by the average number of CLs per nanotube $N = L_T n_{CL}$. Although samples A₀, B₀, C₀ and D₀ have different material densities ρ , they all share same nanotube length L_T and CL density n_{CL} , and hence the mechanical properties are somewhat similar. The analysis of the percolating load-transfer networks in these samples also agree with this conclusion, where it is observed that depending on the material density for a given strain, the qualitative and quantitative difference in the percolating load transfer networks in these samples are not significant (Figure 4.26).

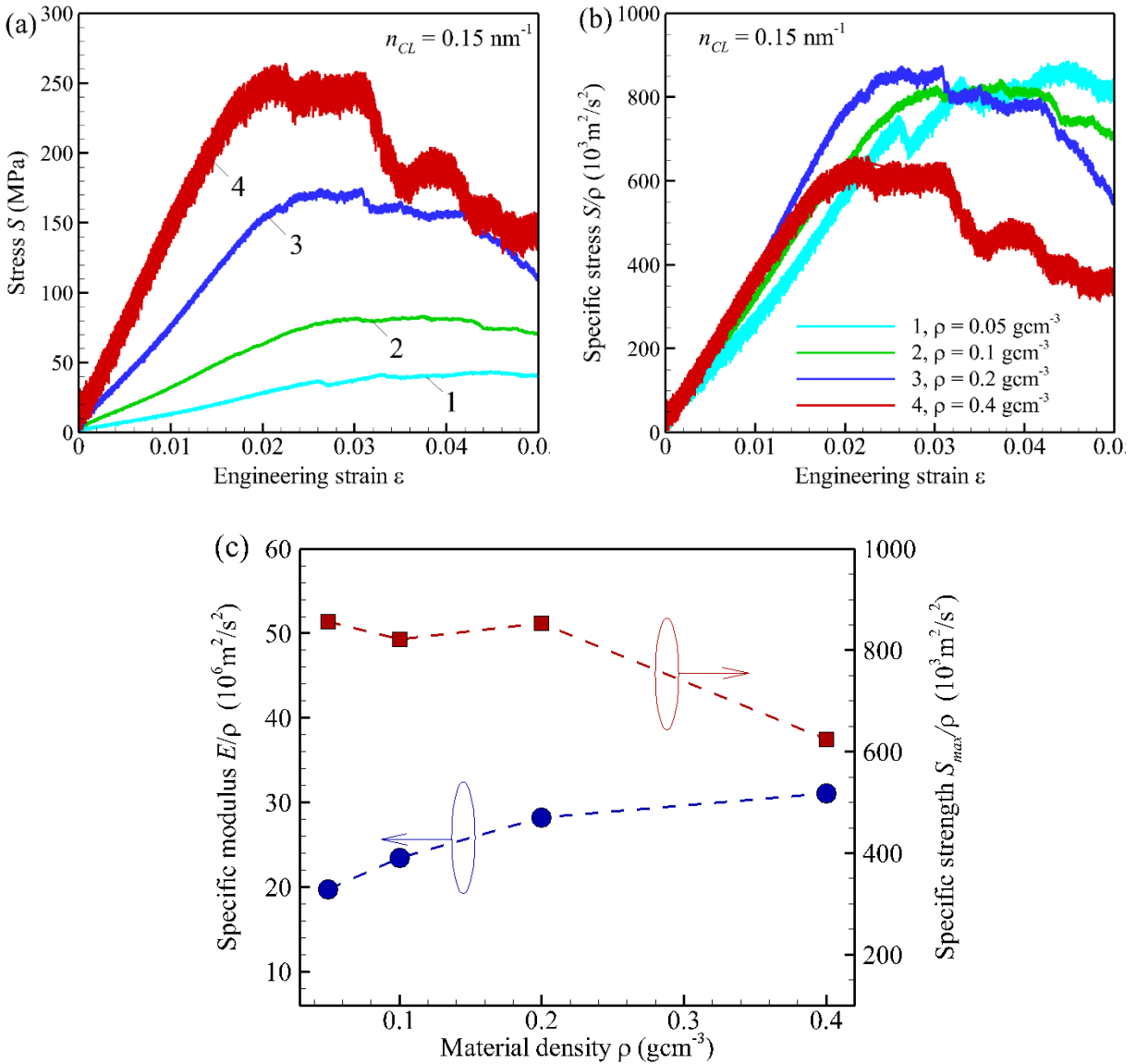


Figure 4.25. Stress (a) and specific stress S/ρ (b) versus engineering strain ϵ obtained in stretching simulations of samples composed of (10,10) CNTs at a material densities $\rho = 0.05 \text{ gcm}^{-3}$ (curves 1, cyan), 0.1 gcm^{-3} (curves 2, green), 0.2 gcm^{-3} (curves 3, blue), 0.4 gcm^{-3} (curves 4, red), and linear CL density $n_{CL} = 0.15 \text{ nm}^{-1}$. Panel (c) shows the specific modulus E/ρ and specific strength S_{max}/ρ versus material density.

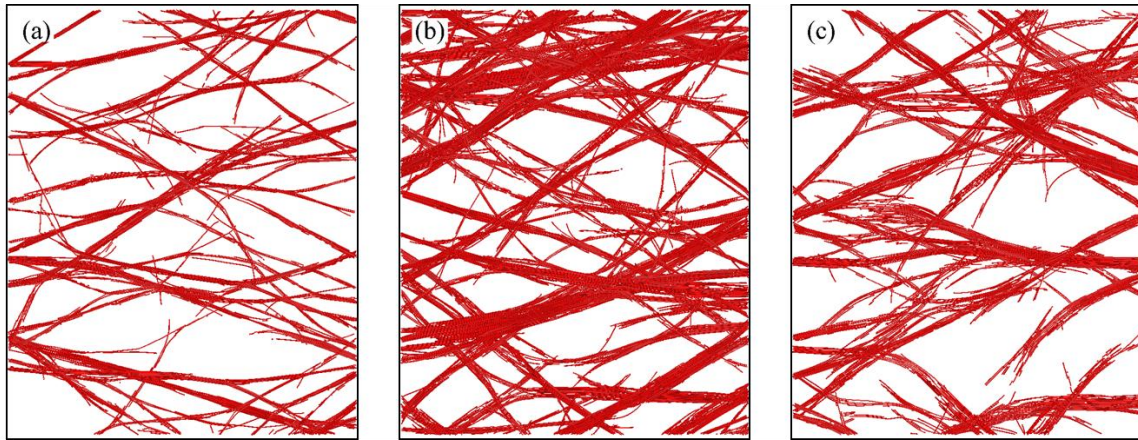


Figure 4.26. Top views of CNT film samples under stretching at a strain $\varepsilon = 0.02$ with density $\rho = 0.05 \text{ gcm}^{-3}$ (a), 0.2 gcm^{-3} (b), 0.4 gcm^{-3} (c) and CL density $n_{CL} = 0.15 \text{ nm}^{-1}$. Mesoscopic elements that are not part of the percolating load transfer networks or included into the clip layers are not shown. The mass fractions of percolating load transfer network f_p in panel (a), (b), and (c) is equal to 0.07, 0.13, and 0.09, respectively.

4.8 In-Plane Compression of Cross-Linked CNT Films

To reveal the difference between microscopic pictures of deformation of CNT films under compression and stretching, in-plane compression is performed with the same film sample mentioned in section 4.2 (i.e., the CNT film composed of (26, 0) CNT of length $L_T = 400 \text{ nm}$ at a material density of 0.1 gcm^{-3} and CL density $n_{CL} = 0.05 \text{ \AA}^{-1}$ with the lateral sizes $1 \mu\text{m} \times 1 \mu\text{m}$ and film thicknesses of 40 nm) and same magnitude of the deformation velocity and thermostat temperature. In this case, the nanotubes in every clip layer are moved towards each other with velocity $V_D/2$. The film compressed up to the strain of -0.14 is shown in Figure 4.27(a). In the stretched film, relatively small number of nanotubes forms percolating network (Figure 4.2), while in the compressed film (Figure 4.27(a)) the total amount of compressed (shown by blue) and stretched (shown by red) CNTs is much larger, stretched or compressed

CNTs separately from each other do not form a network “connecting” two clip layers, and the film can be divided into a few intermitting layers where either stretched or compressed CNTs dominate.

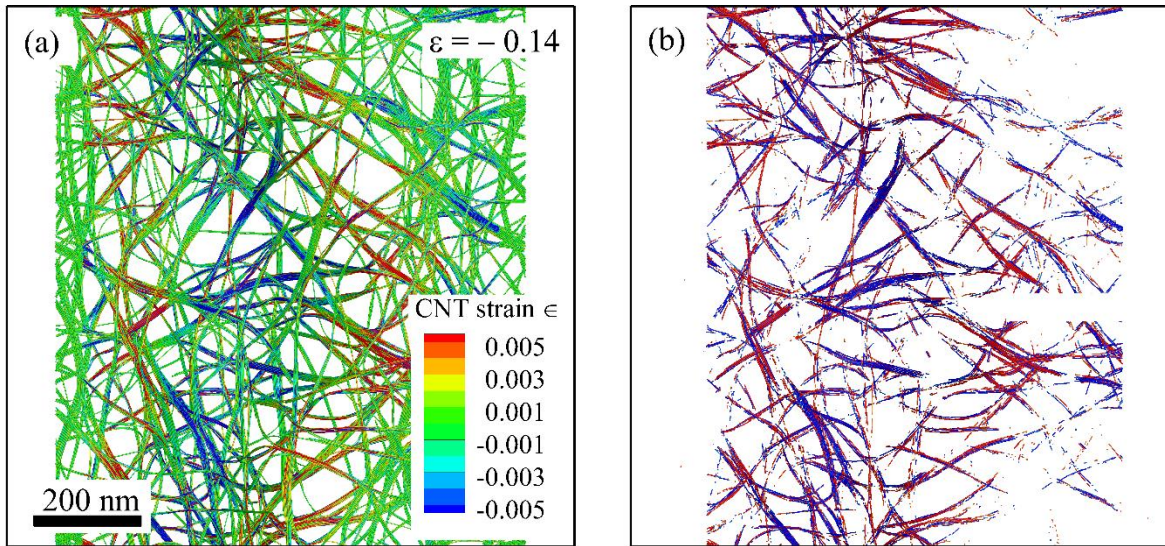


Figure 4.27. Top views of the CNT film after compression at an engineering strain of -0.14. Individual CNT are colored according to their local strain ϵ . Both (a) and (b) show the same sample, but in (b) all CNT segments where $|\epsilon| \leq 0.004$ are blanked. Black rectangles mark boundaries of the non-deformed sample.

The formation of these layers is explained by the collective buckling of bundles in the film. During an initial stage of compression, the bending deformation of individual bundles is uncorrelated (Figure 4.28(a)). The collective bending of bundles evolves gradually (Figure 4.28(b) and (c)) and result in the formation of apparent depressions and bumps spanning the hole film in the direction perpendicular to the direction of deformation (vertical direction in Figure 4.28) after about 10 % of strain (Figure 4.28 (d)). At an engineering strain of -0.14 (Figure 4.28 (e)), the difference between minimum and maximum surface heights at one side of the film

reaches 127 nm. This process resembles wrinkling of a thin CNT films on a polymer substrate [137]. In simulations, however, the collective bending of CNT in a free-standing film is observed. In this regard, the micromechanics of collective effects in simulations of this work can share common features with the collective buckling of forests of vertically aligned CNT arrays under compressive load [151,152].

Energetically, gradually increasing degree of bending of CNTs results in much larger increase of the bending energy of nanotubes during compression compared to stretching (cyan curves in Figure 4.29 and Figure 4.5). During compression, the stretching energy monotonously increases and reaches its maximum only at $\varepsilon \approx -0.14$, although the maximum values of U_{str} during stretching and compression are about the same. Relatively small variation of the van der Waals energy during compression is in agreement with the previous conclusion that the bundle size distribution in the film does not exhibit pronounced changes in the course of compression. The magnitude of the CL energy during compression decreases much slower than during stretching.

At compression, the stresses inside the film are initially developed due to compression of nanotubes, which results in the raise of the absolute value of stress up to a maximum of ~ 20 MPa at a strain of -0.01 (Figure 4.30(a)). This maximum stress is about three times smaller than the maximum stress during stretching of the same film (Figure 4.7(a)). The compression also induces bending of individual nanotubes and bundles. The bending of bundle becomes dominant at further compression of the film, when increasing deformation increases the degree of nanotube bending and the absolute stress decreases.

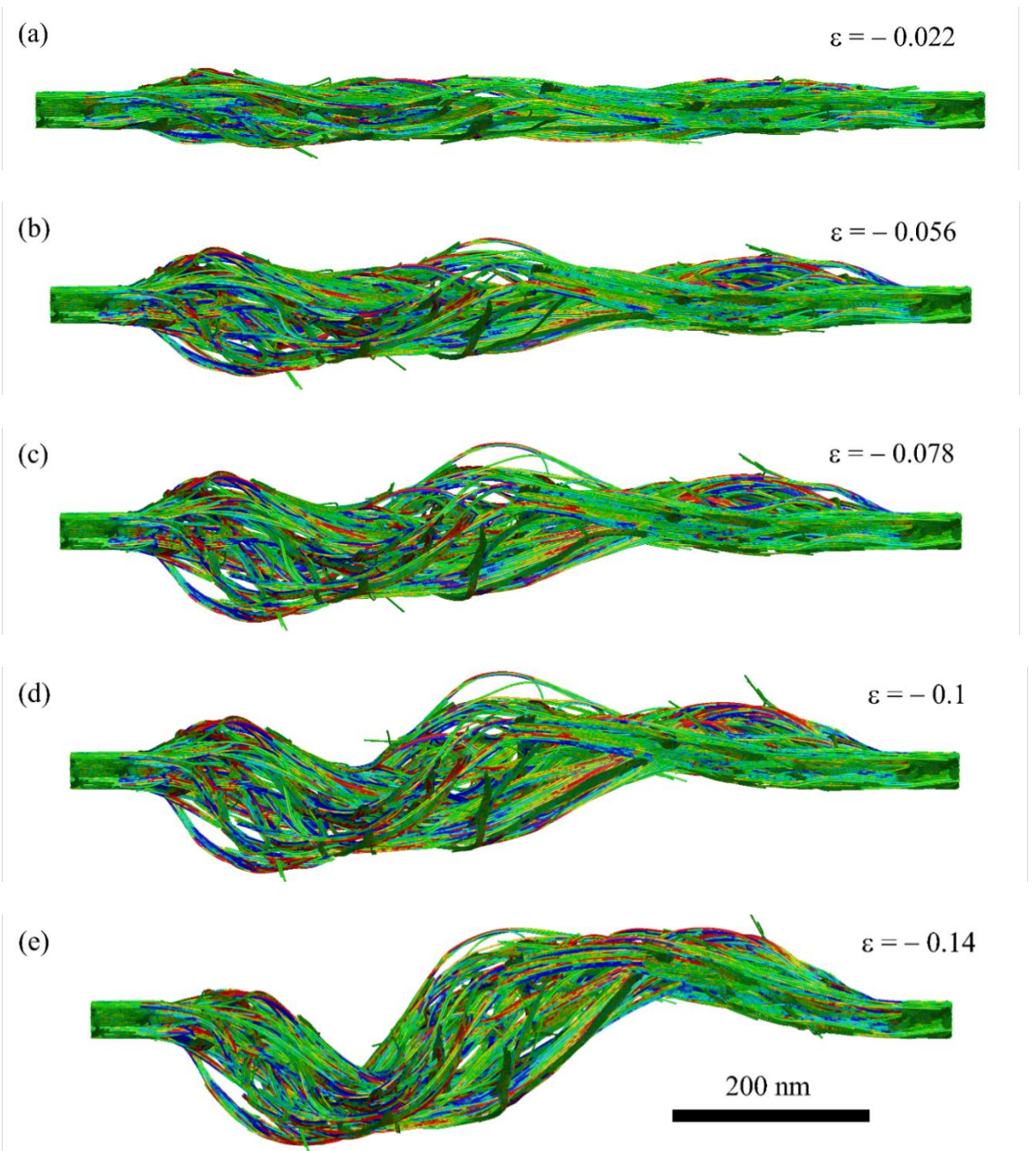


Figure 4.28. Side views of the CNT film in the course of compression in the in-plane (horizontal) direction at various strains: (a), $\varepsilon = -0.033$; (b), $\varepsilon = -0.056$; (c), $\varepsilon = -0.078$; (d), $\varepsilon = -0.1$; and (e), $\varepsilon = -0.14$. Individual CNTs are colored according to the local CNT strain with the color table given in Figure 4.27(a).

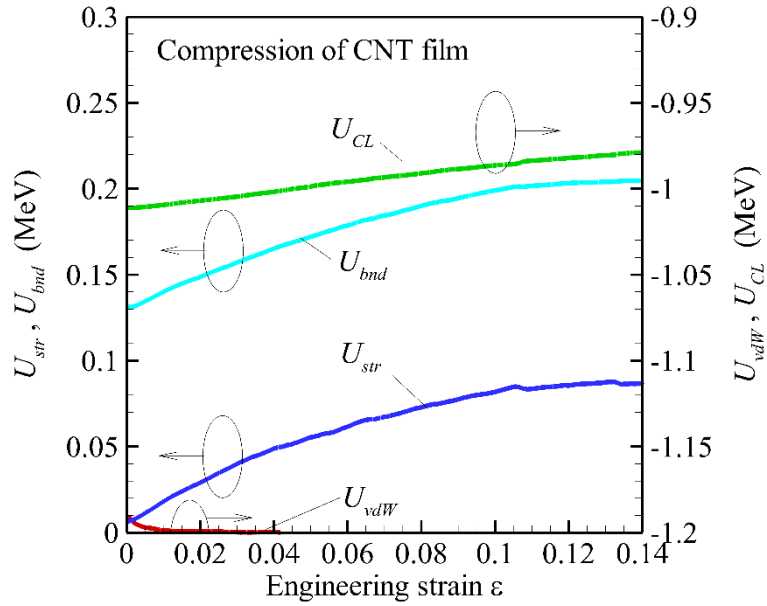


Figure 4.29. Total energies of stretching U_{str} , bending U_{bnd} , van der Waals interaction U_{vdW} , and CL U_{CL} versus engineering strain ϵ obtained during compression simulation of the CNT film.

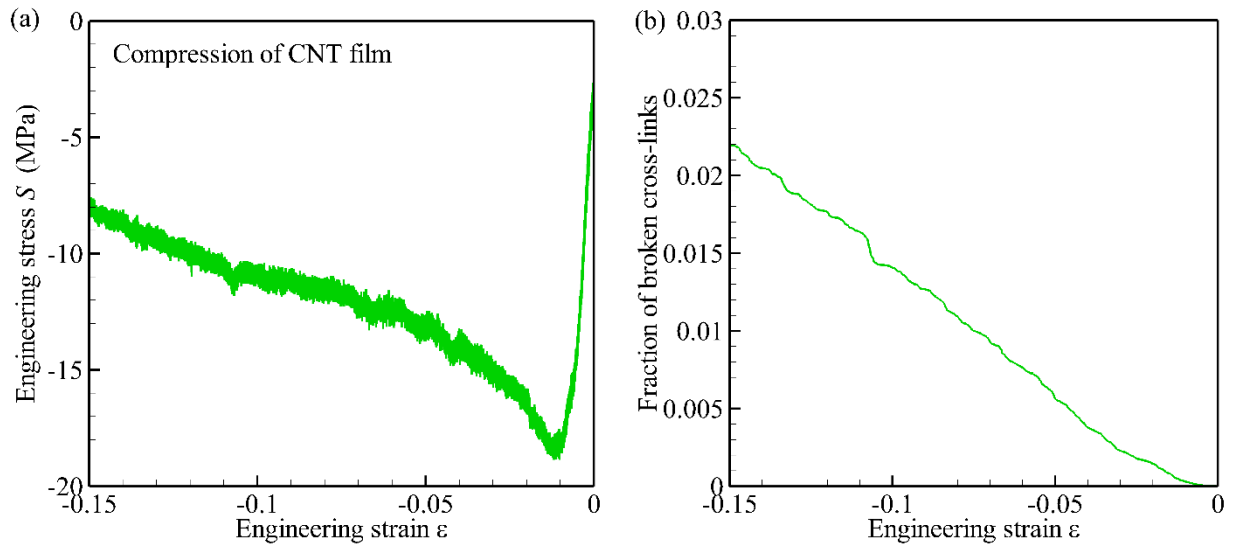


Figure 4.30. Engineering stress S (a) and fraction of broken CLs (b) versus engineering strain ϵ obtained during stretching simulations of the CNT film.

The number of broken CLs increases almost linearly with strain, but the rate of CL breaking is about three times smaller than in the case of stretching (Figure 4.30(b)). It suggests smaller effects of non-reversible deformation during compression than during stretching.

The mesoscopic simulations in this work produce compression results, e.g. mode of deformation, that are independent of sample size, and agree with the experimental observation of wrinkling of CNT membranes under compression (Figure 4.31). The typical wavelength and relief height of compressed films in mesoscopic simulations are $1\ \mu\text{m}$ and $230\ \text{nm}$, respectively, which are similar to observed values in experiment [137].

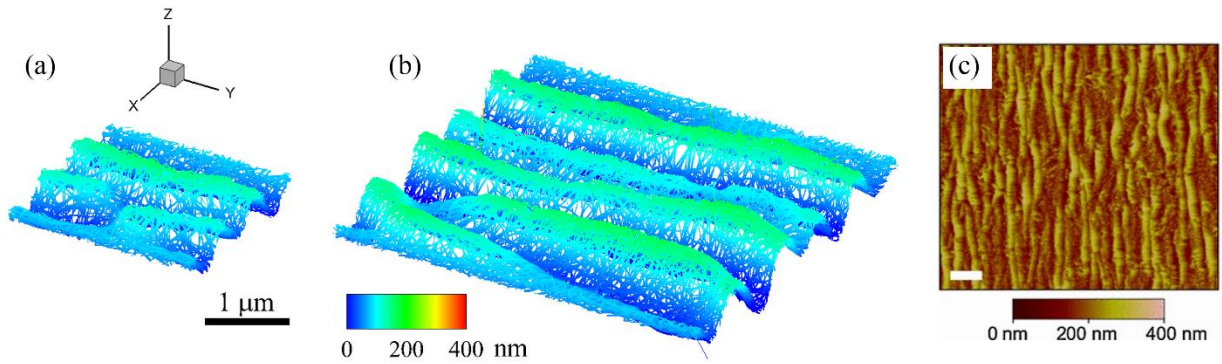


Figure 4.31. (a)-(b) Three-dimensional views of (26,0) CNT films with nanotube length $L_T = 1000\ \text{nm}$, film thickness $H = 40\ \text{nm}$, material density $\rho = 0.1\ \text{gcm}^{-3}$, lateral sample size $L = 2.5\ \mu\text{m}$ (a) and $5\ \mu\text{m}$ (b) at a CL density $n_{CL} = 0.05\ \text{nm}^{-1}$ compressed in the in-plane direction to a strain of $\varepsilon = -0.04$. In all panels, individual nanotubes are colored according to their height (coordinate z in panel (a) and (b)). (c) AFM images (top view) of wrinkling of CNT membrane at sample strain $\varepsilon = -0.05$. The scale in panel (c) is $5\ \mu\text{m}$. Picture in panel (c) is taken from Ref. [137].

Various modes of compression depending on physical parameters, e.g., CNT length L_T , average bundle-size $\langle N_B \rangle$, are studied in large-scale compression simulations with lateral sample

size $L = 2.5 \mu\text{m}$, film thickness $H = 40 \text{ nm}$ and material density $\rho = 0.1 \text{ gcm}^{-3}$, and are discussed in the following section.

4.9 Effects of Nanotube Length and Network Morphology on the Compression Modes

At a fixed CL density, films with various CNT lengths demonstrate similar response to the applied compressive deformation in terms of the magnitude of stress, but the deformation can proceed through the formation of different surface landscapes. The discussion of computational results is focused in this section, therefore, on the effect of the CNT length and network structure on the qualitative picture of compressive deformation. Under all conditions considered in simulation, the films deform at compression through collective bending of nearby bundles which leads to collective folding of the whole films (Figure 4.32 and Figure 4.33). Here, CLs prohibit relative sliding of nanotubes without inducing significant strains inside CNTs. The simulations show that small amount of CLs can induce collective bending of bundles and folding of the films, as the degree of cross-linking f_{CL} for the samples considered in Figure 4.32 and Figure 4.33 is equal to $2.05 \cdot 10^{-4}$. These results also suggest that the collective folding of the CNT films at compression can be observed also without CLs, when a small fraction of nanotubes with defective atomic structures or bending buckling kinks, [67] as well as impurities, e.g., residual metal nanoparticle, can serve as obstacles for the inter-tube sliding.

The formation of a wavy pattern and folding explains a reduced resistance of thin films to compression compared to tension. At the smallest CL density, $n_{CL} = 0.05 \text{ nm}^{-1}$, the film wrinkles form a complex two dimensional landscape in a case of a film composed of short, 200 nm long nanotubes Figure 4.32(a) and Figure 4.33(a), when positions of individual bumps and depressions are not correlated along the direction perpendicular to the direction of applied deformation (y direction in Figure 4.32).

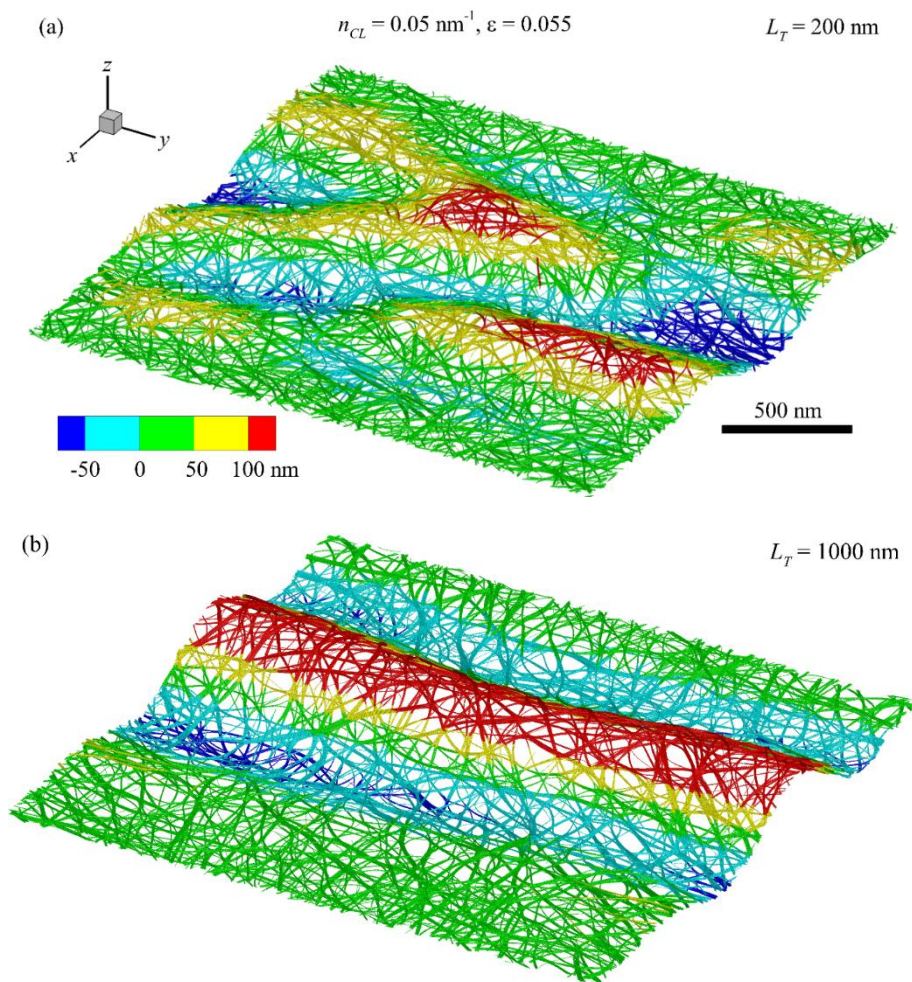


Figure 4.32. Three-dimensional views of CNT films with a nanotube length $L_T = 200 \text{ nm}$ (sample CN200, a) and $L_T = 1000 \text{ nm}$ (sample CN1000 b) at a CL density $n_{CL} = 0.05 \text{ nm}^{-1}$ compressed along x direction to a strain of $\varepsilon = -0.055$. The individual nanotubes are colored according to the height (coordinate z) that is counted from the bottom of the non-deformed films.

For films composed of longer nanotubes, the compression results in the formation of a nearly perfect one-dimensional wavy pattern of bumps and depression (see Figure 4.32(b) and Figure

4.33(b)-(c)). The maximum height of the landscape h (the difference between the height of top film surface at the tallest bump and deepest depression) is practically independent of the CNT length. For all films shown in Figure 4.33, h varies in the range of 210 – 230 nm. In the range of compressive strains considered in simulations of this work, this process is practically reversible, since it is accompanied with small rates of CL breaking (Figure 4.34(a)) and bundling of nanotubes (Figure 4.34(b)). Moreover, the rates of CL breaking and bundling strongly decrease after a short initial stage of compression, when the strain $|\varepsilon|$ becomes larger than 0.01. The compression simulations of films at $n_{CL} = 0.5 \text{ nm}^{-1}$ show that the compression proceeds through the correlated bending of the whole film and formation of one-dimensional wavy pattern independently of the CNT length.

The compression of the film with random distribution of CNT lengths also results in the correlated bending of the whole film (Figure 4.33(d)). It indicates that the response of the CNT films to compression depends on the length of nanotubes that form the scaffold of large bundles, while the presence of large number of relatively short nanotubes does not affect the regime of compressive deformation. In the sample CNW considered in Figure 4.33(d), the scaffold of the network is formed by relatively long nanotubes (the average CNT length is equal to 620 nm), so that the pattern of the compressed films is similar to the patterns of films composed of constant-length nanotubes with $L_T \geq 400 \text{ nm}$.

With increasing strain, the surface landscape of the compressed film composed of short 200 nm long CNT changes from two-dimensional to one-dimensional with individual bumps and depression spanning the whole sample along y direction in Figure 4.35. The maximum height of the landscape h increases roughly proportionally to strain and reaches 390 nm at $\varepsilon = -0.125$ for the sample CN200.

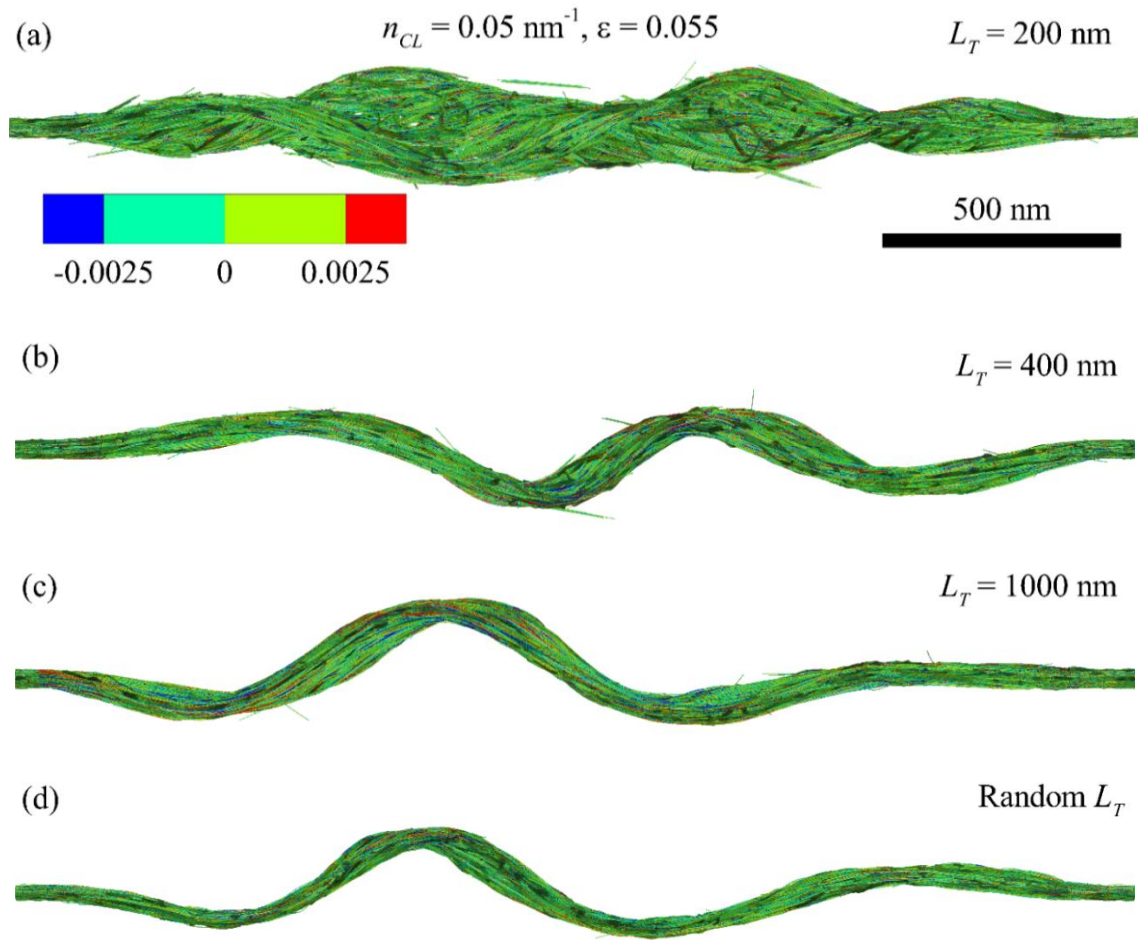


Figure 4.33. Side views of CNT films after in-plane compression at a strain of $\varepsilon = -0.055$ for various nanotube length: $L_T = 200 \text{ nm}$ (sample CN200, a), $L_T = 400 \text{ nm}$ (sample CN400, b), $L_T = 1000 \text{ nm}$ (sample CN1000, c), and random Weibull distribution of L_T , Eq. (3.1), with $b = 2.08$ and $a = 430 \text{ nm}$ (sample CNW, d). The CL density is equal to $n_{CL} = 0.05 \text{ nm}^{-1}$. The individual nanotubes are colored according to their local strain ε and color table shown in panel (a). Panels (a) and (c) corresponds to the films shown in Figure 4.32(a) and (b), respectively.

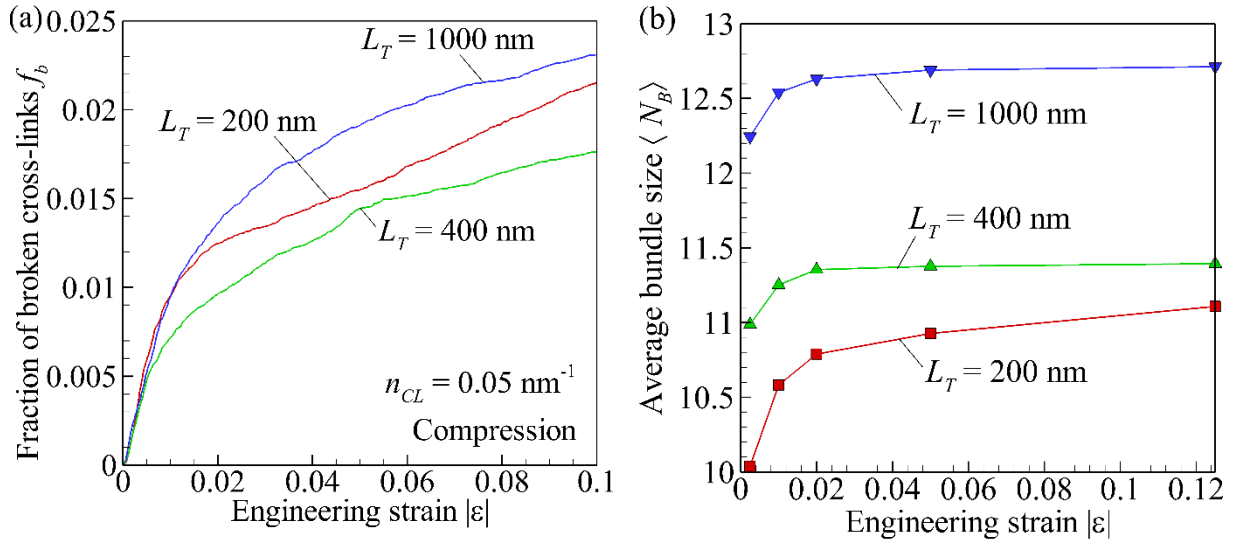


Figure 4.34. Fraction of broken CLs f_b (a) and average bundle size $\langle N_B \rangle$ (b) versus engineering strain $|\epsilon|$ obtained at compression of CNT films with continuous networks of bundles at a CL density $n_{CL} = 0.05 \text{ nm}^{-1}$ and CNT length $L_T = 200$ nm (sample CNT200, red curves and squares), $L_T = 400$ nm (sample CN400, green curves and triangles), and $L_T = 1000$ nm (sample CN1000, blue curves and gradients). In panel (b), the symbols correspond to calculated values, while the curves are drawn only to guide the eye.

A similar increase in the relief height without breaking the network structure is observed for other samples composed of longer nanotubes. The compression simulation of the films with a network of dispersed nanotubes always result in the one-dimensional wavy pattern independently of the CNT length. The surface landscapes of the folded films composed of dispersed nanotubes are quantitatively close to the film with the network of bundles composed of long nanotubes and shown in Figure 4.32(b) and Figure 4.33(c). These results indicate that the degree of connectivity of the network is the key factor that affects the regime of compressive deformation of thin cross-linked CNT films.

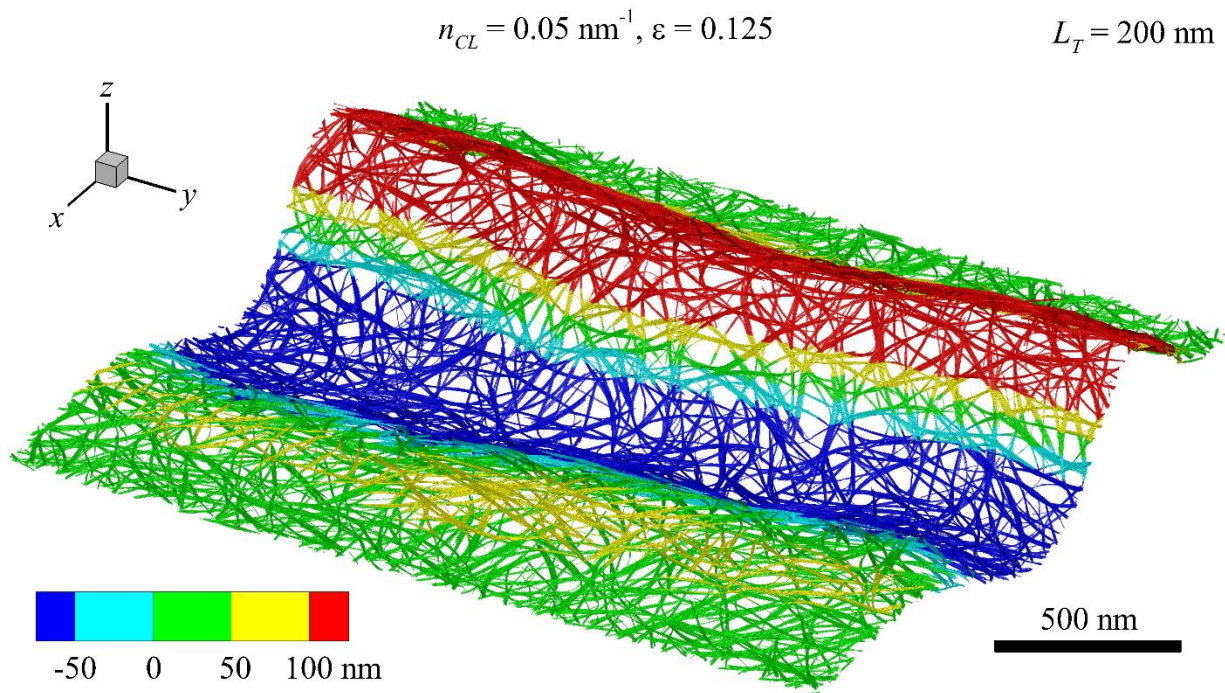


Figure 4.35. Three-dimensional view of the CNT film with a nanotube length $L_T = 200 \text{ nm}$ (sample CN200) at a CL density $n_{CL} = 0.05 \text{ nm}^{-1}$ compressed along x direction to a strain $\varepsilon = -0.125$. Individual nanotubes are colored according to the height (coordinate z) that is counted from the bottom of the non-deformed film.

The picture of compressive deformation of the free-standing films obtained in mesoscopic simulations resembles the experimentally observed wrinkling or folding of thin CNT films on a polymer substrate [137]. The experiments reveal hierarchical folding of films, when the surface landscape is a superposition of multiple harmonics with progressively decreasing length scales. At $\varepsilon = -0.05$, the maximum relief height is equal to $\sim 200 \text{ nm}$, when the wavelength of the dominant wrinkling mode is larger than $\sim 2 \mu\text{m}$ [153]. Simulations predict the single-mode deformation with practically the same maximum relief height equal to 210 - 230 nm

and twice smaller wavelength equal to $\sim 1 \mu\text{m}$ at $\varepsilon = -0.055$. The simulation results, however, are not expected to ideally coincide with the experimental results in Ref. [137] as the simulations are performed for free-standing films with somewhat different physical properties. Since the wavelength of the wrinkling mode in simulation is about a half of the sample size, it is believed that the samples of larger size are necessary to capture the wrinkling modes with the largest wavelength.

CHAPTER 5

CONCLUSIONS

5.1 Summary of Results Obtained in the Present Study

The mesoscopic model for cross-linked CNT network material presented in this work is based on a coarse-grained description of the dynamic behavior of CNTs along with a model of covalent bond or CLs between CNTs. The mesoscopic CL is developed to describes load transfer between CNTs through individual covalent CLs. Contrary to majority of the mesoscopic models in literature, the developed CL model in this work accounts for both tangential and normal CL force and can simulate the effect of CLs on the variation of inter-tube gaps. In the CL model, the energy of individual CL is described by Morse potential as a function of the CL bond length. Two geometric bond models are developed to evaluate length of individual CLs. After proper parameterization, both models predict quantitatively similar results in terms of mechanical properties of large scale stretching and compression simulations of cross-linked films. The developed mesoscopic CL model is proved computationally effective, robust and can be implemented for general mesoscopic computer code.

A general approach to parameterize the CL model is developed and applied to find best-fit parameters based on the results of atomistic simulations of pulling out a central tube from a seven-tube cross-linked bundle. For this purpose, an intermediate “bundle model” is developed,

which predicts both normal and shear load transfers in cross-linked CNT bundles. The results obtained with the general mesoscopic and specific bundle models in simulations of the pullout test are in a good agreement with each other, suggesting that multiple simplifying assumptions adopted in the bundle model are insignificant and, thus, the bundle model can be effectively used for accurate parameterization of the mesoscopic CL model. The best-fit parameters of the mesoscopic CL model are strikingly different for relatively low and high CL densities. It suggests strong collective or crowding effects between CLs at large density and independent performance of CLs at small density.

Although in the present study the effective bond model is used only for bundles and films composed of (26,0) and (10,10) nanotubes, this model can be used for much broader class of material systems. The model can be used for materials composed of various single- and multi-walled CNTs, if the results of atomistic simulations of the pullout test are available and allow one to find the model parameters. Besides CLs formed by interstitial carbon atoms, the model can be also presumably applied in a case, when CLs are induced by means of chemical functionalization of CNTs. The developed model can be also straightforwardly applied to describe the load transfer via CLs between CNT and polymer material in nanocomposites with polymer matrix and CNT reinforcement. In this case, the bundle model can be re-designed for parametrization of the effective bond model based on result of the pullout simulation of an individual nanotube from a bulk polymer. The bundle model can be also used to predict the transient effects of dynamic breaking and reformation of CLs in the sliding regime. Finally, the large-scale mesoscopic simulations of cross-linked CNT films can be extended to other types of CNT-based materials, including CNT fibers, vertically aligned arrays, and aerogels, as well as corresponding composite materials.

The *in silico* CNT fibers and cross-linked CNT films sample of varying material density, CL density, nanotube length are generate and equilibrated. The structures of the *in silico* generated fibers and films are characterized in terms of the bundle size distribution, average and maximum bundle sizes, the magnitude of the Herman orientation factor, the average tilt of CNT segments with respect to the direction of nanotube alignment in the fiber structures, and the average tortuosity of the nanotubes. The structural parameters of the computational samples are compared with available experimental data and the ability of the developed computational procedure to produce structures closely matching those observed in experiments is demonstrated. Moreover, the structural parameters of the computational fiber samples are found to exhibit a nearly linear dependence on the maximum angle of the initial inclination of nanotubes with respect to the direction of CNT alignment, thus providing an opportunity to precisely engineer the microstructure of computational fiber samples to match those of particular experimental materials of interest. Equilibration times of high and low temperature self-assembly of CNT films also found to be a potential method to generate in-silico CNT sample of desired morphology.

Free-standing film sample is subjected to quasi-static stretching and compression simulations to reveal mechanisms of deformation and load transfer in cross-linked CNT films. It is found that stretching of nanotube segments is the dominant mode of load transfer in cross-linked CNT film sample during stretching, while bending and buckling of nanotubes is the dominant mode of load-transfer during compression. Mechanical load is found to be transmitted through local structures inside the sample that looks like force chain observed in granular materials. In a cross-linked film, nanotubes and bundles are inter-connected through CLs. Such interconnected nanotubes and bundles form percolating load transfer networks throughout the

sample, which work as a mean to transfer load along the sample boundary. The observed modulus and strength of the film materials in simulations agree with values from experiment.

In simulations, two types of the films with different morphology of the underlying network of nanotubes are considered, namely, the films with continuous networks of bundles of nanotubes, which are obtained in preliminary dynamic simulations of spontaneous self-assembly of nanotubes driven by van der Waals interactions, and the films consisting of intentionally dispersed nanotubes, where CLs preclude formation of bundles. The simulations reveal strong effects of the nanotube length and CL density on the load transfer and mechanical properties. The tensile modulus and strength, in particular, increase with increasing CNT length and CL density. The average number of CLs per nanotube is the primary parameter that controls the elastic and inelastic properties of CNT films at tension. The values of the tensile modulus and strength obtained in the mesoscopic simulations tend to follow to the power-type scaling laws depending on the average number of CLs per CNT. The exponents in the scaling laws for the modulus and strength are strongly different from each other. The dispersion of nanotubes in the films without formation of thick bundles can increase the modulus and strength from a few times to an order of magnitude.

The structural and mechanical properties of a CNT film with random distribution of the nanotube length are found to be only moderately different from the corresponding properties for a film, where all CNTs have a constant length equal to the mean value of random nanotube lengths. The tension of cross-linked CNT films is accompanied by strong irreversible structural changes associated with breaking of CLs, and to a small extent, with de-bundling. As a result, the elastic limit of the in silico generated films is found to be small and corresponds to a strain of ~ 0.005 . These findings are explained by the effect of CNT length, CL density, and dispersion of

nanotubes on the degree of connectivity of the load transfer network that appears in cross-linked CNT films in response to applied deformation. It is found that the material density of the film has a weak effect on the specific mechanical properties, which are mainly determined by tube length and CLs density.

The simulations reveal the collective bending of bundles in CNT films under in-plane compression, which leads to folding of the whole films. The surface landscape of the compressed films depends on the CNT length. For films composed of short nanotubes and at moderate compressive strains, the landscape represents a complex two-dimensional surface pattern of bumps and depressions. The films composed of long nanotubes are folded into a one-dimensional structure, where bumps and depressions span the whole sample in the direction perpendicular to the deformation direction. The compression of the films induces breaking of relatively small fraction of CLs. The process of bundling of nanotubes occurs only during an initial stage of the deformation when the absolute strain does not exceed 0.02. At larger strains, the folding of the films composed of relatively long nanotubes is found to be a practically reversible process.

5.2 Directions for Future Research

The current implementation of the mesoscopic force field does not account dynamic friction between sliding CNTs. To study unsteady dynamic loading in CNT bulk materials, dynamic friction between sliding nanotubes need to be accounted. Based on the literature data, an appropriate model for dynamic friction between CNTs can be adopted and parameterized.

The mesoscopic model, where the dynamic friction is accounted for, can be applied to investigate multiple unsteady phenomena in CNT materials. For example, such model can be used to characterize the acoustic wave propagation in cross-linked CNT materials subjected to deformation disturbance in the form of a longitudinal wave induced by moving the sample

boundary by a deformation function with predefined period and amplitude. The understanding of mechanism of acoustic wave propagation and characterization in CNT materials is important in term of its application as actuators and sensors and many other practical situations of cyclic loading.

REFERENCES

- [1] N. Hamada, S. Sawada, A. Oshiyama, New one-dimensional conductors: Graphitic microtubules, *Phys. Rev. Lett.* 68, 1579 (1992).
- [2] R.A. Jishi, L. Venkataraman, M.S. Dresselhaus, G. Dresselhaus, Symmetry properties of chiral carbon nanotubes, *Phys. Rev. B* 51, 11176 (1995).
- [3] S. Iijima, Helical microtubules of graphitic carbon, *Nature* 354, 56–58 (1991).
- [4] M.M.J. Treacy, T.W. Ebbesen, J.M. Gibson, Exceptionally high Young's modulus observed for individual carbon nanotubes, *Nature* 381, 678–680 (1996).
- [5] J.P. Lu, Elastic properties of carbon nanotubes and nanoropes, *Phys. Rev. Lett.* 79, 1297–1300 (1997).
- [6] A. Krishnan, E. Dujardin, T.W. Ebbesen, P.N. Yianilos, M.M.J. Treacy, Young's modulus of single-walled nanotubes, *Phys. Rev. B* 58, 14013–14019 (1998).
- [7] D. Sánchez-Portal, E. Artacho, J.M. Soler, A. Rubio, P. Ordejón, Ab initio structural, elastic, and vibrational properties of carbon nanotubes, *Phys. Rev. B* 59, 12678–12688 (1999).
- [8] J.-P. Salvetat, G.A.D. Briggs, J.-M. Bonard, R.R. Basca, A.J. Kulik, T. Stöckli, N.A. Burnham, L. Forró, Elastic and shear moduli of single-walled carbon nanotube ropes, *Phys. Rev. Lett.* 82, 944–947 (1999).
- [9] M.-F. Yu, B.S. Files, S. Arepalli, R.S. Ruoff, Tensile loading of ropes of single wall carbon nanotubes and their mechanical properties, *Phys. Rev. Lett.* 84, 5552–5555 (2000).
- [10] M.-F. Yu, O. Lourie, M.J. Dyer, K. Moloni, T.F. Kelly, R.S. Ruoff, Strength and breaking mechanism of multiwalled carbon nanotubes under tensile load, *Science* 287, 637–640 (2000).
- [11] X. Gui, A. Cao, J. Wei, H. Li, Y. Jia, Z. Li, L. Fan, K. Wang, H. Zhu, D. Wu, Soft, Highly Conductive Nanotube Sponges and Composites with Controlled Compressibility, *ACS Nano* 4, 2320-2326 (2010).
- [12] J. Zou, J. Liu, A.S. Karakoti, A. Kumar, D. Joung, Q. Li, S.I. Khondaker, S. Seal, L. Zhai, Ultralight Multiwalled Carbon Nanotube Aerogel, *ACS Nano* 4, 7293-7302 (2010).
- [13] T.V. Sreekumar, T. Liu, S. Kumar, L.M. Ericson, R.H. Hauge, R.E. Smalley, Single-Wall Carbon Nanotube Films, *Chem. Mater.* 15, 175-178 (2003).
- [14] F. Hennrich, S. Lebedkin, S. Malik, J. Tracy, M. Barczewski, H. Rosner, M. Kappes, Preparation, characterization and applications of free-standing single walled carbon nanotube thin films, *PCCP* 4, 2273-2277 (2002).
- [15] H. Muramatsu, T. Hayashi, Y.A. Kim, D. Shimamoto, Y.J. Kim, K. Tantrakarn, M. Endo, M. Terrones, M.S. Dresselhaus, Pore structure and oxidation stability of double-walled carbon nanotube-derived bucky paper, *Chem. Phys. Lett.* 414, 444-448 (2005).

-
- [16] W. Ma, L. Song, R. Yang, T. Zhang, Y. Zhao, L. Sun, Y. Ren, D. Liu, L. Liu, J. Shen, Z. Zhang, Y. Xiang, W. Zhou, S. Xie, Directly Synthesized Strong, Highly Conducting, Transparent Single-Walled Carbon Nanotube Films, *Nano Lett.* 7, 2307-2311 (2007).
- [17] M. Xu, D.N. Futaba, M. Yumura, K. Hata, Alignment Control of Carbon Nanotube Forest from Random to Nearly Perfectly Aligned by Utilizing the Crowding Effect, *ACS Nano* 6, 5837-5844 (2012).
- [18] D.N. Futaba, K. Hata, T. Yamada, T. Hiraoka, Y. Hayamizu, Y. Kakudate, O. Tanaike, H. Hatori, M. Yumura, S. Iijima, Shape-engineerable and highly densely packed single-walled carbon nanotubes and their application as super-capacitor electrodes, *Nat. Mater.* 5, 987-994 (2006).
- [19] Z. Wang, Z. Liang, B. Wang, C. Zhang, L. Kramer, Processing and property investigation of single-walled carbon nanotube (SWNT) buckypaper/epoxy resin matrix nanocomposites, *Composites Part A: Applied Science and Manufacturing* 35, 1225-1232 (2004).
- [20] R.L.D. Whitby, T. Fukuda, T. Maekawa, S.L. James, S.V. Mikhalovsky, Geometric control and tuneable pore size distribution of buckypaper and buckydiscs, *Carbon* 46, 949-956 (2008).
- [21] P. Poulin, B. Vigolo, P. Launois, Films and fibers of oriented single wall nanotubes, *Carbon* 40, 1741-1749 (2002).
- [22] X. Zhang, K. Jiang, C. Feng, P. Liu, L. Zhang, J. Kong, T. Zhang, Q. Li, S. Fan, Spinning and Processing Continuous Yarns from 4-Inch Wafer Scale Super-Aligned Carbon Nanotube Arrays, *Adv. Mater.* 18, 1505-1510 (2006).
- [23] N. Behabtu, C.C. Young, D.E. Tsentelovich, O. Kleinerman, X. Wang, A.W.K. Ma, E.A. Bengio, R.F. ter Waarbeek, J.J. de Jong, R.E. Hoogerwerf, S.B. Fairchild, J.B. Ferguson, B. Maruyama, J. Kono, Y. Talmon, Y. Cohen, M.J. Otto, M. Pasquali, Strong, Light, Multifunctional Fibers of Carbon Nanotubes with Ultrahigh Conductivity, *Science* 339, 182 (2013).
- [24] L. Zhang, G. Zhang, C. Liu, S. Fan, High-Density Carbon Nanotube Buckypapers with Superior Transport and Mechanical Properties, *Nano Lett.* 12, 4848-4852 (2012).
- [25] E. Mayhew, V. Prakash, Thermal conductivity of high performance carbon nanotube yarn-like fibers, *J. of App. Phys.* 115, 174306 (2014).
- [26] <https://www.compositesworld.com/articles/the-end-of-delamination>
- [27] M. Kalbacova, M. Kalbac, L. Dunsch, U. Hempel, Influence of single-walled carbon nanotube films on metabolic activity and adherence of human osteoblasts, *Carbon*, vol. 45, Issue II, 2266-2272 (2007).
- [28] Mylvaganam, K., Zhang, L-C., Ballistic resistance capacity of carbon nanotubes, *Nanotechnology* 18, 475701 (2007).
- [29] M. D. Lima, M. W. Hussain, G. M. Spinks, S. Naficy, D. Hagenasr, J. S. Bykova, D. Tolly, R. H. Baughman, Efficient, absorption-powered artificial muscles based on carbon nanotube hybrid yarns, *Small* 11, 3113-3118 (2015).
- [30] P. Avouris, Z. Chen, and V. Perebeinos, Carbon-based electronics, *Nature Nanotechnology* 2 605–615 (2007).

-
- [31] Y. Fu, N. Nabiollahi, T. Wang, S. Wang, Z. Hu, B. Carlberg, Y. Zhang, X. Wang, and J. Liu, A complete carbon-nanotube-based on-chip cooling solution with very high heat dissipation capacity, *Nanotechnology* 23, 045304 (2012).
- [32] S. Kaur, N. Raravikar, B. A. Helms, R. Prasher, and D. F. Ogletree, Enhanced thermal transport at covalently functionalized carbon nanotube array interfaces, *Nature Communications* 5, 3082 (2014).
- [33] H. Wang, A. S. Tazebay, G. Yang, H. T. Lin, W. Choi, and C. Yu, Highly deformable thermal interface materials enabled by covalently-bonded carbon nanotubes, *Carbon* 106, 152-157 (2016).
- [34] S. L. Kim, K. Choi, A. Tazebay, and C. Yu, Flexible power fabrics made of carbon nanotubes for harvesting thermoelectricity, *ACS Nano* 8, 2377–2386 (2014).
- [35] S. Park, M. Vosguerichian, and Z. Bao, A review of fabrication and applications of carbon nanotube film-based flexible electronics, *Nanoscale* 5, 1727-1752 (2013).
- [36] N. Akizuki, S. Aota, S. Mouri, K. Matsuda, and Y. Miyauchi, Efficient near-infrared up-conversion photoluminescence in carbon nanotubes. *Nature Communications* 6, 8920 (2015).
- [37] L. V. Titova, C. L. Pint, Q. Zhang, R. H. Hauge, J. Kono, and F. A. Hegmann, Generation of terahertz radiation by optical excitation of aligned carbon nanotubes, *Nano Lett.* 15, 3267–3272 (2015).
- [38] Q. Cao and J. A. Rogers, Ultrathin films of single-walled carbon nanotubes for electronics and sensors: A review of fundamental and applied aspects, *Adv. Mater.* 21, 29-53 (2009).
- [39] C. Peng, S. Zhang, D. Jewell, G. Z. Chen, Carbon nanotube and conducting polymer composites for supercapacitors, *Prog. In Nat. Sci.*, 18(7), 777-788, (2008).
- [40] G. S. Tulevski, A. D. Franklin, D. Frank, J. M. Lobe, Q. Cao, H. Park, A. Afzali, S.-J. Han, J. B. Hannon, and W. Haensch, Toward high-performance digital logic technology with carbon nanotubes, *ACS Nano*, 8, 9, 8730-8745 (2014).
- [41] W. Ma, L. Song, R. Yang, T. Zhang, Y. Zhao, L. Sun, Y. Ren, D. Liu, L. Liu, J. Shen, Z. Zhang, Y. Xiang, W. Zhou, and S. Xie, Directly synthesized strong, highly conducting, transparent single-walled carbon nanotube films, *Nano Lett.* 7, 2307-2311 (2007).
- [42] M. R. Falvo, R. M. Taylor II, A. Helsen, V. Chi, F. P. Brooks Jr, S. Washburn, and R. Superfine, Nanometre-scale rolling and sliding of carbon nanotubes, *Nature* 397, 236-238 (1999).
- [43] S.-H. Syue, S.-Y. Lu, W.-K. Hsu, and H.-C. Shih, Internanotube friction, *Appl. Phys. Lett.* 89, 163115 (2006).
- [44] O. Suekane, A. Nagataki, H. Mori, and Y. Nakayama, Static friction force of carbon nanotube surfaces, *Appl. Phys. Express* 1, 064001 (2008).
- [45] B. Bhushan and X. Ling, Adhesion and friction between individual carbon nanotubes measured using force-versus-distance curves in atomic force microscopy, *Phys. Rev. B* 78, 045429 (2008).

-
- [46] B. Bhushan, Nanotribology of carbon nanotubes, *J. Phys.: Condens. Matter* 20, 365214 (2008).
- [47] M. F. L. De Volder, S. H. Tawfick, R. H. Baughman, and A. J. Hart, Carbon nanotubes: Present and future commercial applications, *Science* 339, 535-539 (2013).
- [48] A. Kis, G. Csanyi, J.-P. Salvetat, T.-N. Lee, E. Couteau, A.J. Kulik, W. Benoit, J. Brugger, and L. Forro, Reinforcement of single-walled carbon nanotube bundles by intertube bridging, *Nat. Materl.* 3, 153-157 (2004).
- [49] P. Poulin, B. Vigolo, and P. Launois, Films and fibers of oriented single wall nanotubes, *Carbon* 40 1741-1749 (2002).
- [50] T. V. Sreekumar, T. Liu, S. Kumar, L. M. Ericson, R. H. Hauge, and R. E. Smalley, Single-wall carbon nanotube films, *Chem. Mater.* 15, 175-178 (2013).
- [51] S. Malik, H. Rösner, F. Hennrich, A. Böttcher, M. M. Kappes, T. Beck, and M. Auhorn, Failure mechanism of free standing single-walled carbon nanotube thin films under tensile load, *Phys. Chem. Chem. Phys.* 6, 3540-3544 (2004).
- [52] H. Muramatsu, T. Hayashi, Y. A. Kim, D. Shimamoto, Y. J. Kim, K. Tantrakarn, M. Endo, M. Terrones, and M. S. Dresselhaus, Pore structure and oxidation stability of double-walled carbon nanotube-derived bucky paper, *Chem. Phys. Lett.* 414, 444-448 (2005).
- [53] P. G. Whitten, G. M. Spinks, and G. G. Wallace, Mechanical properties of carbon nanotube paper in ionic liquid and aqueous electrolytes, *Carbon* 43, 1891-1896 (2005).
- [54] F. M. Blighe, P. E. Lyons, S. De, W. J. Blau, and J. N. Coleman, On the factors controlling the mechanical properties of nanotube films, *Carbon* 46, 41-47 (2008).
- [55] R. H. Baughman, C. Cui, A. A. Zakhidov, Z. Iqbal, J. N. Barisci, G. M. Spinks, G. G. Wallace, A. Mazzoldi, D. De Rossi, A. G. Rinzler, O. Jaschinski, S. Roth, and M. Kertesz, Carbon nanotube actuator, *Science* 284, 1340-1344 (1999).
- [56] U. Dettlaff-Weglikowska, V. Skákalová, R. Graupner, S. H. Jhang, B. H. Kim, H. J. Lee, L. Ley, Y. W. Park, S. Berber, D. Tománek, and S. Roth, Effect of SOCl₂ treatment on electrical and mechanical properties of single-wall carbon nanotube networks, *J. Am. Chem. Soc.* 127, 5125-5131 (2005).
- [57] S. V. Ahir, E. M. Terentjev, S. X. Lu, and B. Panchapakesan, Thermal fluctuations, stress relaxation, and actuation in carbon nanotube networks, *Phys. Rev. B.* 76, 165437 (2007).
- [58] S. Wang, Z. Liang, B. Wang, and C. Zhang, Statistical characterization of single-wall carbon nanotube length distribution, *Nanotechnology* 17, 634-639 (2006).
- [59] H. Wan, F. Delale, and L. Shen, Effect of CNT length and CNT-matrix interphase in carbon nanotube (CNT) reinforced composites, *Mech. Res. Comm.* 32, 481-489 (2005).
- [60] M. M. Sohkhrieh and R. Rafiee, Investigation of nanotube length effect on reinforcement efficiency in carbon nanotube based composites, *Composite Structures* 92, 2415-2420 (2010).

-
- [61] B. Chen, J. Shen X. Ye, L. Jia, S. Li, J. Umeda, M. Takahashi, and K. Kondoh, Length effect of carbon nanotubes on the strengthening mechanisms in metal matrix composites, *Acta Materialia* 140, 317-325 (2017).
- [62] Y. Li and M. Kröger, A theoretical evaluation of the effects of carbon nanotube entanglement and bundling on the structural and mechanical properties of buckypaper, *Carbon* 50, 1793-1806 (2012).
- [63] H. Chen, L. Zhang, J. Chen, M. Becton, X. Wang, and H. Nie, Effect of CNT length and structural density on viscoelasticity of buckypaper: A coarse-grained molecular dynamics study, *Carbon* 109, 19-29 (2016).
- [64] S. Sakurai, F. Kamada, D. N. Futaba, M. Yumura, and K. Hata, Influence of lengths of millimeter-scale single-walled carbon nanotube on electrical and mechanical properties of buckypaper, *Nanoscale Res. Lett.* 8, 1-7 (2013).
- [65] J. Zhang and D. Jiang, Influence of geometries of multi-walled carbon nanotubes on the pore structures of buckypaper, *Composites Part A* 43, 469-474 (2012).
- [66] A. V. Krasheninnikov, and K. Nordlund, Ion and electron irradiation-induced effects in nanostructured materials, *J. Appl. Phys.* 107, 071301 (2010).
- [67] T. Filleter, H.D. Espinosa, Multi-scale mechanical improvement produced in carbon nanotube fibers by irradiation cross-linking, *Carbon* 56, 1-11 (2013).
- [68] S. Wang, Z. Liang, B. Wang, and C. Zhang, High-strength and multifunctional macroscopic fabric of single-walled carbon nanotubes, *Adv. Mater.* 19, 1257-1261 (2007).
- [69] M. Locascio, B. Peng, P. Zapol, Y. Zhu, S. Li, T. Belytschko, H.D. Espinosa, Tailoring the load carrying capacity of MWCNT through inter-shell atomic bridging, *Exp. Mech.* 49, 169-182 (2009).
- [70] T. Filler, R. Bernal, S. Li, and H.D. Espinosa, Ultrahigh strength and stiffness in cross-linked hierarchical carbon nanotube bundles, *Adv. Mater.* 23, 2855-2860 (2011).
- [71] S. G. Miller, T.S. Williams, J.S. baker, F. Solá, M. Lebron-Colon, L. S. McCorkle, N. G. Wilmoth, J. Gaier, M. Chen, and M. A. Meador, Increased tensile strength of carbon nanotube yarn and sheets through chemical modification and electron beam irradiation, *ACS Appl. Mater. Interfaces* 6, 6120-6126 (2014).
- [72] B. Ni, R. Andrews, D. Jacques, D. Qian, M. B. J. Wijesundara, Y. Choi, L. Hanley, and S. B. Sinnott, A combined computational and experimental study of ion-beam modification of carbon nanotube bundles, *J. Phys. Chem. B* 105, 12719-12725 (2001).
- [73] E. Salonen, A.V. Krasheninnikov, and K. Nordlund, Ion-irradiation-induced defects in bundles of carbon nanotubes, *Nucl. Instr. Meth. Phys. Res. B* 193, 603-608 (2002).
- [74] J.A.V. Pomoell, A. V. Krasheninnikov, K. Nordlund, and J. Keinonen, Ion ranges and irradiation-induced defects in multiwalled carbon nanotubes, *J. Appl. Phys.* 96, 2864-2871 (2004).
- [75] M. A. McCarthy, E. M. Byrne, N. P. O'Brien, and T. Murmu, Improved mechanical performance of CNT and CNT fibers in nanocomposites through inter-wall and inter-tube

-
- coupling, in K. I. Tserpes and N. Silvestre (eds.), *Modelling of Carbon Nanotubes, Graphene and their Composites*, Springer Series in Materials Science 188 (Springer 2014).
- [76] N. P. O'Brien, M. A. McCarthy, W. A. Curtin, Improved inter-tube coupling in CNT bundles through carbon ion irradiation, *Carbon* 51, 173-184 (2013).
- [77] N. P. O'Brien, M. A. McCarthy, W. A. Curtin, A theoretical quantification of the possible improvement in the mechanical properties of carbon nanotube bundles by carbon ion irradiation, *Carbon* 53, 346-356 (2013).
- [78] J. Zhang, D. Jiang, H.-X. Peng, and F. Qin, Enhanced mechanical and electrical properties of carbon nanotube buckypaper by in situ cross-linking, *Carbon* 63, 125–132 (2013).
- [79] C. F. Cornwell, and C. R. Welch, Very-high-strength (60-GPa) carbon nanotube fiber design based on molecular dynamics simulations, *J. Chem. Phys.* 134, 204708 (2011).
- [80] D. Frenkel, B. Smit, *Understanding Molecular Simulation: From Algorithms to Applications*, Academic Press. London, 1996. ISBN 978-0-12-267351-1.
- [81] D.C. Rapaport, *The Art of Molecular Dynamics Simulation*, ISBN 9780511816581.
- [82] L. V. Zhigilei, C. Wei, and D. Srivastava, Mesoscopic model for dynamic simulations of carbon nanotubes, *Phys. Rev. B* 71, 165417 (2005).
- [83] M. Huhtala, A. V. Krasheninnikov, J. Aittoniemi, S. J. Stuart, K. Nordlund, and K. Kaski, Improved mechanical load transfer between shells of multiwalled carbon nanotubes, *Phys. Rev. B* 70, 045404 (2004).
- [84] S. J. V. Frankland, A. Caglar, D. W. Brenner, and M. Griebel, Molecular Simulation of the Influence of Chemical CL on the Shear Strength of Carbon Nanotube–Polymer Interfaces, *J. Phys. Chem. B* 106, 12, 3046–3048 (2002).
- [85] M. Wong, M. Paramsothy, X.J. Xu, Y. Ren, S. Li, K. Liao, Physical interactions at carbon nanotube-polymer interface, *Polymer* 44 (25), 7757-7764 (2003).
- [86] S. Namilaee, N. Chandra, Mechanical behavior of functionalized nanotubes, *Chem. Phys. Lett.* 387 (4-6), 247-252 (2004).
- [87] S. Govindjee, J. L. Sackman, On the use of continuum mechanics to estimate the properties of nanotubes, *Solid State Communications* 110(4), 227-230 (1999).
- [88] C.Q. Ru, Column buckling of multiwalled carbon nanotubes with interlayer radial displacements, *Phys. Rev. B* 62, 16962 (2000).
- [89] M. J. Leamy, Bulk dynamic response modeling of carbon nanotubes using an intrinsic finite element formulation incorporating interatomic potentials, *Int. J. Solids Struct.* 44, 874-894 (2007).
- [90] M. J. Buehler, Mesoscale modeling of mechanics of carbon nanotubes: Self-assembly, self-folding, and fracture, *J. Mater. Res.* 21, 2855-2869 (2006).
- [91] A. N. Volkov and L. V. Zhigilei, Mesoscopic interaction potential for carbon nanotubes of arbitrary length and orientation, *J. Phys. Chem. C* 114, 5513-5531 (2010).

-
- [92] A. N. Volkov and L. V. Zhigilei, Structural stability of carbon nanotube films: The role of bending buckling, *ACS Nano* 4, 6187-6195 (2010).
- [93] I. Ostanin, R. Ballarini, D. Potyondy, and T. Dumitrică, A distinct element method for large scale simulations of carbon nanotube assemblies, *J. Mech. Phys. Solids* 61, 762-782 (2013).
- [94] H. Torabi, H. Radhakrishnan, and S. Dj. Mesarovic, Micromechanics of collective buckling in CNT turfs, *J. Mech. Phys. Solids* 72, 144-160 (2014).
- [95] M. R. Maschmann, Integrated simulation of active carbon nanotube forest growth and mechanical compression, *Carbon* 86, 26-37 (2015).
- [96] J. A. Aström, A.V. Krasheninnikov, and K. Nordlund, Carbon nanotube mats and fibers with irradiation-improved mechanical characteristics: A theoretical model, *Phys. Rev. Lett.* 93, 215503 (2004).
- [97] I. Ostanin, R. Ballarini, T. Dumitrică, Distinct element method for multiscale modelling of cross-linked carbon nanotube bundles: From soft to strong nanomaterials, *J. Mater. Res.* 30, 19-25 (2015).
- [98] A. N. Volkov and A. H. Banna, Mesoscopic computational model of covalent CL and mechanisms of load transfer in cross-linked carbon nanotube films with continuous networks of bundles, *Comp. Mater. Sci.* 176, 109410 (2020).
- [99] H. L. Cox, The elasticity and strength of paper and other fibrous materials, *Br. J. Appl. Phys.* 3, 72-79 (1952).
- [100] B. K. Wittmaack, A. N. Volkov, and L. V. Zhigilei, Mesoscopic modeling of the uniaxial compression and recovery of vertically aligned carbon nanotube forests, *Composites Sci. Technol.*, 166, 66-85 (2018).
- [101] B. K. Wittmaack, A. N. Volkov, and L. V. Zhigilei, Phase transformation as the mechanism of mechanical deformation of vertically aligned carbon nanotube arrays: Insights from mesoscopic modeling, *Carbon* 143, 587-597 (2019).
- [102] A. H. Banna, K. W. Kayang, A. N. Volkov, Effects of the nanotube length and network morphology on the deformation mechanisms and mechanical properties of cross-linked carbon nanotube films, *J. of App. Phys.* 129, 105101 (2021).
- [103] L. V. Zhigilei, P. B. S. Kodali, and B. J. Garrison, A microscopic view of laser ablation, *J. Phys. Chem. B* 102, 2845 (1998).
- [104] A. N. Volkov, K. R. Simov, and L. V. Zhigilei, Mesoscopic model for simulation of CNT-based materials, *Proc. of the ASME International Mechanical Engineering Congress and Exposition*, ASME paper IMECE2008-68021, 11 p., (2008).
- [105] M. J. Buehler, Mesoscale modeling of mechanics of carbon nanotubes: Self-assembly, self-folding, and fracture, *J. Mater. Res.* 21, 2855-2869 (2006).
- [106] The cutoff of the nonbonding interaction potential at large distances is not explicitly discussed in Ref. 114 but is used in the computational code implementing the AIREBO potential and provided to authors of Ref. 91 by Steven Stuart of Clemson University.

-
- [107] L. Pastewka, P. Pou, R. Perez, P. Gumbsch, and M. Moseler, Describing bond-breaking processes by reactive potentials: importance of an environment-dependent interaction range, *Phys. Rev. B* 78, 161402 (2008).
- [108] J.J. Vilatela, J.A. Elliott, A.H. Windle, A model for the strength of yarn-like carbon nanotube fibers, *ASC Nano* 5, 1921-1297 (2011).
- [109] M. S. Dresselhaus, G. Dresselhaus, and R. Saito, Physics of carbon nanotubes, *Carbon* 33, 883-891 (1995).
- [110] L.A. Girifalco, M. Hodak, R.S. Lee, Carbon nanotubes, buckyballs, ropes, and a universal graphitic potential, *Phys. Rev. B* 62, 13104-13110 (2000).
- [111] C.-H. Sun, L.-C. Yin, F. Li, G.-Q. Lu, and H.-M. Cheng, Van der Waals interactions between two parallel infinitely long single-walled nanotubes, *Chem. Phys. Lett.* 403, 343-346 (2005).
- [112] C.-H. Sun, G.-Q. Lu, and H.-M. Cheng, Simple approach to estimating the van der Waals interaction between carbon nanotubes, *Phys. Rev. B* 73, 195414 (2006).
- [113] D. W. Brenner, O.A. Shenderova, J.A. Harrison, S.J. Stuart, B. Ni, and S.B. Sinnott, A second-generation reactive empirical bond order (REBO) potential energy expression for hydrocarbons, *J. Phys.: Condens. Matter* 14, 783-802 (2002).
- [114] S.J. Stuart, A.B. Tutein, and J.A. Harrison, A reactive potential for hydrocarbons with intermolecular interactions, *J. Chem. Phys.* 112, 6472-6486 (2000).
- [115] J. Tersoff, New empirical approach for the structure and energy of covalent systems, *Phys. Rev. B* 37, 6991-7000 (1988).
- [116] The MD simulation of the pullout process for a cross-linked bundle of (10,10) CNTs were performed by Arun B. Thapa using LAMMPS particle simulator.
- [117] M. P. Allen, D. J. Tildesley, *Computer Simulation of Liquids* (Clarendon Press, Oxford, 1987).
- [118] H.J.C. Berendsen, J.P.M. Postma, W.F. van Gunsteren, A. DiNola, J.R. Haak, Molecular dynamics with coupling to an external bath, *J. Chem. Phys.* 81, 3684-3690 (1984).
- [119] <http://volkov.eng.ua.edu/>
- [120] Y. Won, Y. Gao, M. A. Panzer, R. Xiang, S. Maruyama, T. W. Kenny, W. Cai, and K. E. Goodson, Zipping, entanglement, and the elastic modulus of aligned single-walled carbon nanotube films, *PNAS* 110, 20426-20430 (2013).
- [121] A. N. Volkov, K. R. Simov, and L. V. Zhigilei, Mesoscopic simulation of self-assembly of carbon nanotubes into a network of bundles, *Proceedings of the 47th AIAA Aerospace Sciences Meeting*, AIAA paper 2009-1544 (2009).
- [122] S. W. Cranford and M. J. Buehler, In silico assembly and nanomechanical characterization of carbon nanotube buckypaper, *Nanotechnology* 21, 265706 (2010).
- [123] A. N. Volkov and L. V. Zhigilei, Scaling laws and mesoscopic modeling of thermal conductivity in carbon nanotube materials, *Phys. Rev. Lett.* 104, 215902 (2010).
- [124] E.A. Colbourn (ed.), *Computer Simulation of Polymers* (Longman, Harlow, 1994).

-
- [125] B. Xie, Y. Liu, Y. Ding, Q. Zheng, and Z. Xu, Mechanics of carbon nanotube networks: microstructural evolution and optimal design, *Soft Matter* 7, 10039-10047 (2011).
- [126] C. Wang, B. Xie, Y. Liu, and Z. Xu, Mechanotunable microstructures of carbon nanotube networks, *ACS Macro Letters* 1, 1176-1179 (2012).
- [127] Y. Li and M. Kröger, Viscoelasticity of carbon nanotube buckypaper: Zipping-unzipping mechanism and entanglement effects, *Soft Matter* 8, 7822-7830 (2012).
- [128] Y Li and M Kröger, A theoretical evaluation of the effects of carbon nanotube entanglement and bundling on the structural and mechanical properties of buckypaper, *Carbon* 50, 1793-1806 (2012).
- [129] Y. Li and M. Kröger, Computational study on entanglement length and pore size of carbon nanotube buckypaper, *Appl. Phys. Lett.* 100, 021907 (2012).
- [130] M.G. Hahm, H. Wang, H.Y. Jung, S. Hong, S.-G. Lee, S.-R. Kim, M. Upmanyu, Y.J. Jung, Bundling dynamics regulates the active mechanics and transport in carbon nanotube networks and their nanocomposites, *Nanoscale* 4, 3584-3590 (2012).
- [131] J. Zhao, J.-W. Jiang, L. Wang, W. Guo, T. Rabczuk, Coarse-grained potentials of single-walled carbon nanotubes, *J. Mech. Phys. Solid.* 71, 197-218 (2014).
- [132] D. Janas and K. K. Koziol, Carbon nanotube fibers and films: synthesis, applications and perspectives of the direct spinning method, *Nanoscale* 8 19475-19490 (2016).
- [133] H. Yue, V. Reguero, E. Senokos, A. Monreal-Bernal, B. Mas, J. P. Fernández-Blázquez, R. Marcilla, and J. J. Vilatela, Fractal carbon nanotube fibers with mesoporous crystalline structure, *Carbon* 122, 47-53 (2017).
- [134] A. V. Neimark, S. Ruetsch, K. G. Kornev, P. I. Ravikovitch, P. Poulin, S. Badaire, and M. Maugey, Hierarchical pore structure and wetting properties of single-wall carbon nanotube fibers, *Nano Lett.* 3, 419-423 (2003).
- [135] B. K. Wittmaack, A. H. Banna, A. N. Volkov, L. V. Zhigilei, Mesoscopic modeling of structural self-organization of carbon nanotubes into vertically aligned networks of nanotube bundles, *Carbon* 130, 69-86 (2018).
- [136] Wang, Z. Liang, G. Pham, Y.-B. Park, B. Wang, C. Zhang, L. Kramer, P. Funchess, Controlled nanostructure and high loading of single-walled carbon nanotubes reinforced polycarbonate composite, *Nanotechnology* 18, 095708 (2007).
- [137] E. K. Hobbie, D. O. Simien, J.A. Fagan, J.Y. Huh, J.Y. Chung, S.D. Hudson, J. Obrzut, J.F. Douglas, and C.M. Stafford, Wrinkling and strain softening in single-wall carbon nanotube membranes, *Phys. Rev. Lett.* 104, 125505 (2010).
- [138] J. M. Harris, G. R. S. Iyer, D. O. Simien, J. A. Fagan, J. Y. Huh, J. Y. Chung, S. D. Hudson, J. Obrzut, J. F. Douglas, C. M. Stafford, and E. K. Hobbie, Structural stability of transparent conducting films assembled from length purified single-wall carbon nanotubes, *J. Phys. Chem. C* 115, 3973-3981 (2011).
- [139] T. V. Sreekumar, T. Liu, S. Kumar, L. M. Ericson, R. H. Hauge, and R. E. Smalley, Single-wall carbon nanotube films, *Chem. Mater.* 15, 175-178 (2013).

-
- [140] S. Malik, H. Rösner, F. Hennrich, A. Böttcher, M. M. Kappes, T. Beck, and M. Auhorn, Failure mechanism of free standing single-walled carbon nanotube thin films under tensile load, *Phys. Chem. Chem. Phys.* 6, 3540-3544 (2004).
- [141] Z. Wang, Z. Liang, B. Wang, C. Zhang, and L. Kramer, Processing and property investigation of single-walled carbon nanotube (SWNT) buckypaper/epoxy resin matrix nanocomposites, *Composites Part A* 35, 1225-1232 (2004).
- [142] W. Ma, L. Song, R. Yang, T. Zhang, Y. Zhao, L. Sun, Y. Ren, D. Liu, L. Liu, J. Shen, Z. Zhang, Y. Xiang, W. Zhou, and S. Xie, Directly synthesized strong, highly conducting, transparent single-walled carbon nanotube films, *Nano Lett.* 7, 2307-2311 (2007).
- [143] F. M. Blighe, P. E. Lyons, S. De, W. J. Blau, and J. N. Coleman, On the factors controlling the mechanical properties of nanotube films, *Carbon* 46, 41-47 (2008).
- [144] S. Wang, Z. Liang, G. Pham, Y.-B. Park, B. Wang, C. Zhang, L. Kramer, P. Funchess, Controlled nanostructure and high loading of single-walled carbon nanotubes reinforced polycarbonate composite, *Nanotechnology* 18, 095708 (2007).
- [145] Y. J. Ma, X. F. Yao, Q. S. Zheng, Y. J. Yin, D. J. Jiang, G. H. Xu, F. Wei, and Q. Zhang, Carbon nanotube films change Poisson's ratios from negative to positive, *Appl. Phys. Lett.* 97, 061909 (2010).
- [146] H. W. Zhu, C. L. Xu, D. H. Wu, B. Q. Wei, R. Vajtai, and P. M. Ajayan, Direct synthesis of long single-walled carbon nanotube strands, *Science* 296, 884-886 (2002).
- [147] A. G. Nasibulin, A. Kaskela, K. Mustonen, A. S. Anisimov, V. Ruiz, S. Kivisto, S. Rackauskas, M. Y. Timmermans, M. Pudas, B. Aitchison, M. Kauppinen, D. P. Brown, O. G. Okhotnikov, and E. I. Kauppinen, Multifunctional free-standing single-walled carbon nanotube films, *ACS Nano* 5, 3214-3221 (2011).
- [148] J. Zhang, D. Jiang, H.-X. Peng, and F. Qin, Enhanced mechanical and electrical properties of carbon nanotube buckypaper by in situ cross-linking, *Carbon* 63, 125-132 (2013).
- [149] M.B. Jakubinek, B. Ashrafi, J. Guan, M.B. Johnson, M.A. White, and B. Simard, 3D chemically cross-linked single-walled carbon nanotube buckypapers, *RSC Adv.* 4, 57564-57573 (2014).
- [150] S. V. Ahir, E. M. Terentjev, S. X. Lu, and B. Panchapakesan, Thermal fluctuations, stress relaxation, and actuation in carbon nanotube networks, *Phys. Rev. B.* 76, 165437 (2007).
- [151] A. Cao, P. L. Dickrell, W. G. Sawyer, M. N. Ghasemi-Nejhad, and P. M. Ajayan, Super-compressible foamlike carbon nanotube films, *Science* 310, 1307-1310 (2005).
- [152] A. A. Zbib, S. D. Mesarovic, E. T. Lilleodden, D. McClain, J. Jiao, and D. F. Bahr, The coordinate buckling of carbon nanotube turfs under uniform compression, *Nanotechnology* 19, 175704 (2008).
- [153] The values of the relief features height are not directly available in Ref. [137] and are only roughly estimated based on the provided AFM image of a wrinkled CNT film.